

---

# Mixing processes in stellar interiors: new insights from asteroseismology

Víctor Silva Aguirre

---



München 2011



---

# Mixing processes in stellar interiors: new insights from asteroseismology

Víctor Silva Aguirre

---

Dissertation  
an der Fakultäts für Physik  
der Ludwig–Maximilians–Universität  
München

vorgelegt von  
Víctor Silva Aguirre  
aus Santiago, Chile

München, den 14.10.2011

Erstgutachter: Priv. Doz. Dr. Achim Weiß

Zweitgutachter: Priv. Doz. Dr. Joachim Puls

Tag der mündlichen Prüfung: 30.11.2011

# Contents

<b>Zusammenfassung</b>	<b>xiii</b>
<b>Summary</b>	<b>xiv</b>
<b>Preface</b>	<b>xvi</b>
<b>1 Basic principles of stellar structure and evolution</b>	<b>1</b>
1.1 Preliminary considerations . . . . .	1
1.1.1 Relevant time scales . . . . .	1
1.1.2 Nuclear reactions and chemical composition . . . . .	2
1.2 Evolution across the Hertzsprung–Russell Diagram . . . . .	5
1.2.1 Pre-main sequence phase . . . . .	5
1.2.2 Main sequence evolution . . . . .	6
1.2.3 Subgiants, giants, and clump giants . . . . .	8
1.2.4 Advanced stages of evolution . . . . .	10
1.3 Modeling stars: a naive first look . . . . .	11
1.3.1 Macrophysics . . . . .	12
1.3.2 Microphysics . . . . .	15
1.3.3 Modeling stars with GARSTEC . . . . .	16
1.4 Pulsating stars . . . . .	17
<b>2 Stellar oscillations</b>	<b>23</b>
2.1 Fluid dynamics . . . . .	23
2.1.1 Continuity equation . . . . .	24
2.1.2 Euler’s equation . . . . .	24
2.1.3 Energy equation . . . . .	25
2.1.4 Heat transfer . . . . .	26
2.2 Equations of non-radial stellar oscillations . . . . .	27
2.2.1 Equilibrium structure and perturbation theory . . . . .	27
2.2.2 Separation of variables . . . . .	29
2.2.3 Modes, frequencies and asymptotic analysis . . . . .	31
2.2.4 Frequency differences . . . . .	36
2.3 The CoRoT and <i>Kepler</i> missions . . . . .	40

<b>3</b>	<b>Mixing processes in stellar cores</b>	<b>47</b>
3.1	Motivation: the case of HD 49933 . . . . .	47
3.2	Ingredients of the stellar models . . . . .	52
3.2.1	Boundaries of convective and semiconvective zones . . . . .	52
3.2.2	Prescription for semiconvective layers . . . . .	53
3.3	Impact on the stellar models . . . . .	54
3.3.1	Convective boundary definition criteria . . . . .	55
3.3.2	Main-sequence evolution . . . . .	57
3.3.3	Effects of mixing in semiconvective layers . . . . .	58
3.4	Discussion . . . . .	60
<b>4</b>	<b>Asteroseismic diagnoses for stellar interiors</b>	<b>63</b>
4.1	Introduction . . . . .	63
4.2	Seismic variables suited to isolate the core . . . . .	64
4.3	Sensitivity of $r_{10}$ and $r_{01}$ to the core . . . . .	65
4.4	Influence of mixing prescriptions on $r_{10}$ and $r_{01}$ . . . . .	68
4.5	Breaking the degeneracy: splitting mixing prescriptions and finding convective cores . . . . .	71
4.6	Discussion . . . . .	74
<b>5</b>	<b>Ensemble asteroseismology using <i>Kepler</i> data</b>	<b>77</b>
5.1	Introduction . . . . .	77
5.2	Extracting mass and radius from asteroseismic data . . . . .	78
5.3	Data analysis and stellar properties determination . . . . .	80
5.4	Results . . . . .	82
5.5	Discussion . . . . .	87
5.6	Conclusions . . . . .	89
<b>6</b>	<b>Sounding deep stellar interiors: convective cores in <i>Kepler</i> main-sequence targets</b>	<b>91</b>
6.1	Introduction . . . . .	91
6.2	Characteristics of the chosen targets . . . . .	92
6.3	Grid-based analysis . . . . .	93
6.4	The frequency ratios: precise mass estimations . . . . .	95
6.5	The frequency ratios: unveiling convective cores . . . . .	102
6.6	Discussion and perspectives . . . . .	110
<b>7</b>	<b>Conclusions and future outlook</b>	<b>115</b>
7.1	Mixing, convective cores, and main-sequence evolution . . . . .	115
7.2	Probing convective cores with stellar pulsations . . . . .	116
7.3	From dreams to data: stellar cores as seen by <i>Kepler</i> . . . . .	117
7.4	From individual stars to stellar populations and galaxies: the future of asteroseismology . . . . .	118

<b>A Variable separation and spherical harmonics</b>	<b>121</b>
<b>Bibliography</b>	<b>127</b>
<b>Acknowledgments</b>	<b>138</b>
<b>Curriculum Vitae</b>	<b>141</b>



# List of Figures

1.1	Hertzsprung-Russell Diagram for different masses at a fixed composition . . . . .	6
1.2	Hertzsprung-Russell Diagram of main-sequence and red giant evolution for 1 $M_{\odot}$ and 8 $M_{\odot}$ stars . . . . .	7
1.3	Evolution in the HRD of a low-mass star in the helium burning phase . . . . .	10
1.4	Pulsation HR Diagram . . . . .	19
1.5	Power spectra of stars from the main-sequence to red giant phase showing oscillations . . . . .	21
1.6	Power spectra of some red giant stars with oscillations detected . . . . .	22
2.1	Lamb and buoyancy frequency in a model of the present Sun . . . . .	33
2.2	Dimensionless frequency in different evolutionary stages . . . . .	35
2.3	Ray propagation in the solar interior . . . . .	36
2.4	Large and small frequency separation in a portion of the solar spectrum . . . . .	38
2.5	Solar Echelle Diagram . . . . .	39
2.6	Eigenfunctions of selected p-modes . . . . .	41
2.7	Eigenfunctions of selected g-modes . . . . .	42
2.8	Main-sequence and subgiant oscillators in the <i>Kepler</i> field . . . . .	44
2.9	Period spacings of red giants in the <i>Kepler</i> field . . . . .	45
3.1	Echelle diagram of the star HD 49933 from the first run of data . . . . .	48
3.2	Evolutionary tracks for best-fit models for HD 49933 . . . . .	49
3.3	Echelle diagram for the models of HD 49933 . . . . .	50
3.4	Internal structure of a 1.5 $M_{\odot}$ stellar model in the main-sequence phase . . . . .	54
3.5	Evolution of the convective core boundary for two criteria for convective boundary definition . . . . .	55
3.6	Hertzsprung-Russell diagram for different masses and convective boundary definition. . . . .	57
3.7	Central hydrogen content during their main sequence evolution. . . . .	59
3.8	Hydrogen profiles for 1.5 $M_{\odot}$ models using different mixing prescriptions . . . . .	60
4.1	Frequency ratios and evolution of 1.1 $M_{\odot}$ models with and without convective core. . . . .	66
4.2	Frequency ratios of 1.1 $M_{\odot}$ models with and without convective core at the same central hydrogen content. . . . .	67

4.3	Comparison of frequency ratios for $1.3 M_{\odot}$ models at equal central hydrogen contents. . . . .	69
4.4	Comparison of frequency ratios for $1.3 M_{\odot}$ models at equal large frequency separation value. . . . .	70
4.5	Slope versus mean diagram of the frequency ratios. . . . .	73
5.1	Power spectrum of the Sun obtained by the Birmingham Solar- Oscillations Network (BiSON) . . . . .	79
5.2	$T_{\text{eff}}-\nu_{\text{max}}$ for the complete sample of <i>Kepler</i> main-sequence stars with detected oscillations . . . . .	80
5.3	Position in the $\log g-T_{\text{eff}}$ plane of <i>Kepler</i> targets with masses within $1 M_{\odot} \pm 15\%$ . . . . .	82
5.4	Comparison of stellar parameters determined by asteroseismology with those obtained from spectroscopy . . . . .	84
5.5	Frequency ratios of selected models from the $1.0 M_{\odot}$ and $1.15 M_{\odot}$ tracks at solar metallicity . . . . .	85
5.6	Metallicity distribution of the <i>Kepler</i> field simulated with SMAUG . . . . .	86
6.1	Echelle diagram of Perky showing clear signatures of oscillations detected . . . . .	93
6.2	Echelle diagram of Dushera showing clear signatures of oscillations detected . . . . .	94
6.3	Evolutionary tracks of models for Perky of different masses . . . . .	96
6.4	Echelle diagram of the solar BiSON data and the standard solar model . . . . .	97
6.5	Echelle diagram for models of Perky . . . . .	98
6.6	Large frequency separation and frequency ratios for three models of Perky of different masses . . . . .	99
6.7	Evolutionary tracks of models for Perky for different metallicities . . . . .	100
6.8	Large frequency separation and frequency ratios for models of Perky at different metallicities . . . . .	101
6.9	Evolutionary tracks of models for Dushera at different masses . . . . .	103
6.10	Large frequency separation and frequency ratios for three models of Dushera of different masses . . . . .	104
6.11	Frequency ratios for models of Dushera of different masses, with and without overshooting . . . . .	106
6.12	Frequency ratios for models of Dushera of different metallicities, including overshooting . . . . .	107
6.13	Slope versus mean diagram for the data of Dushera and the best-fit models . . . . .	108
6.14	Small frequency separations for models of Dushera of different metallicities, including overshooting . . . . .	110
A.1	Example of the geometry of spherical harmonics . . . . .	125

# List of Tables

1.1	Chains for hydrogen burning . . . . .	3
4.1	Properties of models for different masses and mixing prescriptions with the same large frequency separation value. . . . .	71
5.1	Stellar parameters determined by asteroseismology , IRFM and spectroscopy . . .	83
6.1	Stellar and global seismic parameters of two <i>Kepler</i> targets . . . . .	92
6.2	Characteristics of the evolutionary grids of models . . . . .	94
6.3	Input stellar parameters used in the grid-based analysis of <i>Kepler</i> targets . . . . .	95
6.4	Masses for two <i>Kepler</i> targets estimated using the direct and the grid-based methods	95
6.5	Characteristics of the Dushera models for different masses and metallicities . . .	105
6.6	Comparison of a model of Dushera with fits to M67 . . . . .	112



# Zusammenfassung

Das Verständnis der physikalischen Prozesse, welche die Sternentwicklung bestimmen, sowie die präzise Bestimmung der stellaren Parameter wie Alter, Masse, Radius und Metallizität ist von herausragender Bedeutung für viele Bereiche der Astrophysik. Aus der stellaren Entwicklung abgeleitete Größen werden regelmäßig verwendet, um die Struktur, Entstehungsgeschichte sowie Dynamik von Sternpopulationen zu untersuchen. Ein fundamentaler Bestandteil der Theorie der Sternentwicklung ist der Energietransport durch Konvektion. Man geht davon aus, dass Sterne mit Massen über  $1.1 M_{\odot}$  während ihrer Hauptreihenentwicklung eine homogen durchmischte Zentralregion ausbilden, deren genaue Ausdehnung jedoch nicht mit Hilfe von einfachen Annahmen abgeleitet werden kann. In der vorliegenden Arbeit beschreibe ich den Einfluss von verschiedenen konvektiven Stabilitäts- und Grenzdefinitionen auf die Größe des konvektiven Kerns und die allgemeine Entwicklung von Hauptreihensternen im Massenbereich um  $1.3 \pm 0.2 M_{\odot}$ .

Durch Berücksichtigung von Durchmischungsprozessen jenseits der formalen Grenzbedingungen wie Semikonvektion oder 'Overshooting' untersuche ich den Einfluss der Größe des konvektiven Kerns auf die Hauptreihenlebensdauer. Die Bedeutung jener Prozesse in Evolutionsrechnungen bedingt die Untersuchung tiefliegender Sternschichten mit Hilfe von Techniken, welche über einfaches Anpassen von Isochronen hinausgehen. Asteroseismologie hat sich in diesem Zusammenhang als die leistungsfähigste Methode erwiesen, um äußere Sternschichten zu durchdringen und das Sterninnere zu untersuchen.

Durch die Verwendung geeigneter Kombinationen von Schwingungsfrequenzen entwickeln wir ein asteroseismisches Instrument, welches sensitiv für die tiefsten Sternschichten ist. Wir testen dieses Instrumentarium mit Hilfe theoretischer Schwingungsrechnungen. Dabei stellt sich heraus, dass wir damit in der Lage sind, zwischen Sternen mit und ohne konvektivem Kern zu unterscheiden. Ebenso ist es möglich, die Größe eines eventuellen Kernes mit großer Genauigkeit zu bestimmen. Da eine seismische Diagnose eine genaue Kenntnis der Sternmasse voraussetzt, untersuchen wir ebenfalls die Möglichkeit, die Masse mit Hilfe von genau bekannten Werten der Sonne sowie entsprechenden asteroseismischen Skalenrelationen abzuschätzen.

Die Verwendung der Daten des *Kepler* Satelliten, der die Oszillationen hunderter Sterne genauestens vermisst, erlaubt uns erstmalig, eine Sequenz von Feld-Sternen mit Massen vergleichbar der Sonne anhand ihrer seismischen Parameter und Effektivtemperaturen aufzustellen. Zwei dieser Sterne wurden lange genug beobachtet, um individuelle Frequenzen mit hoher Präzision zu bestimmen. Die detaillierte Modellierung dieser Sterne, sowie die asteroseismische Analyse der beobachteten Frequenzen erlaubt es, zwischen einem Stern ohne und einem mit konvektivem Kern zu unterscheiden, sowie zum ersten Mal die Größe eines vollständig durchmischten Kernes innerhalb eines Sternes mit einer Unsicherheit von weniger als 1% zu messen.



# Summary

Understanding the physical processes governing stellar evolution and determining stellar parameters such as ages, masses, radii and metallicities is of paramount importance for many fields in astrophysics. Derived quantities from evolutionary calculations are routinely used to constrain composite stellar populations and determine their structure, formation history, dynamics, and kinematics. One key ingredient of the theory of stellar evolution is that of energy transport by convective motions. It is believed that stars with masses larger than  $\sim 1.1 M_{\odot}$  develop a homogeneously mixed central region during their main-sequence evolution, but its exact extent cannot be derived from first principles.

In this thesis, we describe the impact that different convective stability and boundary definitions have in the size of convective cores and overall evolution of main-sequence stars of masses  $1.3 \pm 0.2 M_{\odot}$ . By considering mixing processes beyond the formal boundaries such as semiconvection and overshooting, we study the influence of the convective core size in quantities such as main-sequence lifetimes. While assessing the importance of a precise description of these processes in evolutionary calculations, we also realize the necessity of probing the deep layers of stars with a technique more accurate than isochrone fitting. In this respect, asteroseismology has been shown to be the most powerful technique capable of piercing the outer layers of stars and probing their interiors.

Using suitable combinations of oscillation frequencies, we develop an asteroseismic tool sensitive to the deepest layers of stellar interiors. We test this tool using theoretical frequency calculations and find that it is capable of discriminating between stars with and without a convective core, while setting tight constraints on the size of a convective core when this is present. As the application of this seismic diagnosis requires a good estimate of stellar mass, we explore the possibility of determining stellar masses using asteroseismic scaling relations from the accurately known solar values.

Taking advantage of the hundreds of stars with oscillations detected by the *Kepler* mission, we are for the first time able to correctly identify a sequence of field stars with masses similar to the Sun using their global seismic parameters and effective temperatures. Two of these targets have been observed long enough for individual frequencies to be determined with high level of precision. Doing detailed modeling of these stars and applying our asteroseismic tool to the observed frequency combinations, we are able to disentangle a star without a convective core and directly measure, for the first time, the size of the fully mixed core in a star with an uncertainty of less than 1%.



# Preface

A comprehensive view on how stars evolve and interact with their surrounding medium is crucial for many fields in astrophysics. Current techniques used to estimate parameters such as ages, masses, radii and metallicities in stellar populations heavily rely on having adequate evolutionary calculations of their member stars. This impacts the results in diverse topics of study such as structure and formation history of galaxies, dynamics and kinematics of stellar systems, or characterization of parent stars in planetary systems, just to name a few. These evolutionary models, however, require an accurate description of the relevant evolutionary phases for different stellar masses; we can only accomplish this by correctly describing the physical processes taking place in stellar interiors during a star's lifetime.

The luminosity flux radiated from the surface of a star is naturally a consequence of the intricate processes taking place in the stellar interior. Although the main ingredients of the theory of stellar evolution are well established, large uncertainties still remain in cases where empirical evidence is lacking or the physical descriptions are not well understood and thus parametrized to a simple form. How stars produce, transport, and emit their energy; how they burn and mix chemical elements; how is the stellar matter constituted and what is its state, etc., are some of the important topics where still many uncertainties exist.

A crucial example of these cases is mixing due to convective motions in stellar interiors, which due to its complexity and short relevant time scales is usually parametrized in stellar evolution calculations. During the main-sequence phase in low- and intermediate-mass stars, the existence and size of a central convectively mixed zone determines the total amount of fuel available for nuclear burning, the size of the remaining helium core, and to a large extent the age of stars at the turn-off. This not only affects the subsequent evolution once hydrogen in the center is exhausted, but it also critically impacts the most commonly used techniques to determine stellar ages such as isochrone fitting.

Up to now, the existence and size of convective cores in the main-sequence phase cannot be directly inferred from classical observations, and are usually estimated by reproducing features observed in the Color Magnitude Diagram of certain simple stellar populations. However, this technique is affected by many other ingredients of stellar evolution that are not accurately known, such as the helium abundances, distribution of metals, nuclear reaction rates, etc. To overcome this limitation, we need a different approach that allows us to pierce the outer layers of a star and probe its inner regions.

In this respect, stellar pulsations have been long known to be an indicator of the conditions in the deep layers of stars. Although radial pulsations in stars such as Cepheids and RR Lyrae

are mostly used as distance indicators (e.g., Leavitt & Pickering 1912; Catelan et al. 2004), their period of pulsation is intrinsically dependent on the state of stellar matter in the ionization zones. However, a dramatic leap forward occurred in the field when oscillations in the Sun were discovered (Leighton et al. 1962), giving birth to the field of helioseismology. These data have served for extracting the adiabatic sound speed and density profiles of the Sun, determining the location of the solar helium second ionization zone and the base of the convective envelope, constraining the solar surface abundances, and providing the constraints that finally led to the solution of the solar neutrino problem (see Christensen-Dalsgaard 2002; Basu & Antia 2008, and references therein).

Helioseismology has so far provided the best example of indirect observations of the interior of a star by piercing the outer layers of the Sun using the oscillations observed at its surface. Extending these techniques to other stars by means of asteroseismology requires long continuous observations to detect the global oscillations in stars much further away. With this purpose in mind, the CoRoT (Convection, Rotation and planetary Transits Baglin et al. 2006) and *Kepler* (Borucki et al. 2009) missions were launched to monitor thousands of stars for a period of several years and detect their oscillations.

With the idea of taking advantage of the current flow of data, this thesis deals with the topic of mixing processes in stellar interiors, in particular convective mixing in stellar cores, and the potential of asteroseismology to constrain these processes and derive more accurate stellar parameters. We<sup>1</sup> have implemented in an evolutionary code different scenarios for convective mixing in stellar cores, and tested their impact on the evolution of stars where oscillations are expected to be detected by the aforementioned space missions. We have developed an asteroseismic diagnostic tool sensitive to the deepest layers of stars and analyzed its behavior according to the conditions in the stellar center. This allowed us to put constraints in the existence and size of convective cores in main sequence stars, and derive precise ages and evolutionary stages for main-sequence stars observed by the *Kepler* mission.

This dissertation consists of seven chapters of which two are introductory, four contain articles published or in preparation for refereed publications, and one summarizing the main conclusion and future prospects. Chapter 1 contains the basic picture of stellar evolution, giving context of the current status and challenges in the field particularly related to asteroseismology. In Chapter 2 the theory of stellar oscillations is described, emphasizing the dependence on the inner structure of stars and how this information has been used to constrain processes in stellar interiors. Chapter 3 describes the implementation of the mixing processes for stellar cores in our evolutionary code, and shows the impact they have during main-sequence evolution of low- and intermediate-mass stars.

With this in mind, in Chapter 4 we apply to our theoretical models a combination of frequencies sensitive to the deep interior, and study the variations of this frequency combination according to different conditions in the stellar core. However, this frequency combination needs information about the stellar mass, which is why we explore in Chapter 5 a technique to determine the mass of a star from its global asteroseismic parameters and effective temperature.

---

<sup>1</sup>The pronoun ‘we’ is used throughout this dissertation only as a matter of formal semantics. Unless otherwise specified, ‘we’ refers to work developed and led by the author of this thesis.

Finally, we apply in Chapter 6 the asteroseismic tools developed to disentangle a star without a convective core using its individual frequency determinations, and to constrain the size of a convective core in a star containing a homogeneously mixed central region.

I am the main author of all the sections in this thesis, although the introductory chapters have been based on the references I mention at the beginning of them. I am co-author of some papers that are mentioned in Chapters 1 and 2, although the topic of those publications is not directly related to the core of the work I have developed for this thesis.



# Chapter 1

## Basic principles of stellar structure and evolution

The following chapter briefly introduces the basics of stellar evolution theory, with particular emphasis on those topics related to stellar pulsations and asteroseismology. The interested reader can find much more detailed accounts on these subjects in several of the standard astrophysics textbooks consulted for this chapter, such as Clayton (1983); Kippenhahn & Weigert (1990); Hansen et al. (2004); Salaris & Cassisi (2005), and Weiss et al. (2005), just to name a few. There are also reviews available in the literature for different types of stars and evolutionary phases, such as those of Salaris et al. (2002); Catelan (2007), and Catelan (2009).

### 1.1 Preliminary considerations

The vast majority of stars are currently in long-lasting phases of their evolution, in which the time scales involved for appreciable change to occur are too large to be observed. Stellar matter is naturally victim of interacting forces such as gravitation and pressure, but if no acceleration of material takes place a stage of mechanical equilibrium is maintained. This equilibrium in a star, referred to as hydrostatic equilibrium, is one of the pillars of stellar structure studies.

#### 1.1.1 Relevant time scales

Stars owe their brightness to a delicate interplay between gravitational contraction and thermonuclear reactions as energy generation sources, both mechanisms not always acting simultaneously. This interaction produces changes in the star of different relevance and time scales, which are important for stellar oscillations.

When nuclear reactions are not efficient in producing energy, the physical conditions in stellar interiors evolve with the rate of change of the gravitational potential and internal energy. We can consider that the star contracts gradually while maintaining sphericity and that this is the sole responsible for the stellar luminosity. The corresponding time scale a star can shine by this

mechanism is called the *Kelvin-Helmholtz* time scale,

$$\tau_{\text{kh}} \simeq \frac{GM^2}{2RL}, \quad (1.1)$$

where  $G$  is the Newtonian constant of gravitation,  $M$  is the mass of the star,  $R$  its radius, and  $L$  the associated luminosity produced by the contraction. For a  $1 M_{\odot}$ <sup>1</sup> star, this is approximately 15 Myr.

The shortest relevant time scale describes the time a star needs to recover its equilibrium when the balance between gravitational forces and pressure is disturbed by some dynamical process. For a star close to hydrostatic equilibrium, it is the free-fall time scale of the star, or the *dynamical* time scale

$$\tau_{\text{dyn}} \simeq \sqrt{\frac{R^3}{GM}} \simeq \sqrt{\frac{1}{G\langle\rho\rangle}}, \quad (1.2)$$

where  $\langle\rho\rangle$  corresponds to the mean density of the star. In the case of the Sun, the free-fall time scale is of the order of 20 min.

Finally, the longest relevant time scale involved is the *nuclear* time scale,

$$\tau_{\text{nuc}} = \frac{\epsilon q M c^2}{L}, \quad (1.3)$$

where  $c$  is the speed of light,  $q$  the fraction of the total stellar mass involved in the nuclear burning, and  $\epsilon$  the amount of mass that is converted into energy as a result of the nuclear reaction processes. Essentially, this time scale describes how long a star can shine with nuclear fusion as its sole source of energy. If the Sun was made of pure hydrogen and the central 10% of its mass would contribute to nuclear reactions, it could shine through this mechanism for around 10 Gyr.

### 1.1.2 Nuclear reactions and chemical composition

Thermonuclearly fueled reactions in stellar interiors produce energy that is carried out through radiation, convection or conduction (see Sect. 1.3.1). We mention here briefly the main channels for burning hydrogen into helium, the longest evolutionary phase in the lifetime of a star, and the reaction network to transform helium into heavier elements.

There are two reaction chains that transform four protons into one  ${}^4\text{He}$  nucleus, namely the *p-p chain* and the *CNO cycle* (see Table 1.1). Presence of C, N, or O isotopes is necessary for the CNO cycle to begin, and since they are both destroyed and produced during the cycle they act as catalysts for the reactions. These p-p chain and the CNO cycle usually take place simultaneously in a star but with different efficiencies depending on the total stellar mass.

The nuclear energy generation rate ( $\epsilon$ ) of these channels has different temperature sensitivities, meaning that the conditions in the stellar interior will define the efficiency each one of them operates with. The p-p chain has a commonly adopted average relation of the order of  $\epsilon_{\text{pp}} \propto T^4$  at  $T \approx 15 \times 10^6$  K, while the CNO cycle has a higher value of  $\epsilon_{\text{CNO}} \propto T^{18}$  at  $T \approx 20 \times 10^6$  K. As

<sup>1</sup>The symbol  $\odot$  is commonly adopted in astrophysics to refer to the solar values.

Table 1.1: Reaction networks involved in the *p-p chain* and the *CNO cycle*

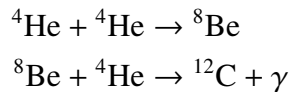
<i>p-p chain</i>		
pp I	pp II	pp III
${}^1\text{H} + {}^1\text{H} \rightarrow {}^2\text{D} + e^+ + \nu_e$	${}^3\text{He} + {}^4\text{He} \rightarrow {}^7\text{Be} + \gamma$	${}^3\text{He} + {}^4\text{He} \rightarrow {}^7\text{Be} + \gamma$
${}^2\text{D} + {}^1\text{H} \rightarrow {}^3\text{He} + \gamma$	${}^7\text{Be} + e^- \rightarrow {}^7\text{Li} + \nu_e$	${}^7\text{Be} + {}^1\text{H} \rightarrow {}^8\text{B} + \gamma$
${}^3\text{He} + {}^3\text{He} \rightarrow {}^4\text{He} + {}^1\text{H} + {}^1\text{H}$	${}^7\text{Li} + {}^1\text{H} \rightarrow {}^4\text{He} + {}^4\text{He}$	${}^8\text{B} \rightarrow {}^8\text{Be} + e^+ + \nu_e$
		${}^8\text{Be} \rightarrow {}^4\text{He} + {}^4\text{He}$

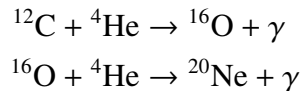
<i>CNO cycle</i>	
CN cycle	NO cycle
${}^{12}\text{C} + {}^1\text{H} \rightarrow {}^{13}\text{N} + \gamma$	${}^{15}\text{N} + {}^1\text{H} \rightarrow {}^{16}\text{O} + \gamma$
${}^{13}\text{N} \rightarrow {}^{13}\text{C} + e^+ + \nu_e$	${}^{16}\text{O} + {}^1\text{H} \rightarrow {}^{17}\text{F} + \gamma$
${}^{13}\text{C} + {}^1\text{H} \rightarrow {}^{14}\text{N} + \gamma$	${}^{17}\text{F} \rightarrow {}^{17}\text{O} + e^+ + \nu_e$
${}^{14}\text{N} + {}^1\text{H} \rightarrow {}^{15}\text{O} + \gamma$	${}^{17}\text{O} + {}^1\text{H} \rightarrow {}^{14}\text{N} + {}^4\text{He}$
${}^{15}\text{O} \rightarrow {}^{15}\text{N} + e^+ + \nu_e$	
${}^{15}\text{N} + {}^1\text{H} \rightarrow {}^{12}\text{C} + {}^4\text{He}$	

an example, in the center of the sun  $T \approx 15 \times 10^6$  K and more than 90% of the energy budget corresponds to the p-p chain. An important consequence of the temperature sensitivities is that, if the H-burning process is dominated by the CNO cycle, it will be confined towards the very central regions of the star. This results in a larger energy flux arising from the innermost regions which favors the presence of a convective core.

Following the exhaustion of hydrogen in the center, stars begin burning helium as soon as the central temperature increases enough as to produce the *triple alpha* ( $3\alpha$ ) reaction:



The temperature sensitivity is quite strong for the  $3\alpha$  reaction:  $\epsilon_{3\alpha} \propto T^{40}$  at  $T \approx 10^8$  K. Thus, for the same physical reason as in the case of the CNO cycle, stars burning helium via  $3\alpha$  mechanism have extended convective cores. For the sake of completeness, we mention the other important nuclear reactions involved in the helium burning process:



It is clear by looking at these reactions that helium burning transforms  ${}^4\text{He}$  particles mainly into  ${}^{12}\text{C}$ ,  ${}^{16}\text{O}$  and  ${}^{20}\text{Ne}$ . These elements have burning processes in more advanced stages of stellar evolution. We refer the reader to the monograph by Clayton (1983) for a detailed description of

the above mentioned reactions, and further explanations on the reaction networks of elements heavier than helium.

Before closing this section, some general comments regarding the chemical composition of stars. In evolutionary calculations, abundances are represented with the letters  $X$ ,  $Y$ ,  $Z$ , determining the mass fraction of hydrogen, helium, and all elements heavier than helium ('metals'), respectively. In the case of photometric or spectroscopic observations of stars, the chemical composition is usually given in terms of logarithmic abundances ratios with respect to the solar value, normalized to  $10^{12}$  atoms of hydrogen. For the species  $i$  and  $j$ , this is expressed as

$$\log(i/j) - \log(i/j)_{\odot} \equiv [i/j]. \quad (1.4)$$

Clearly, the observed abundances of stars depend on the solar reference value. In particular, to estimate the logarithmic mass fraction of heavy elements from the observed iron abundance in stars, it is assumed that

$$\log(Z/X) - \log(Z/X)_{\odot} \simeq [\text{Fe}/\text{H}], \quad (1.5)$$

and that the fraction of each element comprising  $Z$  is distributed accordingly to the chosen set of solar abundance ratios (or solar 'mixture').

The topic of the surface abundances in the Sun has been one of hot debate in the past years, where the latest determinations of the individual abundances values have decreased considerably the total metallicity of the Sun. However, no set of solar abundances is yet completely accepted by the astrophysics community, and determinations such as those given by Grevesse & Noels (1993); Grevesse & Sauval (1998); Asplund et al. (2005) and Asplund et al. (2009) are widely applied according to personal preference. The reader is referred to Basu & Antia (2004); Bahcall et al. (2005) and Serenelli et al. (2009) for further explanations on the topic and its implications for helioseismology.

Equation 1.5 is not sufficient to estimate the three necessary components  $X$ ,  $Y$ , and  $Z$ , of the stellar composition. Moreover, it is not possible to directly measure helium abundances in stars of temperatures lower than  $\sim 10^4$  K. Thus, a so called 'galactic chemical evolution law' is applied (Peimbert & Torres-Peimbert 1976), which basically tells the amount of fresh helium supplied by stars to the interstellar medium relative to their supply of heavy elements:

$$\frac{\Delta Y}{\Delta Z} = \frac{Y - Y_{\text{ref}}}{Z - Z_{\text{ref}}}. \quad (1.6)$$

The value of  $\Delta Y/\Delta Z$  is usually considered to be around 1.5-2.5 (e.g., Pagel & Portinari 1998; Casagrande et al. 2007). In Eq. 1.6 one must provide a reference value for  $Y$  and  $Z$ ; big bang nucleosynthesis values can be considered ( $Z_{\text{ref}} = 0$  and  $Y_{\text{ref}} \sim 0.245$ ), or the primordial solar  $Z$  and  $Y$  values obtained from a solar calibration (see Sect. 1.3.1 below). In the latter case, the chosen set of today's surface abundances in the Sun plays an important role, although it has been suggested the initial helium abundance of the Sun could be independent of them (Serenelli & Basu 2010). Finally, the third equation comes from the obvious fact that  $X + Y + Z = 1$ .

## 1.2 Evolution across the Hertzsprung–Russell Diagram

The ultimate fate of a star depends mostly in its initial mass and chemical composition, properties related to the place and time where the star was born and possible interactions with the medium surrounding it. It is customary to analyze the main phases of stellar evolution following the path described by the surface luminosity,  $L$ , and effective temperature,  $T_{\text{eff}}$ , throughout the star's lifetime. This is the so-called *Hertzsprung-Russell Diagram* (HRD), and it is shown for several masses in Fig. 1.1 for a given chemical composition. In the particular case of this thesis, we will be interested in evolution of stars with masses below  $\sim 2.5\text{--}3.0 M_{\odot}$ , from the beginning of the hydrogen burning phase until helium is exhausted in the center. Nevertheless, we will also broadly describe the evolution of more massive stars. For better guidance through the different evolutionary stages, Fig. 1.2 presents two HR Diagrams of different evolutionary phases for stars of the same metallicity as that of the tracks in Fig. 1.1. The left panel shows a  $1 M_{\odot}$  star evolving from the pre-main sequence until helium ignition, while the right panel depicts a  $8 M_{\odot}$  star in similar evolutionary phases.

### 1.2.1 Pre-main sequence phase

Protostars form through condensation of interstellar matter at low temperatures in hydrostatic equilibrium. Giant molecular clouds with masses large enough to undergo gravitational collapse fragment into smaller subunits due to the presence of inhomogeneities. Each of these subregions forms an hydrostatic core and accretes free-falling gas from its surroundings. Once this accretion process is complete, the protostar collapses again until hydrostatic equilibrium is restored, giving birth to a new star.

A star in this phase is fully convective, has a low temperature, a large radius and a high luminosity. It evolves almost vertically in the HRD (at roughly constant temperature) in the so-called *Hayashi track* (see point 'A' in Fig. 1.2(a)), its exact location depending on the initial mass and chemical composition. Once a radiative core appears, the star leaves the Hayashi track and moves to higher effective temperatures while its convective envelope slowly retreats. The star contracts increasing its central temperature and density until fusion of hydrogen to helium becomes efficient and releases enough energy to counteract the gravitational force. At this point, the star has reached the Zero Age Main Sequence (ZAMS, point 'B' in both panels of Fig. 1.2).

Due to the temperature sensitivity of the reaction networks, stars of masses  $M \leq 1.3 M_{\odot}$  burn hydrogen mainly through the p-p chain (see Table 1.1), the exact transition mass value depending on the initial chemical composition (it is  $\approx 1.3 M_{\odot}$  at solar metallicity). Before reaching the ZAMS, some nuclear burning occurs in these stars, such as transforming deuterium into  ${}^3\text{He}$ . While this reaction takes place and the abundance of  ${}^3\text{He}$  is not high enough as to complete the ppI branch of the p-p chain, the star is forced to reach higher temperatures and densities in order to satisfy its energy needs. This higher temperature also induces the first three reactions of the CNO cycle, burning  ${}^{12}\text{C}$  into  ${}^{14}\text{N}$ . A small convective core appears as a consequence of an energy generation more concentrated to the center; it only survives until the  ${}^{12}\text{C}$  abundance decreases and the amount of  ${}^3\text{He}$  increases enough for the p-p reactions to become more important and the energy generation to be redistributed over a larger area.

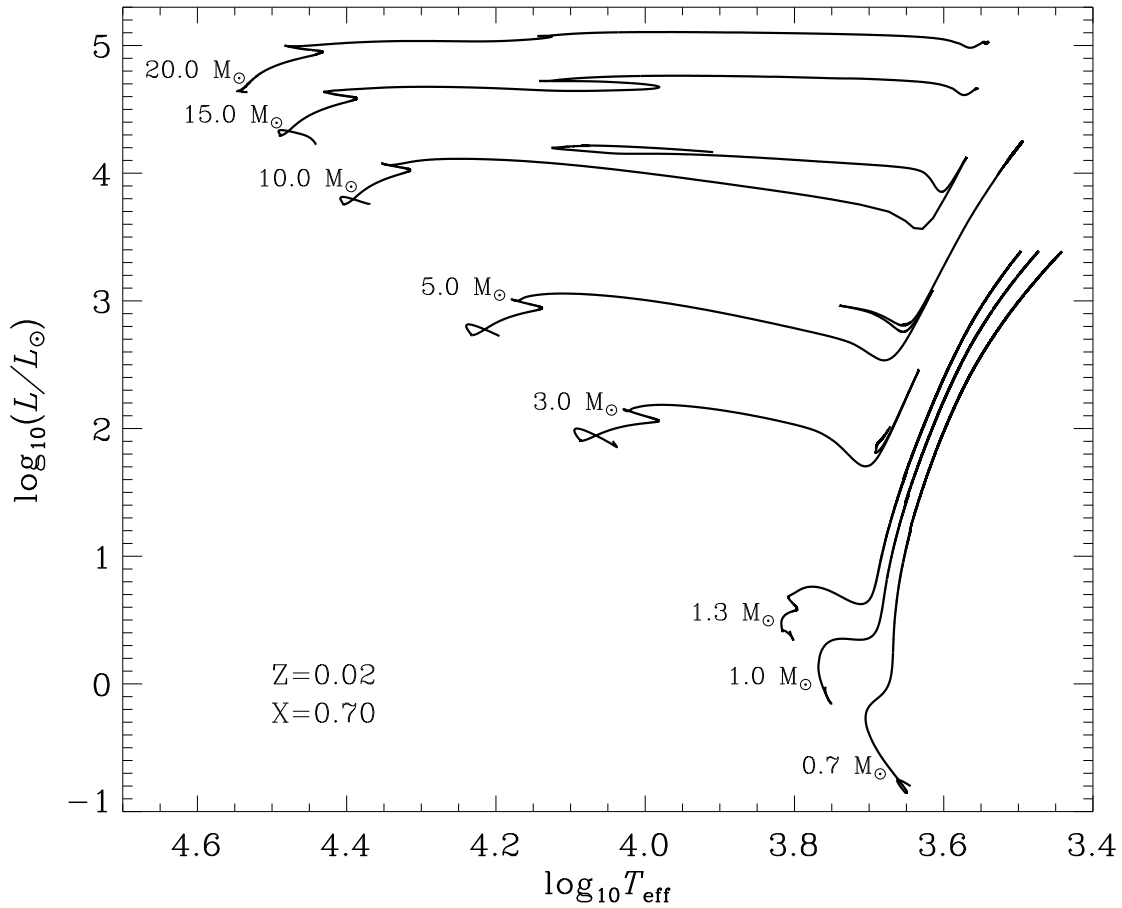


Figure 1.1: Hertzsprung-Russell Diagram plotted for different masses at a fixed chemical composition, shown in the figure. The tracks cover the evolution from the beginning of the main sequence to the red giant phase or, for  $M \geq 3.0 M_{\odot}$ , also the helium burning phase. Evolutionary tracks courtesy of A. Weiss. See text for details.

### 1.2.2 Main sequence evolution

The main sequence corresponds to the phase in which a star transforms hydrogen into helium at its center, and it is the longest of the evolutionary phases in a star's lifetime (points 'B' to 'C' in Fig. 1.2). Its duration is mainly controlled by the mass of the star, while in comparison the chemical composition and mixing processes play a secondary role. From homology relations (see, e.g. Kippenhahn & Weigert 1990), it exists a mass-luminosity relation that gives the dependence between these parameters in different evolutionary stages. For stars in the main sequence, at a given chemical composition, it is of the order of

$$\left(\frac{L}{L_{\odot}}\right) \propto \left(\frac{M}{M_{\odot}}\right)^{3.5}. \quad (1.7)$$

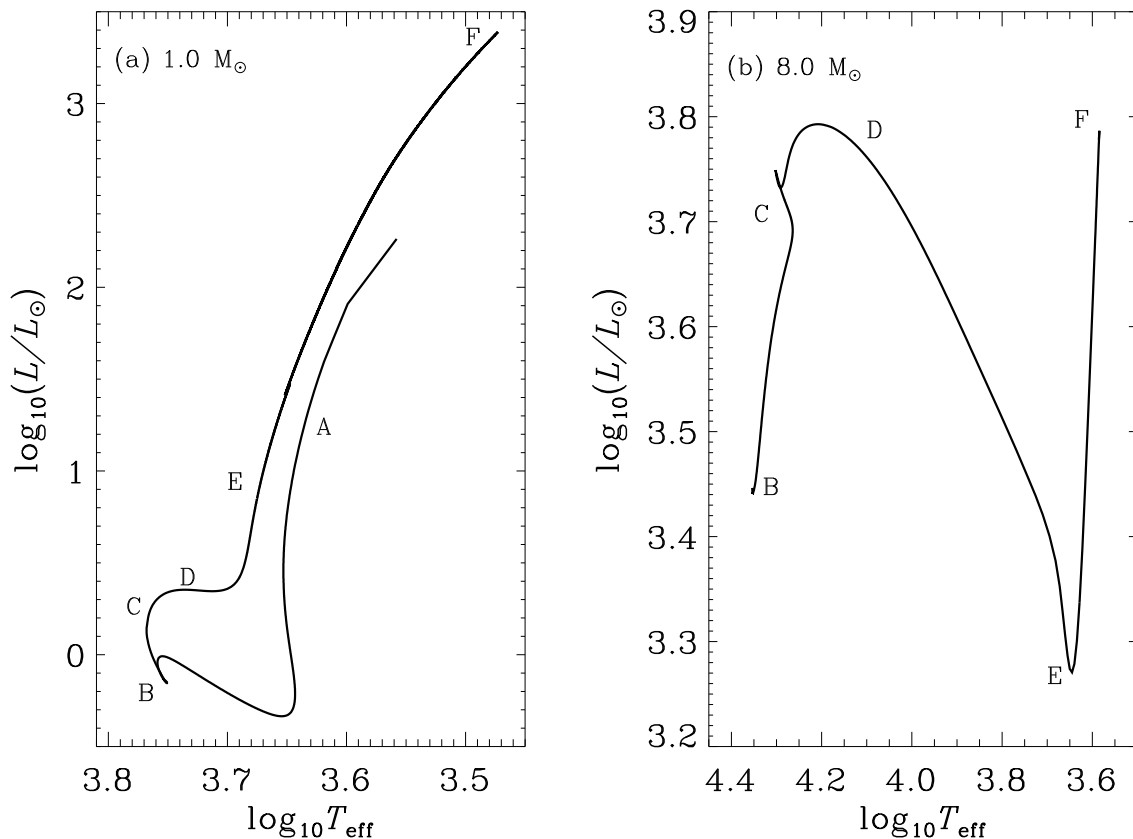


Figure 1.2: Hertzsprung-Russell Diagram for stars at the same metallicity of those in Fig. 1.1. (a) Evolution of a  $1 M_{\odot}$  star from the pre-main sequence to the tip of the red giant branch. (b) Similar evolution of an  $8.0 M_{\odot}$  star, where the pre-main sequence has been removed for better visualization. See text for details and explanation of the letters.

Recalling the nuclear time scale given by Eq. 1.3, and replacing  $L$  with the mass-luminosity relation, it is clear that the time a star can shine with nuclear burning as its energy source decreases for increasing stellar mass. To give some numbers, at solar metallicity a  $1.0 M_{\odot}$  star burns hydrogen for approximately 9 Gyr., while a  $20.0 M_{\odot}$  star does it for 8 Myr.

Stars more massive than  $\sim 1.7 M_{\odot}$  have a convective core and a radiative envelope, while their less massive counterparts have convective envelopes on top of their radiative interiors and can host either radiative or convective cores. The presence of a convective envelope has important consequences for the pulsation properties of stars (see Sect. 1.4).

The main effect of a larger mass is a significant increase of the interior temperature, resulting in different efficiencies of the H-burning reaction networks. Depending on the resulting mechanism employed to burn hydrogen, stars are usually classified in lower main-sequence stars

(masses below  $\sim 1.3 M_{\odot}$  where the p-p chain is the main mechanism) and upper main-sequence stars (more massive stars where the CNO cycle plays the leading role).

When the CNO cycle is the dominant source of energy production, the center of the star becomes convective due to a very high energy flux in the innermost regions. As the mass increases, convective core size also grows as a consequence of the higher temperature in the interior leading to a larger flux.

It is assumed that the convective core is homogeneously mixed, producing a chemical gradient inside of the star that varies during the main-sequence lifetime and determines the amount of available fuel for hydrogen burning. For a star of a given mass and chemical composition, this defines the total time it will spend burning hydrogen, the size of its helium core once the hydrogen in the center is exhausted, and the exact position of the star in the HRD. If the star had a convective core during its main-sequence evolution, its disappearance once the star reaches the *turn-off* point leaves a characteristic hook-like feature in the HRD (compare point ‘C’ in each panel of Fig. 1.2). The existence of this feature in the Color Magnitude Diagram (CMD) of clusters is used to calibrate the amount of mixing beyond the convective core and directly impacts age determinations via isochrone fitting (e.g., Vandenberg et al. 2007). Despite its importance, the exact extension of the convective core is still an open problem due to the uncertainty in the ‘true’ convective boundary definition, and the contribution of the different physical processes that mix material beyond this formal boundary.

### 1.2.3 Subgiants, giants, and clump giants

At the turn-off point (related to hydrogen exhaustion in the center), hydrogen burning ceases to be a central process and becomes a shell-burning process in a layer outside of the He-rich core. At the same time, the stellar envelope expands cooling down the star and moving it to the right in the HRD. This constitutes the *subgiant* phase (point ‘D’ in Fig. 1.2), where stars evolve roughly at the rate of the Kelvin-Helmholtz time scale (Eq. 1.1).

For masses above  $\sim 2.5\text{-}3.0 M_{\odot}$ , the core contracts since it cannot counteract the pressure exerted by the layers above it (the exact relation between core and envelope mass is given by the *Schönberg-Chandrasekhar* limit, Schönberg & Chandrasekhar 1942). A convective envelope develops due to the cooling down of the outer layers, which marks the beginning of the *red giant* (RG) phase (point ‘E’ in Fig. 1.2(b)). From here onwards, the star evolves at a roughly constant temperature, burning hydrogen in a shell while increasing its luminosity and radius and further contracting the core. Eventually, the central temperature reaches values high enough as to ignite helium in the center, marking the end of the RG phase (point ‘F’ in Fig. 1.2(b)). This occurs under non-degenerate conditions, as the central density is low enough to prevent the onset of electron degeneracy. For increasing stellar mass, the time needed to reach He-burning central temperatures is very short and the RG might even disappear.

The case of masses lower than  $\sim 2.5 M_{\odot}$  is slightly different from their more massive counterparts. The gas in the He-rich core is electron-degenerate, providing enough pressure to support the envelope above it and at the same time grow from the production of helium in the H-burning shell. During the subgiant phase, the cooling down of the outer layers results in an inward penetration of the already existing convective envelope, which drags partially processed nuclear

material to the surface. Point ‘E’ in Fig. 1.2(a) shows the position in the HRD where maximum inward penetration of the envelope occurs, a phenomenon called the *first dredge-up*. This is observationally witnessed by the change in CNO abundances due to mixing of former core material dredged-up to the surface.

After this process, the convective envelope begins to retreat and the star continues its vertical ascent through the red giant branch (RGB, the portion of the HRD populated by stars evolving through the RG phase). One must keep in mind that, during the evolution up the RGB, stars lose some amount of mass through stellar winds due to their increasingly larger envelopes. Nevertheless, the mass-loss rates have not been tightly constrained by either observations or theory, and ad-hoc parametrizations are used to reproduce that phenomena such as the one given by Reimers (1975, 1977).

Although helium ignition occurs quietly in massive stars, the case for stars below  $\sim 2.5 M_{\odot}$  is somewhat different. For better visualization, Fig. 1.3 depicts the evolution from the tip of the red giant branch until center helium exhaustion of a  $0.85 M_{\odot}$  star at low metallicity ( $Z = 0.001$ ,  $X = 0.749$ ). In the late stages of the RGB, stars lose large amounts of energy in the form of neutrinos, this form of dissipation being most efficient where the stellar matter is more dense (its center). An inversion of the thermal profile occurs in the He-core, the hottest place being a layer located off-center within the He-rich core. When temperatures high enough to start helium burning are reached, the ignition takes place off-center in a sort of thermonuclear runaway, called the *core helium flash* (point ‘F’ in Fig. 1.2(a) and Fig.1.3).

The reason for this phenomenon has to do with a property of the electron-degenerate gas, which is the decoupling of the temperature dependence from the  $P - \rho$  relation (the equation of state or EOS, see Sect. 1.3.2 below). For such a case, the energy input to the medium due to the nuclear reactions when helium ignites increases the local temperature, but no compensating increase of the pressure takes place. As a consequence, the region where burning takes place does not expand to cool down the material, leading to an increase in the thermonuclear reaction rates, which leads to a further increase in the local temperature, and so forth. The thermodynamical runaway is terminated once the increasing temperature removes degeneracy and the EOS becomes temperature dependent. During this phase, the large amounts of energy produced by the ignition are used to lift up the degeneracy in the core, decreasing considerably the luminosity.; in fact, secondary flashes take place increasingly closer to the center until degeneracy has been lifted throughout the He-core, producing loops in the HRD.

If the ignition of helium is degenerate or not depends on the core mass of the star in the RGB. As a result of the degenerate helium ignition, the magnitude of these stars in the CMD is nearly constant. The star is finally able to burn helium quiescently in a convective core and hydrogen in a shell, marking the end of the RG phase. This evolutionary phase is called the *horizontal branch* phase for stars in Globular Clusters (low-mass metal-poor stars, see point ‘G’ in Fig. 1.3), while it is usually known as the *red clump* for composite populations since their location in the HRD can be closer to the RGB. In this latter case, a secondary (and less luminous) red clump can also be present, comprising the more massive stars that started the He-burning in non-degenerate conditions (Girardi 1999).

The horizontal branch or clump is the second largest evolutionary phase in the life of a star, in which helium is burned in a homogeneously mixed convective core through the  $3\alpha$  mechanism

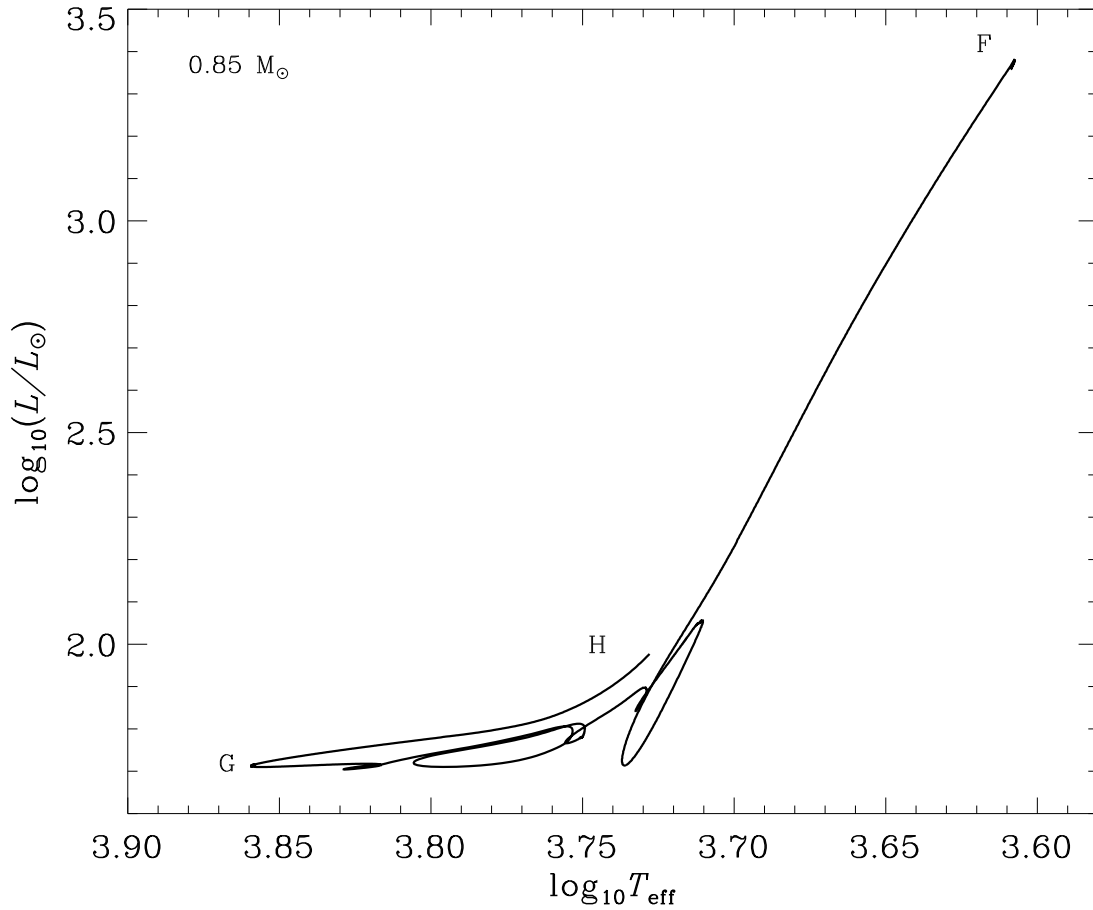


Figure 1.3: Hertzsprung-Russell Diagram of a  $0.85 M_{\odot}$  star from the tip of the red giant branch until center helium exhaustion at low metallicity. See text for details.

(see Sect. 1.1.2), surrounded by a H-burning shell. Evolution until exhaustion of helium in the center is shown in Fig. 1.3 (points ‘G’ to ‘H’), which for this case lasts approximately 80 Myr.

#### 1.2.4 Advanced stages of evolution

Evolutionary phases beyond the helium burning phase are briefly mentioned here for the sake of completeness. Once helium is exhausted in the core, stars with initial masses  $\leq 8.0 M_{\odot}$  shine by helium and hydrogen shell burning. They are said to ascend the *asymptotic giant branch* (AGB), a phase where extinction and re-ignition of helium leads to the occurrence of thermal pulses. During this evolutionary stage, stars undergo large amounts of mixing and complex nuclear reactions, such as slow-neutron capture and carbon burning. Large amounts of mass are lost due to dust-driven winds and large amplitude pulsations. Once hydrogen is largely exhausted in the burning shell, the remaining envelope is rapidly lost and shines due to ionization by the

bare core of the star as a *planetary nebula*. This exposes the central star (a *white dwarf*), which consequently evolves down the white dwarf cooling curve over a time scale of billions of years.

The value of  $\sim 8.0 M_{\odot}$  given above is a very loose approximation of the maximum initial mass a star should have to end its life as a white dwarf. Its ultimate fate will depend on its capability of losing enough mass by stellar winds throughout evolution to have a final mass smaller than the so-called *Chandrasekhar* limiting mass. This limit gives the highest possible final core mass a star can have in order to be a stable a white dwarf, and it is usually considered to be approximately  $\sim 1.45 M_{\odot}$ .

Naturally there are stars that have core masses far higher than the *Chandrasekhar* limiting mass once they have exhausted helium in the center. These stars will ignite carbon under non-degenerate conditions. As they go through several cycles of nuclear burning, they produce shells of heavier elements inside in a so-called *onion skin* model. At last, the core consisting mostly of  $^{56}\text{Fe}$  (or a neighboring nuclei) becomes dynamically unstable and core collapse sets in, resulting in a supernova explosion.

The picture we have sketched in this section is an overwhelmingly simplified one, but it suffices the purpose of the present work. We encourage the reader to refer to the works of Clayton (1983), and Kippenhahn & Weigert (1990) for all the most interesting (and complicated) details of these evolutionary phases.

## 1.3 Modeling stars: a naive first look

The previous section highlighted the major changes experienced by a star throughout its evolution which are of interest for this thesis. This rough picture becomes much more complicated when we consider the subtle details of the physical processes responsible for these changes, that must be somehow taken into account when computing realistic evolutionary models.

The structure and evolution of stars can be described to a considerable extent as a ‘solved’ problem in astrophysics. However, some important considerations must be kept in mind. As shown in Sect. 1.1.1 there are large differences between the relevant time scales for stellar evolution, where  $\tau_{\text{nuc}} \gg \tau_{\text{kh}} \gg \tau_{\text{dyn}}$ . If we intent to follow a large portion of the evolution of a star, the processes occurring in the shortest time scales will have to be consistently parametrized over larger periods. Moreover, some processes are usually neglected due to the lack of a consistent theory describing their effects in the overall stellar evolution, such as rotation and magnetic fields. Therefore, many assumptions and simplifications about the nature of stellar matter and complex physics must be used. It is customary to separate these major ingredients in stellar evolution calculations into *macrophysics* and *microphysics*, which we broadly describe in the following.

### 1.3.1 Macrophysics

The main ingredient of modern theory of stellar studies are the four basic differential equations of stellar structure, namely

$$\frac{\partial r}{\partial m} = \frac{1}{4\pi r^2 \rho}, \quad (1.8)$$

$$\frac{\partial P}{\partial m} = -\frac{Gm}{4\pi r^4}, \quad (1.9)$$

$$\frac{\partial L}{\partial m} = \epsilon - \epsilon_\nu + \epsilon_g, \quad (1.10)$$

$$\frac{\partial T}{\partial m} = -\frac{GmT}{4\pi r^4 P} \nabla, \quad (1.11)$$

where

$$\nabla = \frac{\partial \ln T}{\partial \ln P}. \quad (1.12)$$

In these equations,  $r$  is the distance from the center of the star, and  $m$  the mass contained within this distance.  $P$ ,  $T$  and  $\rho$  are the thermodynamic variables pressure, temperature and density respectively, while  $L$  is the luminosity at the corresponding position of  $r$  (or  $m$ ). The  $\epsilon$  term corresponds to the energy rate generated by nuclear reactions (cf. Sect. 1.1.2),  $\epsilon_\nu$  to the energy rate lost (in form of neutrinos), and  $\epsilon_g$  to the work that is performed on the gas during any expansion or contraction of the star. These equations are, in order of appearance, the *mass conservation equation*, the *hydrostatic equilibrium equation* (briefly mentioned in Sect. 1.1), the *energy conservation equation*, and the *energy transport equation*.

The solutions to the equations are not stationary but rather evolve with time as a consequence of contraction and nuclear reactions taking place, and the resulting changes in the chemical composition and mean molecular weight brought about by them. The first two equations define the mass profile in the stellar interior, while the latter two equations determine the thermal profile inside of the star. In fact, Eq. 1.12 is simply the definition of  $\nabla$ , whose value must be derived from a theory of energy transport.

Under normal circumstances there is a steady flow of energy from the deep stellar interior, where the nuclear reactions take place, to the outermost layers of the star, where energy is radiated to the interstellar medium. Depending on the thermodynamical properties of matter in the interior, such energy transport can occur via *radiative transfer*, *convective motions*, or *conductive transfer*. The last transport method becomes very efficient under degenerate conditions and it is not relevant for the subject of this thesis.

#### Radiative energy transport

In the time-independent three dimensional case, the equation of radiative transfer can be written as

$$\mu_i \frac{\partial \mathbf{I}}{\partial x_i} = -(\kappa_{\text{ab}} + \kappa_{\text{sc}}) \rho \mathbf{I} + \kappa_{\text{ab}} \rho B + \kappa_{\text{sc}} \rho J, \quad (1.13)$$

where  $\mathbf{I}(\mathbf{x}, \boldsymbol{\mu}, t)$  is the specific intensity at  $\mathbf{x}$  in direction  $\boldsymbol{\mu}$ ,  $\kappa_{\text{ab}}$  the mean absorption opacity,  $\kappa_{\text{sc}}$  the scattering opacity,  $B = (ac/4\pi)T^4$  is the integrated Planck intensity and  $J$  the mean intensity. In order to obtain the flux, it is customary to use the *Eddington Approximation* (e.g. Unno & Spiegel 1966). Assuming the intensity to be isotropic, a relation between the zeroth and first order moments of Eq. 1.13 can be obtained, that yields the radiation flux as

$$\mathbf{F} = -\frac{4\pi}{3\rho(\kappa_{\text{ab}} + \kappa_{\text{sc}})}\nabla J. \quad (1.14)$$

The near-isotropy of the radiation intensity is usually associated with a short photon mean free path, where radiation is efficiently trapped (i.e.  $\rho\kappa_{\text{ab}} \rightarrow \infty$ ). For this case, also referred to as the optically thick case, a diffusive mechanism takes place for radiative energy transport leading to the following expression for the energy flux:

$$\mathbf{F} = -\frac{4\pi}{3\rho\kappa}\nabla B = -\frac{4acT^3}{3\rho\kappa}\nabla T, \quad (1.15)$$

where  $\kappa = (\kappa_{\text{ab}} + \kappa_{\text{sc}})$ . This is usually known as the *diffusion approximation*.

The radiation flux then clearly depends on the opacities  $\kappa$ , of which we have so far neglected the natural frequency dependence. This comes from the idea that we can replace the problem of frequency dependence (the *non-grey atmosphere* problem) through some sort of mean opacities. In fact, one can show that a particular average of the opacities can be found by imposing the Eddington approximation in the equation of radiative transfer (Eq. 1.13), thus making the problem frequency-independent. These are called *Rosseland* mean opacities, and are defined as

$$\kappa_{\text{ross}}^{-1} = \frac{\int_0^\infty \frac{1}{\kappa_\nu} \frac{\partial B_\nu}{\partial T} d\nu}{\int_0^\infty \frac{\partial B_\nu}{\partial T} d\nu} = \frac{\pi}{acT^3} \int_0^\infty \frac{1}{\kappa_\nu} \frac{\partial B_\nu}{\partial T} d\nu, \quad (1.16)$$

where  $a$  is the radiation constant.

When essentially all energy is transported outwards by photons (condition of radiative equilibrium), it can be shown that the temperature gradient in Eq. 1.12 takes the form

$$\nabla_{\text{rad}} = \frac{3}{16\pi acG} \frac{\kappa LP}{mT^4}, \quad (1.17)$$

where  $\kappa$  is the Rosseland mean opacity of the stellar matter. A very clear description of the radiation theory in stellar interiors and its connection with stellar atmospheres can be found in Mihalas (1970).

### Convective energy transport

When the temperature gradient indicated in Eq. 1.17 is too steep, radiation is not able to carry all the energy outwards and convective instabilities set in. A theory of convective transport includes a stability criterion for convection to take place, and a consistent description of how energy is transported outwards by convective motions.

Based on a displacement analysis of random bubbles inside of the star, a criterion for the onset of convective stabilities can be derived. In a nutshell, consider a slight temperature fluctuation in a gas element with respect to its surroundings. Assuming that the element remains in pressure equilibrium with the medium, the temperature increase translates into a density decrease when considering an ideal gas law. Thus, this lighter bubble will be lifted upwards by the force of buoyancy. The gas element will travel until its density equalizes that of its surroundings, dissolving into the gas. For adiabatic motions of bubbles, it can be shown that a layer will remain stable if

$$\nabla_{\text{rad}} < \nabla_{\text{ad}} + \frac{\varphi}{\delta} \nabla_{\mu}, \quad (1.18)$$

where  $\nabla_{\text{ad}}$  is the temperature gradient introduced in eq. 1.12 when the displacement of the bubble takes place adiabatically, and

$$\varphi = \left( \frac{\partial \ln \rho}{\partial \ln \mu} \right)_{P,T}, \quad \delta = - \left( \frac{\partial \ln \rho}{\partial \ln T} \right)_{P,\mu}, \quad \nabla_{\mu} = \left( \frac{d \ln \mu}{d \ln P} \right). \quad (1.19)$$

Equation 1.18 is the *Ledoux* criterion for convection (Ledoux 1947), which takes into account variations in the molecular weight  $\mu$  to define the boundaries of convective regions. However, in regions of homogeneous composition one has simply the *Schwarzschild* criterion (Schwarzschild & Härm 1958), according to which a region remains stable against convection as long as

$$\nabla_{\text{rad}} < \nabla_{\text{ad}}. \quad (1.20)$$

This is by far the most commonly used criterion in stellar evolution codes. One reason for this is that, once convection sets in in a certain region, the chemical composition gradient is annihilated by convective mixing and Eq. 1.18 simplifies to Eq. 1.20. However, the application of a different criterion has a large effect in the size of the convective regions, with a subsequent impact in the resulting luminosity, effective temperature, and main sequence lifetime of the star. The issue of convective criteria definition including molecular weight gradients, and determining convective boundaries in stellar interiors is one of the main topics of this thesis and is extensively discussed in Chapter 3.

In a radiative (dynamically stable) layer, a displaced element is pushed back by buoyancy forces. This interaction imprints a certain momentum in the gas element, which will overshoot from its original position when descending and thus start to oscillate. The frequency of this oscillation, when it takes place adiabatically, is called the *Brunt-Väisälä* frequency and is given by:

$$N^2 = \frac{g\delta}{H_p} \left( \nabla_{\text{ad}} - \nabla + \frac{\varphi}{\delta} \nabla_{\mu} \right), \quad (1.21)$$

where  $H_p$  is the pressure scale height given by

$$H_p^{-1} = - \frac{d \ln P}{dr}. \quad (1.22)$$

For the displacement to be oscillatory, and thus for a region to be convectively stable, the condition for the frequency  $N^2 > 0$  must be fulfilled. It is interesting to note that, for stars in the

subgiant and red giant phase of evolution,  $N^2$  reaches very high values in the core of the star due to the strong central condensation and resulting high value of  $g$  (e.g., Christensen-Dalsgaard 2004).

Once a region is found by any stability criteria to be convective, the temperature gradient of that zone needs to be defined (Eq. 1.12). The usual way to do this is using the *mixing-length theory* for convection (MLT) in any of its flavors, most commonly the original formulation given by Böhm-Vitense (1958). The critical free parameter involved in the formulation is the so-called mixing-length parameter  $\alpha_{\text{MLT}} = l/H_p$ ,  $l$  being the distance a bubble will traverse before dissolving into the surrounding medium.

The value of  $\alpha_{\text{MLT}}$  ultimately defines the value of  $\nabla$  in a convective region, but unfortunately it cannot be obtained from first principles. It is normally calibrated from a solar model in order to reproduce the luminosity and radius of the Sun, at present solar age, for a chosen surface composition of the Sun; its value usually ranges between  $1.5 < \alpha_{\text{MLT}} < 2.5$  depending on the input physics and evolutionary code employed. There is a vast amount of literature devoted to the solar calibration problem where the interested reader can find more details, such as Christensen-Dalsgaard et al. (1996); Bahcall et al. (2001); Serenelli et al. (2009), and references therein.

The last layer of complications in the macrophysics of stellar evolution comes from physical processes that are likely to take place in stars and are still poorly understood; among them we can mention atomic diffusion of helium and heavier elements, radiative levitation, rotational mixing, the influence of magnetic fields, stellar winds, etc. (see Pinsonneault 1997, for a review). This physical processes have influence in the frequency of oscillations, thus making asteroseismology an excellent tool to further probe and learn about them (see e.g., Christensen-Dalsgaard & Mauro 2007; Reese et al. 2009; Schunker & Cally 2006). Of great importance for this thesis is the case of mixing beyond the formal boundaries of convective regions (*convective overshooting*) in main-sequence stars, in particular for convective cores (see Sect. 1.2.2). Currently, it is not clear if this process occurs at all inside of stars, and if it does how much extra mixing is actually taking place. Calibration of isochrones in open clusters suggest that some overshooting is needed to reproduce the morphology of their CMD, but the topic remains an open question.

### 1.3.2 Microphysics

Up to now, we have discussed the problem of stellar evolution calculations based on the structure of stars and physical processes taking place inside of them. The correct description of these processes depends critically in the properties of stellar matter, which are termed the microphysics of stellar evolution.

Inspection of the structure equations (Eqs. 1.8 to 1.11) clearly reveals that we are trying to solve a problem for five explicitly shown unknowns ( $r$ ,  $\rho$ ,  $P$ ,  $L$ , and  $T$ ) through a set of four equations. The missing relation is given by the Equation Of State (EOS), which provides one of the thermodynamic quantities in terms of the others (for instance,  $\rho = \rho(P, T, \mu)$ , where  $\mu$  is just an indicator of the general chemical composition). It is customary to refer to the EOS as one of the *constitutive equations* of stellar structure; the other quantities that enter the equations and

need to be defined from the set of constitutive equations. These can be written as,

$$\rho = \rho(P, T, \mu), \quad (1.23)$$

$$c_P = c_P(P, T, \mu), \quad (1.24)$$

$$\kappa_\nu = \kappa_\nu(P, T, \mu), \quad (1.25)$$

$$r_{jk} = r_{jk}(P, T, \mu), \quad (1.26)$$

$$\epsilon_\nu = \epsilon_\nu(P, T, \mu), \quad (1.27)$$

where  $c_P$  is the specific heat at constant pressure,  $\kappa_\nu$  the monochromatic opacity of stellar matter (a particular average of it was introduced in Sect. 1.3.1),  $r_{jk}$  the thermonuclear reaction rate transforming nuclei  $j$  into nuclei  $k$ , with the corresponding energy generation rate  $\epsilon_{jk}$  given by the product of  $r_{jk}$  and the energy released when the transformation takes place. Time evolution of a certain chemical species  $X_i$  when only nuclear reactions create or destroy it is given by

$$\frac{\partial X_i}{\partial t} = \frac{m_i}{\rho} \left( \sum_j r_{ji} - \sum_k r_{ik} \right), \quad (1.28)$$

with the constrain that  $\sum_i X_i = 1$ . If exchange of mass occurs between different stellar layers, diffusive processes also affect the chemical evolution of species.

### 1.3.3 Modeling stars with GARSTEC

The GARching STellar Evolution Code (GARSTEC), is a one-dimensional, hydrostatic code, which does not include the effects of rotation (Weiss & Schlattl 2008). The program in its present version is capable of calculating precise solar models as well as following the evolution of low-mass stars into the latest phases of their evolution, and has been successfully used to follow a star through the He-flash (e.g., Schlattl et al. 2001). The numerical scheme is the usual Henyey-scheme for handling the four equations of stellar structure (cf. Eqs 1.8 to 1.11), extended to solve simultaneously the equations of diffusion if required (see Kippenhahn & Weigert 1990, and references therein).

Regarding the macrophysics, by default GARSTEC applies the Schwarzschild criterion for convection and treats convective motions using the MLT as described by Kippenhahn & Weigert (1990). The full turbulent spectrum theory by Canuto & Mazzitelli (1991, 1992) is also implemented, which includes a different free parameter from  $\alpha_{\text{MLT}}$ . It is possible to treat the mixing in convective regions not instantaneously but as a diffusive process, where the convective velocities are estimated from the MLT.

Mixing of chemical elements beyond the formal convective boundaries can be also included. It is assumed that this process induces mixing but does not modify the thermal structure of the layers (*overshooting*, if we use the terminology given by Zahn 1991). It is implemented in the code as a diffusive process consisting of an exponential decline of the convective velocities within the radiative zone (Freytag et al. 1996). The diffusion constant is given by

$$D_{\text{ov}}(z) = D_0 \exp\left(\frac{-2z}{\xi H_p}\right), \quad (1.29)$$

where  $\xi$  corresponds to an efficiency parameter,  $H_p$  is the pressure scale height,  $z$  the distance from the convective border, and the diffusion constant  $D_0$  is derived from MLT-convective velocities (Kippenhahn & Weigert 1990). An overshooting efficiency of  $\xi = 0.016$  corresponds to the value obtained by calibrating this parameter with open clusters, which is in the range expected for main sequence stars (Herwig et al. 1997). The size of the overshooting region is limited further in the case of small convective cores. This is done in GARSTEC using a geometrical cutoff factor, allowing the overshooting region to extend only to a fraction of the convective zone (see Weiss & Schlattl 2008; Magic et al. 2010, for details). This geometric restriction is strong enough as to inhibit the survival of the pre-main sequence convective core in stars of masses below  $\sim 1.1 M_\odot$  once they reach the zero age main sequence.

Atomic diffusion of elements can be included for hydrogen and helium, and some other elements selected individually. The diffusion coefficients are calculated using the prescription of Thoul et al. (1994). Mass loss, when included, is treated by an analytic formula such as that of Reimers (Reimers 1977).

The outer layers of stars suffer from similar complications as convective zones when it comes to stellar evolution models, and suitable approximation for the temperature stratification in the stellar atmospheres must be used. In GARSTEC, a plane-parallel Eddington atmosphere is used by default for the boundary conditions, matched at an optical depth of  $\tau = 2/3$ . It is also possible to use the Krishna-Swamy  $T - \tau$  relation instead (Krishna-Swamy 1966).

In terms of the microphysics, nuclear reactions are either those compiled by the NACRE collaboration (Angulo et al. 1999) or the ones provided by Adelberger et al. (1998), including updates in some crucial reaction rates (e.g., Marta et al. 2008). The opacities are used as mean Rosseland opacities for suitable mixtures from the OPAL opacity project (Iglesias & Rogers 1996), including conductive opacities from Cassisi et al. (2007) or Itoh et al. (1983). Several EOS are included in the code, the most commonly used being the 2005 version of the OPAL EOS (Rogers et al. 1996; Rogers & Nayfonov 2002) and the MHD EOS (Hummer & Mihalas 1988).

Applications of the code can be found in Schlattl et al. (1997); Serenelli & Weiss (2005); Silva-Aguirre et al. (2008) and Weiss & Ferguson (2009), just to name a few.

## 1.4 Pulsating stars

The picture we have painted so far about the ingredients of stellar evolution is an overly simplified one. There are many complications in the calculations of realistic constitutive equations (such as occupation probabilities of atomic states for the EOS, scattering cross-sections for the nuclear reaction rates, and radiation theory for opacities, just to name a few), as well as for the correct description of physical processes. The study of oscillations in the Sun (*helioseismology*) has helped setting many constraints for these processes in the solar interior (see the reviews by Christensen-Dalsgaard 2002; Basu & Antia 2008, for details). Is it possible to achieve something similar by studying pulsations in stars other than our Sun?

At the current level of precision in our observations ( $\mu\text{mag}$  in photometry and  $\text{cm s}^{-1}$  in radial velocities), there are many different types of stars that are known to pulsate. Figure 1.4 shows

an HRD marking the position of the ones known up to now. It is clear from their location in the figure that a large diversity exists in the masses and evolutionary stage of oscillating stars. However, it is interesting to notice that the stars pulsate with periods given by the dynamical time scale (cf. Eq. 1.2), which is of the order of minutes for the Sun, several hours for red giants, and days for the Cepheids.

The boundaries of the different classes of pulsating stars are not strict and the latests space continuous observations have revealed hybrid pulsators (see, e.g., Grigahcène et al. 2010). Nevertheless, the pulsation mechanisms operating in each case and the oscillation spectra produced by it are directly related to their internal structure.

During a pulsation cycle, stars swell and contract, heat up and cool down. Most of the stellar interior loses energy during the pulsation (*damps* the oscillation); in order for the cycle to continue, some part of the star (the *driving region*) must feed the same amount of energy lost by the rest of the stellar interior. When a certain layer of the star succeeds in driving the oscillation, converting thermal energy into mechanical energy, the star functions as a heat engine. Thus, this pulsation mechanism is known as the *heat engine mechanism* or  $\kappa$  *mechanism*, as it is related to the presence of large opacity sources.

In a nutshell, the ionization layers of an element that largely contributes to the opacity block the radiation from escaping the stellar interior. The gas heats up and the pressure increases, expanding the star beyond its equilibrium point. However, ionization due to the increase in temperature reduces the opacity and allows the gas to flow trough; the region cools down and cannot support the weight of the layers above, so the star contracts. The contraction and temperature decrease allow the chemical element to recombine and absorb flux again: the heat engine mechanism is present, as the layer gains heat again upon compression.

Most of the stars in Fig. 1.4 pulsate via the  $\kappa$  mechanism in helium and hydrogen ionization zones. Oscillations of stars contained within the classical instability strip (Cepheids, RR Lyrae, and  $\delta$  Scuti stars, see Fig. 1.4) are primarily driven by the second helium ionization zone. Mira and stars and semi-regular variables are excited by the heat mechanism in the first ionization zone of hydrogen and helium, thus they lie on the cool side of the instability strip. However, for some cases such as the  $\beta$  Cep and sdBV stars, the opacity contributors to the  $\kappa$  mechanism are iron group elements.

There are cases where the heat engine mechanism is not efficient enough as to drive the oscillations. Nevertheless, the presence of an outer convective envelope can provide sufficient acoustic energy for the star to resonate in some of its natural oscillation frequencies. This mechanism is known as the *stochastic mechanism*, which operates in the Sun and in principle in any star with a large enough convective envelope. This type of pulsations (called *solar-like* oscillations) have been detected in numerous late-type main-sequence and red giant stars.

A third mechanism of excitation theoretically exists and it is called the  $\epsilon$  *mechanism*. It is related to possible variations in the energy generation rate in the stellar center that could drive global pulsations. However, up to now no class of stars are thought to be excited by this mechanism alone.

This thesis deals with oscillations in stars excited by the stochastic mechanism, focused in solar-type pulsators. In Figs. 1.5 and 1.6 several power spectra are shown for stars in different evolutionary stages, observed by instruments on the ground and the *Kepler* space mission. There

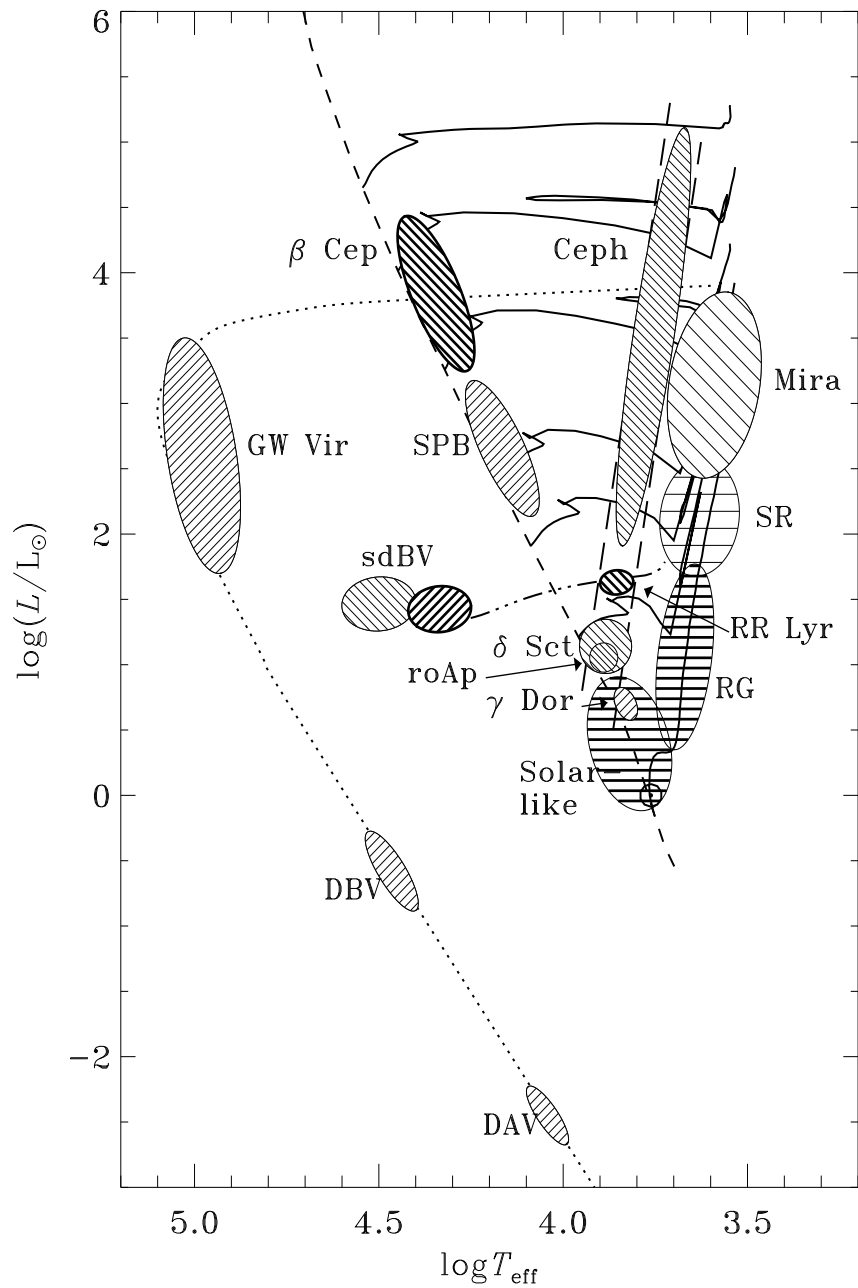


Figure 1.4: Pulsation HRD showing many classes of pulsating stars. Hatched regions mark where stars have been found to pulsate. Dashed line shows the ZAMS, while the dotted line depicts the white dwarf cooling curve. Some evolutionary tracks are also shown (continuous solid line). Two parallel dashed lines delimit the classical instability strip. Figure courtesy of J. Christensen-Dalsgaard.

is clear excess power in each spectrum where the oscillations are located, showing a characteristic 'gaussian-bell' shape. Stars in Fig. 1.5 populate different regions of the HRD: a main-sequence pulsator like the Sun, a subgiant star such as  $\eta$  Bootis, and a red giant star as the case of  $\xi$  Hydrae. The position of the overall oscillations spectrum shifts in frequency as the star evolves, moving to lower frequency values from the main sequence to the subgiant phase (Fig. 1.5), and also along the red giant branch (Figs. 1.6, from bottom to top panels).

From Figs. 1.5 and 1.6 and the discussion in the previous sections it is clear that the internal structure of stars determines its oscillation properties. Thus, study of this pulsations can tell us about the existence or not of convective and ionization layers according the pulsation mechanism, constrain the evolutionary stage of stars depending on its oscillation spectrum, and help us identifying which type of star we are dealing with without the need of further observations. Nevertheless, the full theory of stellar pulsation shows that the oscillations depend on many other physical quantities, allowing us to put even tighter constrains on the stellar interior.

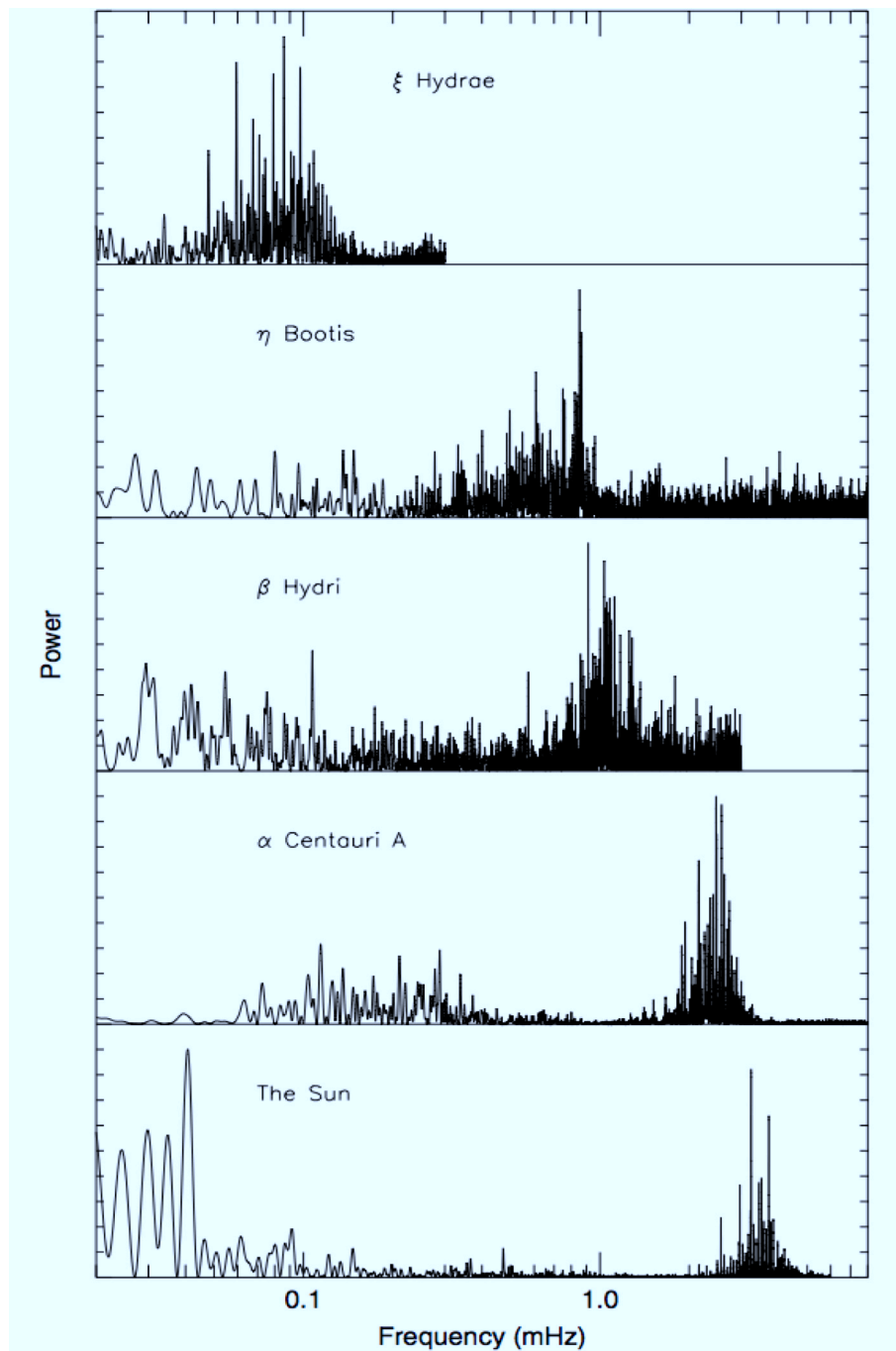


Figure 1.5: Power spectra showing oscillations detected from the ground for stars in the main-sequence (bottom panels), evolving through the subgiant phase until the red giant branch (upper panel). Reproduced with the permission of T. Bedding (from Bedding & Kjeldsen 2003)

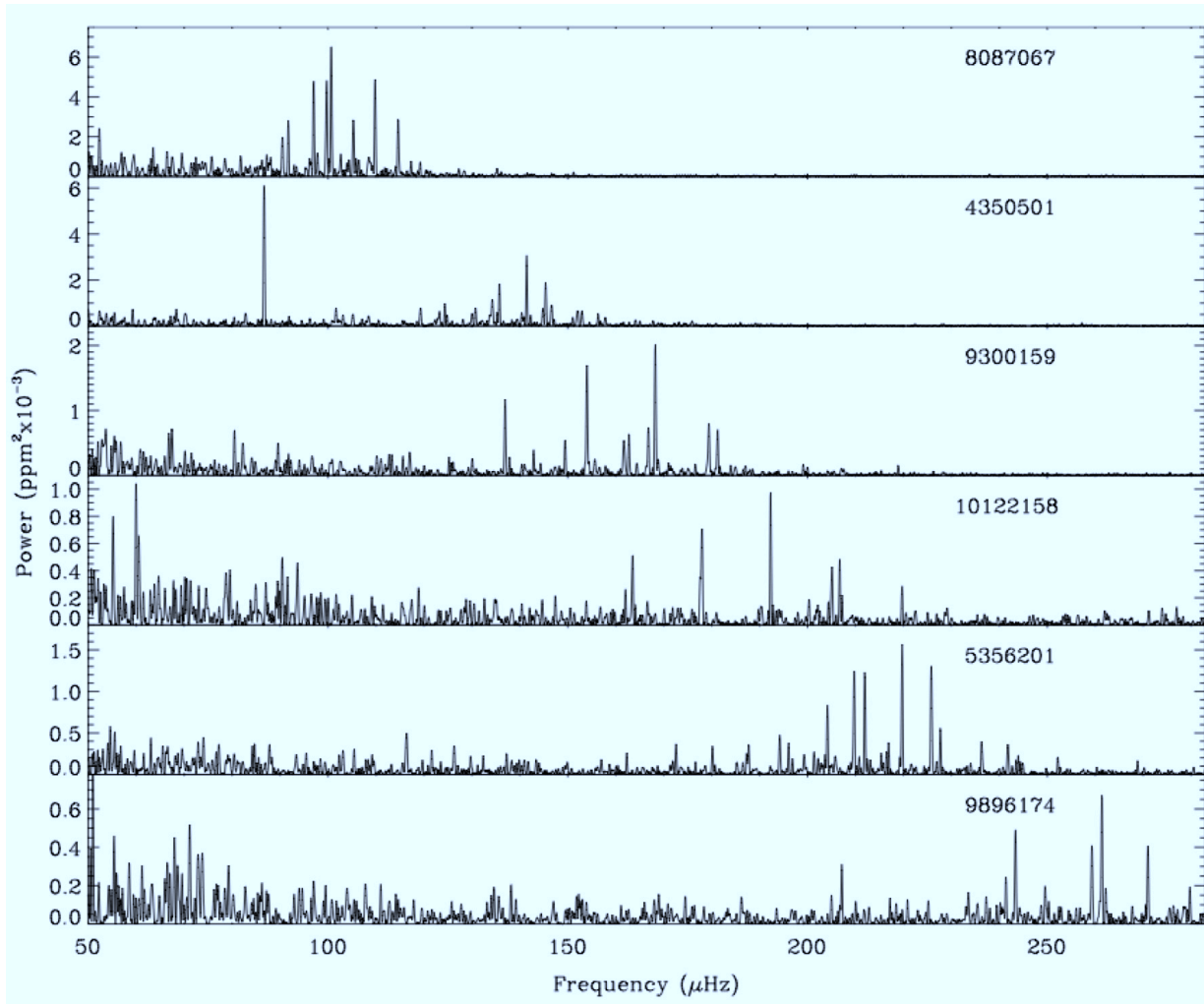


Figure 1.6: Power spectra of red giant stars observed by the *Kepler* satellite, organized by decreasing luminosity (from top to bottom). Reproduced with the permission of T. Bedding (from Bedding et al. 2010a)

# Chapter 2

## Stellar oscillations

The previous chapter described the main phases of stellar evolution for stars of different masses, and showed that we can find pulsating stars in several places across the HRD. We now present the mathematical background of astrophysics fluid dynamics, and set the equations for oscillations in stars. These topics are presented in much more detail in textbooks of fluid dynamics or non-radial oscillations of stars such as Ledoux & Walraven (1958); Landau & Lifshitz (1959); Cox (1980); Unno et al. (1989); Thompson (2006), and Aerts et al. (2010).

### 2.1 Fluid dynamics

Before entering the mathematical description of the oscillations, it is necessary to understand the equations governing the dynamics of any fluid, such as stellar gas. There are two ways to describe the behavior of a continuous fluid medium; the first is to characterize the properties of the fluid, such as its velocity or temperature, as functions of the position  $\mathbf{r}$  and time  $t$ . This is called the *Eulerian* description, where the properties of the gas depend on the point of observation. Another possibility is to follow the motion of a particular fluid element and observe the rate of change of some property of it, which is known as the *Lagrangian* description.

Let  $\phi(\mathbf{r}, t)$  be some quantity describing a property of the fluid. The Lagrangian time derivative  $d\phi/dt$ , following a particular fluid element, is given by

$$\frac{d\phi}{dt} = \frac{\partial\phi}{\partial t} + \mathbf{v} \cdot \nabla, \quad (2.1)$$

where  $\nabla$  is the gradient operator and  $\mathbf{v} = \mathbf{v}(\mathbf{r}, t)$  is the velocity of the fluid.

A full set of equations to completely describe the properties of a fluid consist of: the *continuity equation*, the *equations of motion*, and the *energy equation*.

### 2.1.1 Continuity equation

We can consider a volume  $V$  enclosed by a surface  $S$  where matter is flowing. The mass of fluid contained in the volume is given by

$$m = \int_V \rho dV,$$

and the total mass of fluid flowing into the volume is

$$\oint_S \rho \mathbf{v} \cdot d\mathbf{A} = \int_V \nabla \cdot (\rho \mathbf{v}) dV.$$

Inside of the volume  $V$ , the mass decrease is given by

$$-\frac{\partial}{\partial t} \int_V \rho dV,$$

and equating what enters the volume equals what goes out

$$\int_V \left( \frac{\partial \rho}{\partial t} + \text{div}(\rho \mathbf{v}) \right) dV = 0$$

we obtain the continuity equation:

$$\frac{\partial \rho}{\partial t} + \text{div}(\rho \mathbf{v}) = 0. \quad (2.2)$$

This is a typical conservation of mass equation written in Eulerian coordinates. Using Eq. 2.1 it can also be written as the rate of change in density following the motion,

$$\frac{d\rho}{dt} + \rho \text{div} \mathbf{v} = 0. \quad (2.3)$$

### 2.1.2 Euler's equation

We will consider now the equation of motion for a fluid in which two types of forces are acting upon: surface body forces. Let us consider the force exerted by the pressure on the surface, which can be written as

$$F = - \oint_S P d\mathbf{A} = - \int_V \nabla P dV.$$

Thus, we can consider a force  $-\nabla P$  acting upon a unit of volume as a surface force. The equation of motion for that volume is given by

$$\rho \frac{d\mathbf{v}}{dt} = -\nabla P + \rho \mathbf{f},$$

where  $\mathbf{f}$  represents the possible body forces acting on the unit volume. This equation is written for a specific fluid particle. Using again Eq. 2.1 it is possible to obtain the equation of motion for a specific point in time:

$$\frac{\partial \mathbf{v}}{\partial t} + \mathbf{v} \cdot (\nabla \mathbf{v}) = -\frac{1}{\rho} (\nabla P + \rho \mathbf{f}). \quad (2.4)$$

This is known as *Euler's* equation in the case, such as this one, when the effects of viscosity in the fluid have been ignored. The version of this equation when viscous drag forces are taken into account is called the *Navier-Stokes* equation.

For the particular case of stellar interiors, we will ignore the effects of internal friction (viscosity), and consider gravity as the only body force. The gravitational acceleration  $\mathbf{g}$  can be written as the gradient of the gravitational potential  $\Phi$ :

$$\mathbf{g} = -\nabla\Phi,$$

where  $\Phi$  satisfies the *Poisson equation*:

$$\nabla^2 \Phi = 4\pi G\rho. \quad (2.5)$$

### 2.1.3 Energy equation

To complete the equations, we can consider the principle of conservation of internal energy given by the first law of thermodynamics for purely mechanical pressure,

$$\frac{dq}{dt} = \frac{dE}{dt} + P\frac{dV}{dt} = \frac{dE}{dt} + P\frac{d}{dt}\left(\frac{1}{\rho}\right) = \frac{dE}{dt} - \frac{P}{\rho^2}\frac{d\rho}{dt}, \quad (2.6)$$

where  $q$  corresponds to the heat gained or lost by the system, and  $E$  its internal energy. It will prove useful to consider the case of a system undergoing adiabatic changes. For such a system we can define the three adiabatic exponents:

$$\Gamma_1 = \left(\frac{d \ln P}{d \ln \rho}\right)_{\text{ad}}, \quad \frac{\Gamma_2}{\Gamma_2 - 1} = \left(\frac{d \ln P}{d \ln T}\right)_{\text{ad}}, \quad \Gamma_3 - 1 = \left(\frac{d \ln T}{d \ln \rho}\right)_{\text{ad}}, \quad (2.7)$$

which allow us to write the energy equation in terms of more convenient variables:

$$\frac{dq}{dt} = \frac{1}{\rho(\Gamma_3 - 1)} \left( \frac{dP}{dt} - \frac{\Gamma_1 P}{\rho} \frac{d\rho}{dt} \right) \quad (2.8)$$

$$= c_P \left( \frac{dT}{dt} - \frac{\Gamma_2 - 1}{\Gamma_2} \frac{T}{P} \frac{dP}{dt} \right) \quad (2.9)$$

$$= c_V \left( \frac{dT}{dt} - (\Gamma_3 - 1) \frac{T}{P} \frac{d\rho}{dt} \right), \quad (2.10)$$

where  $c_P$  and  $c_V$  are the specific heats at constant pressure and volume, respectively (cf. Eq. 1.24). It is worth mentioning that for the particular case of an ideal gas,

$$\gamma = \frac{c_P}{c_V} = \Gamma_1 = \Gamma_2 = \Gamma_3 = 5/3. \quad (2.11)$$

### 2.1.4 Heat transfer

As mentioned before, a full set of equations to determine the properties of a fluid consists of the continuity equation, Euler's equation, and the energy conservation equation. When the gravitational potential is the only important body force, Euler's equation is complemented with the Poisson equation to compute the local gravity.

From the sections above, the perceptive reader would have noticed that we face a similar problem as in Sect. 1.3.2 regarding the number of equations and variables: we currently have a system of six equations and seven explicitly shown variables ( $\rho$ , the three components of  $\mathbf{v}$ ,  $P$ ,  $E$  and  $\Phi$ ). Moreover, the energy equation (Eq. 2.6) includes a heat loss and gain term that needs to be computed. This term can be written as

$$\frac{dq}{dt} = \epsilon - \frac{1}{\rho} \operatorname{div} \mathbf{F}, \quad (2.12)$$

where  $\epsilon$  is the rate of energy generation (as in Eq. 1.10) and  $\mathbf{F}$  is the total vector flux of energy. It is clear now that constitutive equations such as those presented in Sect. 1.3.2 (EOS, nuclear reaction rates, etc.) are needed to solve the system, as well as an energy transport theory for the outgoing flux.

The most important contributions to  $\mathbf{F}$  are usually radiation, convection and conduction. In principle, each of the contributions should be calculated and added as an extra term on the right-hand side of Eq. 2.12. However, conduction plays an important role in regions dominated by electron degeneracy (such as the cores of low-mass stars in the RGB, see Sect. 1.2.3) which are nearly isothermal. When necessary, the conductive flux can be treated formally in the same way as the radiative flux. On the other hand, the flux due to radiative energy transport can be computed in a relatively simple way as shown in Sect. 1.3.1.

We mention one extra assumption commonly used to deal with the oscillations. It can be shown (e.g. Aerts et al. 2010) that the time scales for radiation and for energy generation are much larger than the time scale for pulsation, the latter one being usually of the order of hours or minutes. Thus, we assume that the motion due to oscillations occurs *adiabatically* and the heating term can be neglected. For this particular case, Eq. 2.8 yields:

$$\frac{dP}{dt} = \frac{\Gamma_1 P}{\rho} \frac{d\rho}{dt}, \quad (2.13)$$

which gives the necessary relation between  $P$  and  $\rho$ .

The case of the convective flux poses severe theoretical challenges. In principle, a time-dependent theory of convection should be included in the entire hydrodynamical system to correctly address the description of stellar oscillations, as the time scales for convection can be very similar to those of pulsation. However, the resulting equations are too complicated to handle analytically or even numerically. An average over large length scales is usually made to compensate for this, and the convective flux is calculated using the equations of turbulent motion. A classic example of this is the mixing-length theory (see Sect. 1.3.1).

## 2.2 Equations of non-radial stellar oscillations

The continuity equation (Eq. 2.2), the equations of motion (Eq. 2.4), the Poisson equation (Eq. 2.5) and the energy equation (Eq. 2.12), complemented with a set of constitutive equations (Eqs. 1.23 to 1.27) and an energy transport theory, are sufficient to determine completely the future development of the fluid of interest. However, they form a set of non-linear partial differential equations which has exact solutions only in certain cases. Nevertheless, these solutions can be used to construct other by means of perturbation analysis to linearize the equations.

### 2.2.1 Equilibrium structure and perturbation theory

If we know a particular (stable) solution to the equations of hydrodynamics, we can find another (perturbed) solution by means of perturbation analysis. The unperturbed solution is called equilibrium structure and is assumed to be static (no velocities present), so all time derivatives can in principle be neglected.

It is clear that such a solution satisfies immediately the continuity equation Eq. 2.2. For the purpose of our study, the most important equilibrium case is naturally spherical symmetry under the effects of self-gravitation. The structure depends then only on the radial distance  $r$  to the center and we can express vectors as  $\mathbf{g}_0 = g_0 \mathbf{a}_r$ , where the ‘0’ subscript denotes unperturbed quantities and  $\mathbf{a}_r$  the unit vector directed radially outwards. For the equilibrium structure, the equations of motion (Eq. 2.4) reduce to

$$\nabla P_0 = -g_0 \rho_0, \quad (2.14)$$

while the Poisson equation (Eq. 2.5) can be integrated once to obtain

$$g_0 = \frac{Gm_0}{r^2}. \quad (2.15)$$

The flux is directed outwards, so it can be expressed also as  $\mathbf{F} = F_{r,0} \mathbf{a}_r$ . The energy equation (Eq. 2.12) then reduces to

$$\rho_0 \epsilon_0 = \frac{1}{r^2} \frac{d}{dr} (r^2 F_{r,0}), \quad (2.16)$$

where we can express the total flow of energy through the sphere of radius  $r$  by  $L_0 = 4\pi r^2 F_{r,0}$ , and re-write the energy equation as

$$\frac{dL_0}{dr} = 4\pi r^2 \rho_0 \epsilon_0. \quad (2.17)$$

Finally, we use the diffusion approximation (Eq. 1.15) for the flux in the unperturbed solution, which may be written as

$$\frac{dT_0}{dr} = -\frac{3\kappa_0 \rho_0}{16\pi r^2 ac T_0^3} L_0. \quad (2.18)$$

Equations 2.14, 2.15, 2.17 and 2.18 are the familiar equations of stellar structure presented in Sect. 1.3.1. It is clear then from this discussion that we can use the results of a stellar evolution

code (as described in Sect. 1.3.3) as an equilibrium structure for oscillations calculations, and perturb it in order to obtain the other solutions.

We begin by considering a small Eulerian perturbation (at a given point) to the density. This can be expressed as

$$\rho(\mathbf{r}, t) = \rho_0(\mathbf{r}, t) + \rho'(\mathbf{r}, t), \quad (2.19)$$

where  $\rho'$  is the perturbation. In an equivalent way as in Eq. 2.1, the perturbation can be written in the Lagrangian description. Following a fluid particle, if the gas element moves due to the perturbation from  $\mathbf{r}_0$  to  $\mathbf{r}_0 + \delta\mathbf{r}$ , the density perturbation can be written as

$$\delta\rho = \rho'(\mathbf{r}, t) + \delta\mathbf{r} \cdot \nabla\rho_0, \quad (2.20)$$

to leading order in perturbations. It is important to keep in mind that, when the unperturbed solution is an equilibrium one ( $\mathbf{v}_0 = 0$ ), the velocity is given by the time derivative of the displacement:

$$\mathbf{v} = \frac{d\delta\mathbf{r}}{dt} = \frac{\partial\delta\mathbf{r}}{\partial t}. \quad (2.21)$$

Now we apply perturbation analysis to the equations of hydrodynamics and heat flow, neglecting quantities of order higher than one in the perturbations. Using Eq. 2.19 for the density, we can obtain the linearized equation of continuity (Eq. 2.2):

$$\delta\rho + \rho_0 \operatorname{div}(\delta\mathbf{r}) = 0, \quad (2.22)$$

which, by means of Eq. 2.20, can also be expressed in the Lagrangian description:

$$\frac{\partial\rho'}{\partial t} + \operatorname{div}(\rho_0\mathbf{v}) = 0. \quad (2.23)$$

We can integrate it once with respect to time to obtain the most commonly used form of the linearized equation of continuity:

$$\rho' + \operatorname{div}(\rho_0\delta\mathbf{r}) = 0. \quad (2.24)$$

The equations of motion Eq. 2.4 become

$$\rho_0 \frac{\partial^2\delta\mathbf{r}}{\partial t^2} = \rho_0 \frac{\partial\mathbf{v}}{\partial t} = -\nabla P' + \rho_0\mathbf{g}' + \rho'\mathbf{g}_0, \quad (2.25)$$

where  $\mathbf{g}' = -\nabla\Phi'$  and the Poisson equation is satisfied by the perturbed gravitational potential:

$$\nabla^2\Phi' = 4\pi G\rho', \quad (2.26)$$

with

$$\Phi' = -G \int_V \frac{\rho'(\mathbf{r}', t)}{|\mathbf{r} - \mathbf{r}'|} dV'. \quad (2.27)$$

For the equation of energy, we can consider the expression presented in Eq. 2.8 in its perturbed form:

$$\frac{\partial\delta q}{\partial t} = \frac{1}{\rho_0(\Gamma_{3,0} - 1)} \left( \frac{\partial\delta P}{\partial t} - \frac{\Gamma_{1,0}P_0}{\rho_0} \frac{\partial\delta\rho}{\partial t} \right), \quad (2.28)$$

presented here in Lagrangian description due to its simplicity. It can of course be expressed as an Eulerian perturbation. The term of the heating rate needs also to be expressed as a perturbation, which can be easily done from Eq. 2.12 and gives

$$\rho_0 \frac{\partial \delta q}{\partial t} = \delta(\rho \epsilon - \text{div} \mathbf{F}) = (\rho \epsilon - \text{div} \mathbf{F})'. \quad (2.29)$$

Finally, if we consider the adiabatic approximation presented in Eq. 2.13 by neglecting the heating term, we obtain

$$\frac{\partial \delta P}{\partial t} - \frac{\Gamma_{1,0} P_0}{\rho_0} \frac{\partial \delta \rho}{\partial t} = 0, \quad (2.30)$$

or, integrating once over time,

$$\delta P = \frac{\Gamma_{1,0} P_0}{\rho_0} \delta \rho. \quad (2.31)$$

### 2.2.2 Separation of variables

As the equilibrium model is assumed to be non-rotating and we ignore the possible effects of magnetic fields, it depends only on the radial coordinate  $r$ . The perturbations on the other hand are not restricted to be only radial, so a spherical polar coordinate system  $(r, \theta, \phi)$  can naturally be used to describe them. We look for harmonic solutions to the equations, which can be expressed as

$$f(r, \theta, \phi, t) = f_1(r, \theta, \phi) \exp(-i\omega t), \quad (2.32)$$

where  $\omega$  is the angular frequency. Separating the displacement  $\delta \mathbf{r}$  into a radial and a horizontal component,

$$\delta \mathbf{r} = \xi_r(r, \theta, \phi) \mathbf{a}_r + \boldsymbol{\xi}_h(r, \theta, \phi), \quad (2.33)$$

the perturbed equation of continuity Eq. 2.24 becomes

$$\rho' = -\frac{1}{r^2} \frac{\partial}{\partial r} (\rho_0 r^2 \xi_r) - \rho_0 \nabla_h \cdot \boldsymbol{\xi}_h, \quad (2.34)$$

where  $\nabla_h$  is the horizontal component of the divergence (see Eq. A.6 in Appendix A). The equations of motion give

$$-\frac{\partial^2}{\partial t^2} \left[ \rho' + \frac{1}{r^2} \frac{\partial}{\partial r} (r^2 \rho_0 \xi_r) \right] = -\nabla_h^2 P' - \rho_0 \nabla_h^2 \Phi', \quad (2.35)$$

$$\rho_0 \frac{\partial^2 \xi_r}{\partial t^2} = -\frac{\partial P'}{\partial r} - \rho' g_0 - \rho_0 \frac{\partial \Phi'}{\partial r}, \quad (2.36)$$

for the horizontal and radial components, respectively. The Poisson equation may be written as

$$\frac{1}{r^2} \frac{\partial}{\partial r} \left( r^2 \frac{\partial \Phi'}{\partial r} \right) + \nabla_h^2 \Phi' = 4\pi G \rho'. \quad (2.37)$$

It should be noticed that the term  $\nabla_h^2$  contains derivatives only with respect to  $\theta$  and  $\phi$ .

The energy equation suffers from the complication of the heat gain equation. In principle, the result will clearly depend on the form assumed for the flux  $\mathbf{F}$  (c.f Eq.2.29). If we consider the diffusion approximation given by Eq. 1.15, the flux is expressed in terms of the gradient of a scalar (in this case  $T$ ); the heat term then contains only derivatives in  $\theta$  and  $\phi$  in  $\nabla_h^2$ . Thus, by means of variable separation, the horizontal part of the displacement can be further split into a  $\theta$  and  $\phi$  component with a solution in spherical harmonics of the form:

$$f_2(\theta, \phi) = (-1)^m c_{\ell m} P_\ell^m(\cos \theta) \exp(im\phi) \equiv Y_\ell^m(\theta, \phi). \quad (2.38)$$

where  $c_{\ell m}$  is a normalization constant and  $P_\ell^m$  are the associate Legendre functions.  $Y_\ell^m$  is a spherical harmonic characterized by its degree  $\ell$  and its azimuthal order  $m$ , with  $|m| \leq \ell$ . A more detailed derivation of Eq. 2.38, including the complete process of variable separation, definition of the Legendre polynomials and spherical harmonics is given in Appendix A.

The dependent variables in Eqs. 2.35-2.37 can then be written as

$$\xi_r(r, \theta, \phi, t) = \sqrt{4\pi} \tilde{\xi}_r(r) Y_\ell^m(\theta, \phi) \exp(-i\omega t) \quad (2.39)$$

$$P'(r, \theta, \phi, t) = \sqrt{4\pi} \tilde{P}'(r) Y_\ell^m(\theta, \phi) \exp(-i\omega t), \quad (2.40)$$

etc., where the tilde denotes amplitudes. It is clear then that the geometry of the oscillation modes will be defined by the spherical harmonic entering the eigenfunctions.

From the equation of motion, the horizontal displacement is given by

$$\xi_h = \sqrt{4\pi} \tilde{\xi}_h \left( \frac{\partial Y_\ell^m}{\partial \theta} \mathbf{a}_\theta + \frac{1}{\sin \theta} \frac{\partial Y_\ell^m}{\partial \phi} \mathbf{a}_\phi \right) \exp(-i\omega t), \quad (2.41)$$

where

$$\tilde{\xi}_h = \frac{1}{r\omega^2} \left( \frac{1}{\rho_0} P' + \tilde{\phi}' \right).$$

Thus, the displacement vector can be written as

$$\delta \mathbf{r} = \sqrt{4\pi} \Re \left\{ \left[ \tilde{\xi}_r(r) Y_\ell^m(\theta, \phi) \mathbf{a}_r + \tilde{\xi}_h(r) \left( \frac{\partial Y_\ell^m}{\partial \theta} \mathbf{a}_\theta + \frac{1}{\sin \theta} \frac{\partial Y_\ell^m}{\partial \phi} \mathbf{a}_\phi \right) \right] \exp(-i\omega t) \right\}. \quad (2.42)$$

At last, and dropping the '0' for the equilibrium quantities and the tilde for the amplitudes, we can write the final system of equations of oscillations in the adiabatic approximation (Eq. 2.31):

$$\frac{d\xi_r}{dr} = - \left( \frac{2}{r} + \frac{1}{\Gamma_1 P} \frac{dP}{dr} \right) \xi_r + \frac{1}{\rho c_s^2} \left( \frac{S_\ell^2}{\omega^2} - 1 \right) P' + \frac{\ell(\ell+1)}{\omega^2 r^2} \Phi', \quad (2.43)$$

$$\frac{dP'}{dr} = \rho(\omega^2 - N^2) \xi_r + \frac{1}{\Gamma_1 P} \frac{dP}{dr} P' - \rho \frac{d\Phi'}{dr}, \quad (2.44)$$

$$\frac{1}{r^2} \frac{d}{dr} \left( r^2 \frac{d\Phi'}{dr} \right) = 4\pi G \left( \frac{P'}{c_s^2} + \frac{\rho \xi_r}{g} N^2 \right) + \frac{\ell(\ell+1)}{r^2} \Phi', \quad (2.45)$$

where  $c_s^2 = \Gamma_1 P / \rho$  is the square of the adiabatic sound speed. We have made use of two characteristic frequencies, namely the *Lamb* frequency  $S_\ell^2$  and the *buoyancy* or *Brunt-Väisälä* frequency  $N^2$ . The latter had already been introduced in the frame of convective energy transport in stellar interiors (Sect. 1.3.1). The expressions for these frequencies can be written as

$$S_\ell^2 = \frac{\ell(\ell + 1) c_s^2}{r^2}, \quad (2.46)$$

$$N^2 = g \left( \frac{1}{\Gamma_1 P} \frac{dP}{dr} - \frac{1}{\rho} \frac{d\rho}{dr} \right). \quad (2.47)$$

The last ingredient necessary to solve the set of equations just presented is suitable boundary conditions. For the case of small adiabatic oscillations of spherical stars, these are obtained at  $r = 0$  and  $r = R$ . The central condition imposes that the displacement at the center must vanish, while the conditions at the surface demand either continuity of  $\Phi'$  and its derivative, or the pressure to be constant at the stellar surface. We caution the reader that in current numerical computations of stellar oscillations, the atmospheres are assumed to be isothermal due to the simplicity of the boundary conditions arising for those particular cases. A more extensive discussion of this topic can be found in the Appendix D of Aerts et al. (2010).

Before closing this section, it is worth mentioning that the final set of equations can be solved numerically. An equilibrium structure (computed by a stellar evolution code such as GARSTEC) is provided as an input, and an adiabatic oscillations code solves the equations for the perturbed quantities in the manner described above. One example of these codes (and probably the most widely used) is the Aarhus adiabatic oscillation package (ADIPLS, Christensen-Dalsgaard 2008).

### 2.2.3 Modes, frequencies and asymptotic analysis

It must be noted that the oscillations equations have no dependence on the azimuthal order  $m$ . This is a consequence of the assumption that the equilibrium state is independent of the polar axis of the coordinate system. This condition is not satisfied when a preferred axis of symmetry exists, as is for instance the case when stellar rotation is taken into account. We neglect these effects for the purpose of our work and characterize the oscillations only by their radial order  $n$  (number of nodes the eigenfunction has in the stellar interior) and degree  $\ell$ , but the issue of rotation in stellar evolution and asteroseismology is still far from well understood. The reader is referred to the monographs by Maeder (2009) and Aerts et al. (2010) for a more detailed discussion on these topics.

In the previous section we have carefully derived the equations governing adiabatic stellar oscillations, where the solutions to the perturbations contain a geometric component represented by the spherical harmonics and a periodic time dependence characterized by an angular frequency  $\omega$ . This is indeed an *eigenvalue* problem, where for each eigenfrequency  $\omega_{n,\ell}$  the associated eigenfunctions (i.e. the displacements) can be projected over the orthogonal base of the spherical harmonics.

We are still dealing with a fourth order system whose analytic solutions can be obtained in very restricted cases, such as the highly unrealistic case of the homogeneous compressible model

(where density is not a function of position, see Cox (1980)). It would be useful to approximate the equations to a point where they can be discussed analytically, in order to gain some further insight in the behavior of the oscillations. One interesting approximation that can be made is to neglect the perturbation to the gravitational potential  $\Phi'$ . The qualitative justification for this is that rapidly varying perturbation regions with positive and negative  $\rho'$  nearly cancel out in the gravitational potential (cf. Eq. 2.27). Thus,  $\Phi'$  can be considered more or less an average over the star of the effects of the gravitational potential at each point in the star. Neglecting the perturbation in the gravitational potential is called the *Cowling approximation* (Cowling 1941).

The equations of stellar oscillations in the Cowling approximation reduce to a second order system, which can be written as:

$$\frac{d\xi_r}{dr} = -\left(\frac{2}{r} + \frac{1}{\Gamma_1 P} \frac{dP}{dr}\right)\xi_r + \frac{1}{\rho c_s^2} \left(\frac{S_\ell^2}{\omega^2} - 1\right)P', \quad (2.48)$$

$$\frac{dP'}{dr} = \rho(\omega^2 - N^2)\xi_r + \frac{1}{\Gamma_1 P} \frac{dP}{dr}P'. \quad (2.49)$$

This approximation is valid for modes of large degree  $\ell$  or radial order  $n$ . Under these conditions, the eigenfunctions vary much more rapidly than the equilibrium quantities inside the star. Thus, the left hand term in Eq. 2.48 is much larger than the first term in the right hand side. We can make a very rough (but instructive!) approximation by neglecting these terms and the derivatives of the equilibrium quantities, which allow us to obtain a single second-order differential equation:

$$\frac{d^2\xi_r}{dr^2} = \frac{\omega^2}{c_s^2} \left(1 - \frac{N^2}{\omega^2}\right) \left(\frac{S_\ell^2}{\omega^2} - 1\right)\xi_r = -K_s^2(r)\xi_r. \quad (2.50)$$

This is a very crude approximation to the equations of stellar oscillations. In fact, the term  $2/r$  becomes very large near the center, while the neglected pressure derivatives increase towards the stellar surface. However, we must regard Eq. 2.50 as a useful expression to describe the overall properties of the modes.

Not surprisingly, Eq. 2.50 is a classic time-independent wave equation in one dimension. The behavior of  $\xi_r$  depends on the sign of  $K_s^2$ : when  $K_s^2 > 0$ , the solutions are oscillatory functions in  $r$ , when negative they are increasing or decreasing exponential solutions in  $r$ . When the solution is exponential in a certain zone of the stellar interior, it is said that the mode is *evanescent* in that particular region.

For a given mode of oscillation  $K_s^2$  changes in value and sign throughout the stellar interior, thus the solution can oscillate in some regions while it is evanescent in others. In general, one of the oscillatory zones dominates with the solution decaying exponentially from it. The mode is said to be *trapped* in that region, and its frequency is mainly determined by the structure of this zone. The boundaries of the trapping regions are the points where  $K_s^2 = 0$ , usually known as *turning points*.

Equation 2.50 allows us to determine the behavior of the modes depending on the stellar structure. There are two cases when the solutions are oscillatory:

- $|\omega| > |N|$  and  $|\omega| > S_\ell$ : modes with high frequencies called *p-modes*.

- $|\omega| < |N|$  and  $|\omega| < S_\ell$ : modes with low frequencies called *g-modes*.

The reason why the first type of oscillations are called p modes is that they are standing acoustic waves where pressure acts as the only restoring force. On the other hand, modes whose restoring force is buoyancy are trapped internal gravity waves, thus named g modes.

It is evident that the characteristic frequencies  $S_\ell$  and  $N$  defined in Eqs. 2.46 and 2.47 play a very important role determining the type of oscillations present in the stellar interior, and in which region they propagate. These are shown in Fig. 2.1 for a solar model in terms of the cyclic frequency  $\nu = \omega/2\pi$ , including the trapping regions for particular modes of oscillation. It is important to keep in mind that the buoyancy frequency  $N^2$  is negative in convective regions (see Sect. 1.3.1). This means that g modes, as expected, can be effectively trapped only in radiative regions.

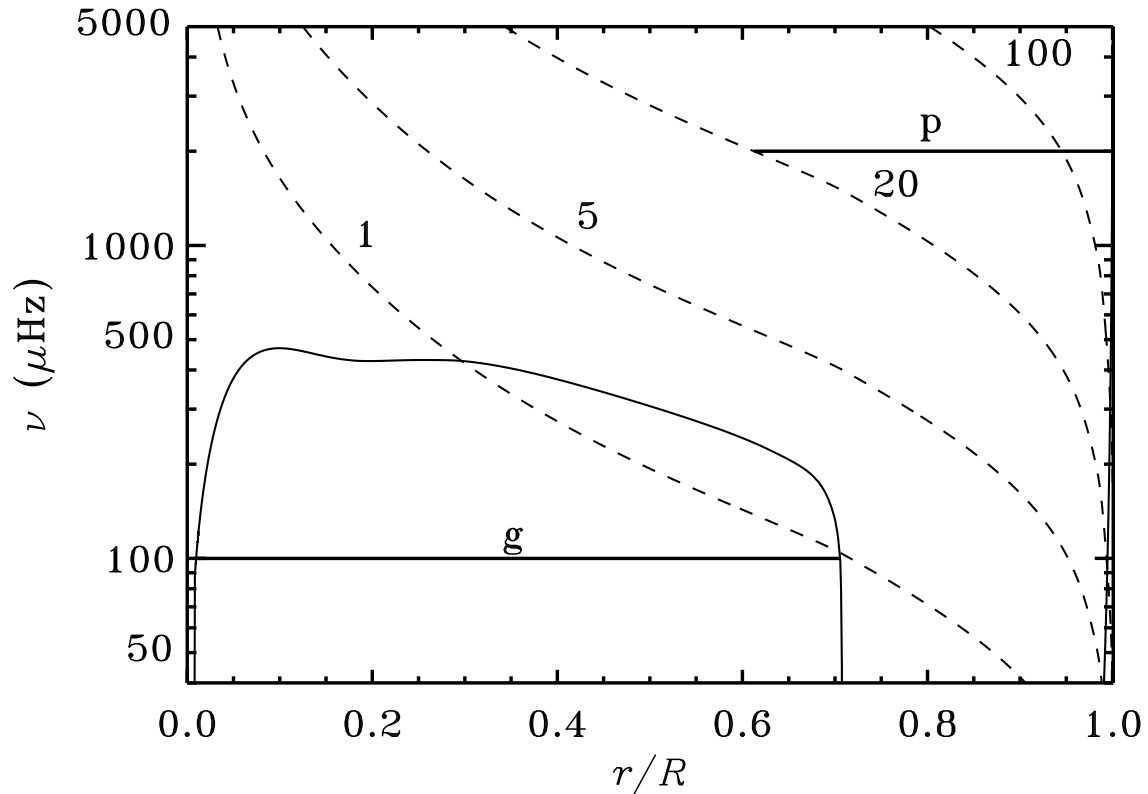


Figure 2.1: Characteristic frequencies  $N$  (solid line) and  $S_\ell$  (dashed line with values of  $\ell$  labelled on each curve) for a model of the present Sun. Solid horizontal lines represent the trapping region of a g mode with frequency  $\nu = 100 \mu\text{Hz}$ , and a p mode of degree  $\ell = 20$  and  $\nu = 2000 \mu\text{Hz}$ . Figure courtesy of C. Aerts (from Aerts et al. 2010)

For the observed modes in the Sun and solar-like oscillators, the typical situation is that  $\omega \gg N$ . In those cases, the behavior of the modes depends only on the variation of the sound

speed across the stellar interior. However, as mentioned in Sect. 1.3.1, there are situations during the evolution of a star when the buoyancy frequency becomes large enough in the stellar center and it is comparable to the value of the Lamb frequency. In those cases, the modes behave as acoustic modes in the outer zones, while they act as g modes in the central region of the star. This dual behavior is characteristic of the so-called *mixed modes* that appear in evolutionary phases such as the subgiant branch. Figure 2.2 shows the characteristic frequencies for a model in the main sequence (the Sun) and a star in the shell H-burning phase. It is clear that for the solar case, the region where g modes are trapped is well below the observed frequency range. In the case of the subgiant star, modes with frequencies in the observable region will present a mixed p-mode and g-mode character. This behavior is also characteristic of stars in the RGB and red clump phases.

While radial p-mode oscillations ( $\ell = 0$ ) travel all the way to the center of the star, non-radial p modes are trapped between an inner turning point  $r = r_t$  and the surface. This turning point is located where  $S_\ell(r_t) = \omega$ , which can be written as

$$\frac{c_s^2(r_t)}{r_t^2} = \frac{\omega^2}{\ell(\ell + 1)}. \quad (2.51)$$

This relation has been derived under the Cowling approximation. A slightly more sophisticated description can be made when considering the gravitational potential using a dispersion relation for plane waves. We write the square length of the wave as the sum of a radial and horizontal component:  $|\mathbf{k}^2| = k_r^2 + k_h^2$ . The dispersion relation is such that  $\omega^2/c_s^2 = k_r^2 + k_h^2$ ; an extra term related to the density is introduced when considering the gravitational potential:  $\omega^2 = c_s^2(k_r^2 + k_h^2) - 4\pi G\rho$  (Jeans 1928). The expression for the inner turning point can now be written as:

$$\frac{c_s^2(r_t)}{r_t^2} = \frac{\omega^2 - 4\pi G\rho(r_t)}{\ell(\ell + 1)}. \quad (2.52)$$

In terms of ray theory for cases where sound speed gradients exist (stellar interiors), the internal reflection of p modes can be understood as a consequence of the increasing sound speed towards the stellar center. In an analogous way as light bends when changing mediums, the mode propagation changes direction as the wave front experiences a higher sound speed and therefore travels faster. In the inner turning point, the wave travels horizontally, which gives the condition presented in either Eq. 2.51 or 2.52 from the dispersion relation. A similar analysis can be made for low frequency g-modes using the condition  $N = \omega$  which for the case of the Sun gives a turning point very close to the center and another just below the convective zone. Figure 2.3 shows an interior section of a solar model where the propagation of p modes and g modes are depicted, including the turning points.

Reflection of p-modes at the surface (or the outer turning point of p-modes) is still a matter of great uncertainty. The full theoretical development results in equations that are very complex to analyze. From the numerical point of view, stellar structure calculations still rely on crude approximations of the real outer structure of stars (those mentioned in Sect. 1.3.3). It is possible to derive a condition for the outer turning point for p modes assuming an isothermal atmosphere,

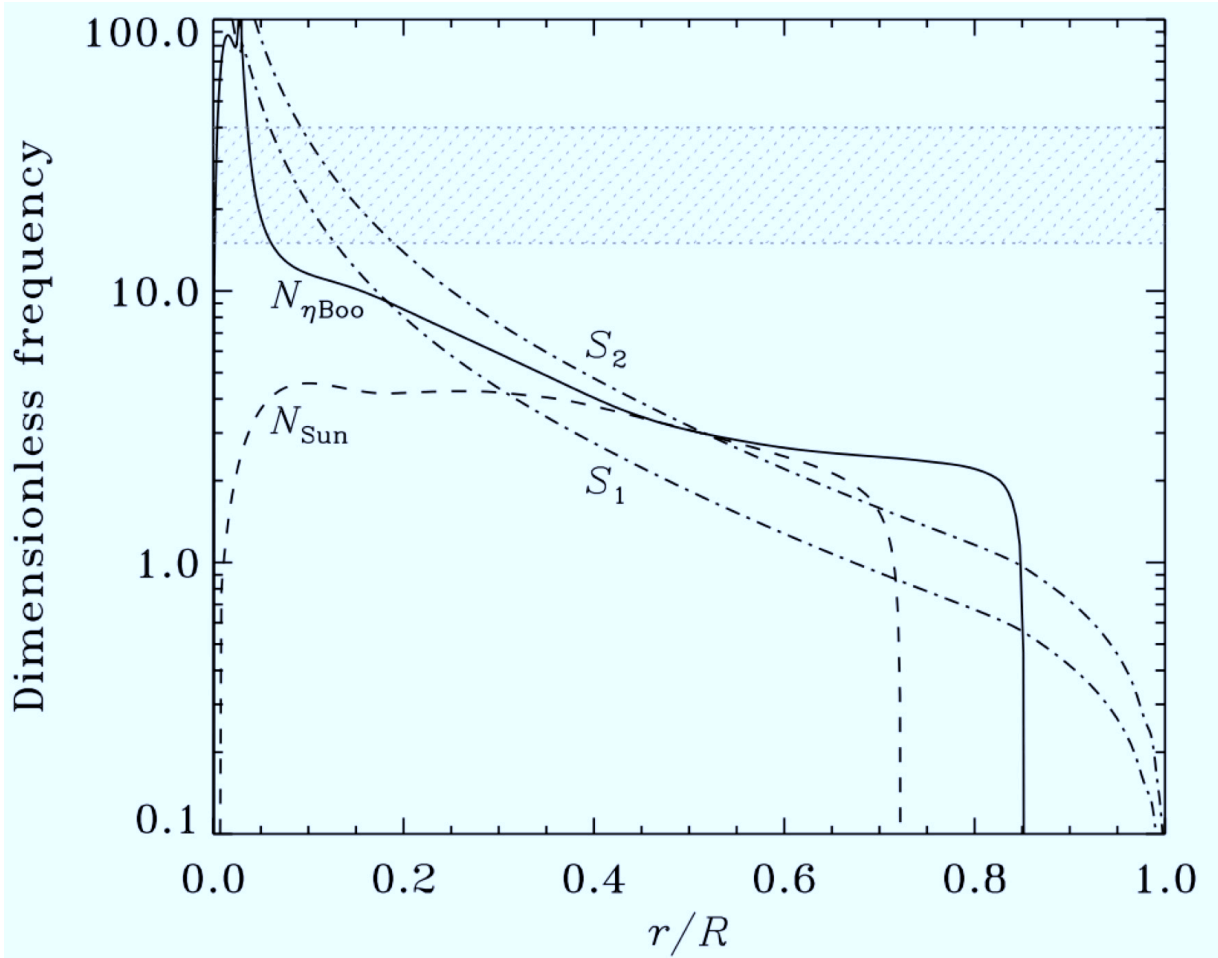


Figure 2.2: Characteristic Lamb and buoyancy frequencies, in units of  $(GM/R^3)^{1/2}$ , for a model of the present Sun and a  $1.63 M_{\odot}$  star in the subgiant phase. The dashed and solid lines show  $N$  in the solar and subgiant model, respectively. The dot-dashed lines show  $S_{\ell}$  for  $\ell = 1, 2$ , essentially indistinguishable in the two models with this scaling. The shaded band roughly indicates the region in frequency corresponding to the observed modes. Reproduced with the permission of J. Christensen-Dalsgaard (from Christensen-Dalsgaard 2004)

which gives a critical frequency of propagation

$$\omega_a = \frac{c_s}{2H_p}. \quad (2.53)$$

called the *acoustic cut-off* frequency. For the case of the Sun, the acoustic cut-off frequency in the solar photosphere is of the order of  $\nu_a \approx 5400 \mu\text{Hz}$ .

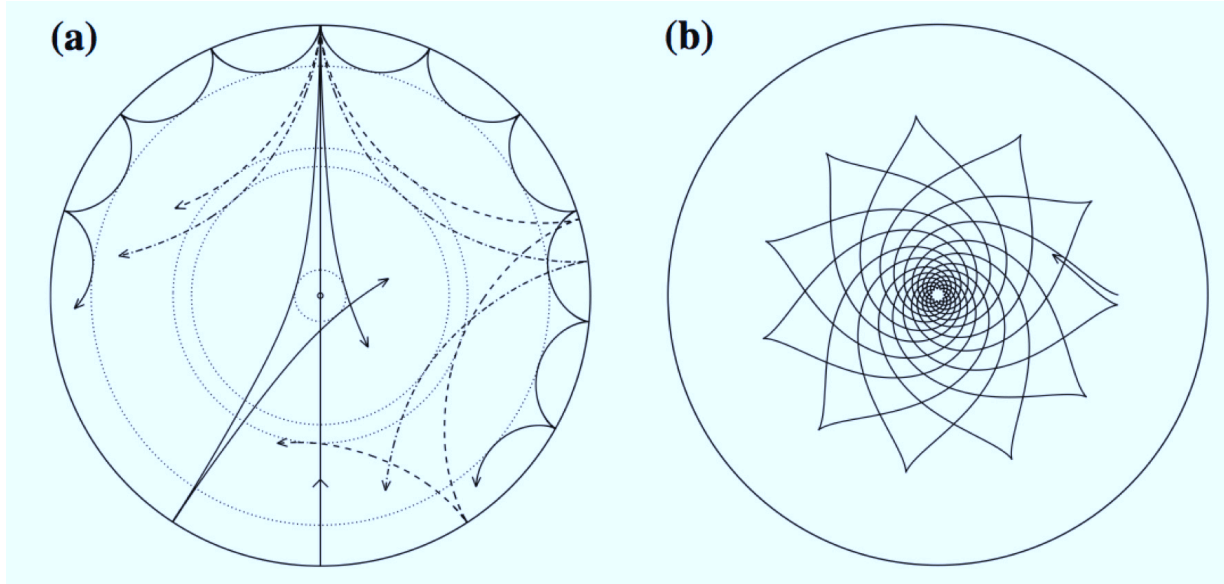


Figure 2.3: Propagation of rays in a cross-section of the solar interior. **(a)** shows the propagation of rays of acoustic p-modes, bending by the increase of the sound speed towards the solar interior. Total reflection occurs in the inner turning point (dotted circles). Rays shown have a frequency of  $\nu = 3000 \mu\text{Hz}$  and angular degrees of  $\ell = 75, 25, 20$  and  $2$  (in order of increasing penetration depth). **(b)** depicts rays of a gravity mode of frequency  $\nu = 190 \mu\text{Hz}$  and degree  $5$ . Reproduced with the permission of M. Cunha (from Cunha et al. 2007)

### 2.2.4 Frequency differences

It is possible to extend the analysis made in the previous section to a slightly more physically sound one, but still simple enough as to be treated analytically. Taking into account the derivatives of the equilibrium structure, with the exception of those in  $\rho$  and  $r$ , and considering the Cowling approximation, Deubner & Gough (1984) derived an asymptotical formalism that results in a second order differential equation:

$$\frac{d^2 X}{dr^2} + \frac{1}{c_s^2} \left[ S_\ell^2 \left( \frac{N^2}{\omega^2} - 1 \right) + \omega^2 - \omega_c^2 \right] X = 0. \quad (2.54)$$

The quantity introduced for the displacement is  $X = c_s^2 \rho^2 \text{div } \delta \mathbf{r}$ , and a generalized formulation for the acoustic cut-off frequency is included as

$$\omega_c^2 = \frac{c_s^2}{4H^2} \left( 1 - 2 \frac{dH}{dr} \right). \quad (2.55)$$

In an isothermal atmosphere,  $H = H_p$  is constant and Eq. 2.53 is recovered.

Equation 2.54 is obviously a wave equation. The behavior of its solutions can be studied by the factor:

$$K^2(r) = \frac{1}{c_s^2} \left[ S_\ell^2 \left( \frac{N^2}{\omega^2} - 1 \right) + \omega^2 - \omega_c^2 \right]. \quad (2.56)$$

Lets consider the case of a region between  $r_1$  and  $r_2$  where  $K^2(r) > 0$  and the solution is oscillatory. Using *JWKB* analysis it has been shown (e.g., Unno et al. 1989) that an approximate expression for the eigenfrequencies can be obtained, namely

$$\int_{r_1}^{r_2} K(r) dr = \left(n - \frac{1}{2}\right)\pi, \quad n = 1, 2, \dots \quad (2.57)$$

For the case of p modes, where  $\omega^2 \gg |N|^2$ , the lower turning point is approximately that defined in Eq. 2.51 since  $\omega_c$  is only large near the surface. The upper turning point  $r_2 \simeq R_t$ , where  $\omega = \omega_c(R_t)$ . The result is the so-called *Duvall* law (Duvall 1982),

$$\int_{r_t}^R \left(1 - \frac{\ell(\ell+1)c_s^2}{\omega^2 r^2}\right)^{1/2} \frac{dr}{c_s} = \left(\frac{[n + \alpha(\omega)]\pi}{\omega}\right), \quad (2.58)$$

where  $\alpha(\omega)$  is a function of frequency determined by the conditions in the stellar surface. In the case of low-degree p-modes, the turning point  $r_t$  is very close to the stellar, center. Thus, the second term in the brackets of the left hand side of Eq. 2.58 is very small, which leads to the following simple relation:

$$\nu_{n,\ell} = \frac{\omega_{n,\ell}}{2\pi} \simeq \left(n + \frac{\ell}{2} + \frac{1}{4} + \alpha\right)\Delta\nu, \quad (2.59)$$

where  $\Delta\nu$  is known as the *large frequency separation*, defined as the inverse of twice the sound travel time between the stellar center an the surface:

$$\Delta\nu = \left[2 \int_0^R \frac{dr}{c_s}\right]^{-1}. \quad (2.60)$$

As  $\Delta\nu$  is a measurement of the time it takes a sound wave to reach the center of the star, it is very sensitive to the total radius of the star. In fact, as pressure modes are dynamical processes that disturb the hydrostatic equilibrium, they are expected to have periods of the order of  $\tau_{\text{dyn}}$  (see Eq. 1.2). Thus,  $\Delta\nu$  is clearly sensitive to the mean density of the star (e.g. Ulrich 1986).

From a similar analysis (e.g., see Appendix E in Aerts et al. 2010), it can be shown that the eigenfunctions of p modes can be written as

$$\rho^{1/2} c_s^{1/2} r \xi_r(r) \simeq A \cos(\omega \tau - (1/4 + \alpha)\pi), \quad (2.61)$$

where  $A$  is an amplitude factor, and  $\tau$  is the acoustic depth given by

$$\tau = \int_r^R \frac{dr}{c_s}. \quad (2.62)$$

This variable measures the travel time of p modes from the surface towards the interior.

The asymptotic behavior of oscillations have been extensively studied (e.g., Tassoul 1980, 1990). For low-degree modes, the asymptotic relation predicts modes evenly spaced in frequency for consecutive radial orders. Thus, the large frequency separation can be characterized as  $\Delta\nu_{n,\ell} =$

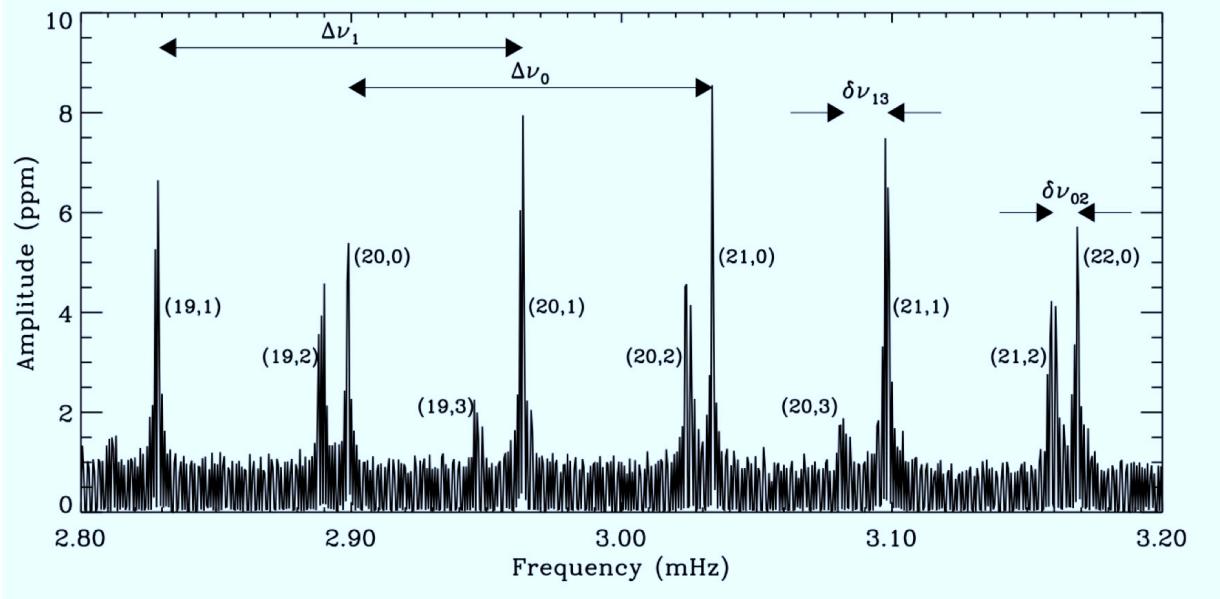


Figure 2.4: Portion of the solar oscillation spectrum showing the large and small frequency separation for low-degree modes. Pairs in brackets show the  $(n, \ell)$  value of each mode. Reproduced with the permission of T. Bedding (from Bedding & Kjeldsen 2003)

$\nu_{n,\ell} - \nu_{n-1,\ell}$ . Also from Eq. 2.59, modes with the same value of  $n + \ell/2$  should be almost degenerate. Departures from this degeneracy are thought to have considerable diagnosis potential, and are characterized by the *small frequency separation*  $\delta\nu_{n,\ell} = \nu_{n,\ell} - \nu_{n-1,\ell+2}$ . These frequency patterns have been observed in the solar frequency spectrum, as it can be seen in Fig. 2.4.

From an observational point of view, it is useful to consider the average  $\Delta\nu_0 = \langle \nu_{n,\ell} - \nu_{n-1,\ell} \rangle_{n,\ell}$  over a certain region of the oscillation spectrum. The individual frequencies can be expressed as reduced modulo  $\Delta\nu_0$ , expressed by

$$\nu_{n,\ell} = \nu_0 + k\Delta\nu_0 + \tilde{\nu}_{n,\ell}, \quad (2.63)$$

where  $\nu_0$  is a chosen reference frequency,  $k$  is an integer such that  $\tilde{\nu}_{n,\ell}$  is between 0 and  $\Delta\nu_0$ . In Fig. 2.5 this so-called *Echelle* diagram is presented for the Sun. This type of diagram separates the oscillation modes into vertical ridges for each angular degree, and is used as a method to identify  $\ell$  in photometric observations of oscillations. If the asymptotic relation in Eq. 2.59 would have been exact, the frequencies would be stacked vertically one exactly on top of the other.

For the g modes, a similar analysis can be carried out of Eq. 2.57 when  $\omega^2 \ll S_\ell^2$ . In this case, the asymptotic approximation leads to a relation between the periods of the oscillation modes. This can be written as:

$$\Pi = \frac{\Pi_0}{\sqrt{\ell(\ell+1)}}(n + \alpha_{\ell,g}), \quad \text{with} \quad \Pi_0 = 2\pi^2 \left( \int_{r_1}^{r_2} N \frac{dr}{r} \right)^{-1}, \quad (2.64)$$

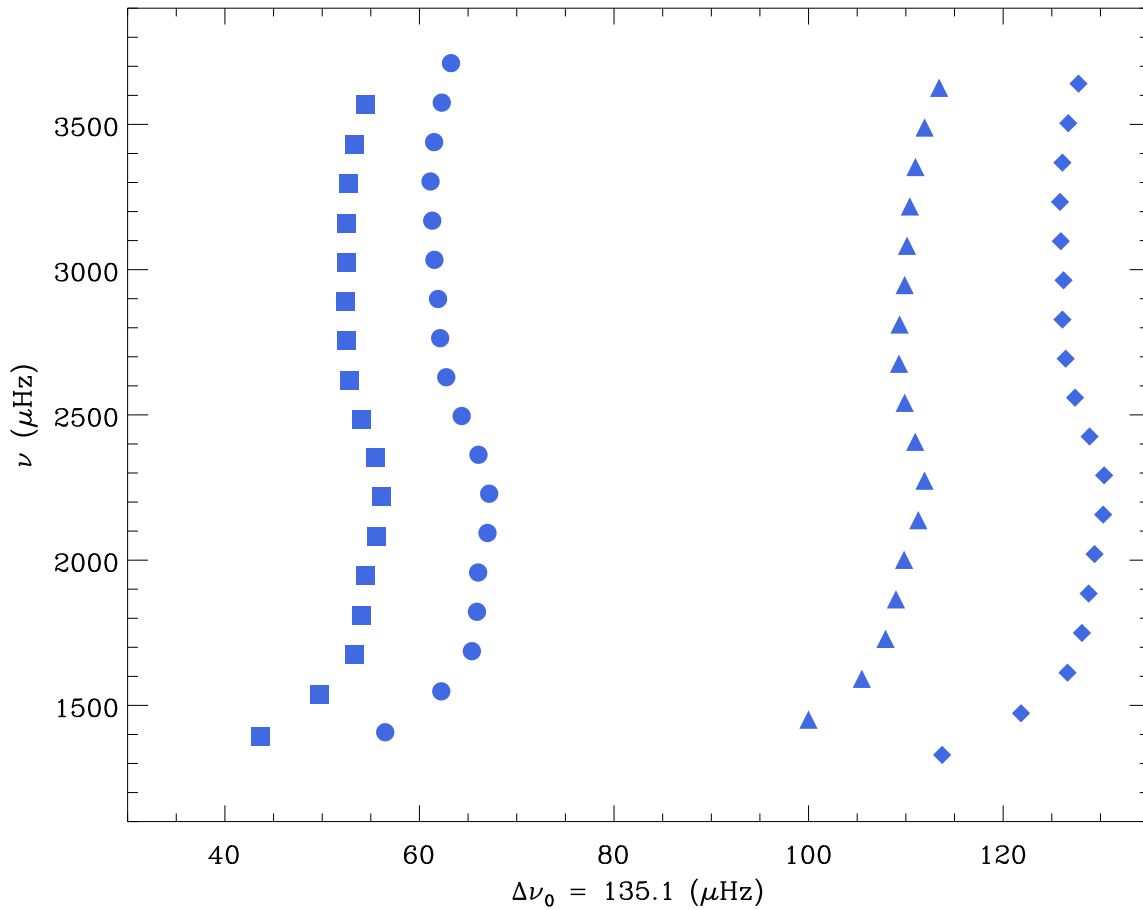


Figure 2.5: Echelle diagram for observed solar frequencies obtained with the Birmingham Solar-Oscillations Network (BiSON Chaplin et al. 2002), plotted for  $\Delta\nu_0 = 135.1 \mu\text{Hz}$ . Circles, diamonds, squares and triangles are used for modes of degree  $\ell = 0, 1, 2$  and  $3$ , respectively. BiSON data kindly provided by W. J. Chaplin.

where  $\alpha_{\ell,g}$  is a phase term that depends on the details of the boundaries of the trapping region ( $r_1$  and  $r_2$ ). This relation shows that, asymptotically, the g-mode periods are equally spaced in the order of the mode, the spacing decreasing with increasing  $\ell$ .

Despite the many approximations we have done so far to gain insight into the nature of the oscillations, numerical calculations can solve the full set of equations for adiabatic oscillations as presented in Eqs. 2.43 to 2.45. In Figs. 2.6 and 2.7 the radial displacement eigenfunctions are plotted for a set of selected oscillation modes. For the p modes (Fig. 2.6) the radial mode ( $\ell = 0$ ) has non-zero amplitudes up to the center of the star, while modes with higher angular degree oscillate inside the cavity delimited by the turning points and decay exponentially beyond them. The amount of zeros of the displacement function (nodes) clearly increases with increasing radial order  $n$ . For the case of g modes (Figs. 2.7), the amplitudes increase towards the center and decay

beyond the convective region. It is worth mentioning that, by convention,  $g$  modes are labelled using negative values of  $n$ .

### 2.3 The CoRoT and *Kepler* missions

The analysis of the oscillations presented in this Chapter reveals the potential of studying stellar pulsations as a tool to probe the internal structure of stars. It is clear that the frequencies of oscillation depend on the mass and radius of the star, as well as the set of equilibrium variables  $P$ ,  $\rho$ ,  $\Gamma_1$ , and  $g$ . Any physical process in the stellar interior affecting these quantities can in principle be tested by comparing the observed frequencies to those obtained from evolutionary calculations including different sets of input physics.

As mentioned in Sect. 1.4, there are many stars where pulsations have been detected. However, it is very challenging to measure these oscillations from the ground due to their small amplitudes. In 1991, Brown et al. (1991) made the claim of possible detection in Procyon of solar-like oscillations. Nevertheless, it took until 1999 for Martić et al. (1999) to definitely establish the pulsation in Procyon to be real. The subsequent determination of individual mode frequencies in  $\alpha$  Cen A (Bouchy & Carrier 2001) and detection of solar-like oscillations in  $\beta$  Hyi (Bedding et al. 2001) opened the doors to new discoveries in the field.

Another particularly interesting case is that of non-radial oscillations in red giant stars. Early detection of excess power in this type of stars revealed pulsations, although it was unclear if they were radial or non-radial modes (e.g., Buzasi et al. 2000; Frandsen et al. 2002).

Regardless of these encouraging results, main-sequence stars with oscillations detected were only a handful, and individual modes of oscillation were very difficult to measure even in multi-site observation campaigns (Bedding & Kjeldsen 2007; Bedding et al. 2010b). The quest for non-radial oscillations in red giants continued and it was hard to see how it would be possible to detect them with the current limitations.

In December 2006, the Convection, Rotation and planetary Transits mission (CoRoT) was successfully launched (Baglin et al. 2006). The satellite consists of a 27 cm primary mirror and four CCD detectors, two devoted to exoplanet research and another two for asteroseismic investigations. During its life span, the mission alternately observes for 6 months two opposite fields in the intersection between the equatorial plane and the galactic plane.

One of the greatest successes of the CoRoT mission was to provide unambiguous detection of non-radial oscillations in red giant stars (De-Ridder et al. 2009), with more than 1800 of them having global oscillation parameters measured (Mosser et al. 2010). Some properties of these stars can be determined from their oscillation spectra that could otherwise only be inferred by using sophisticated galactic chemical evolution models, such as radii and masses (e.g., Miglio et al. 2009).

Following the encouraging results of CoRoT, in March 2009 the *Kepler* mission was launched (Christensen-Dalsgaard et al. 2007; Borucki et al. 2009). The satellite is equipped with a 95 cm diameter corrector and a mosaic of 42 CCD detectors, with the primary goal of finding planets via the transit method. The field of observation is fixed for the full length of the mission (nominal 4 years), with the possibility of a two-year extension. Data is acquired in either short or long

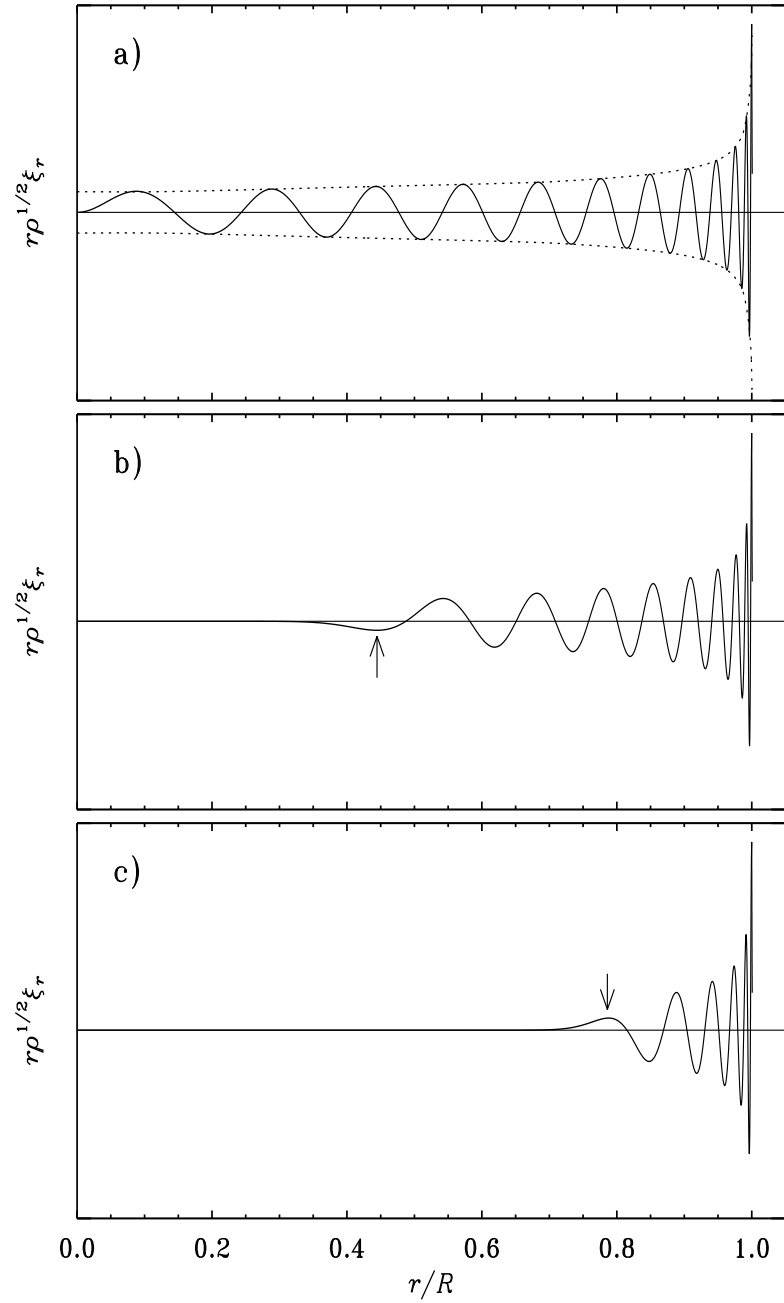


Figure 2.6: Scaled radial displacement eigenfunctions, on an arbitrary scale, for selected p-modes in a solar model. **a)**  $\ell = 0, n = 23, \nu = 3310 \mu\text{Hz}$ ; **b)**  $\ell = 20, n = 17, \nu = 3375 \mu\text{Hz}$ ; **c)**  $\ell = 60, n = 13, \nu = 3234 \mu\text{Hz}$ . In panels **b)** and **c)** the arrows mark the location of the inner turning points (derived with Eq. 2.51). Figure kindly provided by C. Aerts (from Aerts et al. 2010)

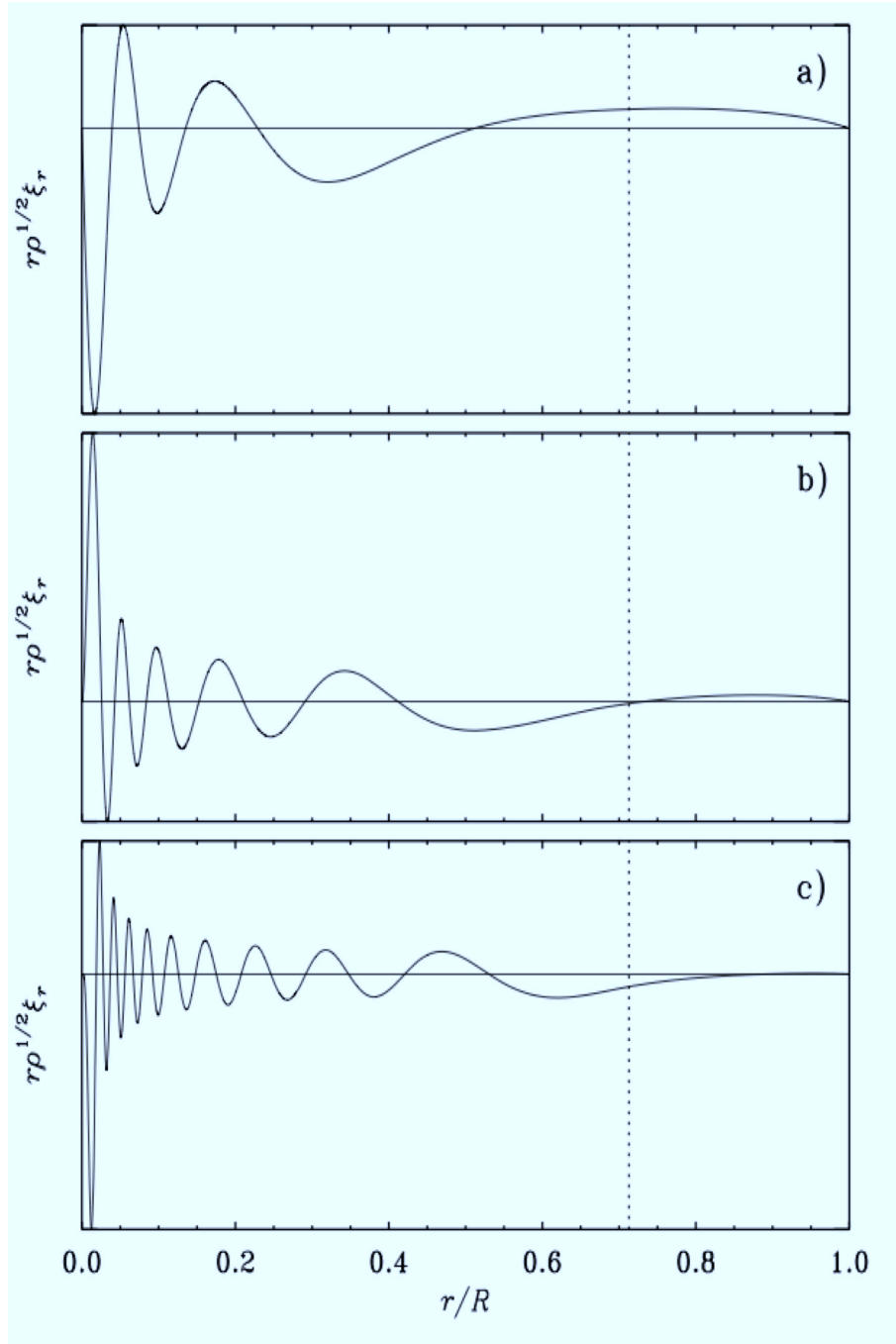


Figure 2.7: Scaled radial displacement eigenfunctions, on an arbitrary scale, for selected g-modes in a solar model. **a)**  $\ell = 1$ ,  $n = -5$ ,  $\nu = 110 \mu\text{Hz}$ ; **b)**  $\ell = 2$ ,  $n = -10$ ,  $\nu = 103 \mu\text{Hz}$ ; **c)**  $\ell = 4$ ,  $n = -19$ ,  $\nu = 100 \mu\text{Hz}$ . The vertical dotted line shows the position of the convective envelope. Reproduced with the permission of J. Christensen-Dalsgaard (from Aerts et al. 2010)

cadence mode, changing the time of sampling from 60 sec to 30 min. Periods of observations are divided into 3-months quarters, with an initial 10 days quarter (Q0) devoted to commissioning. At any given time, a minimum of 512 stars are being observed by the asteroseismology program in short cadence mode to detect solar-like oscillations.

The results obtained by the *Kepler* mission have been outstanding in the amount of stars with detected oscillations and the quality of the data obtained by the satellite. The first seven months of observations comprehended the survey phase, with stars observed only one month each to detect the most promising candidates for long time follow-up. For the short cadence observation mode, more than 500 stars with detected oscillations were found during this period (Chaplin et al. 2011c)<sup>1</sup>, which are shown in Fig. 2.8. These stars comprise the full sample of main-sequence and subgiant stars observed with *Kepler*. As mentioned above,  $\Delta\nu$  is a measurement of the mean density of the star, which decreases during the H-burning evolution due to the increase in the stellar radius. Thus,  $\Delta\nu$  can be considered as a measurement of evolutionary stage and it is customary to use this quantity instead of luminosity to construct this ‘asteroseismic’ HRD. It is important to notice that in order to obtain the average  $\Delta\nu_0$  it is not necessary to identify the angular degree of the oscillation modes, just to measure directly the average separation between the peaks from the power spectrum (see Fig. 2.4). Effective temperatures have been estimated using the available Sloan photometry of the field obtained before the mission was launched to characterize the targets (Brown et al. 2011).

*Kepler* observations have also revealed solar-like oscillations in hundreds of red giant stars (Bedding et al. 2010a). These have been detected in field stars and in the open clusters present in the *Kepler* field of view (Stello et al. 2010)<sup>2</sup>. One of the important results obtained from red giants studies is the possibility of disentangling RGB stars from clump red giants (cf. Sect. 1.2.3) using the detected period spacings of mixed modes (Beck et al. 2011, Bedding et al. 2011<sup>3</sup>). In a nutshell, low- and intermediate-mass stars are expected to show modes with mixed p-mode and g-mode character across their oscillation spectrum when they are in the red giant phases, due to their highly compact cores (see Sect. 2.2.3). That being the case, these modes should be very sensitive to the conditions in the core of these stars. As mentioned in Sect. 1.3.1, stars in the RGB burn hydrogen in a shell surrounding the inert He-rich core, while stars in the red clump are already burning helium in the center and have a convective core. The period spacings for g modes introduced in Eq. 2.64 should be sensitive to these drastic differences in the interiors of both types of stars.

In Fig. 2.9 the large frequency separation versus observed mean g-mode period spacing of a large sample of *Kepler* red giants is presented. There is a clear distinction between two large groups of stars, where the larger period spacing values correspond to those stars in the red clump (red and orange symbols). It has been mentioned by the authors in Bedding et al. (2011) that a secondary population of stars can be seen among those in the central helium burning phase (orange symbols). Models suggest that the reason for this is a mass difference in the progenitor of the red clump star, with those cases where the initial mass was large enough for the helium

<sup>1</sup>V. Silva Aguirre is a coauthor in this paper.

<sup>2</sup>V. Silva Aguirre is a coauthor in this paper.

<sup>3</sup>V. Silva Aguirre is a coauthor in this paper.

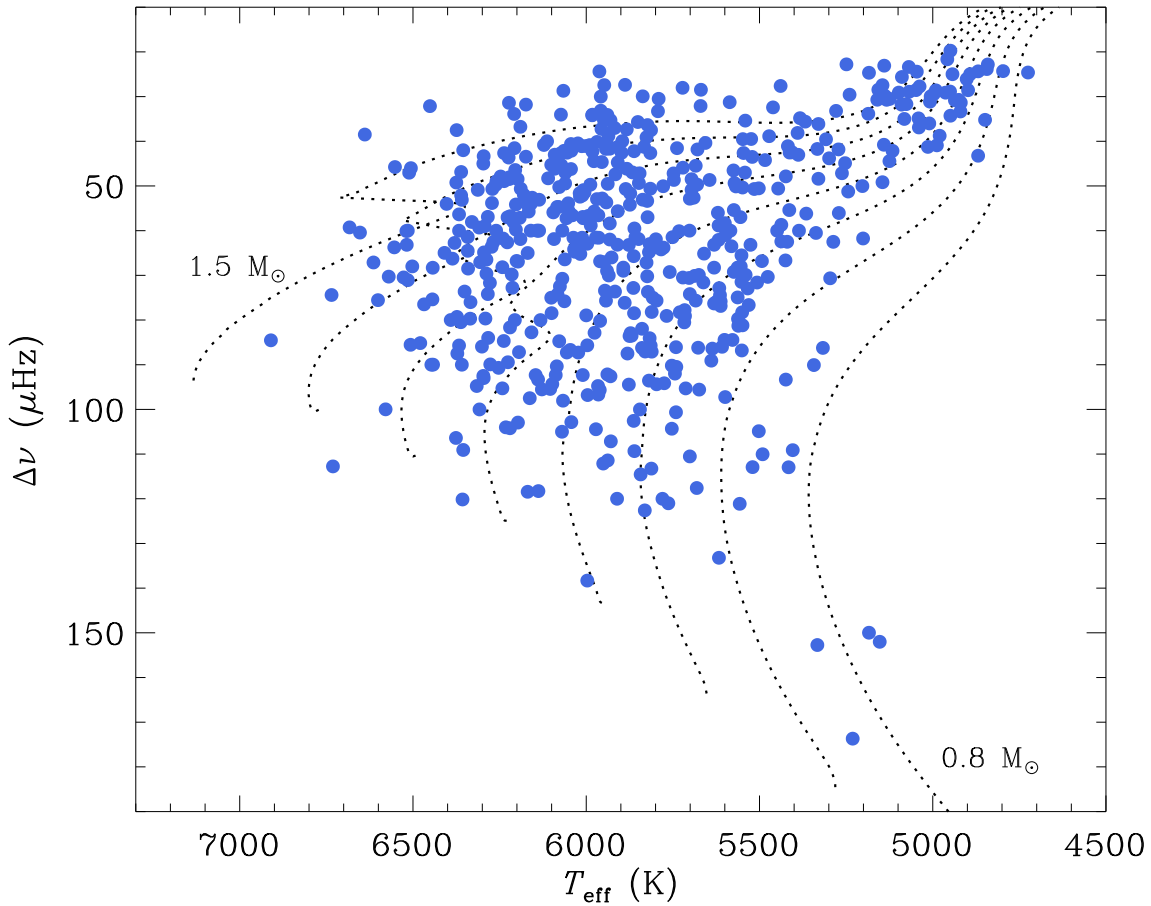


Figure 2.8: Average large frequency separations,  $\Delta\nu_0$ , against effective temperature, for *Kepler* targets with oscillations detected within the first seven months of observations (blue circles). The dotted lines show predicted evolutionary tracks for models of different stellar mass (0.8 to 1.5 solar masses, in steps of 0.1), from the BaSTI database (Pietrinferni et al. 2004). Oscillations data kindly provided by W. J. Chaplin (from Chaplin et al. 2011c)

ignition to occur under non-degenerate conditions separating into the ‘secondary clump’. As pointed out in Sect. 1.2.3, the secondary population in clump stars was already inferred by Girardi (1999) from evolutionary considerations.

The most important parameter defining if the ignition of helium will occur under degenerate conditions or not is the mass of the helium core (e.g., Chiosi et al. 1992). As the threshold for degenerate ignition has been usually believed to be around  $\sim 1.8\text{-}2.3 M_{\odot}$ , any process affecting the extent of the convective core in the main-sequence evolution of these stars will impact the exact value where this transition takes place. However, as mentioned in Sect. 1.3.1, size of convective cores and mixing processes that affect them are still poorly understood.

Another example of the difficulties constraining the interiors comes from the analysis per-

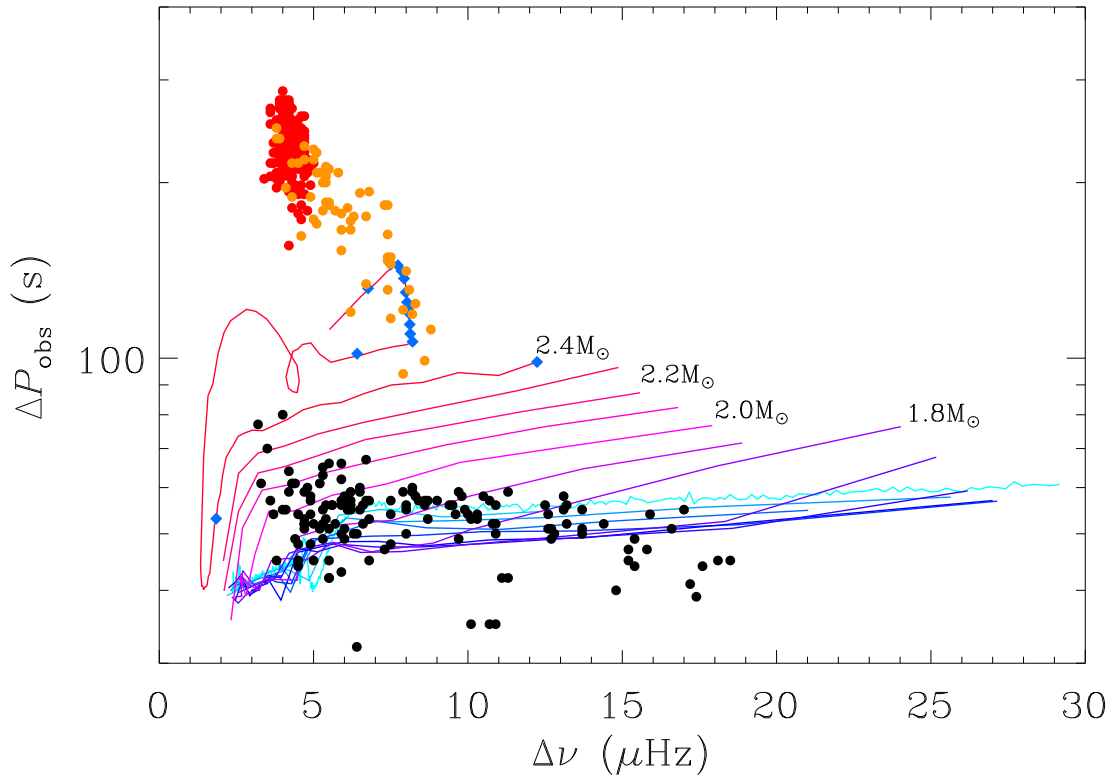


Figure 2.9: Observed period spacing as a function of the large separation in red giants. Model tracks show the evolution for hydrogen shell-burning red giants of near-solar metallicity ( $Z = 0.017$ ) and masses between  $1.0 M_{\odot}$  and  $2.4 M_{\odot}$ . Black dots show  $\Delta P_{\text{obs}}$  as measured from *Kepler* red giant branch stars by Bedding et al. (2011). Red and orange dots show red clump and secondary clump stars. Blue diamonds on the  $2.4 M_{\odot}$  track are equally spaced in time by 10 Myr, starting from 520 Myr. Figure kindly provided by T. White (from White et al. 2011).

formed on a subgiant *Kepler* target nicknamed ‘Gemma’ (Metcalf et al. 2010)<sup>4</sup>. This particular star has a large set of individual frequencies detected, including the presence of mixed modes, and it was simultaneously modeled by several teams. The results yielded two families of equally possible solutions from a statistical point of view. The two families agree in the estimated radius but one set estimates a mass of  $\sim 1.13 M_{\odot}$  and the other of  $\sim 1.24 M_{\odot}$ . Thus, although the possible solutions had very different evolutionary histories (the large-mass family of solutions shows a convective core in the main-sequence phase), our current lack of understanding of mixing processes in the H-burning phase inhibits us from further constraining more advanced stellar evolutionary phases. Moreover, determination of stellar ages crucially depend on the assumptions made on physical processes taking place during the main-sequence evolution. It is expected

<sup>4</sup>V. Silva Aguirre is a coauthor in this paper.

that longer observations of this target will allow to discriminate between the two families of solutions.

In order to get some insight on these topics, and considering the increasing amount of available data coming from the space missions just described, we will study the effects that different mixing processes in stellar interiors have on the overall main-sequence evolution of intermediate-mass stars, in particular related to the issue of convective boundary definition and mixing beyond this formal boundaries.

# Chapter 3

## Mixing processes in stellar cores

The bulk of this chapter forms part of an article published in *Astronomy & Astrophysics* in March 2011 (Silva-Aguirre, Ballot, Serenelli, & Weiss 2011a). It deals with different types of mixing processes in stellar interiors, its implementation in an evolutionary code, and the implications for the overall evolution of main-sequence stars. The initial research was made for a CoRoT target (HD 49933), and then theoretically extended to stars of different masses in the main sequence.

### 3.1 Motivation: the case of HD 49933

Understanding the physical processes dominating stellar interiors and correctly characterizing their impact on the evolution of stars are two of the main goals of stellar astrophysics. For a long time it has been acknowledged that different mixing processes in stars, such as convection, microscopic diffusion, and rotational mixing, strongly influence the overall evolution of stars (e.g. Zahn 1992; Maeder & Meynet 2000; Thoul et al. 1994; Turcotte et al. 1998, and references therein), with subsequent effects on observable quantities, such as luminosity, effective temperature, and surface abundances. This has a direct impact on any determinations of derived parameters relying on evolutionary models still to a large extent, as in the case of stellar masses and ages.

How the boundaries of the convective regions are defined and how the convective zones themselves are treated from the point of view of mixing of elements severely affects the interior structure of the stellar models. As mentioned in Sect. 1.3.1, in evolutionary calculations the boundaries of convective regions are defined by means of a stability criterion, such as the Ledoux (Eq. 1.18) or the Schwarzschild (Eq. 1.20) criterion. When molecular weight gradients exist and the Ledoux criterion is not equivalent to the Schwarzschild one, it can occur that a zone will be convectively unstable or not depending on the applied criterion. A region which is convective according to Schwarzschild but convectively stable according to Ledoux is known as a *semiconvective* region.

If the Ledoux criterion is applied and a semiconvective zone identified, the next issue to consider is how to treat such a region from the point of view of mixing of elements. Depending on the adopted prescription for mixing to take place, these semiconvective layers could maintain

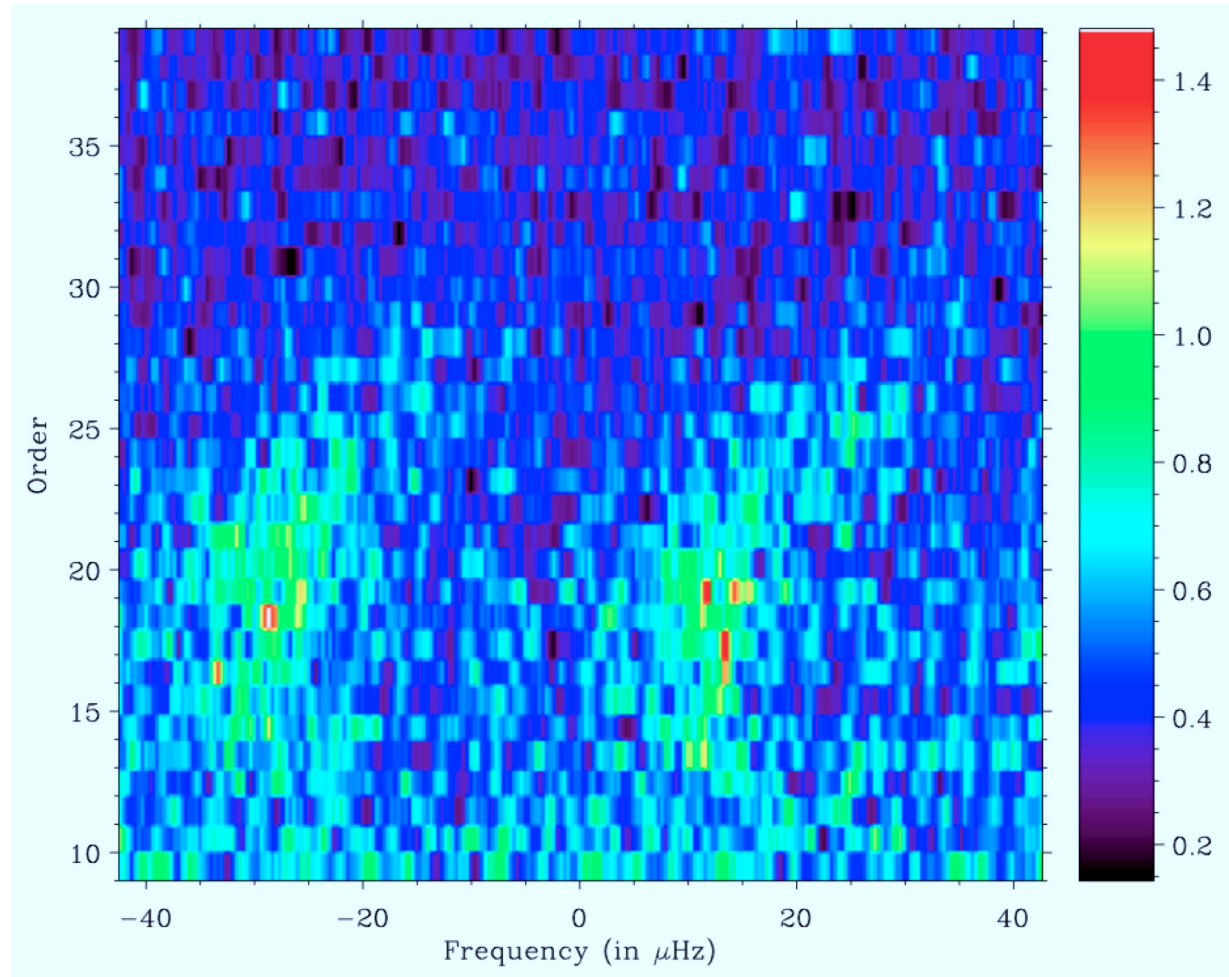


Figure 3.1: Echelle diagram for the 60-day run of observations from CoRoT for the target HD 49933, showing a clear signature of oscillations in the vertically aligned ridges. The identification of the angular degree of the modes is far from trivial. The large separation used is  $\Delta\nu_0 = 85 \mu\text{Hz}$ . Reproduced with the permission of T. Appourchaux (from Appourchaux et al. 2008)

their chemical composition or undergo a mixing process known as semiconvective mixing.

In the case of massive star evolution, the case of semiconvection has been extensively studied. During the hydrogen-burning phase the convective core retreats leaving behind a nonuniform chemical profile determined by the composition of the core at the moment each layer is detached from it. This situation allows semiconvective regions to develop when the Ledoux criterion is considered. Since the pioneering work of Schwarzschild & Härm (1958), several authors have investigated the occurrence of semiconvective mixing and its effects on stellar evolution (e.g. Stothers 1970; Stothers & Chin 1975; Chiosi 1978; Langer et al. 1985). Although it was initially thought to occur only in massive stars, semiconvection was also predicted to take place in low-mass stars (e.g. Mitalas 1972; Faulkner & Cannon 1973; Gabriel & Noels 1977) but with a

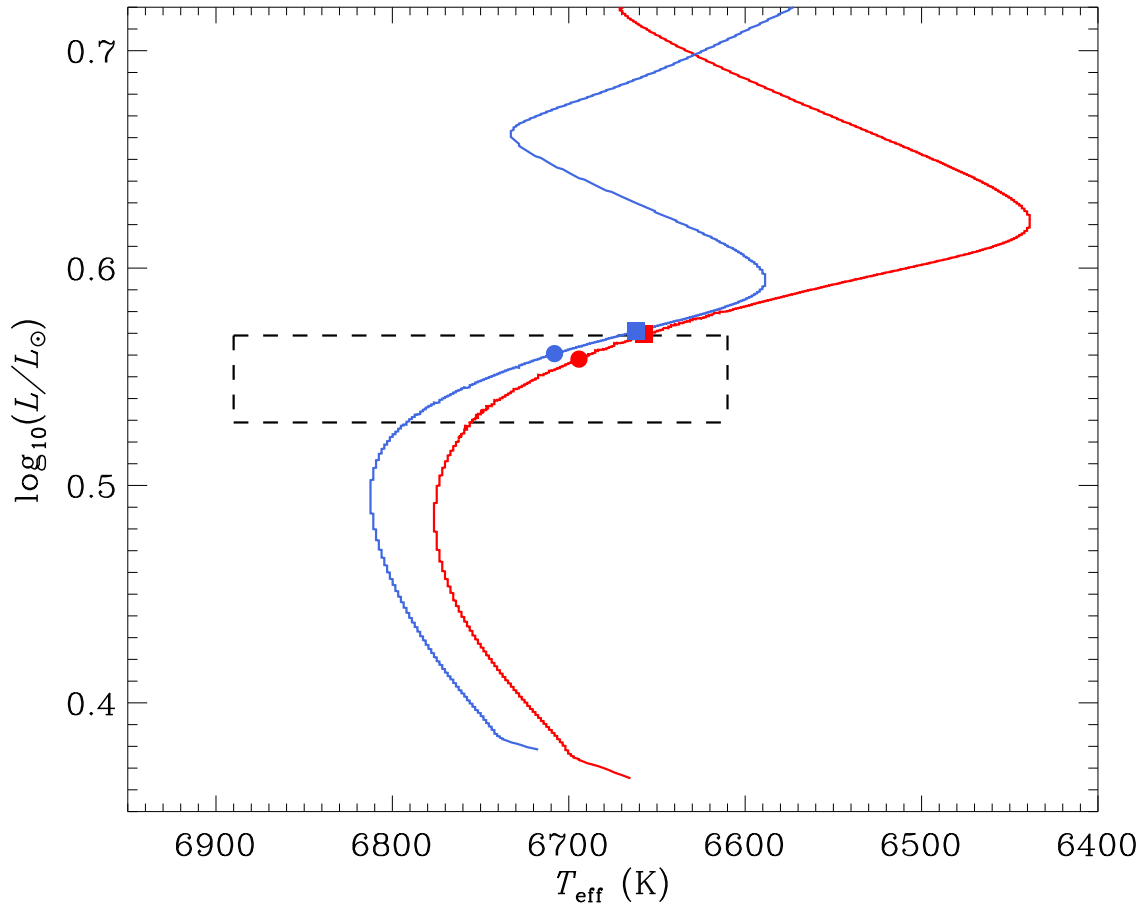


Figure 3.2: Evolutionary tracks for the  $1.2 M_{\odot}$  models for HD 49933 at a metallicity of  $[\text{Fe}/\text{H}] = -0.35$ , depicted in solid lines for the case without (blue) and with overshooting (red). Position of the models for the two possible scenarios are marked: scenario A in filled squares and scenario B with filled circles. See text for details.

stronger impact in the helium-burning phase.

As an example for the importance of semiconvective mixing in low-mass stars, we discuss the case of the CoRoT target HD 49933, one of the priority targets of the mission. HD 49933 is a main-sequence F type star with an absolute visual magnitude of  $M_v = 3.408 \pm 0.026$  derived from Hipparcos parallax measurements (Leeuwen 2007), and an estimated iron abundance of  $[\text{Fe}/\text{H}] = -0.43 \pm 0.09$  (Bruntt et al. 2008). Effective temperature and luminosity were estimated using the parallax information and the InfraRed Flux Method (Casagrande et al. 2010), taking into account random errors in photometry, and uncertainties in parallax and metallicity. The obtained values are  $T_{\text{eff}} = 6750 \pm 140$  K and  $\log(L/L_{\odot}) = 0.549 \pm 0.02$ . This effective temperature value is in accordance with the spectroscopic one derived by Bruntt et al. (2008).

The first asteroseismic results of HD 49933 comprising 60 days of observations were pub-

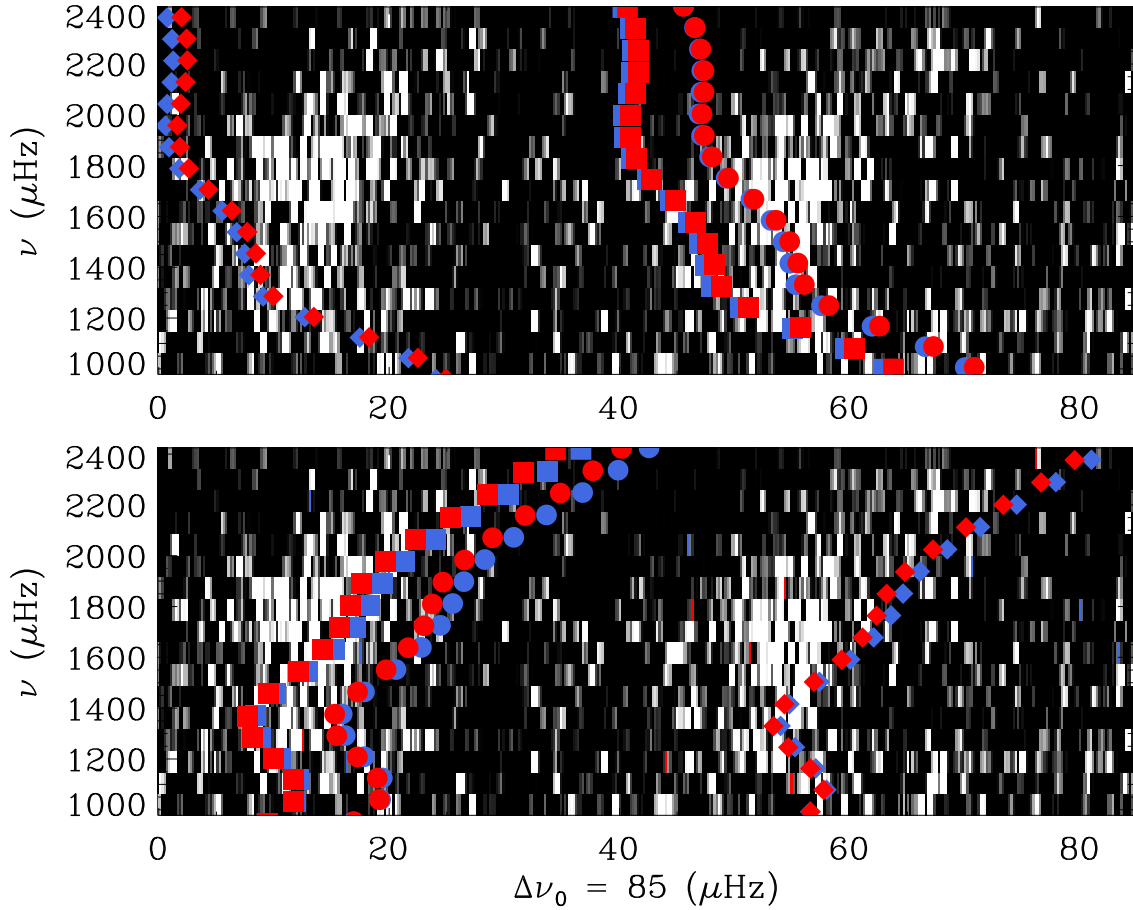


Figure 3.3: Echelle diagram for the 60-day run of observations from CoRoT for the target HD 49933, including the theoretical frequencies for two models: one without (blue) and one with overshooting (red). Symbols represent the angular degrees  $\ell = 0$  (circles),  $\ell = 1$  (diamonds), and  $\ell = 2$  (squares). *Top panel*: models fitting scenario A. *Bottom panel*: models fitting scenario B. Observational data kindly provided by J. Ballot

lished by Appourchaux et al. (2008). In Fig. 3.1 an Echelle diagram of the data is shown, where the y-axis depicts the assumed radial order  $n$  of the modes. From the excess power it is clear that oscillations are detected; however, the identification of the angular degree of the modes is far from evident. It could be that the left-hand side ridge corresponds to the  $\ell = 1$  modes and the right-hand side one to the  $\ell = 0, 2$  modes (scenario A), or the other way around (scenario B). It is worth mentioning that, due to partial cancellation effects, we do not expect to detect  $\ell = 3$  modes yet (see Appendix A). From their analysis, Appourchaux et al. (2008) determined the mean large frequency separation to be  $\Delta\nu_0 = 85.9 \pm 0.15 \mu\text{Hz}$ .

Although the quality of these data does not allow for individual mode identification, we modeled the star in order to predict the most probable configuration in the Echelle diagram from

a theoretical point of view. Two grids of models were constructed using GARSTEC covering the error box in luminosity and effective temperature for a chemical composition adequate to that of HD 49933, with masses ranging between 1.0 and 1.3  $M_{\odot}$ . One of the grids included convective overshooting as described in Sect. 1.3.3 using the calibrated value for the free parameter in Eq. 1.29, which determines the extension of the overshooting region.

For both grids, best-fit models were found matching the large frequency separation to the value given by Appourchaux et al. (2008), and also constraining them to be within the  $1\text{-}\sigma$  uncertainties in the  $T_{\text{eff}}$  and  $\log(L/L_{\odot})$  observational error box. Within these margin of error, it is possible to find models along an evolutionary track that fit both possible ridge identifications in the Echelle diagram. In Fig. 3.2 we show the HRD of the 1.2  $M_{\odot}$  track from each grid, marking the position of the model that agrees with each scenario. For each track the difference between the model fitting the mode identification scenario A and B is of the order of  $\sim 200$  Myr.

Regardless of the grid considered, the curvature of the ridges always favored a solution where the left-hand side ridge corresponds to the  $\ell = 0, 2$  modes (scenario B, see Fig. 3.3). This identification was later confirmed by independent methods when longer data sets for the star were acquired (Benomar et al. 2009). Since one of the grids included overshooting, the two best-fit models found have different ages, size of the convective core, and remaining central hydrogen content. Although the use of the Echelle diagram allowed us to restrict the possible solutions to a subset of models, we cannot use this tool to discriminate between the existence or absence of a convective core, or what the precise evolutionary stage of the star is. Moreover, for the 1.2  $M_{\odot}$  model without overshooting we encountered a semiconvective region outside the fully convective core, reminiscent of the well-known situation for massive stars.

As mentioned in Sect. 1.2.2 stars with masses higher than  $\sim 1.1 M_{\odot}$  develop a convective core during the main-sequence evolution, whose extent is determined by their temperature stratification. As the timescale for mixing of elements in this convective region is much shorter than the nuclear timescale, the core is believed to be homogeneously mixed, and a discontinuity in density appears at the edge of the fully mixed core. This discontinuity is produced either by convective core expansion, owing to the increasing importance of the CNO cycle over the p-p chain (Mitalas 1972), or by the retreating convective core leaving behind a nonuniform chemical profile (Faulkner & Cannon 1973). Both cases produce higher opacities outside the convective core and allow a semiconvective region to develop. If the resulting density barrier is sustained throughout the main-sequence evolution, the homogeneously mixed central region will either be restricted in its growth or not allowed to develop at all, drastically changing the behavior of the evolutionary tracks, especially close to the main sequence turn-off. This has important implications for the use of the color-magnitude diagram (CMD) morphology and the existence of a hook-like feature at the turn-off to estimate properties of stars at the end of the main sequence and the age of a given stellar population (see for instance Maeder 1974a,b; Maeder & Meynet 1991).

With all these in mind, we start by addressing in this chapter the issue of determining convective boundaries and the treatment of zones that present a gradient in the molecular weight. We include in our evolution code the Ledoux criterion for convective instability, with a diffusive approach for semiconvective mixing, and study the impact of these process along the main sequence.

## 3.2 Ingredients of the stellar models

For our model calculations with GARSTEC we used the 2005 version of the OPAL equation of state (Rogers et al. 1996; Rogers & Nayfonov 2002) complemented by the MHD equation of state for low temperatures (Hummer & Mihalas 1988), low-temperature opacities from Ferguson et al. (2005) and OPAL opacities for high temperatures (Iglesias & Rogers 1996), the Grevesse & Sauval (1998) solar mixture, and the NACRE compilation for thermonuclear reaction rates (Angulo et al. 1999). Convective zones are treated with the mixing-length theory (MLT), regardless of the criterion used to define their boundaries. Within these zones, the chemical composition is modified either instantaneously or by a diffusive process that uses the convective velocity estimated from the MLT as described, for instance, in Kippenhahn & Weigert (1990).

For the frequency computations of the specific models analyzed, we used the Aarhus adiabatic oscillation package (ADIPLS, Christensen-Dalsgaard 2008).

### 3.2.1 Boundaries of convective and semiconvective zones

As briefly mentioned in Sect. 1.3.1, the convective zones within a stellar model are defined using a stability criterion. The convectively unstable regions are usually determined with the Schwarzschild criterion by comparing the radiative and adiabatic temperature gradients, denoted  $\nabla_{\text{rad}}$  and  $\nabla_{\text{ad}}$ , respectively (Schwarzschild & Härm 1958). Recalling eq. 1.20, a layer is convective when

$$\nabla_{\text{ad}} < \nabla_{\text{rad}}. \quad (3.1)$$

However, gradients of molecular weight  $\mu$  can have a stabilizing – or destabilizing – effect on the convection process. The Ledoux criterion (Ledoux 1947) takes this effect into account. Within this prescription, a layer is convective when

$$\nabla_{\text{L}} < \nabla_{\text{rad}}, \quad (3.2)$$

with  $\nabla_{\text{L}}$ , the Ledoux temperature gradient, defined as

$$\nabla_{\text{L}} = \nabla_{\text{ad}} + \frac{\varphi}{\delta} \nabla_{\mu}, \quad (3.3)$$

where  $\varphi$ ,  $\delta$ , and  $\nabla_{\mu}$  are those defined in Eq. 1.19. For an equation of state appropriate to a mixture of an ideal gas and black body radiation, Eq. 3.2 reduces to

$$\nabla_{\text{L}} = \nabla_{\text{ad}} + \frac{\beta}{4 - 3\beta} \nabla_{\mu}, \quad (3.4)$$

where  $\beta$  is the ratio of gas pressure to total pressure (Kippenhahn & Weigert 1990).

Including changes in the molecular weight in the definition of the relevant temperature gradients leads to the appearance of zones whose energy transport process will depend on the convective criterion considered. There are regions that would be considered convective if the

Schwarzschild criterion were used, but they are in turn convectively stable if the Ledoux criterion were applied. These zones are called semiconvective zones, and are defined as the regions where

$$\nabla_{\text{ad}} < \nabla_{\text{rad}} < \nabla_{\text{L}}. \quad (3.5)$$

As an example, a model of a  $1.5 M_{\odot}$  star computed using the Ledoux criterion and displaying a semiconvective zone during its main-sequence evolution is depicted in Fig. 3.4. The hydrogen profile in the stellar interior is constant inside the homogeneously mixed convective core, and presents a sharp variation at the position where the edge of the core is located. This feature produces a step in the radiative gradient  $\nabla_{\text{rad}}$  due to the change in the chemical composition and opacities, and the departure of the Ledoux gradient  $\nabla_{\text{L}}$  from the adiabatic gradient  $\nabla_{\text{ad}}$  as a result of the change in the molecular weight. Therefore, a significant semiconvective layer appears at the boundary of the convective core. We notice that, in this example, the semiconvective zone comprehends 60% of the total mass of the convective region itself. If the Schwarzschild criterion were used instead, the semiconvective layer would be part of the convective core.

### 3.2.2 Prescription for semiconvective layers

Throughout the years, several approaches have been proposed to deal with semiconvective regions when they appear in stellar models (Stevenson 1979; Langer et al. 1983; Spruit 1992; Grossman & Taam 1996). According to the chosen prescription, the semiconvective zone is considered to be mixed more or less efficiently (see the comparison made by Merryfield 1995). The amount of mixing in semiconvective layers is crucial, because an efficient mixing process can reduce the molecular weight gradient sufficiently and then trigger convective instability. For the present work, we have implemented the prescription proposed by Langer et al. (1983, 1985) in GARSTEC, based on the description of vibrational instability made by Kato (1966). With this method, the true temperature gradient  $\nabla$  in a semiconvective region is calculated from the relation

$$\frac{L_{\text{sc}}}{L_{\text{rad}}} = \alpha_{\text{sc}} \frac{\nabla - \nabla_{\text{ad}}}{2\nabla(\nabla_{\text{L}} - \nabla)} \left[ (\nabla - \nabla_{\text{ad}}) - \frac{\beta(8 - 3\beta)}{32 - 24\beta - \beta^2} \nabla_{\mu} \right], \quad (3.6)$$

where  $L_{\text{sc}}$  and  $L_{\text{rad}}$  are the semiconvective and radiative luminosities, respectively.

The mixing is treated as a time-dependent diffusive process, with the diffusion coefficient calculated as

$$D_{\text{sc}} = \alpha_{\text{sc}} \frac{\kappa_{\text{r}}}{6 c_{\text{p}} \rho} \frac{\nabla - \nabla_{\text{ad}}}{\nabla_{\text{L}} - \nabla}, \quad (3.7)$$

where  $\kappa_{\text{r}}$  is the radiative conductivity,  $c_{\text{p}}$  the specific heat at constant pressure, and  $\rho$  the density. Both the diffusion coefficient and the temperature gradient in this prescription depend on an efficiency parameter of semiconvection ( $\alpha_{\text{sc}}$ ). The meaning of this parameter is discussed further in Sect. 3.3.2. We stress that this diffusive and time-dependent approach differs significantly from the ones used in previous efforts to treat semiconvection in low-mass stars. In previous studies, the mixing in the semiconvective layer is either performed by adjusting the composition until convective neutrality according to the Schwarzschild criterion is again reached (Crowe &

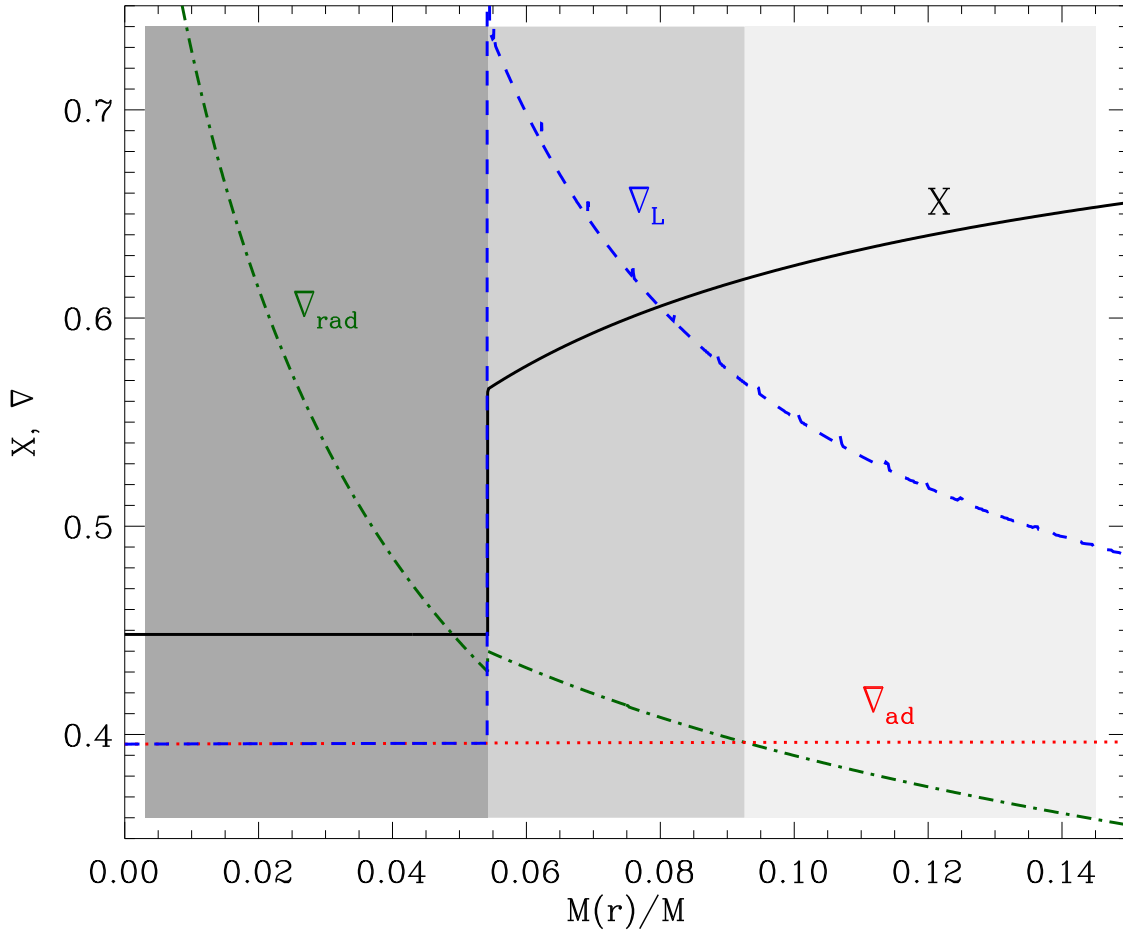


Figure 3.4: Internal structure of a  $1.5 M_{\odot}$  stellar model in the main-sequence phase. The hydrogen abundance profile  $X$  (black solid line), the adiabatic gradient  $\nabla_{\text{ad}}$  (red dotted line), the radiative gradient  $\nabla_{\text{rad}}$  (green dash-dotted line), and the Ledoux gradient  $\nabla_{\text{L}}$  (blue dashed line) are plotted as functions of the mass fraction. From left to right, tones of gray fill regions of different energy transport processes: convective zone, semiconvective zone, and radiative zone. See text for details.

Mitalas 1982; Miglio et al. 2008), or approximating the results obtained by Spruit (1992) with a two-step function (Popielski & Dziembowski 2005).

### 3.3 Impact on the stellar models

Several models were computed using the different mixing prescriptions and definition of the convective boundaries. Within a convective zone, the mixing is performed diffusively using the MLT, while in a semiconvective region the mixing is carried out as explained in Sect. 3.2.2. Cal-

culations were done for both the Schwarzschild and the Ledoux criterion for the definition of the convective zones, with and without including extra mixing due to overshooting and semiconvection. All the models considered here are computed for solar metallicity. We explore the effects of these processes for masses ranging from  $1.2 M_{\odot}$  to  $2 M_{\odot}$  starting at the pre-zero age main sequence and evolved until hydrogen exhaustion in the core.

### 3.3.1 Convective boundary definition criteria

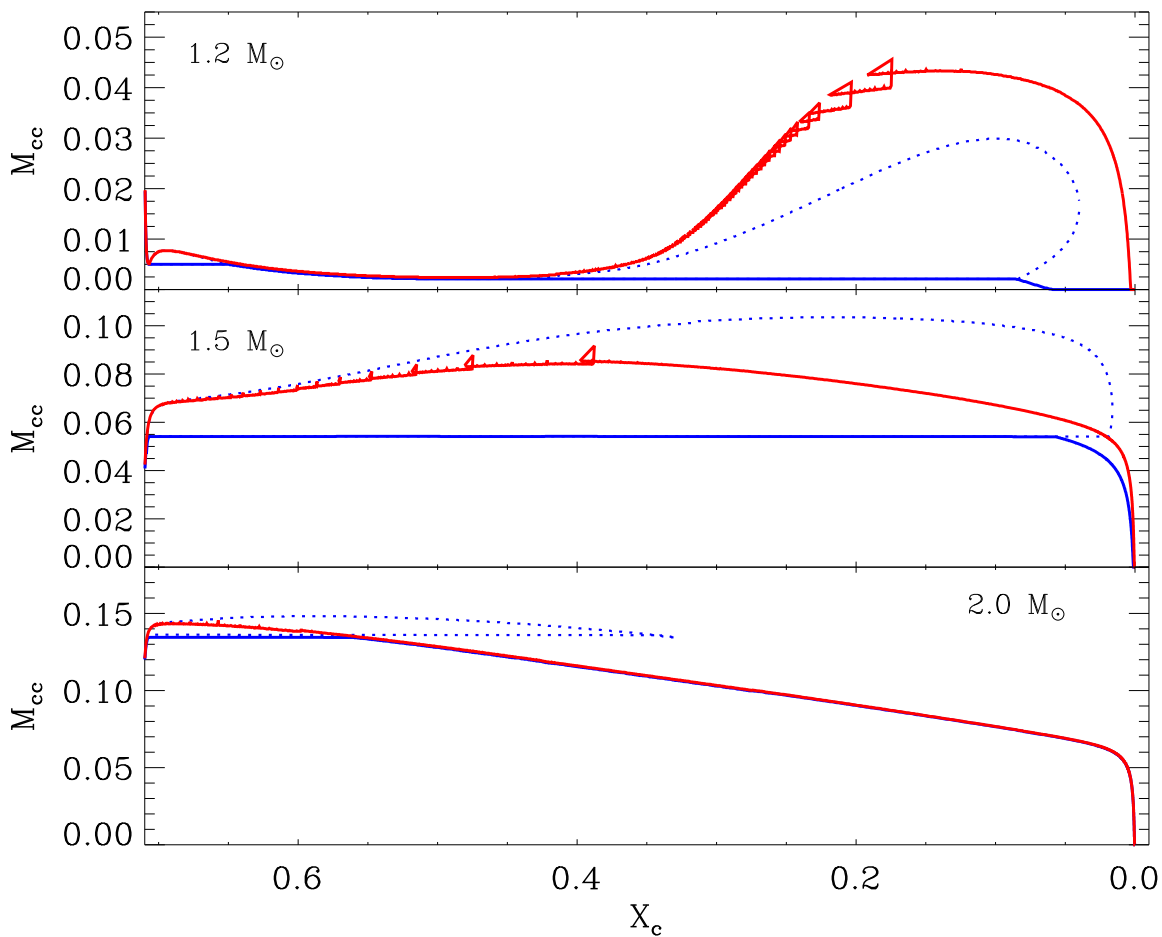


Figure 3.5: Evolution of the convective core boundary in mass coordinate as a function of central hydrogen content during the main sequence phase for the two considered convective boundary definition criteria: Ledoux (solid blue lines) and Schwarzschild (solid red lines). Blue dotted lines depict semiconvective zones when the Ledoux criterion is applied. (By definition there are no semiconvective zones when the Schwarzschild criterion is applied.) The panels represent different masses:  $1.2 M_{\odot}$  (top),  $1.5 M_{\odot}$  (middle), and  $2.0 M_{\odot}$  (bottom).

Applying either the Schwarzschild or the Ledoux criterion influences the appearance and the

size of convective cores as a function of stellar mass. To study these effects, we computed models with no convective overshoot and no mixing throughout the semiconvective regions when these were present ( $\alpha_{\text{sc}} = 0$ ).

In Fig. 3.5 we present the evolution during the main sequence of convective and semiconvective regions in the interiors of three representative models, computed with the two criteria:

- a model where the including the Ledoux criterion inhibits the growth of the convective core in the late phase of the main sequence evolution (1.2  $M_{\odot}$  model, Fig. 3.5 *top panel*);
- a model with a convective core increasing in size during the hydrogen-burning phase, whose growth is restrained if the Ledoux criterion is applied (1.5  $M_{\odot}$  model, Fig. 3.5 *middle panel*);
- a model where the convective core recedes during the main sequence, leaving behind a chemical discontinuity (2.0  $M_{\odot}$  model, Fig. 3.5 *bottom panel*).

There are clear differences in the convective core behavior for the two considered criteria. For growing convective cores (Fig. 3.5 top and middle panels), the molecular weight discontinuity at the edge of the convective zone produces a steep increase in the opacity, which translates into a sharp discontinuity in the radiative gradient (as shown in Fig. 3.4).

If the Schwarzschild criterion is applied, the profile of the convective core presents wrinkles throughout the evolution, signature of a convective process not properly taken into account (Lebreton et al. 2008). The exact position of the convective core edge will depend largely on the numerics of the evolutionary code and the way the mesh points are placed where the discontinuity in the molecular weight is located (Miglio et al. 2008). Slight variations in the radiative gradient are induced by, for instance, the interpolation in the opacity tables, the allowed time-step, and the accuracy of the calculations, resulting in a small region right outside the core edge becoming convective and supplying fresh hydrogen to the outer layer of the core. The core expands and produces the crumple profiles (backwards loops) observed in the top and middle panels of Fig. 3.5, in a phenomena similar to the so-called *breathing pulses* in horizontal branch stars (see for example Catelan 2007, for a detailed discussion and further references on the topic).

If the Ledoux criterion is applied instead, the convective core profile remains flat and continuous throughout the main sequence evolution, because the molecular weight discontinuity at its edge inhibits its growth. The semiconvective zone appearing outside the core is not mixed through and thus becomes larger during the hydrogen-burning phase. At the end of the main-sequence evolution, the convective core recedes leaving a radiative layer between it and the semiconvective zone, causing a change in the temperature gradients and ultimately making the semiconvective region disappear.

In a model with a receding core, the convective central region reaches its largest size during the initial phase of hydrogen-burning, and the Schwarzschild criterion allows it to grow to a slightly greater extent than the Ledoux criterion (Fig. 3.5, bottom panel). The chemical discontinuity left behind by the retreating core leaves an imprint on the molecular weight, which permits a semiconvective zone to develop, but the radiative gradient decreases following the shrinking of the core, which in turn transforms the zone into a radiative one. Since the effect is almost

negligible in this case, we focus for the rest of the paper on the models where the inclusion of the Ledoux criterion plays an important role (masses below  $\sim 1.7 M_{\odot}$  with growing convective cores).

### 3.3.2 Main-sequence evolution

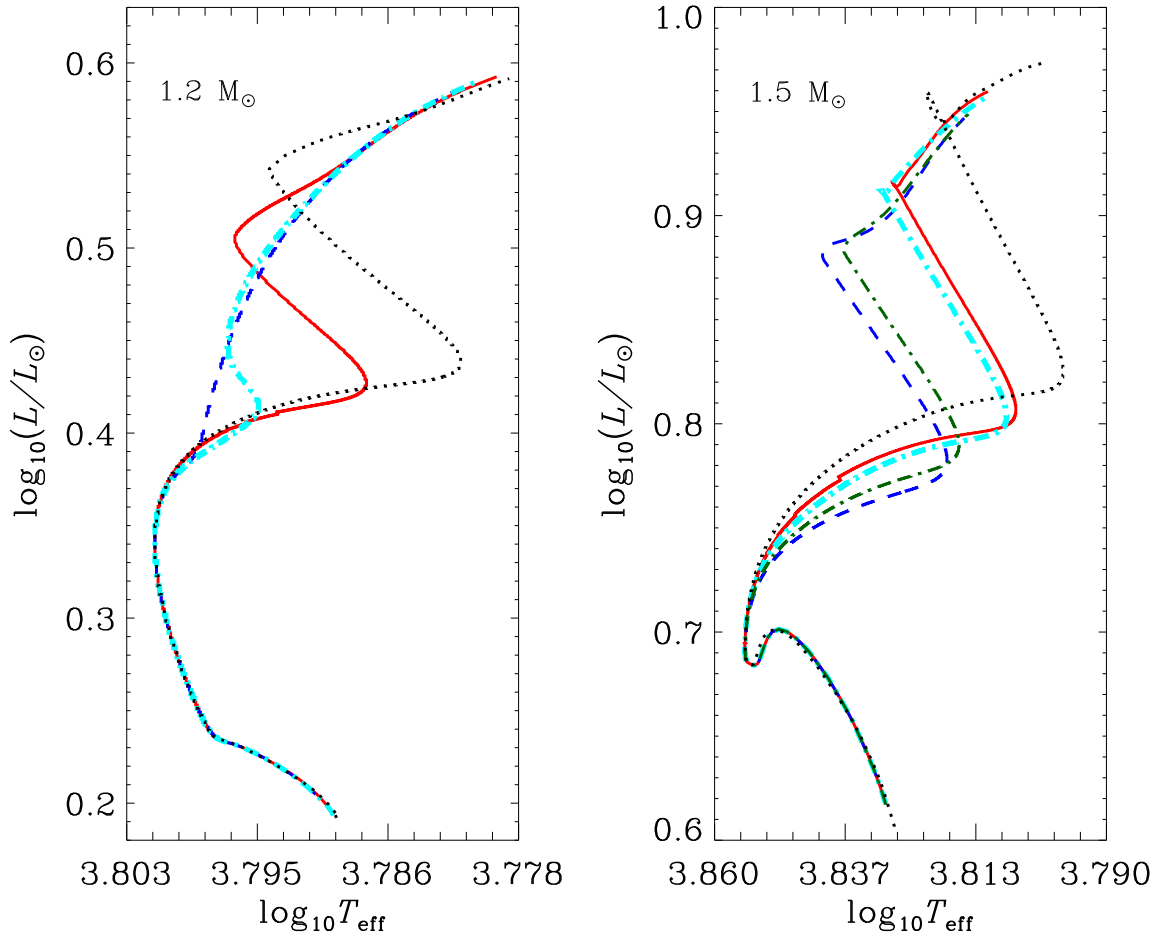


Figure 3.6: Hertzsprung-Russell diagram for  $1.2 M_{\odot}$  (*left panel*) and  $1.5 M_{\odot}$  (*right panel*) models. Computations with the Ledoux criterion and no mixing in the semiconvective regions are plotted with dashed blue lines, Schwarzschild criterion with solid red lines, and dotted black lines correspond to tracks with Schwarzschild criterion and overshooting. Two values for the semiconvective efficiency  $\alpha_{sc}$  are also plotted in thin green dash-dotted line ( $\alpha_{sc} = 0.001$ ; not shown for the  $1.2 M_{\odot}$  as it overlaps with the dashed track) and thick light blue dash-dotted line ( $\alpha_{sc} = 0.01$ ). The tracks span the evolution from the Zero-Age main sequence until hydrogen exhaustion in the core.

In the previous section we have shown the impact that different mixing prescriptions have on

the size of the homogeneously mixed central region during the main sequence evolution. The size (and existence) of the convective core will determine the appearance (or lack) of a hook-like feature in the CMD at the end of the hydrogen-burning phase. This feature at the turn-off is used in the determination of the age of stellar populations by fitting isochrones reproducing the shape of the hook at a certain metallicity, thus setting constraints on the stellar mass at the end of the main sequence for a given set of input physics (as an example, see Vandenberg et al. 2007; Magic et al. 2010, for the specific case of M67). As discussed in Sect. 3.3.1, using the Ledoux criterion can inhibit the growth of the convective core for the  $1.2 M_{\odot}$  model and therefore the appearance of the hook feature in the evolutionary track. This is the case where no mixing is performed within the developing semiconvective region ( $\alpha_{sc} = 0$ ) and the molecular weight barrier caused by hydrogen burning does not allow the core to grow.

The amount of semiconvective mixing is controlled by the efficiency parameter  $\alpha_{sc}$ . Its value is restricted to  $\alpha_{sc} < 1$ , but has normally been used in the range  $0.001 < \alpha_{sc} < 0.1$  according to the desired superadiabaticity level of the semiconvective region (Langer et al. 1985; Langer 1991; Merryfield 1995). Higher values of  $\alpha_{sc}$  mean faster mixing velocities, which is equivalent to using the Schwarzschild criterion. In Fig. 3.6 we have plotted evolutionary tracks for  $1.2$  and  $1.5 M_{\odot}$  cases calculated with different mixing prescriptions and semiconvective efficiency parameters. By increasing the value of  $\alpha_{sc}$  the convective core develops to a greater extent, and the evolutionary tracks resemble the one calculated with the Schwarzschild criterion. For the  $1.2 M_{\odot}$  case, the evolutionary sequence computed with  $\alpha_{sc} = 0.001$  does not increase the size of the convective core with respect to the one calculated with no mixing in the semiconvective zone, thus their tracks overlap in the HRD. One interesting aspect is that a position in the HRD can be shared by stars with the same mass but different evolutionary stages, internal structures, and stellar ages.

Changing the prescription for convection has an impact on the stellar age at which the end of the main sequence is reached. In the diffusive prescription we use for semiconvective zones,  $\alpha_{sc}$  modifies the value of the diffusion coefficient and also the true temperature gradient in the semiconvective zone. The growth of the convective core is not enhanced but restricted owing to the molecular weight gradient, and no extra fuel supply is added to the core, which translates into shorter main sequence lifetimes. In Fig. 3.7 we present the hydrogen contents at the center of the models as a function of age, where the differences are clearly visible for the considered mixing prescriptions and can amount to 30% of the main sequence lifetimes.

### 3.3.3 Effects of mixing in semiconvective layers

In Fig. 3.8 we present hydrogen profiles near the center for  $1.5 M_{\odot}$  models calculated with the Ledoux criterion and different semiconvective mixing efficiency values, with the Schwarzschild criterion and with overshooting. The sizes of the homogeneously mixed zones are different as is the shape of the chemical profile at the edge of the convective core. It is worth noticing that, for the  $1.5 M_{\odot}$  case considered in this paper, a semiconvective coefficient of  $\alpha_{sc} \sim 0.01$  is already efficient enough to very closely reproduce the results obtained when the Schwarzschild criterion is applied (see the evolutionary tracks in Fig. 3.6). The same is true for  $\alpha_{sc} \sim 0.1$  in the  $1.2 M_{\odot}$  model. This suggests that the value of the semiconvective efficiency required to reproduce the

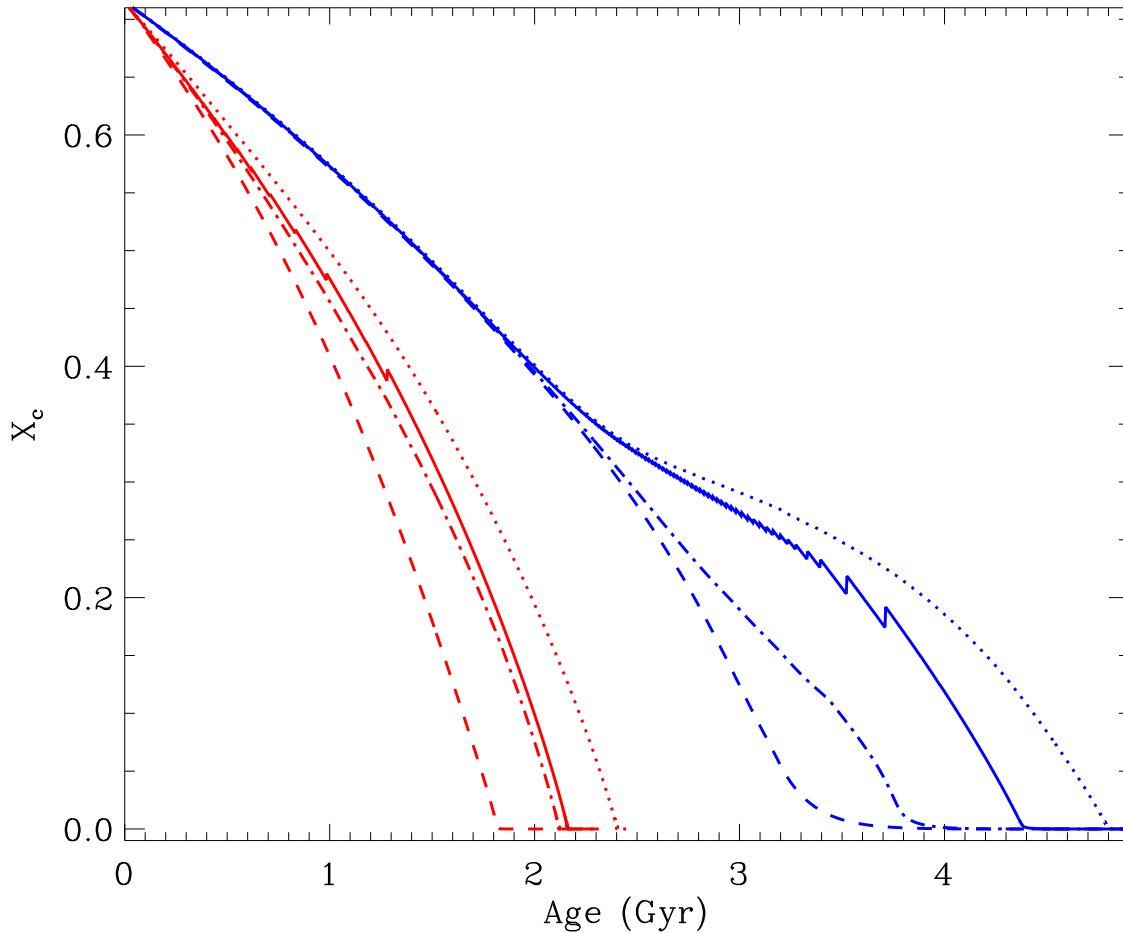


Figure 3.7: Central hydrogen content of the selected models during their main sequence evolution:  $1.2 M_{\odot}$  (blue) and  $1.5 M_{\odot}$  (red). *Solid lines*: Schwarzschild criterion without overshooting. *Dashed lines*: Ledoux criterion with no semiconvective mixing ( $\alpha_{\text{sc}} = 0$ ). *Dash-dotted lines*: Ledoux criterion and a semiconvective efficiency of  $\alpha_{\text{sc}} = 0.01$ . *Dotted lines*: models with convective overshooting.

results obtained with the Schwarzschild criterion decreases with mass. In relative terms, the extent of the semiconvective zone compared to the total convective core size is smaller at higher masses, leading to a shorter mixing timescale.

Convective overshooting has for long been thought of as a natural process capable of smoothing out molecular weight gradients close to the convective core (e.g. Maeder 1974a,b; Langer 1991; Noels et al. 2010). We computed models using the Ledoux criterion and the overshooting prescription described in Sect. 1.3.3 and realized that this is also the case for low-mass stars using our calibrated value for the overshooting efficiency. One should keep in mind, though, that the calibration itself was based on certain assumptions about convection (e.g. Pietrinferni et al. 2004; Vandenberg et al. 2006).

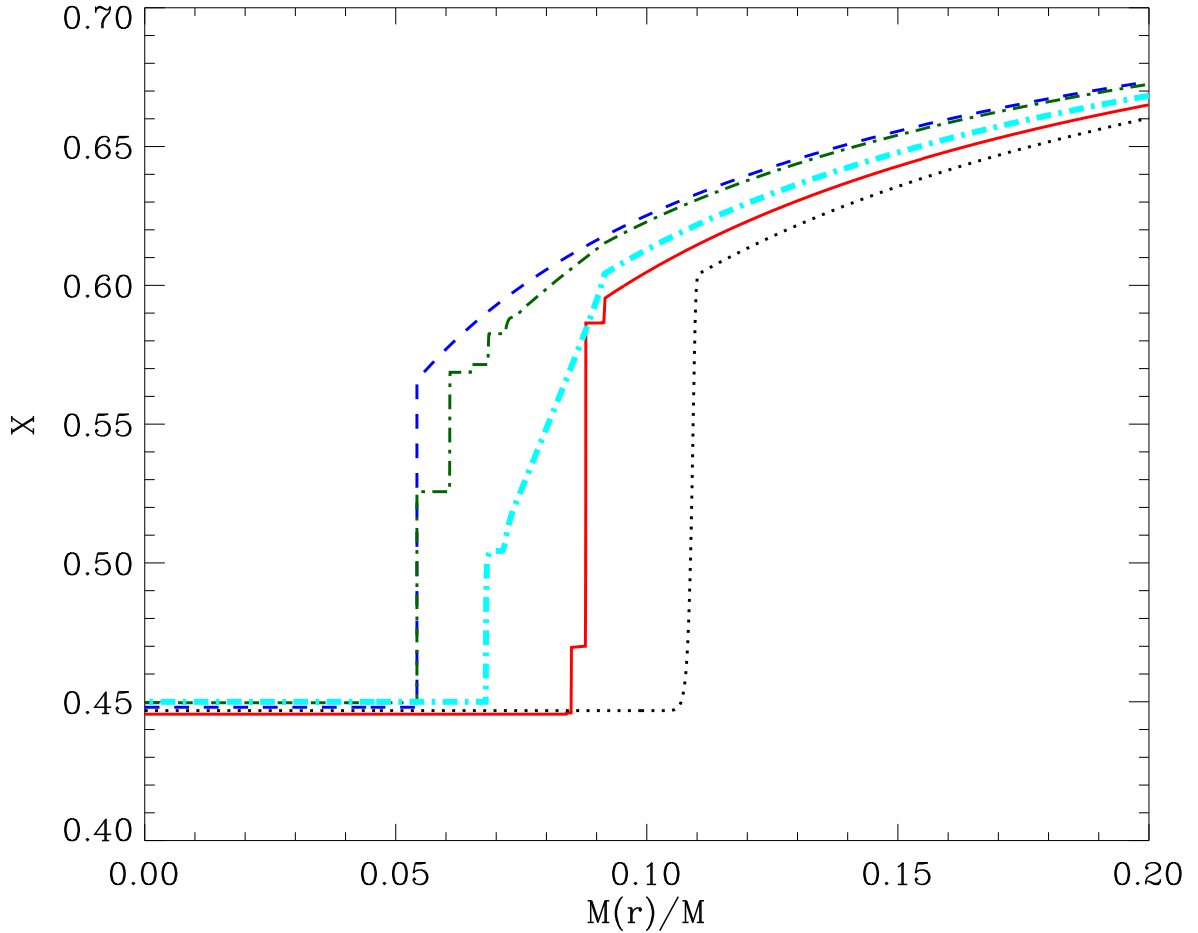


Figure 3.8: Hydrogen profiles for similar central hydrogen contents of the  $1.5 M_{\odot}$  models and different mixing prescriptions: Ledoux criterion and no mixing in the semiconvective zones (dashed blue line),  $\alpha_{\text{sc}} = 0.001$  (thin dash-dotted green line),  $\alpha_{\text{sc}} = 0.01$  (thick dash-dotted light blue line), Schwarzschild criterion (solid red line), and one model including convective overshooting (dotted black line).

### 3.4 Discussion

We have presented the results of our study of the influence of different convective boundary definitions and prescriptions for chemical mixing on main sequence evolution of low-mass stars. This has important consequences for the overall evolution of these stars: the resulting luminosity, temperature, and main sequence lifetime of the star are strongly affected by these processes. We focused our study on the effects of the existence and size of convective cores on stellar ages and CMD morphology.

The definition of convective zone boundaries and the treatment of these regions from the point of view of mixing has significant impact in derived quantities from stellar models. For stars

such as HD 49933, where precise observational constraints such as metallicity, parallaxes, and effective temperatures exists, we have shown that models for a given mass can differ significantly in their inner structure by considering different criteria for convective boundary definition and mixing processes. Although for the particular case of HD 49933 measuring the large frequency separation reduces the parameter space of possible best-fit models, a large uncertainty remains as models with completely different convective core sizes can reproduce this feature within the HRD observational error box.

The age of a star at the end of the main sequence phase depends on the amount of fuel available for core burning. In the prescriptions we considered, this is governed by the size of the homogeneously mixed zone in the center. The implementation of the Ledoux criterion for convection and no mixing beyond the formal boundaries of the central convective region produces the smallest convective core and consequently the shortest main sequence age for a given stellar mass and composition. The time-dependent diffusive mixing in the semiconvective region increases the amount of hydrogen in the center, reaching the same convective core size as the Schwarzschild criterion for mixing efficiencies that are sufficiently high. Convective overshoot can increase even more the extension of the mixed zone and the associated age value at the end of the main sequence.

The appearance of a hook-like feature at the end of the central hydrogen-burning phase can be shifted to higher mass values by including the Ledoux criterion, as we showed for a  $1.2 M_{\odot}$  model. This has relevant consequences when isochrones are used to reproduce the shape of the CMD of a stellar population given a chemical composition and a set of input physics (Vandenberg et al. 2007; Magic et al. 2010). Previous methods of analysis do not allow us to ensure the existence or absence of a semiconvective region in stellar interiors. Further development of numerical simulations and asteroseismic tools, such as the one presented here, can be the key to solving this interesting issue (Bascoul 2007; Miglio et al. 2008). In the same line, constraining the existence and size of the central mixed region is another step towards a comprehensive understanding of mixing processes.

While investigating different convective zone boundary definitions, we have seen that using the Schwarzschild criterion for models with growing convective cores leads to inconsistencies in the exact location of these regions. The layers at the top of the core may suddenly be mixed into the central region increasing the central hydrogen content and developing loops in the convective core boundary evolution (*breathing pulses* phenomenon). The question that arises then is how to treat these zones. In the study by Crowe & Mitalas (1982), the authors took these layers into account by mixing them until convective neutrality according to the Schwarzschild criterion was recovered. The convective core grows beyond its previously established boundary, and a new supply of fresh hydrogen is added to the core, also increasing the time a star spends transforming hydrogen into helium.

Another option for dealing with these *breathing pulses* is to use convective overshoot as implemented in GARSTEC, producing a smooth convective core profile during the main sequence evolution. This prescription does not modify the thermal structure of the overshooting layers. When an adiabatic stratification of the convective zone is considered instead (convective penetration), small fluctuations at the edge of the core still appear but are smaller than the ones presented in Fig. 3.5 (M. Salaris, private communication). These fluctuations are not likely to

affect the computation of adiabatic frequencies.

Overshooting is an interesting topic in itself, but a detailed analysis of it goes beyond the scope of this thesis. However, we can mention two important aspects we think deserve attention. One is the temperature gradient in the overshooting region. We have assumed in our study that the temperature stratification in the radiative zone is not affected by the convective motions beyond the formal boundary, while convective penetration assumes an adiabatic stratification in this layer. Currently there is no consensus on this issue, and it is expected that numerical simulations and asteroseismology will cast some light on the topic (Godart 2007). The other important aspect is the size of the overshooting region. An exponential decay of the convective velocities is an alternative to an adiabatic extension to a fraction of a scale height of the convective region (see Ventura 2007, for details). However, numerical simulations are not yet able to reproduce the conditions of stellar interiors (Dintrans 2009).

Regarding the impact of overshooting in semiconvective layers, our calibrated value for the overshooting efficiency washes out the molecular weight discontinuity that produces semiconvective regions. However, it has been suggested that the presence of a molecular weight barrier at the edge of the core might reduce the amount of overshooting from it (Canuto 1999), thus it could be possible for a semiconvective region to exist even with overshooting. As an example, when using half of our calibrated value for the efficiency of overshooting, a semiconvective region still exists for masses of the order  $1.2 M_{\odot}$ .

The type of overshooting implemented in GARSTEC considers an exponential decay of the convective velocities, producing a smooth chemical profile in the overshoot region. Other evolutionary codes employ a different approach for this process, such as extending the convective region from its boundary by a certain fraction of a pressure scale height, and fully mixing this region. The net effect is to produce a larger convective core, but the sharp discontinuity in the molecular weight remains at the edge of the overshoot region. It may be possible for semiconvective zones to develop under these circumstances.

# Chapter 4

## Asteroseismic diagnoses for stellar interiors

This chapter contains the second part of the article published in *Astronomy & Astrophysics* in March 2011 (Silva-Agüirre, Ballot, Serenelli, & Weiss 2011a). We explore the possibility of determining the presence of a convective core and distinguishing different sizes of homogeneously mixed central regions and evolutionary stages by means of asteroseismology. We do this by studying the effects that different types of convective mixing processes have on asteroseismic variables obtained by means of frequency combinations, in agreement with the expected quality of data being obtained by the aforementioned space missions.

### 4.1 Introduction

We have highlighted in Chapter 3 the importance of the different mixing prescriptions considered in this paper on structure and evolution of low-mass stars. In practical terms, these convective processes translate into different convective core sizes, ages, and evolutionary stages for compatible positions in the HRD. The quest for detecting the variations in stellar interiors produced by differences in the mixing and energy transport processes can be fulfilled by a technique capable of piercing the outer layers of stars, and which is sensitive to density discontinuities.

There have been many efforts to discover the physics of stellar interiors by understanding the influence that different physical phenomena have on the observed frequency spectra. In particular, it is known that a discontinuity in the chemical profile of a star produces a sharp variation in the adiabatic sound speed, which in turn introduces an oscillatory component in the frequencies (Vorontsov 1988; Gough 1990; Provost et al. 1993). This fact has already been applied to determine the position of the base of the convective envelope in the Sun (Christensen-Dalsgaard et al. 1991), to constrain the amount of overshoot below it (Monteiro et al. 1994; Roxburgh & Vorontsov 1994; Christensen-Dalsgaard et al. 1995), and to constrain the properties of the solar helium second-ionization zone (Christensen-Dalsgaard & Hernández 1991; Antia & Basu 1994; Monteiro & Thompson 2005). The same technique has been proposed to determine the position of the base of the convective envelope and estimate the helium abundance for stars other than the Sun (Monteiro et al. 2000; Monteiro & Thompson 1998).

Following this principle, convective cores in low-mass stars have been the subject of several

studies by means of asteroseismology aiming to determine the evolutionary state and size of the mixed central region in stars (e.g Audard & Provost 1994; Audard et al. 1995; Mazumdar & Antia 2001; Mazumdar et al. 2006; Cunha & Metcalfe 2007). Most of these investigations have focused their attention on constraining the size and chemical composition of the convective core, while only a few of them have acknowledged the impact of its boundary definition and extra mixing processes such as semiconvection and overshooting in the oscillation frequencies (Popielski & Dziembowski 2005; Godart 2007; Miglio et al. 2008; Lebreton et al. 2009). In this section we aim at finding a seismic tool that isolates the stellar core and which is sensitive to its size and central hydrogen content, allowing us to disentangle the different mixing prescriptions.

## 4.2 Seismic variables suited to isolate the core

To study the inner structure of a star using asteroseismology, we first need to find an appropriate seismic variable that allows us to probe the desired region of the star and extract the required information. Different combinations of low-degree  $p$  modes have been suggested as suitable probes of the physical characteristics of a star, the most commonly used being the so-called large and small frequency separations defined as

$$\Delta_\ell(n) = \nu_{n,\ell} - \nu_{n-1,\ell} \quad (4.1)$$

$$d_{\ell,\ell+2}(n) = \nu_{n,\ell} - \nu_{n-1,\ell+2}, \quad (4.2)$$

where  $\nu_{n,\ell}$  is the mode frequency of angular degree  $\ell$  and radial order  $n$ . These combinations are affected by the outer layers of the star where turbulence on the near surface is almost never taken into account in stellar modeling (e.g. Ballot et al. 2004).

In our case, we need to isolate the signal arising from the interior of the star from surface contamination in order to properly quantify the effects in the frequency spectra of the presence of a convective core. Roxburgh & Vorontsov (2003) proposed to use the smooth 5-points small frequency separations and the ratio of small to large separations, and showed that these quantities are mainly determined by the inner structure of the star. They are constructed as

$$d_{01}(n) = \frac{1}{8}(\nu_{n-1,0} - 4\nu_{n-1,1} + 6\nu_{n,0} - 4\nu_{n,1} + \nu_{n+1,0}) \quad (4.3)$$

$$d_{10}(n) = -\frac{1}{8}(\nu_{n-1,1} - 4\nu_{n,0} + 6\nu_{n,1} - 4\nu_{n+1,0} + \nu_{n+1,1}) \quad (4.4)$$

$$r_{01}(n) = \frac{d_{01}(n)}{\Delta_1(n)}, \quad r_{10} = \frac{d_{10}(n)}{\Delta_0(n+1)}. \quad (4.5)$$

The small frequency separations have already been used to identify the location of the convective envelope and the helium second-ionization zone in the Sun by applying them to observational data (Roxburgh 2009), while it has been shown that the ratios (Eq. 4.5) fairly cancel out the influence in the frequencies of the outer layers (Roxburgh 2004, 2005; Oti-Floranes et al. 2005).

We can consider the ratios  $r_{10}$  and  $r_{01}$  as a single set of data (dubbed  $r_{010}$ ), alternately centered on  $\ell = 0$  and  $\ell = 1$ .

As mentioned before, sharp variations in the adiabatic sound speed produce a shift in the eigenfrequencies relative to those in a corresponding star with a smooth sound speed profile. The shift is an oscillatory function of the frequency itself, whose period is related to the position of such a discontinuity. Thus, the frequencies can be expressed as a combination of two components:

$$\nu_{n,\ell} = \nu_{n,\ell}^{\text{smooth}} + \delta\nu_{n,\ell}, \quad (4.6)$$

where  $\nu_{n,\ell}^{\text{smooth}}$  corresponds to the smooth component and  $\delta\nu_{n,\ell}$  represents the perturbation introduced by the discontinuity in the sound speed.

The period of the oscillatory signal relates to the travel time of the wave through the acoustic cavity, hence to the radial coordinate where the discontinuity is located (Monteiro et al. 1994; Roxburgh & Vorontsov 1994, 2001). As shown in Sect. 2.2.4 (Eqs. 2.61 and 2.62), the travel time of the wave is given by the acoustic depth  $\tau$ . There is an alternative representation of this acoustic depth called the acoustic radius, given by

$$\tilde{\tau} = \int_0^r \frac{dr}{c_s} \quad (4.7)$$

which measures the travel time from the center towards the surface. Therefore, if the total acoustic radius is given by  $\tau_c = \tilde{\tau}(R)$ , then clearly  $\tau = \tau_c - \tilde{\tau}$ . If the location of the density discontinuity is given by, say,  $r_1$  in radial coordinates, and that same position is represented in acoustic radius and acoustic depth by  $\tilde{\tau}_1$  and  $\tau_1$  respectively, the periods of the oscillation in frequency space induced by this sharp variation are  $1/(2\tilde{\tau}_1)$  and  $1/(2\tau_1)$ , according to the considered seismic variable in Eq. 2.61. That being the case, if either the ratios or the small separations are only affected by the position of the convective core, we could extract this information from the frequency data.

### 4.3 Sensitivity of $r_{10}$ and $r_{01}$ to the core

If the differences and ratios defined in Eqs. 4.3, 4.4, and 4.5 are indeed sensitive to the deep stellar interior, they should be strongly influenced by the presence of a convective core or a steep gradient in the adiabatic sound speed near the center (Roxburgh & Vorontsov 2007). To test this, we produced two sets of evolutionary tracks for a  $1.1 M_\odot$  star, one using the normal Schwarzschild criterion and the other including overshooting without the geometrical restriction described in Sect. 1.3.3. This way, we produced a  $1.1 M_\odot$  model with a growing convective core during the hydrogen-burning phase, while the Schwarzschild model has a radiative core. To compare the effects of the presence of the core, we plotted the evolution of these models during the main sequence in Fig. 4.1. The left panels present the ratios as a function of frequency, while the center panels show the adiabatic sound speed in the stellar core for the selected models, whose position in the observational plane is depicted by a filled circle in the right panels of the figure.

The frequency ratios present a common component in the low frequency domain (see left panels), which therefore should be dependent on the global seismic properties of the star: the

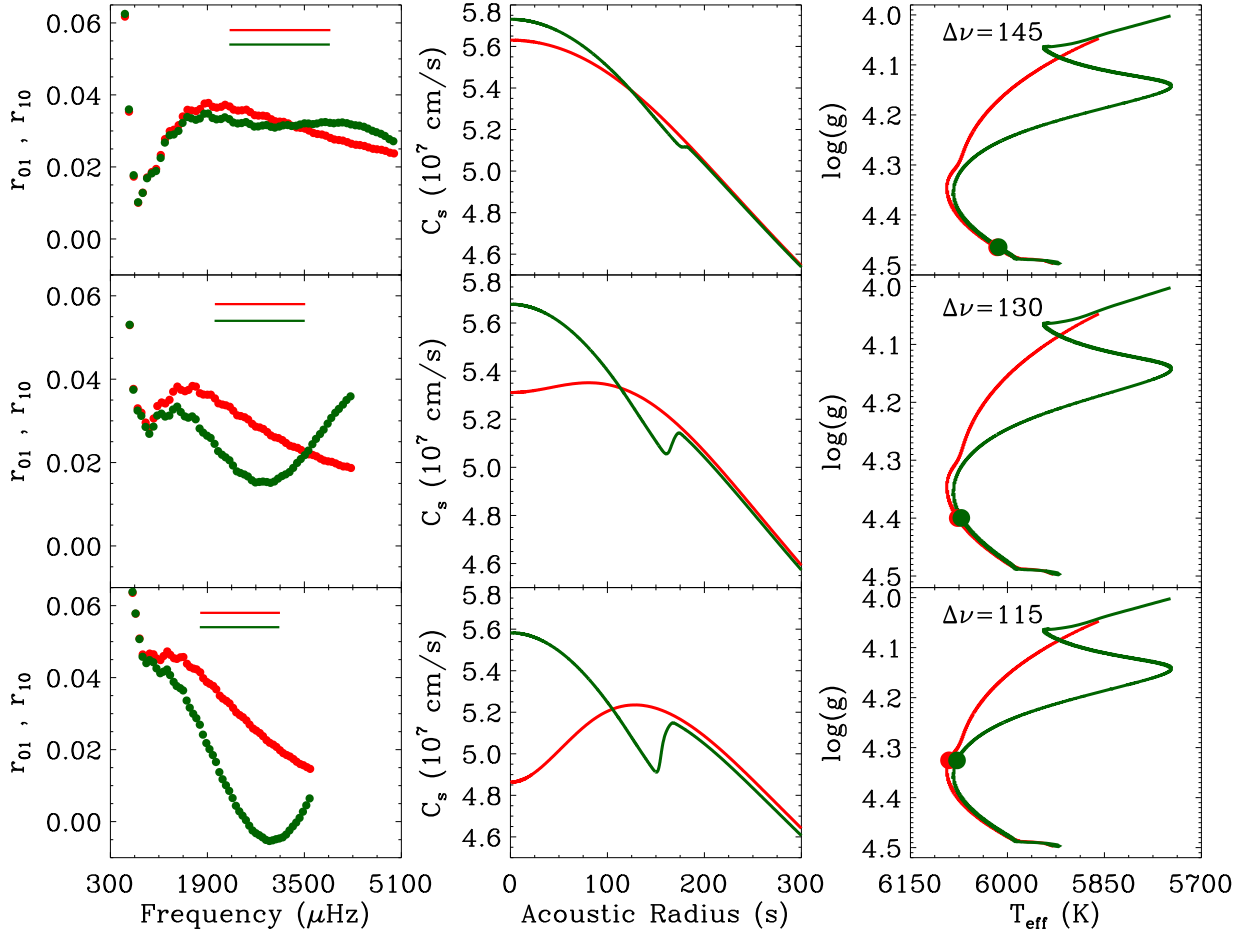


Figure 4.1:  $1.1 M_{\odot}$  models with a convective core (green) and without one (red) during the main-sequence evolution. Each row depicts models sharing the same large frequency separation. *Left Panels:* frequency ratios as defined in Eq. 4.5. Horizontal lines show a typical observable frequency range for each mixing prescription of radial orders  $n=15-27$ . *Central Panels:* adiabatic sound speed as a function of the acoustic radius. *Right Panels:* evolutionary tracks for the two cases considered, the position of the studied models being represented by a filled circle. Values of the selected large frequency separations are given (in  $\mu\text{Hz}$ )

selected models have the same large frequency separation. At higher frequencies, the ratios deviate from each other, revealing the structural differences between the models. This part of the frequency domain presents two contributions: one given by the presence of a convective core and another one dominated by the evolutionary state of the model (equivalent to the central hydrogen content). The oscillatory component observed in the ratio of the model calculated with overshooting is related to the presence of a convective core.

A straight line can be drawn between the point where the ratios start deviating from each

other and the frequency value where the oscillatory component of the model with the convective core shows its first minimum. We refer to this part of the frequency domain as the *linear range* from here on. Independently of the presence of a convective core, we observe an increase in the slope – strictly speaking of its absolute value – with evolution, suggesting that it traces the central hydrogen content of the star (hence stellar age). Thus, the sole presence of a negative slope does not ensure the existence of a convective core (see also Brandão et al. 2010).

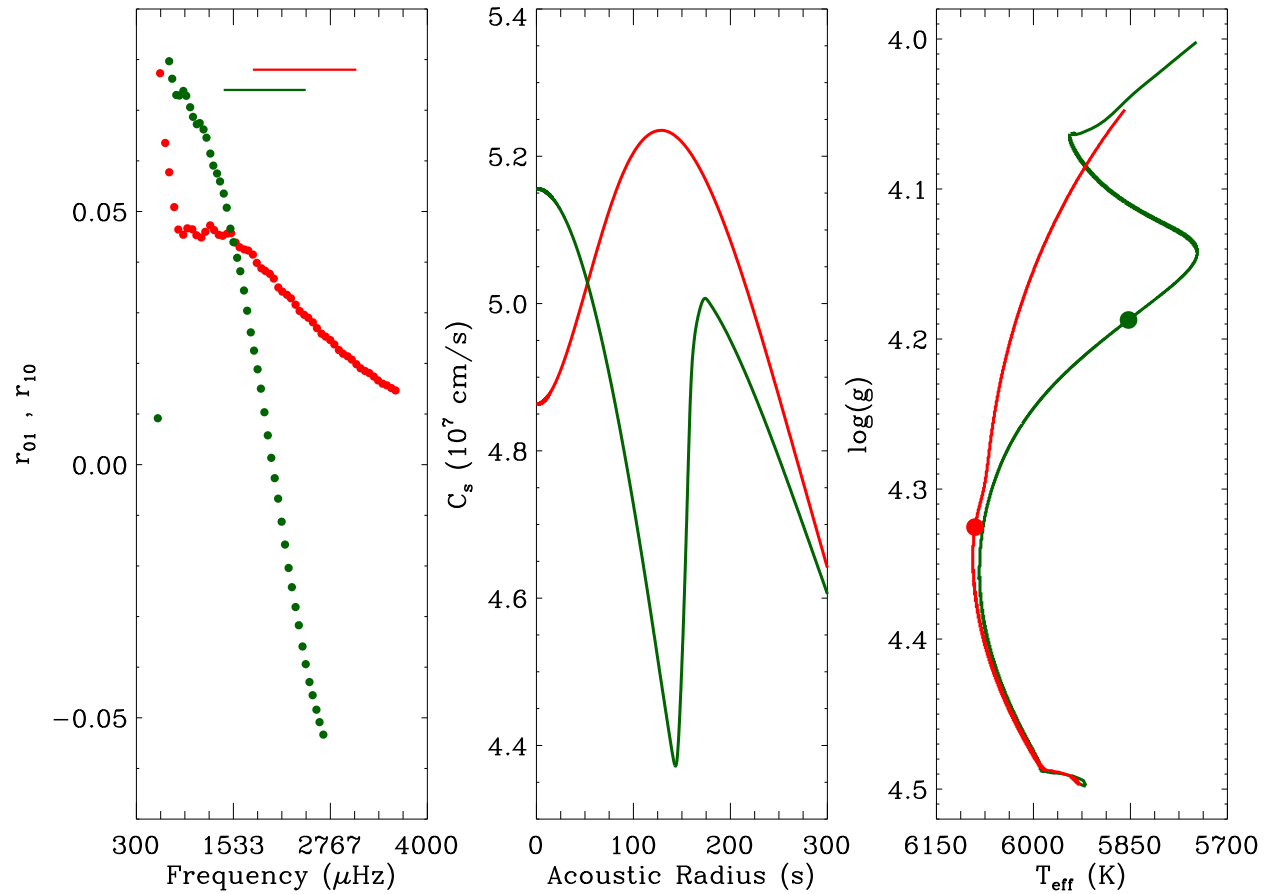


Figure 4.2: Same as Fig. 4.1 for  $1.1 M_{\odot}$  models having a similar central hydrogen content of  $X_c \sim 0.14$ . See text for details.

However, in the last row of panels in Fig. 4.1, the plotted models have very different central hydrogen abundances ( $X_c \sim 0.14$  versus  $X_c \sim 0.4$  for the model without and with convective core, respectively). In the model without a convective core, the increase in the slope mainly comes from the growth of the density gradient in the center, built during hydrogen burning. Nevertheless, the slope is noticeably higher for the model with a convective core, even if this star is less evolved. In fact, we show in Fig. 4.2 the difference in the frequency ratios and sound

speed profiles of the model without convective core at  $X_c \sim 0.14$  and the equivalent model with convective core at the same central hydrogen content. It is clear in the figure that, regardless of having the same central hydrogen content, the model with a convective core shows a much larger absolute slope in its frequency ratios. This difference is clearly a clue to the presence or absence of a convective core and will be discussed in Sect. 4.5.

The global behavior of the small frequency separations is the same as the one observed in the frequency ratios. Thus, we will focus the analysis in the ratios keeping in mind that the same conclusions are applicable to the case of the separations.

#### 4.4 Influence of mixing prescriptions on $r_{10}$ and $r_{01}$

When considering only those models that do have a convective core, we can study the sensitivity of the ratios to the position and size of the convective core and to the size of the density discontinuity. We explore the behavior of  $1.3 M_\odot$  models in the three most extreme cases in terms of the size of the mixed region: Ledoux criterion with no extra mixing in the semiconvective region, the normal Schwarzschild criterion, and one evolutionary sequence including overshooting. An error of  $0.2 \mu\text{Hz}$  in the frequency determinations was assumed, as expected from the CoRoT and *Kepler* missions (Baglin et al. 2006; Christensen-Dalsgaard et al. 2007).

In Fig. 4.3 we present a similar diagram as in Fig. 4.1 showing the changes of this seismic diagnose as a function of the central hydrogen content, therefore mapping the main sequence evolution. When considering one mixing prescription (indicated by different colors) we notice that the absolute value of the slope of the frequency ratios increases with evolution. The considered models have the same central hydrogen content, so when observing this behavior of the ratios nothing can be said about the exact evolutionary stage of the star. However, the size of the discontinuity in the adiabatic sound speed is indeed different, as is the size of the cores, the largest being the one with the most negative slope.

One is tempted to interpret this as a direct relation between the size of the discontinuity and the absolute slope of the ratios, but two details must be taken into account: for the Ledoux criterion, the change in the slope during the main sequence evolution is much smaller than for the other cases, and the acoustic radius of the fully mixed region remains almost constant (while for the other prescriptions it increases). It is clear that the value of the absolute slope has contributions from the position of the convective core and the size of the sound speed discontinuity.

Bearing this in mind, instead of using the central hydrogen content as a proxy for the evolution of the ratios, we considered models with the same large frequency separation, as it is the parameter first and most easily obtained from seismic observations. Figure 4.4 shows this case for the  $1.3 M_\odot$  models with large separations equal to  $\Delta\nu = 110, 100, 95,$  and  $88 \mu\text{Hz}$ . Due to the differences in the mixing prescriptions, the selected models do not have the same central hydrogen content but almost the same age. As a side remark it is worth mentioning that, as  $\Delta\nu$  is a measure of the mean density, models with equal masses and large frequency separations have also the same radius. Recalling the mass-luminosity relation for main-sequence stars introduced in Sect. 1.2.2 (Eq. 1.7), the effective temperature of the stars must also be the same. Thus, it is not surprising that the models overlap in the HRD, as shown in the right panels of Fig. 4.4.

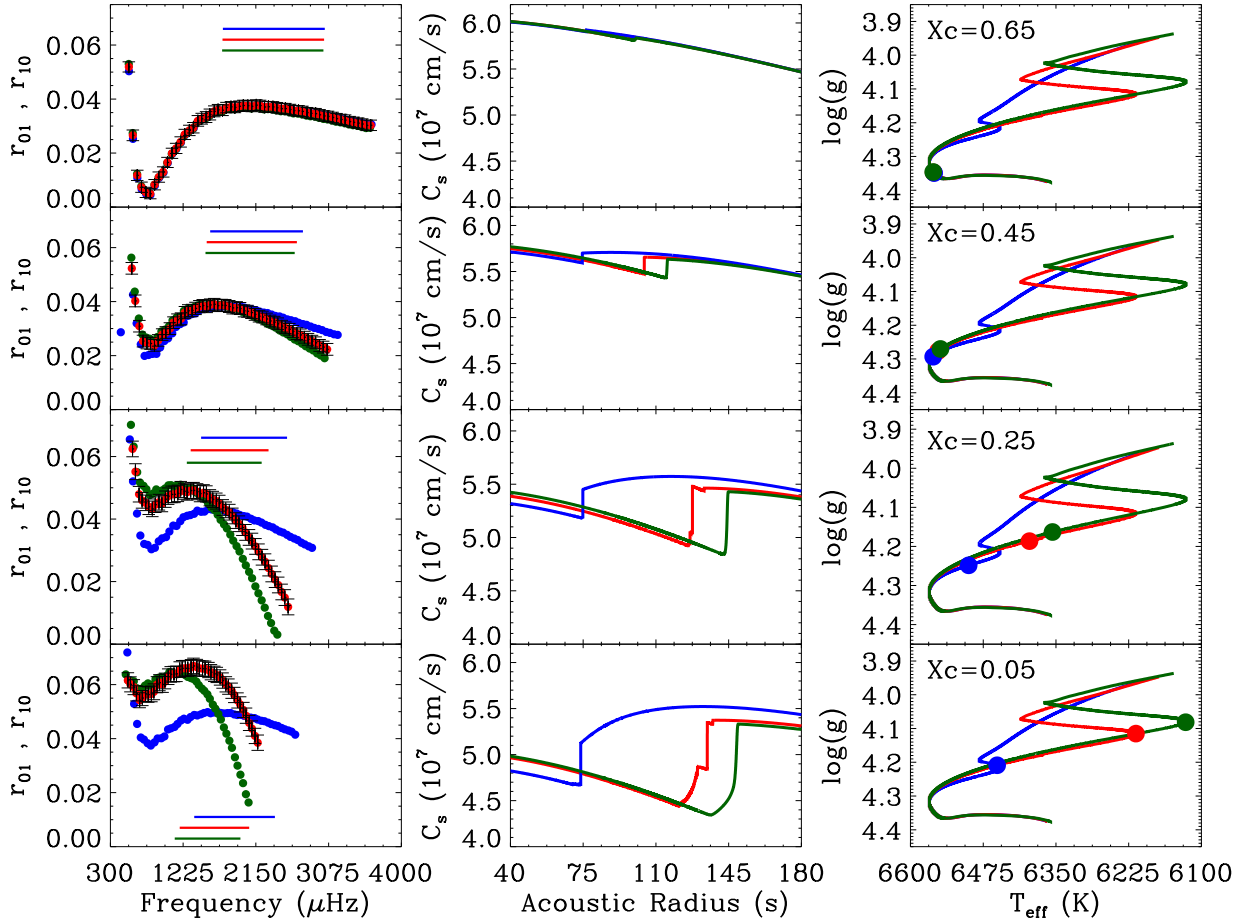


Figure 4.3: Comparison of  $1.3 M_{\odot}$  models using different mixing prescriptions: Ledoux (blue), Schwarzschild (red) and overshooting (green). Each row of models represents a value of the central hydrogen content (from top to bottom):  $X_c = 0.65$ ,  $X_c = 0.45$ ,  $X_c = 0.25$ , and  $X_c = 0.05$ . *Left Panels*: frequency ratios as defined in Eq. 4.5. Horizontal lines show a typical observable frequency range for each mixing prescription of radial orders  $n=15-27$ . *Central Panels*: adiabatic sound speed showing the position of the density discontinuity and therefore of the edge of the homogeneously mixed core. *Right Panels*: evolutionary tracks for the three selected prescriptions, and the position of the studied models is represented by a filled circle. Error bars have been plotted for reference in the models computed with the Schwarzschild criterion.

The behavior at the low-frequency range ( $\nu \lesssim 1200 \mu\text{Hz}$ ) is the same for the three mixing prescriptions for a given value of the large frequency separation. As already mentioned in Sect. 4.3, this is an indication that this part of the frequency spectrum is dominated by the global seismic properties of the star, while the frequency values above  $\sim 1200 \mu\text{Hz}$  seem to be sensitive to the differences in the interior (the *linear range*).

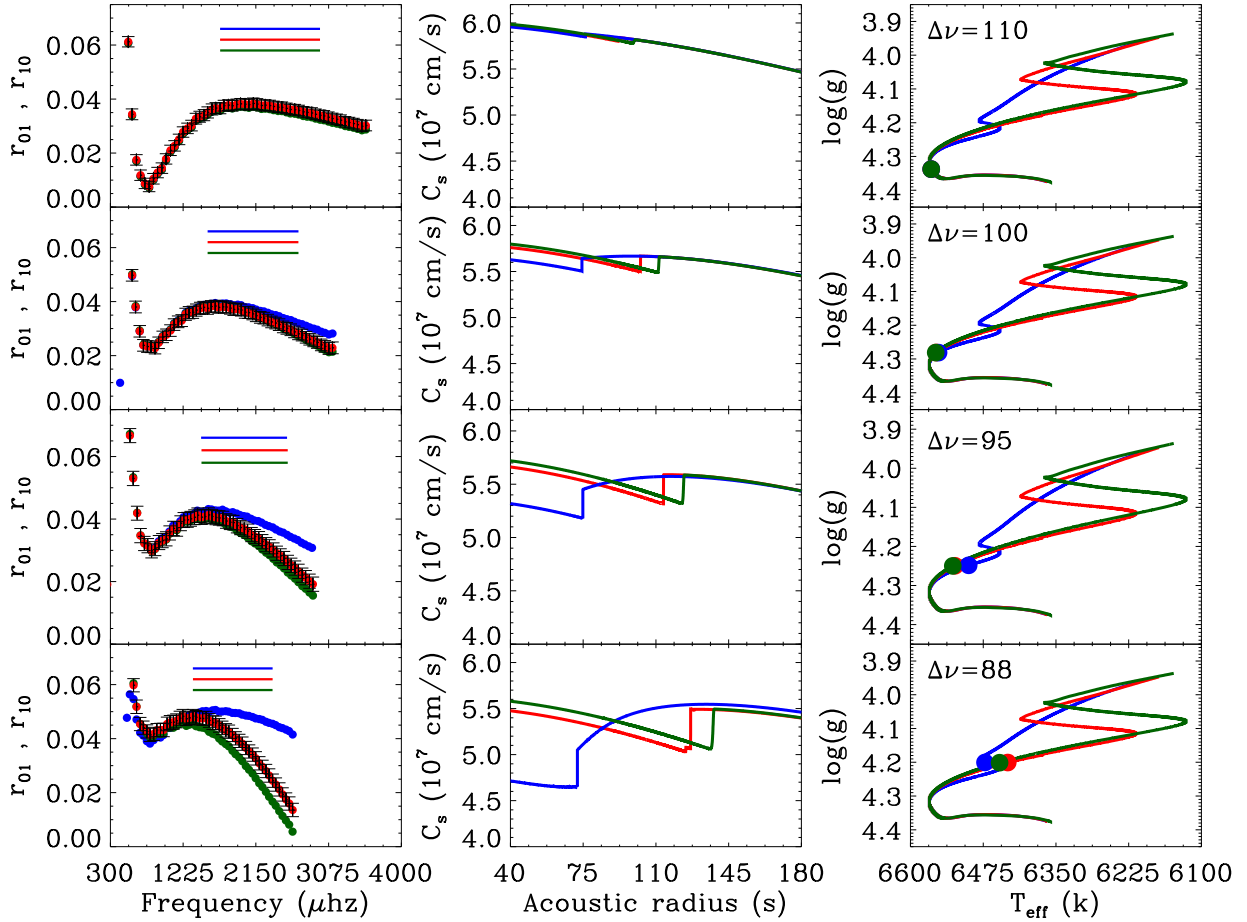


Figure 4.4: Same as Fig. 4.3 but each row represents models with the same value of the large frequency separation, which is given in the right panel of each row (in  $\mu\text{Hz}$ ).

Within this frequency region where the information of the core is contained, we can compare in Fig. 4.4 a case opposite to the one in Fig. 4.3: the last row presents models with the same size of discontinuity of the adiabatic sound speed ( $\sim 0.27 \times 10^7$  cm s $^{-1}$ ). The hydrogen content of the Ledoux (blue) model is only  $\sim 2\%$  while for the the Schwarzschild criterion and for the model with overshooting it is  $\sim 28\%$  and  $\sim 32\%$ , respectively. The model calculated with the Ledoux criterion again has the lowest absolute slope value and the smallest size of the convective core.

We stress that the absolute value of the slope cannot be attributed only to the size of the adiabatic sound speed discontinuity. In fact, we can distinguish three effects directly linked to the global behavior of the ratios:

- a decrease in the central hydrogen content produces an increase in the slope in the *linear range*, which is visible no matter whether a convective core is present or not;

## 4.5 Breaking the degeneracy: splitting mixing prescriptions and finding convective cores<sup>71</sup>

$\Delta\nu$ ( $\mu\text{Hz}$ )	Model	$T_{\text{eff}}$ (K)	$\log(g)$	Age (Myr)	$X_c$	Jump ( $10^7$ $\text{cm s}^{-1}$ )	$\text{Arad}_{\text{cc}}$ (s)	Slope	Mean	
96	1.10 $M_{\odot}$	Sch	6048	4.22	6130.4	1e-5	—	—	$-23 \times 10^{-4}$	0.049
		Ove	5955	4.22	6531.1	0.216	0.610	150	$-71 \times 10^{-4}$	0.007
	1.25 $M_{\odot}$	Led	6379	4.22	2636.2	0.016	0.225	62	$-8 \times 10^{-4}$	0.046
		Sch	6332	4.22	2636.2	0.245	0.434	115	$-21 \times 10^{-4}$	0.041
		Ove	6343	4.22	2630.4	0.287	0.430	125	$-26 \times 10^{-4}$	0.034
	1.30 $M_{\odot}$	Led	6463	4.23	1812.8	0.159	0.370	75	$-6 \times 10^{-4}$	0.043
		Sch	6496	4.23	1812.8	0.347	0.338	117	$-15 \times 10^{-4}$	0.038
		Ove	6499	4.23	1810.5	0.376	0.329	128	$-19 \times 10^{-4}$	0.033
	1.35 $M_{\odot}$	Led	6628	4.24	1146.8	0.346	0.255	90	$-4 \times 10^{-4}$	0.041
		Sch	6651	4.24	1146.8	0.444	0.213	122	$-10 \times 10^{-4}$	0.035
		Ove	6655	4.24	1144.6	0.465	0.228	131	$-12 \times 10^{-4}$	0.034

Table 4.1: Main properties of the models for a chosen value of the large frequency separation. See text for details.

- when a convective core is present, an increase in the size of the discontinuity in the adiabatic sound speed at the core boundary increases the amplitude of the oscillatory signature, making the slope of the ratios steeper;
- the extent of the convective core also affects the slope: a larger convective core reduces the period of the oscillatory component in the ratios, increasing in turn the absolute value of the slope.

It is not straightforward to determine how much influence each of these effects have on the slope. A differential comparison must be made in order to assess where the major contributions are coming from. Nevertheless, now that the key processes affecting the frequency ratios have been identified, we can use this information to disentangle those models with different central mixed zones sizes and evolutionary stages.

## 4.5 Breaking the degeneracy: splitting mixing prescriptions and finding convective cores

In the examples above we have shown that the frequency ratios are sensitive to the central hydrogen content, the existence and extent of a convective core, and the amplitude of the discontinuity in the adiabatic sound speed, hence the importance of being able to disentangle the different mixing prescriptions. An attempt to do so was presented by Popielski & Dziembowski (2005), where they characterized the size of the mixed zone in stellar models using the small frequency separation. The authors studied differences between two types of semiconvective mixing and two

values of convective overshooting by averaging the small frequency separation over a range of radial orders and using its slope. We apply a similar approach to the frequency ratios using the radial orders  $n=15-27$ , a typical range that is expected to be detected by the CoRoT and *Kepler* missions (see left panels of Figs. 4.1, 4.3, and 4.4).

Thus, following Popielski & Dziembowski (2005), we define the mean value of the frequency ratios  $r_{010}$  for the total of 26 modes (13 for each  $\ell$  value) in the range mentioned above as

$$\langle r_{010} \rangle = \frac{1}{2(n_2 - n_1 + 1)} \sum_{n_i=n_1}^{n_2} r_{01}(n_i) + r_{10}(n_i), \quad (4.8)$$

where  $(n_1, n_2) = (15, 27)$  are the radial orders aforementioned. We use a normalized mean slope defined as follows:

$$r_s = \overline{\Delta_0} \frac{d r_{010}}{d \nu}, \quad (4.9)$$

where the derivative is determined by a linear fit in the considered radial orders, and  $\overline{\Delta_0}$  is the mean large frequency separations of the  $\ell = 0$  modes in that range.

In Fig. 4.5 we present a slope ( $r_s$ ) versus mean ( $\langle r_{010} \rangle$ ) diagram in the observable range of the frequency ratios, for the complete main sequence evolution of different masses and mixing prescriptions. For each mass value and mixing prescription, we have also selected one model with a large frequency separation value of  $96 \mu\text{Hz}$ , their properties presented in Table 4.1. The position of the zero-age main sequence model for a given mass value is the same regardless of the applied mixing prescription, as the interiors are the same until that point. Once the models start evolving, the different behaviors in their frequency ratios make them clearly distinguishable. The tracks reach a minimum value in slope near the exhaustion of the hydrogen in the center (when the convective core starts receding if present).

For the  $1.1 M_\odot$  tracks, the two cases present very different values of slopes throughout the evolution, allowing us to differentiate a star with a convective core from one that has a radiative interior. This is particularly interesting because the stellar parameters are almost the same for both stars, so their positions in the CMD overlap within the usual observational uncertainties (see Table 4.1). The potential of this technique has only recently started to be exploited (Deheuvels et al. 2010; De-Meulenaer et al. 2010).

For more massive models, we show how this type of diagram can help us identify different convective core sizes, evolutionary stages, and therefore mixing prescriptions. Keeping in mind the results presented in Fig. 4.4, for a given mass value the diagram plotted in Fig. 4.5 can disentangle between different convective core sizes, as tracks of a given mass and composition neatly separate according to the mixing prescription applied. With an accurate measurement of the large frequency separation, as expected from the space missions, we can identify the size of the convective core and, since the mass and composition are known, the evolutionary stage.

Nevertheless, mass values determined from a combination of asteroseismic measurements and modeling are usually precise within 5-10 % when metallicity is known (Metcalf et al. 2010; Gai et al. 2011). In Table 4.1 we present the parameters of models for each mixing prescription, including central hydrogen content ( $X_c$ ), size of the sound speed discontinuity at the edge of the convective core (Jump), position of the edge of the convective core in terms of acoustic radius

## 4.5 Breaking the degeneracy: splitting mixing prescriptions and finding convective cores<sup>73</sup>

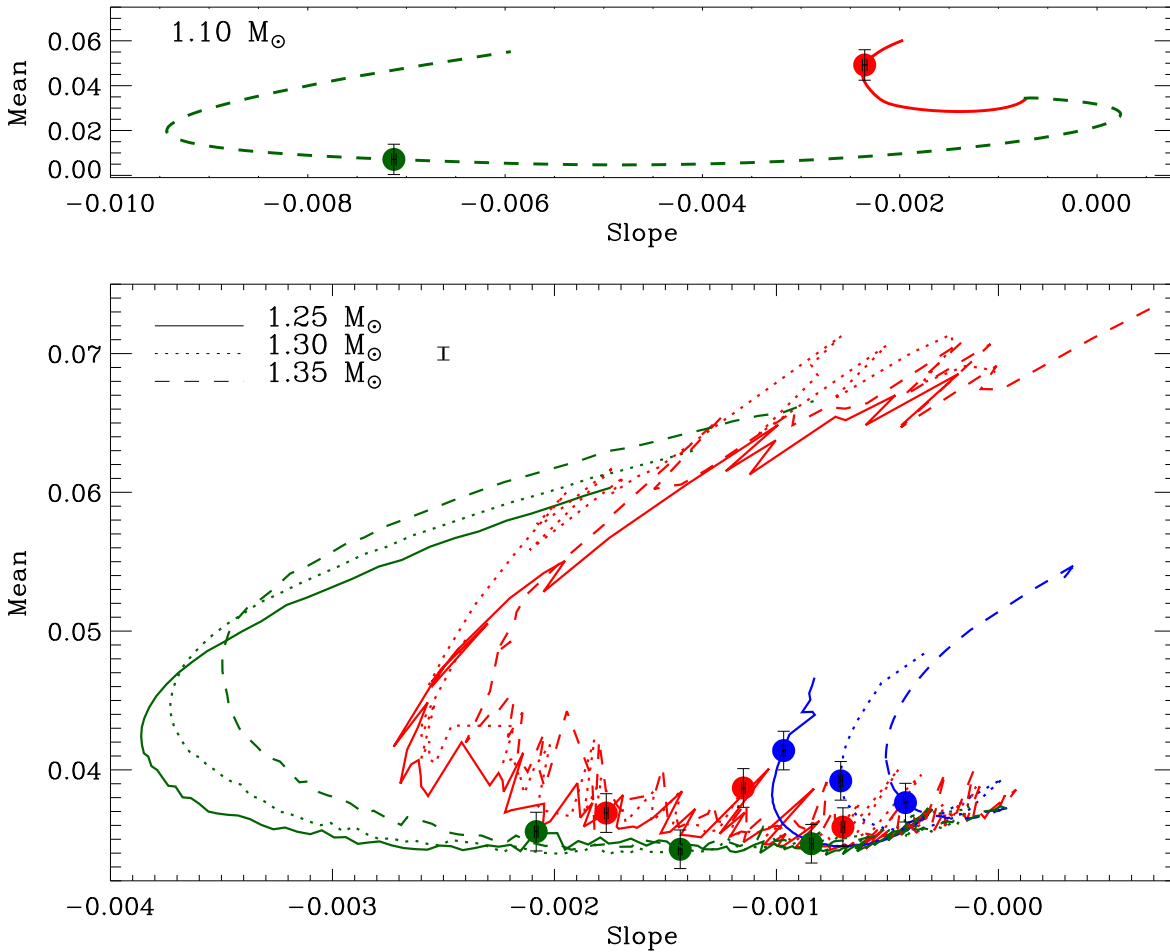


Figure 4.5: Slope versus mean value diagram of the frequency ratios (defined in Eqs. 4.9 and 4.8 respectively) in the assumed observable range throughout the main sequence evolution. *Top panel:*  $1.1 M_{\odot}$  models without overshooting (solid red line) and with overshooting (dashed green line). *Bottom panel:* different mass values for the three considered mixing prescriptions: Ledoux (blue), Schwarzschild (red), and Overshooting (green). A representative  $1\text{-}\sigma$  error bar is plotted at the top left. Models marked with a filled circle have the same value of the large frequency separation, and error bars correspond to  $3\text{-}\sigma$  uncertainties in the frequencies. See text for details.

( $\text{Arad}_{\text{cc}}$ ), and the slope and mean values of the frequency ratios in the radial order  $n=15\text{-}27$ . These models have a mass difference of up to  $\sim 8\%$  and are neatly distinguishable in Fig. 4.5 for the considered error bars, showing that our method is able to break the degeneracy between mass value and mixing process. We stress again that this analysis relies on known seismic and stellar parameters, in particular frequencies and metallicity. The effective temperature differences for the mass range considered in Table 4.1 within a mixing prescription are  $\sim 150$  K, a typical observational error bar. Stars with a greater mass difference for this composition will have an effective temperature that is incompatible with the observations at the same large frequency separation,

which allows us to exclude them from the analysis.

As a closing remark, we notice that in Fig. 4.5 the track representing the evolution according to the Schwarzschild criterion shows abrupt jumps in its slope and mean values. This effect is a consequence of the convective process that was not properly taken into account at the edge of the core, and the abrupt variations correspond to the loops in the convective core profiles (see Sect. 3.3.1). However, the same general behavior as in the other mixing prescription is present, so a mean value can be considered for comparisons.

## 4.6 Discussion

We focused our attention upon using frequency combinations sensitive to the convective core size and the evolutionary stage of the star to discriminate the different mixing prescriptions. For this purpose, we have chosen the frequency ratios and analyzed their behavior throughout the main sequence evolution for different masses and mixing prescriptions. The ratios present a low-frequency domain that is governed by the global seismic properties of the star (especially the large frequency separation). However, for higher frequencies the behavior of the ratios changes together with the inner conditions of the star. These are all high order low-degree modes and correspond to what we have termed the *linear range*.

We have shown that the frequencies in the *linear range* are sensitive to the central regions of the star. However, it is not straightforward to determine whether the modes are reaching the convective core. The radial ( $l = 0$ ) modes propagate down to the center of the star, but the situation is different for the  $l = 1$  modes. Different estimations of the turning points can be made if the perturbation in the gravitational potential is neglected (the Cowling approximation, Cowling 1941) or taken into account (Jeans 1928). In fact, it has been suggested that for stars with convective cores the dipolar modes reach the very center of the star (Takata 2005, 2006). This is an interesting topic where further development is surely needed.

From the results presented in this Chapter we can say that it is possible to estimate the size of the homogeneously mixed zone using seismic data. In particular, we can distinguish between stars with and without a convective core. This has important implications to, for instance, the study of the pre-main sequence evolution. As mentioned in Sect. 1.2.1, stars in this phase develop a small convective core, consequence of the spatially concentrated energy generation which disappears once it is distributed over larger areas. Nevertheless, if the amount of overshooting in the pre-main sequence phase is large enough, the convective core can survive and be sustained during the main-sequence evolution. This will also impact on the minimum mass where a convective core is prone to exist, and is a matter related to other interesting topics such as the solar abundance determinations (see Vandenberg et al. 2007; Magic et al. 2010). Seismic observations of low-mass main-sequence stars could shed new light into this hotly debated topic.

There are, however, several assumptions behind our prediction of discriminating between the presence and absence of a convective core. Besides the expected frequency data, we assume that there are determinations of stellar parameters from either spectroscopy or photometry, with an uncertainty in effective temperature of  $\sim 150$  K. Given these observables we are only limited by the value of the stellar mass, which might be estimated within 5-10% precision for a given mixing

prescription using isochrones and asteroseismic scaling relations (Stello et al. 2009b; Basu et al. 2010; Gai et al. 2011).

The frequency ratios seem to isolate the signal arising from the stellar core enough to allow us to study the central conditions of a star. Another asteroseismic tool aimed at studying small convective cores was proposed by Cunha & Metcalfe (2007), where a combination of small and large separations was constructed and analyzed using modes of angular degree  $l = 0, 1, 2, 3$ . In their work, Cunha & Metcalfe (2007) find that the sharp discontinuity formed at the edge of the convective core has a direct impact on the slope of their proposed quantity when plotted against frequency, showing that the absolute value of the slope increases as a function of the size of the chemical discontinuity (and therefore with decreasing amount of central hydrogen content). Since observing  $l = 3$  modes is very challenging owing to severe amplitude reduction, Cunha & Brandão (2011) extended this study by using the small frequency separations defined in Eqs. 4.3 and 4.4 and analyzing the changes in the slope, reaching the same conclusions as Cunha & Metcalfe (2007).

The behavior with evolution is the same for the small frequency separations, the frequency ratios, and the asteroseismic tool proposed by Cunha & Metcalfe (2007). Thus, our findings are applicable to all of them. We have shown in Sect. 4.4 that, although there is a relation between the size of the discontinuity in the adiabatic sound speed and the absolute slope of the ratios, the total extent of the convective core and the central hydrogen content heavily influence the frequency ratios. Three models with the same large frequency separation and similar size of chemical discontinuity at the edge of the core have very different absolute slopes thanks to their different convective core sizes and central hydrogen contents. On the other hand, models that barely change the size of the convective core during the hydrogen burning phase show the mildest change in the absolute slope of the ratios.

Using this *linear range*, our findings predict that we can distinguish stars with and without convective cores, constrain the size of the homogeneously mixed central region and disentangle the effects from stellar mass. All of these provided we use an adequate frequency combination for isolating the signal coming from the core. The method relies on our knowledge of the stellar composition, where large uncertainties can still be present. Nevertheless, the extensive and highly accurate sets of observations obtained by the CoRoT and *Kepler* missions (e.g. Michel et al. 2008; Stello et al. 2010; Chaplin et al. 2010; Christensen-Dalsgaard et al. 2010) open an exciting possibility for stellar physics: to apply differential analysis to stars with a common property, such as metallicity, and pin down the differences arising from the inner layers of their structure.

From the analysis performed in this Chapter, we have a clear theoretical understanding of the different contributions in the *linear range* of the frequency domain and how to distinguish the effects of mass and type of mixing for realistic error expectations in the observables. We have based our study of the frequency ratios assuming that the oscillations are pure p modes, but this assumption breaks down when modes with mixed p-mode and g-mode character appear (see Aerts et al. 2010, and references therein). These mixed modes carry information from the deep interior and are very sensitive to the core conditions, making them ideal probes for age calibrations in subgiant stars and mixing processes occurring during the main sequence (e.g. Dziembowski & Pamyatnykh 1991; Straka et al. 2005; Deheuvels & Michel 2010; Metcalfe et al.

2010). For instance, they could be detected in main sequence F-type stars with shallow convective envelopes, where these avoided crossings could more easily reach the visible frequency range. However, different analysis tools from the ones presented in here must be developed to fully exploit their potential.

# Chapter 5

## Ensemble asteroseismology using *Kepler* data

In the preceding Chapter we presented an asteroseismic tool sensitive to the central conditions of main-sequence stars. In particular, we showed how these frequency combinations are dependent on the presence of a convective core, its size, and the evolutionary stage of the star. However, as emphasized in Sects. 4.5 and 4.6, we have based our analysis under the assumption that accurate stellar parameters are available for the targets, and that the mass is known within  $\sim 10\%$ . This kind of precision is usually not possible to achieve by means of stellar track fitting; the commonly obtained error bars in  $T_{\text{eff}}$ ,  $\log g$ , and  $[\text{Fe}/\text{H}]$ , allow solutions to fulfill the observations for different input physics and chemical compositions spanning a mass range larger than  $\sim 10\%$ .

Nevertheless, asteroseismology provides a different approach that can be used to determine the mass and radius of pulsating stars. The following chapter contains a slightly extended version of an article accepted by *The Astrophysical Journal Letters* in August 2011 (Silva-Aguirre et al. 2011c). In it, we study the possibility of identifying analogues of stars along the main-sequence and subgiant phases using their global asteroseismic parameters, and thus construct for the first time an evolutionary sequence in a model-independent way.

### 5.1 Introduction

The high-precision photometric observations obtained by the NASA *Kepler* mission (Borucki et al. 2009) have led to a dramatic increase in the number of main-sequence and subgiant stars with detected oscillations (Chaplin et al. 2010; Gilliland et al. 2010a). Data on hundreds of these stars are now available to test our knowledge of solar-like oscillations and their dependence on stellar parameters. Moreover, extremely precise information can be extracted on fundamental stellar properties and compared to population synthesis models of our galaxy (e.g., Chaplin et al. 2011c).

The large ensemble of stars with detected oscillations allows us to select cohorts of targets sharing one or more common properties. By performing comparative studies on these stars, it should be possible to suppress the dependence of the modeling results on the shared charac-

teristic, opening an exciting possibility for further constraining the internal physical processes. This is the basis for *differential asteroseismology*: a detailed seismic comparison of the inner structures of stars showing some similar property.

To exploit this technique, one must be able to identify stars with common characteristics. Comparing the quantities extracted from conventional observations such as spectroscopy is not sufficient to fully constrain stellar properties, and evolutionary models must be employed to determine, e.g., masses and radii. Asteroseismology allows us to go one step further by providing a tool to find pairs or groups of stars with similar characteristics.

In this Chapter, we use global seismic properties of solar-type targets observed by *Kepler* to construct an observational sequence of field stars with masses similar to that of the Sun, in a model-independent way.

## 5.2 Extracting mass and radius from asteroseismic data

There are two asteroseismic parameters that can be readily extracted from the p-mode oscillation spectrum without the need for individual frequency determinations. As mentioned in Sect. 2.3, one of them is the large frequency separation,  $\Delta\nu$ , which denotes the frequency difference between modes of the same degree and consecutive radial order (see Fig. 2.4). It has been shown that, to very good approximation,  $\Delta\nu$  scales as the square root of the mean density (see Sect. 2.2.4). This gives the following relation:

$$\frac{\Delta\nu}{\Delta\nu_{\odot}} = \sqrt{\frac{\rho}{\rho_{\odot}}} \simeq \frac{(M/M_{\odot})^{0.5}(T_{\text{eff}}/T_{\text{eff},\odot})^3}{(L/L_{\odot})^{0.75}}, \quad (5.1)$$

$\Delta\nu_{\odot} = 135.1 \mu\text{Hz}$  and  $T_{\text{eff},\odot} = 5777 \text{ K}$  are the observed values in the Sun.

The other parameter is the frequency of maximum oscillation power,  $\nu_{\text{max}}$ . In Fig. 5.1 we show a power spectrum of the oscillations observed in the Sun, where the 'bell-shape' pattern of the oscillations can be clearly seen and the position of its maximum inferred. The value of the solar frequency maximum oscillation power is usually considered to be  $\nu_{\text{max},\odot} = 3150 \mu\text{Hz}$  (e.g., Chaplin et al. 2011a), although values down to  $\nu_{\text{max},\odot} = 3050 \mu\text{Hz}$  have also been used in the literature (e.g., Mosser et al. 2010). The fact that  $\nu_{\text{max},\odot}$  is defined for the total power (area) under the peak of the highest  $\ell = 0$  mode, combined with realization noise, contribute to values that can have of the order of  $\sim 100 \mu\text{Hz}$  difference.

The quantity  $\nu_{\text{max}}$  is related to the dynamical timescale of the atmosphere (e.g., Brown et al. 1991; Kjeldsen & Bedding 1995), as represented by the acoustic cut-off frequency given in Eq. 2.53. This depends on the structure of the outer layers of the star, where the temperature, pressure and density stratification will define the maximum frequency before oscillations become evanescent. We remind the reader that, as mentioned in Sects. 1.3.3 and 2.2.2, simple approximations are normally used in stellar evolution calculations to model the outer atmosphere. The relation for  $\nu_{\text{max}}$  reads

$$\frac{\nu_{\text{max}}}{\nu_{\text{max},\odot}} \simeq \frac{\nu_{\text{a}}}{\nu_{\text{a},\odot}} \simeq \frac{(M/M_{\odot})(T_{\text{eff}}/T_{\text{eff},\odot})^{3.5}}{(L/L_{\odot})}, \quad (5.2)$$

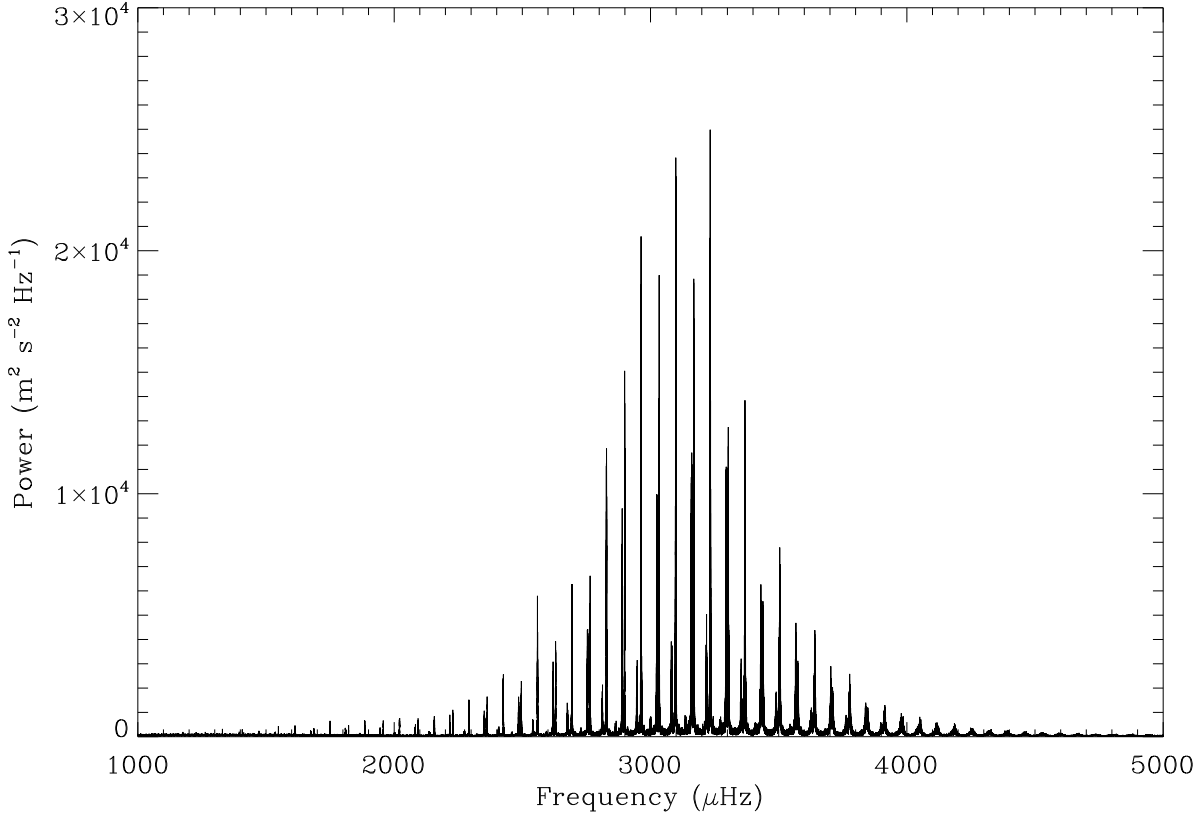


Figure 5.1: Power spectrum of the Sun obtained by the Birmingham Solar- Oscillations Network (BiSON). The 'gaussian-bell' shape forming the envelope of the well-defined peaks is clearly visible, and the position of the frequency of maximum oscillation power can also be observed. Figure courtesy of A.-M. Broomhall (from Broomhall et al. 2009).

where  $\nu_a$  and  $\nu_{a,\odot}$  are the acoustic cut-off frequency of the star and the Sun, respectively (cf., Eq 2.53). The exact nature of this relation is not yet fully understood.

The two global asteroseismic quantities  $\Delta\nu$  and  $\nu_{\max}$  are tightly correlated over a wide range of values, and the scaling relations they follow from the accurately known solar parameters (Eqs. 5.1 and 5.2) have been extensively used in asteroseismic investigations (e.g. Hekker et al. 2009; Stello et al. 2009a; Hekker et al. 2011a). These scaling relations can be written as

$$\frac{M}{M_{\odot}} \simeq \left( \frac{\nu_{\max}}{\nu_{\max,\odot}} \right)^3 \left( \frac{\Delta\nu}{\Delta\nu_{\odot}} \right)^{-4} \left( \frac{T_{\text{eff}}}{T_{\text{eff},\odot}} \right)^{3/2}, \quad (5.3)$$

$$\frac{R}{R_{\odot}} \simeq \left( \frac{\nu_{\max}}{\nu_{\max,\odot}} \right) \left( \frac{\Delta\nu}{\Delta\nu_{\odot}} \right)^{-2} \left( \frac{T_{\text{eff}}}{T_{\text{eff},\odot}} \right)^{1/2}, \quad (5.4)$$

From these two equations it is evident that, provided we have a measurement of  $T_{\text{eff}}$ , the global seismic observables give a determination of stellar mass and radius for a given star that

is independent of evolutionary models. This is the so-called *direct method*, and it has so far been used to constrain the fundamental properties of red giant stars and distinguish different populations of stars (e.g., Miglio et al. 2009; Kallinger et al. 2010; Huber et al. 2010; Hekker et al. 2011b). It can now be applied to the hundreds of solar-type stars for which *Kepler* has detected oscillations (Chaplin et al. 2011c), and find stars that have the mass of the Sun.

### 5.3 Data analysis and stellar properties determination

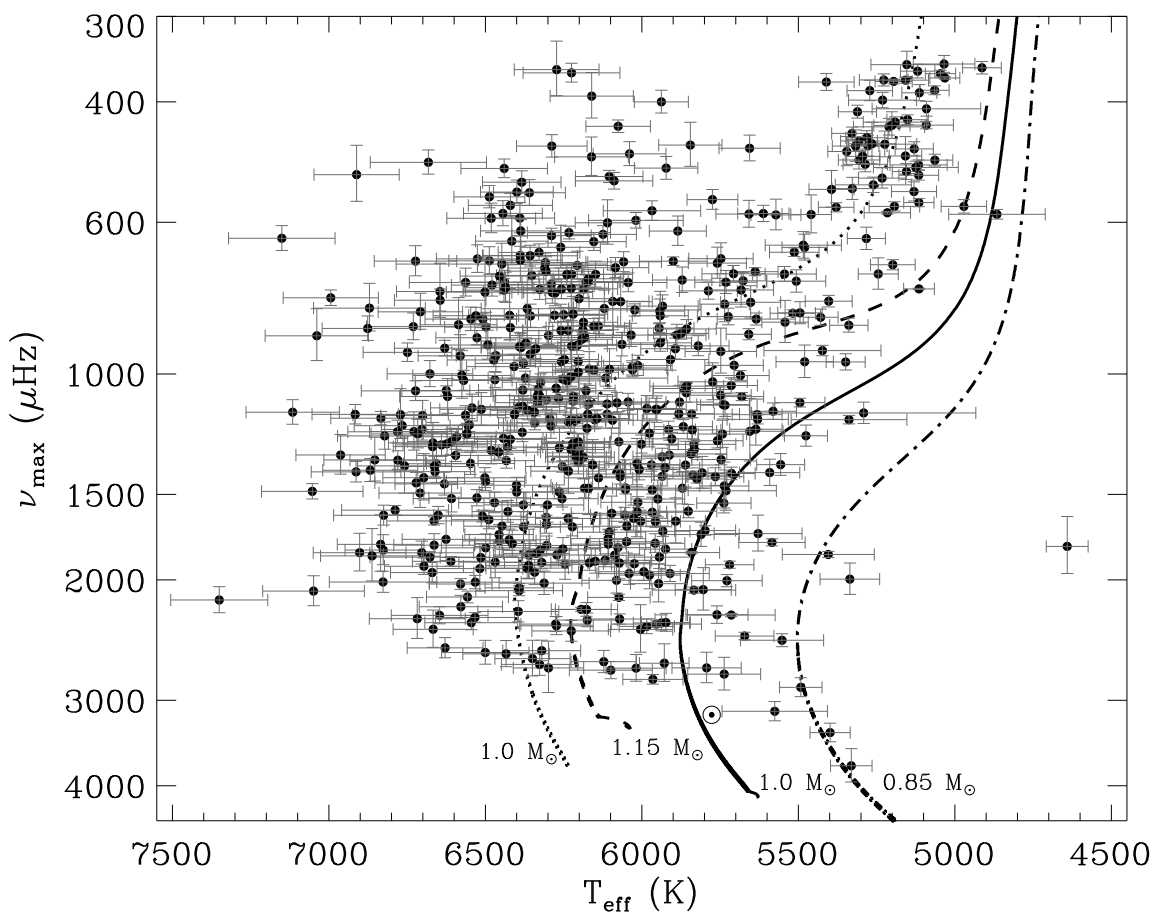


Figure 5.2:  $T_{\text{eff}}-\nu_{\max}$  diagram for the complete sample of targets with detected oscillations. Evolutionary tracks are also plotted: at solar ( $[\text{Fe}/\text{H}]=0.0$ ) metallicity for  $0.85 M_{\odot}$  (dash-dotted line),  $1.0 M_{\odot}$  (solid line), and  $1.15 M_{\odot}$  (dashed line), and at sub-solar metallicity ( $[\text{Fe}/\text{H}]=-0.5$ ) for  $1.0 M_{\odot}$  (dotted line). The Sun is marked with its usual symbol.

We examined asteroseismic results for 2000 solar-type stars observed by *Kepler* during the first seven months of science operations, with oscillations detected in more than 500 of them

(Chaplin et al. 2011c; Verner et al. 2011). Each star was observed for one month in short-cadence mode (58.85 s sampling; see Gilliland et al. 2010b). Time series were prepared for asteroseismic analysis as described by García et al. (2011), using procedures that work on the raw light curves. The prepared light curves were analyzed by different teams, who detected and extracted the basic properties of the solar-like oscillations ( $\Delta\nu$  and  $\nu_{\max}$ ). The methods of extraction and descriptions of each pipeline may be found in Chaplin et al. (2010); Huber et al. (2009); Mosser & Appourchaux (2009); Hekker et al. (2010); Mathur et al. (2010); Campante et al. (2010), and Karoff et al. (2010).

Effective temperatures have been derived via the InfraRed Flux Method (IRFM) described by Casagrande et al. (2010), using the available Sloan and Two Micron All Sky Survey (2MASS) photometry compiled for the targets in the Kepler Input Catalog (KIC; Brown et al. 2011). Comparison shows that the KIC effective temperatures are on average  $\sim 250$  K cooler than the ones derived used in this study. This difference is within the uncertainties of both methods, and in agreement with the results obtained from detailed spectroscopic analysis (Molenda-Żakowicz et al. 2011).

As mentioned in Sect. 1.4, the position of the oscillations in the power spectrum shifts towards lower frequencies as the star evolves. Thus, the value of the maximum power of the oscillations can be considered as a proxy of evolutionary stage. Since we are interested in main-sequence and subgiant stars with masses similar to that of the Sun, we have omitted stars with  $\nu_{\max}$  below  $350 \mu\text{Hz}$  which are beyond the subgiant phase of evolution.

Figure 5.2 shows a  $T_{\text{eff}}-\nu_{\max}$  diagram for all the targets constructed from results of different pipelines, where we demanded that at least two of them reported oscillations in a star to consider a detection. These results have been consolidated to take into account the different methods for estimating uncertainties of each pipeline (as described by Verner et al. 2011). We have overplotted evolutionary tracks for different masses and metallicities calculated with GARSTEC, scaled from the Grevesse & Sauval (1998) solar mixture considering a helium enrichment ratio of  $\Delta Y/\Delta Z = 1.8$  (Casagrande et al. 2007) and not including diffusion of helium and heavy elements (which is why the solar metallicity  $1 M_{\odot}$  track does not overlap the position of the Sun).

It is already clear in Fig. 5.2 that a number of oscillating stars are located on or very close to the evolutionary tracks and thus are potentially  $1 M_{\odot}$  stars. Interestingly, the stars are concentrated in two main regions, with an apparent gap between them (around  $T_{\text{eff}} \sim 5300$  K and  $\nu_{\max} \sim 600 \mu\text{Hz}$ ). This feature suggests a rapid evolutionary stage where few stars are found, which could be identified as the transition between the main-sequence turn-off and the base of the red giant branch, or the disappearance of a convective core following the hydrogen exhaustion in the center which is not predicted by the models. It has also been suggested that an increase in the surface magnetic activity due to evolution can account for the lack of detections in this region, since activity depresses the oscillation amplitudes (Gilliland 1985; Chaplin et al. 2011b). The concentration of stars above the gap (around  $T_{\text{eff}} \sim 5200$  K and  $\nu_{\max} \sim 400 \mu\text{Hz}$ ) further supports the latter idea.

## 5.4 Results

We have applied the direct method to the sample in Fig. 5.2 and determined  $\log g$  values using the asteroseismic results extracted by the Queen Mary of London University (QML) pipeline, which has been used as reference for comparison with other pipelines (Verner et al. 2011). In order to identify stars with masses similar to the Sun for constructing the evolutionary sequence, we selected targets that according to their determined masses and uncertainty, propagated from Eq. 5.3, had a probability larger than 68 % to be in the  $0.85\text{--}1.15 M_{\odot}$  range.

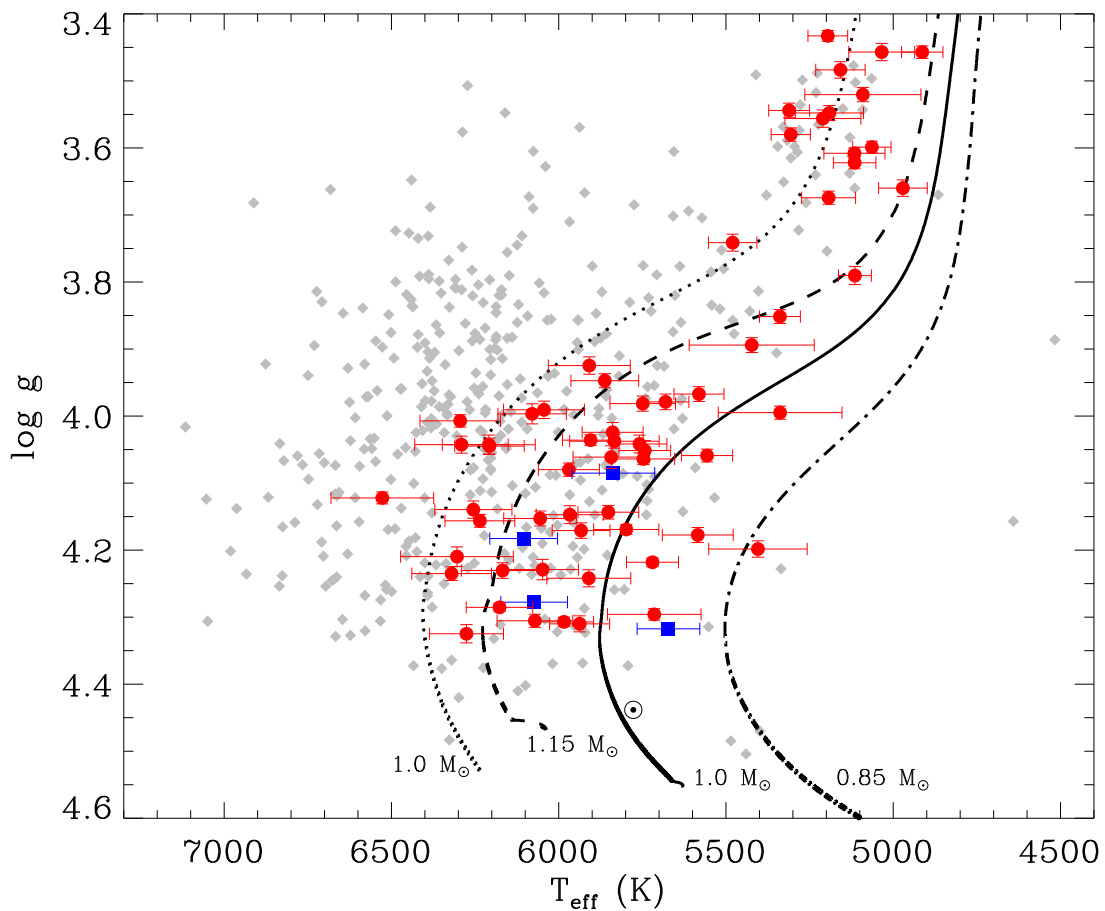


Figure 5.3: Position in the  $\log g$ - $T_{\text{eff}}$  plane of the targets, where  $\log g$  was obtained from the scaling relations. Stars with masses determined to be  $1 M_{\odot} \pm 15\%$  are plotted in red circles, and stars with oscillations detected that do not match the criterion are plotted as gray diamonds (without error bars to reduce clutter). Blue squares are stars with available spectroscopic results. Stellar tracks and position of the Sun are plotted as in Fig. 5.2.

Figure 5.3 shows these stars in the  $\log g$ - $T_{\text{eff}}$  plane, where 72 targets are found to match the selection criterion. The distribution of matches in the observational plane is neatly contained

by the stellar tracks, pointing towards an agreement between the asteroseismic mass values and evolutionary predictions. As in Fig. 5.2, a gap can be seen around  $T_{\text{eff}} \sim 5300$  K and  $\log g \sim 3.7$ , again identified with the separation between the end of the main-sequence and the red giant phases.

In Fig. 5.3 it is also clear that most of the matches fall on the hotter side of the solar-metallicity  $1 M_{\odot}$  track. There are two possible reasons for this. The first is that the amplitudes of the oscillations increase with increasing  $L/M$  ratio (or some variant of it, see Samadi et al. 2007; Mosser et al. 2010; Chaplin et al. 2011b; Kjeldsen & Bedding 1995, 2011), resulting in a detection bias in our ensemble that favors hotter (higher-than-solar-mass) main-sequence and subgiant stars. However, for our considered threshold, only 53 % of the matches have a determined mass larger than  $1 M_{\odot}$ , suggesting a mass distribution barely skewed to higher values than our target mass. The second reason is a spread due to different chemical compositions of the stars because, for a given mass, a lower metallicity will imply a higher luminosity (and vice versa).

Table 5.1: Stellar parameters of the four targets with available spectroscopic observations.

Star	Mass ( $M_{\odot}$ ) <sup>a</sup>	$T_{\text{eff}}$ IRFM (K)	$T_{\text{eff}}$ (K) <sup>b</sup>	$\log g$ <sup>a</sup>	$\log g$ <sup>b</sup>	[Fe/H] <sup>b</sup>	Source
1	$0.96 \pm 0.051$	$5671 \pm 94$	$5715 \pm 82$	$4.32 \pm 0.007$	$4.31 \pm 0.14$	$0.30 \pm 0.06$	ARES
2	$1.04 \pm 0.043$	$6073 \pm 100$	$6073 \pm 78$	$4.28 \pm 0.006$	$4.38 \pm 0.12$	$-0.10 \pm 0.06$	ARES
3	$1.07 \pm 0.051$	$6105 \pm 101$	$5940 \pm 70$	$4.18 \pm 0.006$	$4.21 \pm 0.08$	$-0.10 \pm 0.07$	VWA
4	$1.07 \pm 0.062$	$5836 \pm 124$	$5870 \pm 70$	$4.09 \pm 0.008$	$4.07 \pm 0.08$	$-0.01 \pm 0.07$	VWA

<sup>a</sup> From the direct method.

<sup>b</sup> From spectra.

Keeping this in mind, we can infer from the position of the stellar tracks in Fig. 5.3 that the spread is most likely due to differences in the chemical compositions of the stars. The effects of different masses and other physical processes such as microscopic diffusion (estimated by the separation between the  $1 M_{\odot}$  solar metallicity track and the position of the Sun) are not large enough to account for this spread. Unfortunately, we do not yet have spectroscopic determinations of metallicity for most of the stars we are studying, so the question arises: can we reliably identify stars with similar masses, or does the direct method provide incorrect mass determinations that are camouflaged by the unknown stellar parameters?

We can have a first glimpse at the answer by using spectroscopic results which are available for four of our targets (blue squares in Fig. 5.3). The stellar parameters have been determined using the Automatic Routine for line Equivalent widths in stellar Spectra (ARES; Sousa et al. 2008) and the projected rotational Velocity, Wavelength shift, and Abundance analysis (VWA; Bruntt et al. 2010) methods. It is worth mentioning that we selected the spectroscopic set of parameters with  $\log g$  value closer to the direct method determination. These are shown in Table 5.1, where it can be seen that the uncertainties in  $\log g$  from the direct method are of the order of 10 times smaller than those coming from high-resolution spectroscopy. Our  $T_{\text{eff}}$  input values (IRFM) for these four stars are compatible with the spectroscopic results.

In Fig. 5.4 we compare the results of the direct method for the four stars with evolutionary predictions by showing deviations in  $T_{\text{eff}}$  between our IRFM input parameter and stellar tracks

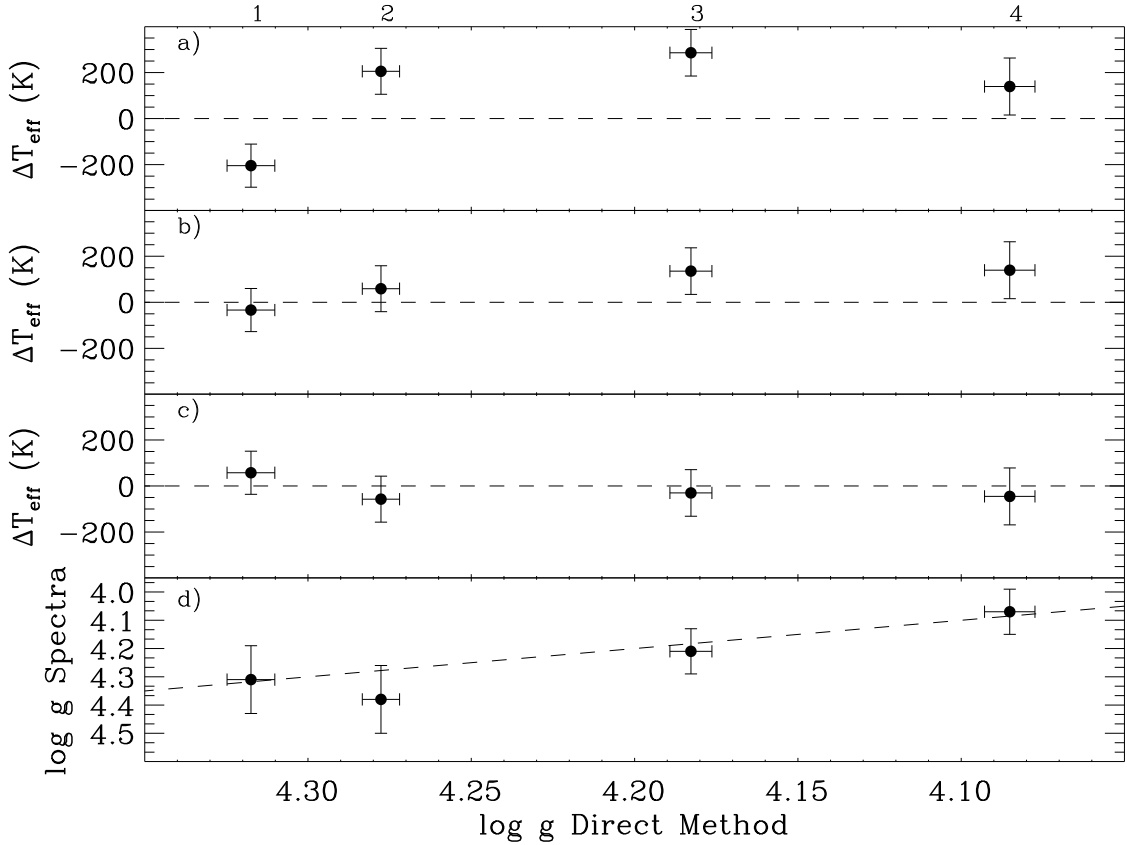


Figure 5.4: First three panels show the  $T_{\text{eff}}$  difference (IRFM-model) for the four targets marked in Fig. 5.3 and: **(a)** the  $1 M_{\odot}$  track at solar metallicity, **(b)** a  $1 M_{\odot}$  track at the spectroscopic metallicity for that star, and **(c)** a track of the mass determined by the direct method and the spectroscopic metallicity for that star. Panel **(d)** shows the  $\log g$  values obtained from spectroscopy compared to those determined with the direct method, with the dashed line indicating the one-to-one relation.

at the  $\log g$  value determined from the direct method. Figure 5.4(a) shows the  $T_{\text{eff}}$  difference between our targets and a  $1 M_{\odot}$  evolutionary track at solar metallicity, with large deviations arising from a combination of different metallicities and masses. The following panels show the results when we take these differences into account step by step. Firstly, Fig. 5.4(b) depicts the difference in  $T_{\text{eff}}$  between our targets and  $1 M_{\odot}$  tracks at the metallicity obtained from spectroscopy. Stars 1 and 2 are already compatible with the stellar tracks, which is encouraging as their masses determined with the direct method are consistent with  $1 M_{\odot}$  within their  $1\text{-}\sigma$  uncertainties. The other two stars have slightly higher-than-solar mass determinations. In Fig. 5.4(c) the difference is calculated with respect to evolutionary tracks of the metallicity measured by spectroscopy and

mass determined from the direct method. It is clear that the agreement improves as we include the effects of mass and chemical composition, reinforcing the conclusion that the direct method predicts masses for field stars compatible with evolutionary tracks at the metallicities obtained from spectroscopy, in a model-independent way. Moreover, the  $\log g$  values determined with the direct method are in agreement with the spectroscopic results, as shown in Fig. 5.4(d).

Unfortunately, individual frequency determinations are not yet available for the four targets with spectroscopic metallicities determined. Further confirmation of the stellar masses could be provided by the behavior of some frequency combinations, such as the ratios  $r_{010}$  introduced in Chapter 4. As an example, we show these quantities in Fig. 5.5 for models from the  $1.0 M_{\odot}$  and  $1.15 M_{\odot}$  tracks from Figs. 5.2 and 5.3, selected at the large frequency separation value of the four targets with spectroscopic data.

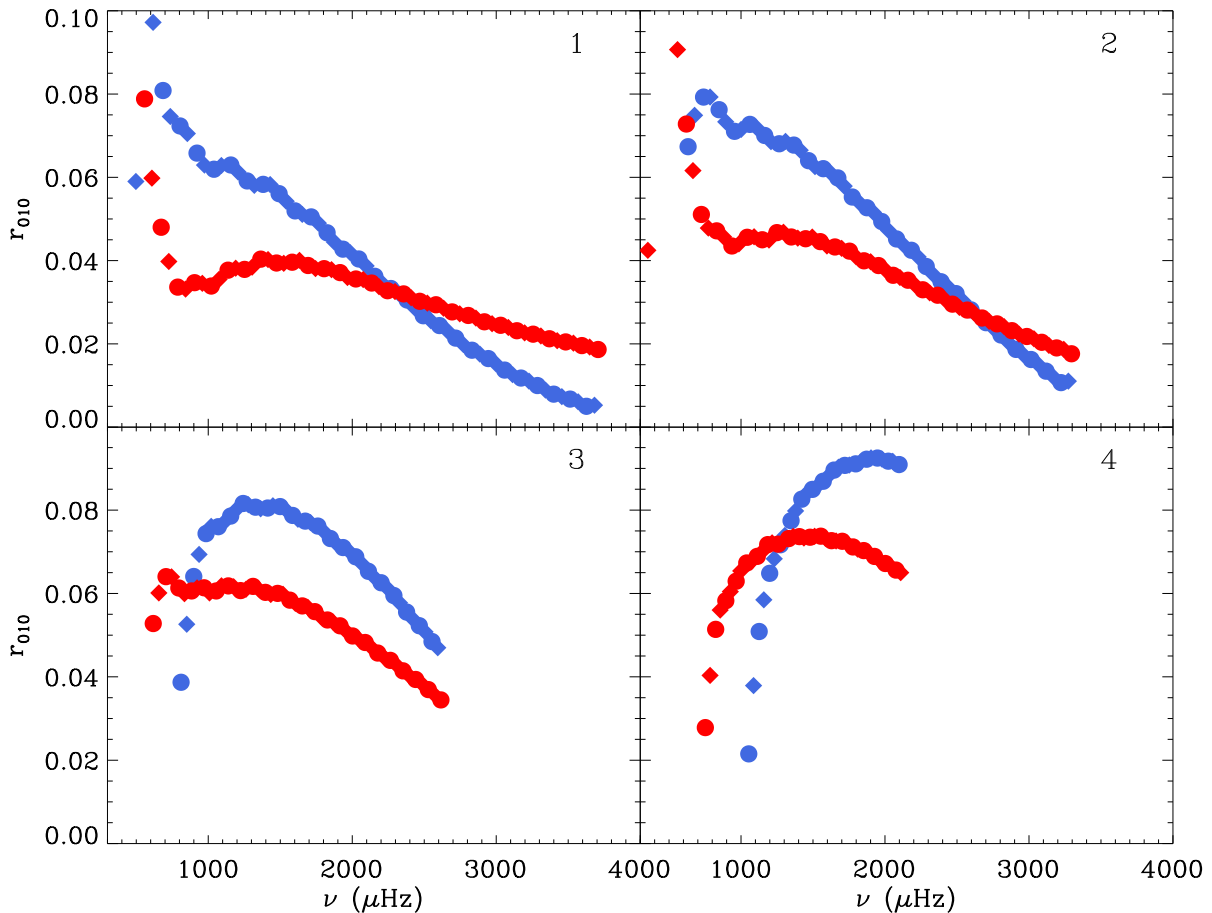


Figure 5.5: Frequency ratios  $r_{010}$  for models of  $1.0 M_{\odot}$  (blue) and  $1.15 M_{\odot}$  (red) at solar metallicity, selected at the large frequency separation of the four targets with spectroscopic data. Labeling of the targets is given in the upper-right corner of each panel, where the numbers correspond to those given in Table 5.1 and Fig. 5.4.

A similar analysis was presented in Sect. 4.3, where models with the same mass but differing in their means for energy transport in the stellar core were presented. It was clear from that example that the frequency ratios are very sensitive to the existence of a convective core. In the comparison shown in Fig. 5.5, both models have radiative interiors, but different central hydrogen contents. The ratios  $r_{010}$  are clearly different for the cases considered, hinting towards the interesting possibility of discriminating between stars of different masses by means of these frequency combinations. This possibility is further explored, and applied to *Kepler* data, in Sect. 6.4 below. It is also interesting to notice that for the most evolved target (number ‘4’), the range of frequencies that could be potentially observed reaches only the beginning of the linear range in  $r_{010}$ . This must be kept in mind when trying to characterize the stars using this frequency combination.

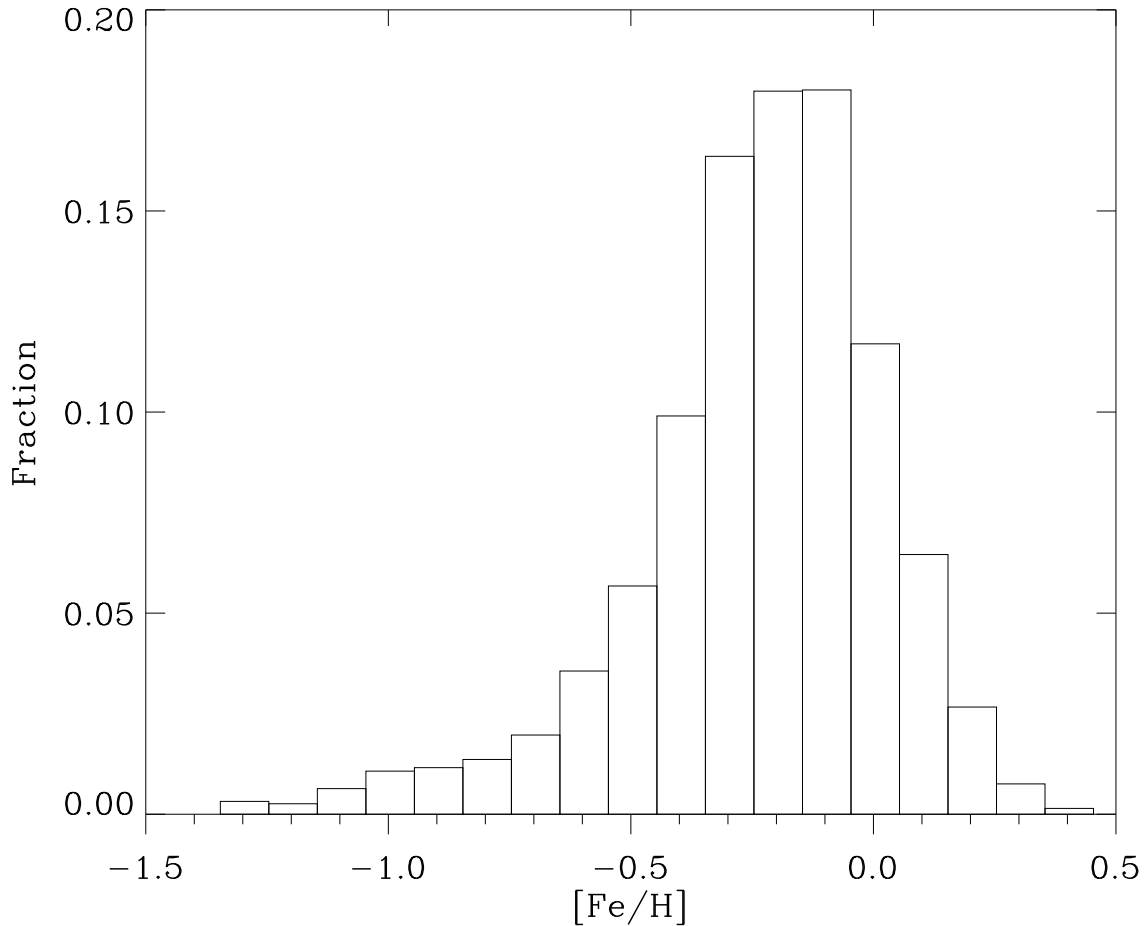


Figure 5.6: Metallicity distribution in the *Kepler* field as simulated by the SMAUG code, showing stars with a probability higher than 90 % to have oscillations detected after one month of observations.

For the rest of the targets, however, the issue of the chemical composition still remains.

In order to obtain some information on the expected metallicities for the rest of our targets, we simulated the stellar population in the *Kepler* field using the Simple Model for Analytic Understanding of our Galaxy code (SMAUG; Schönrich & Binney 2009a,b). The outcome of the simulation has been filtered to retain only synthetic stars that, according to their radius, effective temperature and visual magnitude, have a probability greater than 90% for the *Kepler* satellite to detect oscillations in one-month-long observations (Chaplin et al. 2011b). The resulting subset has been further restricted to stars with  $T_{\text{eff}} \leq 7000$  K,  $\log g \geq 3.4$ , and  $m_v \leq 12.5$ . The metallicity distribution of that population is shown in Fig. 5.6, and it peaks at a sub-solar value with the bulk of stars contained in a range for chemical composition that makes them clearly compatible with the position of our matches and stellar tracks in Fig. 5.3.

## 5.5 Discussion

The sequence of field stars identified in the previous section shows very good agreement with the expected position of  $1 M_{\odot}$  stars in the  $\log g$ - $T_{\text{eff}}$  plane. For those targets with metallicity measurements available, the masses and radii determined with the direct method are fully compatible with evolutionary tracks and spectroscopic  $\log g$  determinations. Nevertheless, we must keep in mind that uncertainties in the observables and the scaling relations can affect our derived quantities.

From Eqs. 5.3 and 5.4 it is clear that the mass and radius determinations are mostly sensitive to the uncertainties arising from the asteroseismic parameters. Although the errors in effective temperature determinations cannot be neglected, the fractional uncertainties in  $\nu_{\text{max}}$  are currently up to four times larger than those in  $T_{\text{eff}}$  and  $\Delta\nu$ . Therefore, the uncertainties in the frequency of maximum oscillation power currently account for most of the error budget.

Masses and radii determined from the direct method have an intrinsic uncertainty associated with two effects: deviations from the scaling relations and unknown stellar properties that can change the pulsation characteristics of the star. The scaling relation between the large frequency separation and the mean stellar density has been shown by theoretical models to be quite robust (Stello et al. 2009a). It is more complicated to estimate the uncertainties arising from the  $\nu_{\text{max}}$  scaling, since it relies on the relation between  $\nu_{\text{max}}$  and the acoustic cut-off frequency under the assumption of an isothermal atmosphere (e.g., Brown et al. 1991). Although a partial theoretical basis for this relation has only recently been developed (Belkacem et al. 2011), comparisons under this assumption with stellar models predict that it holds within a few percent for cool models (close to solar-mass, see; Stello et al. 2009a). Observational results for stars whose parameters are accurately known confirm this result (Bedding & Kjeldsen 2003). Realistic model atmospheres could help to assess its deviations, as could comparisons with direct observational methods to measure stellar properties, such as long-baseline interferometry.

The other main source of uncertainties is related to unknown stellar parameters, such as chemical composition. It is possible to complement the direct method with our knowledge of stellar evolution and match the seismic observables to their expected values from previously calculated evolutionary models. This so-called *grid-based method* has been shown by simulations to perform as well as the direct method for constraining the radius (Stello et al. 2009b; Basu

et al. 2010; Kallinger et al. 2010). When accurate metallicity measurements are available, the grid-based method is supposed to reduce the uncertainty in the mass determination (Gai et al. 2011). However, this study has shown that the scaling relations are not too sensitive to stellar composition.

A few words of caution regarding the grid-based asteroseismic analysis. To find the mass and radius of a target, the grid-based method calculates the maximum likelihood of the set of observables  $\Delta\nu$ ,  $\nu_{\max}$ ,  $T_{\text{eff}}$ ,  $[\text{Fe}/\text{H}]$ , and their uncertainties, with respect to pre-calculated evolutionary tracks (Basu et al. 2010; Gai et al. 2011). In order to do so, the same set of input parameters must be estimated for the stellar models, which will naturally depend on several considerations used to build the grid. In particular, estimations of  $\Delta\nu$  and  $\nu_{\max}$  are normally made from the relations given in Eqs. 5.1 and 5.2. Thus, for a given mass, any process affecting the outgoing effective temperature and luminosity will change the value of the global seismic parameters.

A clear example of this are the estimates of metallicity. As this comparisons are made in terms of  $[\text{Fe}/\text{H}]$ , the results will depend on the set of chosen solar abundances and reference  $Z$  and  $Y$  values (cf. Sect. 1.1.2), and the possible inclusion of any process that can alter the surface chemical composition during evolution (such as atomic diffusion). This has a direct impact in the obtained  $T_{\text{eff}}$  and luminosities. Same occurs with the other physical processes described in Sect. 1.3.1, where the inclusion of overshooting, or the chosen value of the mixing-length parameter  $\alpha_{\text{MLT}}$  have an impact in the resulting  $T_{\text{eff}}$ . The impact in the obtained masses and radii using the grid-based method of the different ingredients of stellar evolution remains to be tested thoroughly.

In the future, we expect another validation of our results to be made by comparing the  $\log g$  values determined with the direct method to the parallaxes that will be obtained from the *Kepler* (Gilliland et al. 2010a) and Gaia missions in the future, given that a variation in mass of 10 % translate into a change in  $\log g$  of approximately 0.04 dex (Casagrande et al. 2011).

In this work, we constructed the evolutionary sequence by applying the selection criterion to the parameters extracted by one particular pipeline. Different pipelines produced similar results in terms of the distribution of the matches in the HRD and the spread around the evolutionary tracks (see Fig. 5.3). A natural step forward would be to combine the results of several pipelines to restrict further the matches and make the results even more robust. However, there is still some variation between the extraction methods in the determination of  $\nu_{\max}$ . The reason probably lies in the low signal-to-noise ratio of some of the observations and the relatively short time-span of the data currently available (Verner et al. 2011).

Finally, our selection criterion can be arbitrarily modified to accept, for instance, stars with masses within 10 % of  $1 M_{\odot}$ . In such case only 20 targets satisfy the criterion, while increasing the threshold to 20 % results in 120 matching stars. We have kept the 15 % threshold as a good compromise between a required high precision and the uncertainties described in the previous paragraphs.

## 5.6 Conclusions

Constructing empirical evolutionary sequences from asteroseismic data offers the exciting possibility of performing differential analysis on field stars of similar masses, allowing us to test stellar properties very precisely through different evolutionary phases. Scaling relations using global asteroseismic parameters and  $T_{\text{eff}}$  measurements allowed us to determine masses of stars in a model-independent way. The position of our matches in Fig. 5.3 suggests that we have successfully identified an evolutionary sequence of field stars with masses very close to  $1 M_{\odot}$ . The results are encouraging and for the first time we can construct such a sequence without parallax information, spectroscopic  $\log g$ , or masses estimated from evolutionary tracks. Longer time series and ground-based follow-up spectroscopy will further enhance the capabilities of this technique, allowing us to reach a higher level of precision.

The results from Sect. 5.4 indicate that our mass and radius determinations are very robust. Using these results and the input effective temperature, together with a grid of stellar models, it should be possible to derive the expected metallicity distribution of the targets. This distribution will depend on the input parameters used to calculate the grid, most notably the selected solar abundances,  $\Delta Y/\Delta Z$  value,  $\alpha_{\text{MLT}}$  parameter, and the inclusion of mixing processes such as diffusion. Future comparisons of this metallicity distribution with accurate chemical composition determinations could help to constrain the input parameters of the grid models that produce the largest variation in the resulting metallicities.

When suitable analogues are found in different evolutionary stages and their individual frequencies determined, a differential analysis can be performed to better constrain the interior physics of stars throughout their evolution. If targets with masses higher than solar are chosen instead, we could differentially study the effects of mixing processes in their interiors and constrain processes that still rely mostly on empirical calibrations, such as convective core evolution and overshooting (e.g. De-Meulenaer et al. 2010; Silva-Aguirre et al. 2011a). For example, by selecting a sequence of stars of very similar mass it could be possible to produce a precise relative age calibration.

Asteroseismology has provided us with a method to disentangle stars still ascending the red giant branch from those already burning helium in their cores (Bedding et al. 2011). Our work can be extended to identify evolutionary sequences from the main sequence to the red clump. Differential analysis of these targets can provide further constraints on the main-sequence physical processes and shed light on the progenitors of horizontal branch stars.

In the near future, it will be interesting to construct evolutionary sequences and select twins of very well-studied main-sequence stars, both seismically and in terms of their stellar parameters. From the ensemble it is already possible to identify sequences for  $\alpha$  Cen A and B, although for the latter case the number of analogues is much smaller due to our bias toward higher amplitudes than the Sun. Some twins of  $\alpha$  Cen A are already present in the ensemble, and longer time-series will allow us to expand the search to lower temperatures and find twins of our Sun and  $\alpha$  Cen B. The potential of combining asteroseismic data with spectroscopic determinations for solar twins has only recently begun to be exploited (see Bazot et al. 2011).



# Chapter 6

## Sounding deep stellar interiors: convective cores in *Kepler* main-sequence targets

This chapter presents the preliminary results of the seismic analysis of two main-sequence *Kepler* targets, where individual frequencies have been determined. The work is organized as a working package among the *Kepler* collaboration, and it is being led by V. Silva-Aguirre. The results will be described in a forthcoming article which is currently in preparation (Silva-Aguirre et al. 2011b). In order to fulfill the regulations of the non-disclosure agreement signed by every member of the Kepler Asteroseismic Science Consortium (KASC), the identity of the targets discussed in this chapter must remain anonymous. For simplicity, we will assign them ‘cat’ nicknames<sup>1</sup>.

### 6.1 Introduction

We have now all the necessary ingredients to carry out a thorough analysis of oscillations frequency data to detect and constrain the properties of convective cores in main-sequence stars. In Chapter 3 we evaluated the impact and importance of the size of the convective core for the hydrogen-burning evolutionary phase, with special attention to the age differences. With this in mind, in Chapter 4 we developed and tested an asteroseismic tool to probe the inner regions of stars and studied its sensitivity to the presence and size of a convective core. However, we recognized the necessity of a mass determination of the targets precise to  $\sim 10\%$ . The large ensemble of stars with oscillations detected by the *Kepler* mission gave us the opportunity to apply scaling relations from the global seismic parameters and identify stars of similar masses along an evolutionary track. In Chapter 5 we showed that our mass determinations using the direct method are compatible with stellar evolution models constructed using spectroscopically determined chemical compositions, giving us confidence that we are in fact able to identify stars of a certain mass with the required precision.

---

<sup>1</sup>The ‘cat’ names assigned to the stars are unique among the *Kepler* collaboration, and are commonly used in the publications related to *Kepler* targets. Upon publication of the paper, the catalogue names and coordinates of the objects will be revealed.

From the hundreds of main-sequence targets the *Kepler* mission has provided asteroseismic data for (e.g., Chaplin et al. 2011c; Silva-Aguirre et al. 2011c), individual frequencies have now been determined for some of them from time-series spanning several months. We carry out here the first investigation of two of these targets, with the aim of detecting convective cores, constraining their size, and narrowing down the age uncertainties from those obtained by fitting stellar tracks. Choosing suitable frequency combinations, we show that the current asteroseismic data allows us to discriminate between existence or not of convective cores, and that it is also sensitive to its total extent. We discuss our results in comparison with those obtained from the direct method (presented in Sect. 5.2) and grid-based analysis for the stellar masses, and briefly discuss the issue of the spectroscopically determined stellar parameters.

## 6.2 Characteristics of the chosen targets

The stars ‘Perky’ and ‘Dushera’<sup>2</sup> selected to perform this study have been continuously observed by the *Kepler* satellite for periods of 6 and 9 months, respectively. This has allowed the detection of oscillations spanning several radial orders for both targets, which can be clearly seen in the Echelle diagrams shown in Figs. 6.1 and 6.2. The length and quality of the observations allow a clear identification of the  $\ell = 0, 1$  and 2 modes, as the excess power is neatly aligned into the expected vertical ridges. It is important to notice that no signature of mixed-modes are present in the diagrams (cf., Sect. 2.2.3), suggesting that both targets are in fact main-sequence stars. Using the QML pipeline (Verner et al. 2011), we have obtained the global seismic parameters  $\Delta\nu$  and  $\nu_{\max}$ .

The stars have also been monitored from the ground. The available photometric information from the KIC (Brown et al. 2011) has allowed the estimation of effective temperatures via the IRFM (Casagrande et al. 2010), and high-resolution spectra obtained for both targets and analyzed using the VWA method (Bruntt et al. 2010) has complemented the set of stellar parameters. In the case of Dushera, low-resolution spectra has also been obtained and analyzed using ARES (Sousa et al. 2008). The stellar and global seismic parameters obtained for both stars are given in Table 6.1. It is important to notice that the low- and high-resolution spectroscopic determinations

Table 6.1: Parameters determined from the observations of the *Kepler* mission, ground based photometry, and spectroscopy for both stars.

Star	$\nu_{\max}$ ( $\mu\text{Hz}$ )	$\Delta\nu$ ( $\mu\text{Hz}$ )	$T_{\text{eff}}$ (K) <sup>a</sup>	$T_{\text{eff}}$ (K)	$\log g$	[Fe/H]
Perky	$2210.73 \pm 11.95$	$104.20 \pm 0.04$	$6155 \pm 73$	$5990 \pm 70^b$	$4.31 \pm 0.04^b$	$-0.12 \pm 0.07^b$
Dushera	$1833.13 \pm 12.82$	$88.41 \pm 0.14$	$6337 \pm 104$	$6065 \pm 70^b$ $6358 \pm 99^c$	$4.21 \pm 0.04^b$ $4.45 \pm 0.13^c$	$-0.12 \pm 0.07^b$ $0.11 \pm 0.07^c$

<sup>a</sup> From the IRFM.

<sup>b</sup> From VWA.

<sup>c</sup> From ARES.

<sup>2</sup>Cat-names given to the stars to comply with the KASC restrictions.

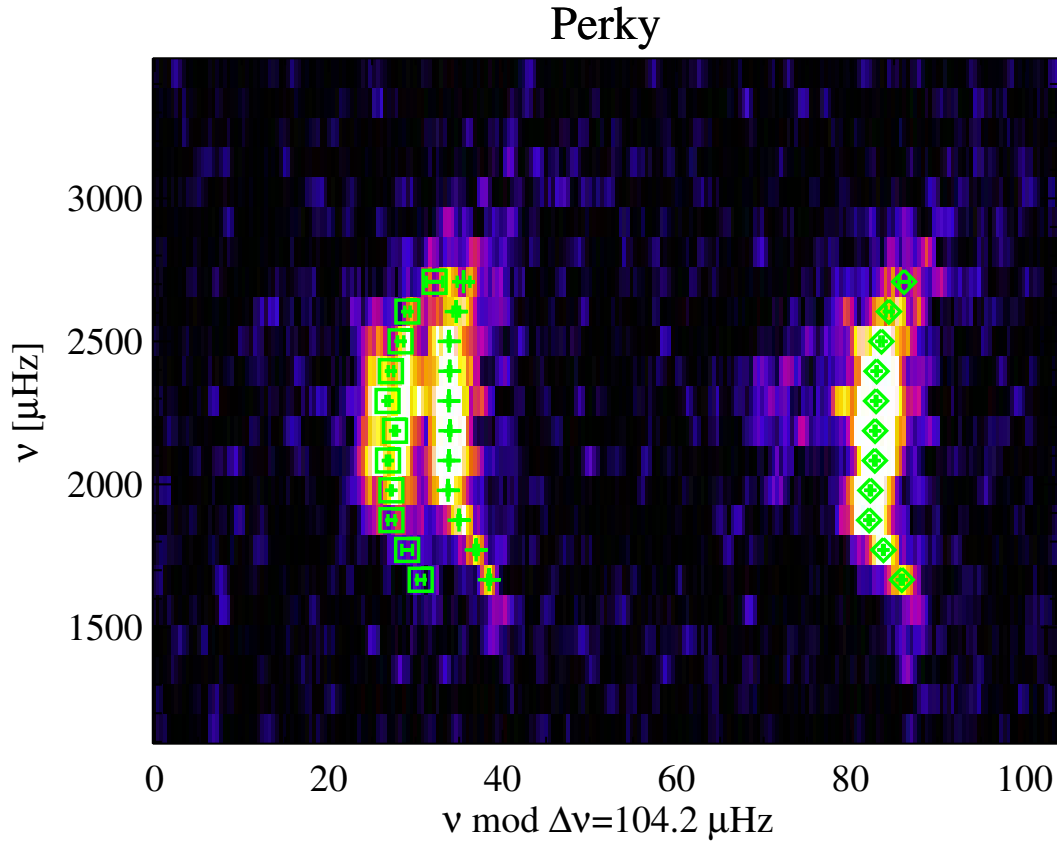


Figure 6.1: Echelle diagram of Perky showing the signature of oscillations from 6 months observations. The vertical ridges are (from left to right) the  $\ell = 2, 0, 1$  modes. Position of individual fitted frequencies has been marked with green squares ( $\ell = 2$ ), crosses ( $\ell = 0$ ), and diamonds ( $\ell = 1$ ), including the error bars.

of stellar parameters for Dushera do not agree, even when considering the  $1-\sigma$  uncertainties. The values of  $\log g$  given for the VWA analysis were obtained by means of the grid-based method using seismic data, and applied as an input to determine the other stellar parameters. The validity of such an approach remains to be tested.

### 6.3 Grid-based analysis

In principle, since the chemical composition is determined by spectroscopy for both targets, we can complement the seismic global parameters with this information and perform a grid-based analysis. As mentioned in Sect. 5.5, when accurate metallicities are available the grid-based method is supposed to narrow down the mass uncertainty with respect to those obtained by the direct method. We performed a grid-based analysis for the two targets, using several pipelines constructed from different evolutionary codes to search for their solutions of the best-fit model

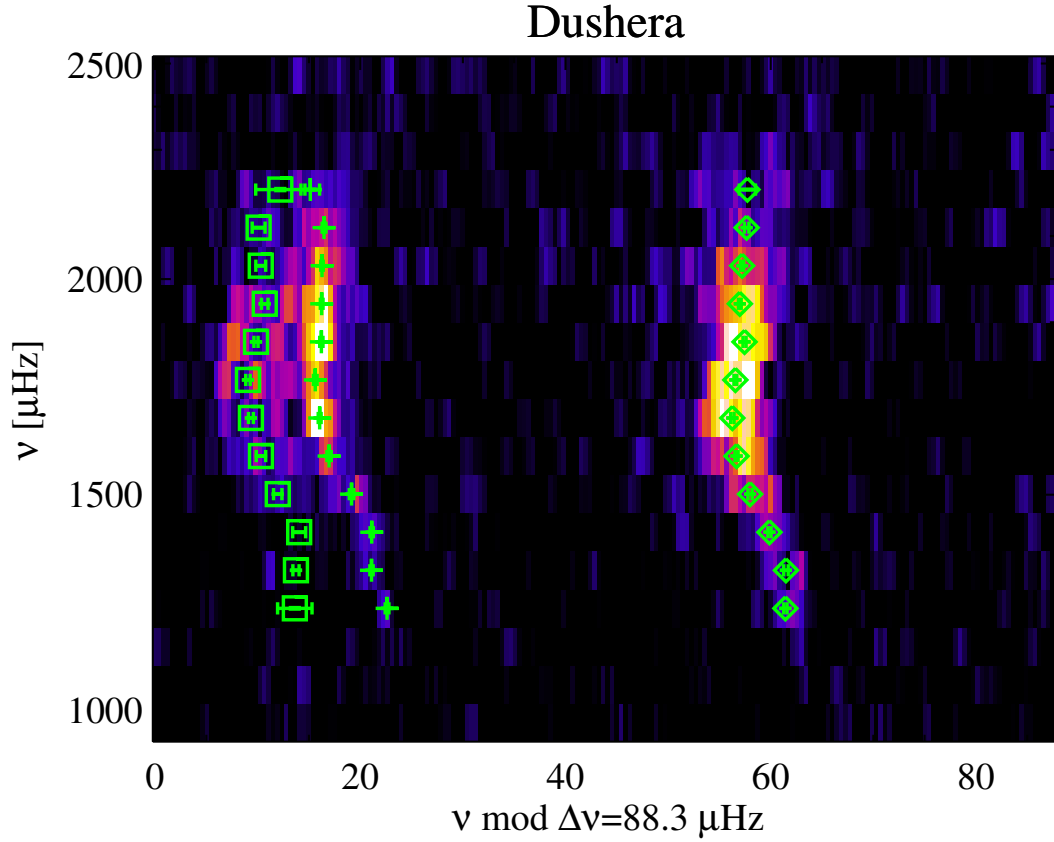


Figure 6.2: Same as Fig. 6.1 for the 9 month-long observations of the target Dushera.

to the seismic and spectroscopic data. The main characteristics of the input physics included in each grid of models is shown in Table. 6.2. The details on how each grid of evolutionary

Table 6.2: Some characteristics of the input physics included in the evolutionary grids of models.

Grid	Mixture	Overshooting	Diffusion
YB	Grevesse & Sauval (1998)	Yes	Yes
RADIUS	Grevesse & Noels (1993)	No	No
GARSTEC	Grevesse & Sauval (1998)	Yes	Yes
SEEK	Grevesse & Sauval (1998)	Yes	No

calculations was built and the different search methods can be found in the references of the pipelines: Basu et al. (2010) (Yale-Birmingham or YB), Stello et al. (2009b) (RADIUS), and Quirion et al. (2010) (SEEK). One more grid of models was constructed using GARSTEC, and the best set of parameters for the models was found applying the same procedure as presented in Basu et al. (2010).

Table 6.3 shows the stellar parameters that were given to the teams performing the grid

based analysis, which were naturally accompanied with  $\nu_{\max}$  and  $\Delta\nu$ . The uncertainties in the

Table 6.3: Input stellar parameters used by different teams to perform grid-based search of a best-fit models for the two targets.

Star	$T_{\text{eff}}$ (K)	$\log g$	[Fe/H]
Perky	$6100 \pm 200$	$4.27 \pm 0.1$	$-0.08 \pm 0.1$
Dushera	$6200 \pm 200$	$4.30 \pm 0.2$	$0.0 \pm 0.15$

parameters, in particular for the case of Dushera, were chosen large enough to encompass as best as possible the discrepant values provided by the spectroscopic analysis (those shown in Table 6.1).

Table 6.4 shows the results obtained with each pipeline for the mass of the two targets, including their  $1\text{-}\sigma$  uncertainties. It is worth mentioning that the grid of models of each pipeline have been constructed using different sets of input physics, solar abundances, opacities, equation of state, etc., which can account for some of the differences seen in the results. The last column shows, for comparison, the mass value obtained with the direct method we presented in Chapter 5.

Table 6.4: Masses (in solar units) as determined from each pipeline for the two targets. Also shown is the mass value determined from the direct method. See text for details.

Star	YB	RADIUS	GARSTEC	SEEK	Direct
Perky	$1.013 \pm 0.0691$	$1.020 \pm 0.0297$	$1.167 \pm 0.0978$	$1.200 \pm 0.1162$	$1.060 \pm 0.0549$
Dushera	$1.161 \pm 0.1087$	$1.190 \pm 0.1046$	$1.298 \pm 0.1145$	$1.300 \pm 0.1241$	$1.195 \pm 0.0635$

The average values of the mass determinations from the grids are  $1.10 M_{\odot}$  for Perky and  $1.23 M_{\odot}$  for Dushera. Within a 10% uncertainty of this average values, all the central masses obtained by the pipelines are contained. However, when taking into account the  $1\text{-}\sigma$  uncertainties given by each grid, mass values between  $\sim 0.94\text{-}1.31 M_{\odot}$  are possible for Perky, and between  $\sim 1.05\text{-}1.42 M_{\odot}$  for Dushera. These differences of more than  $\sim 0.35 M_{\odot}$  are much larger than expected from the grid-based analysis, and the reason why they arise is yet to be tested for the pipelines here involved.

## 6.4 The frequency ratios: precise mass estimations

Giving the difficulties for finding a precise mass determination using the grid-based analysis, we turn our attention into detailed modeling of the two targets. We intent to use individual frequency determinations and apply the tool developed in Chapter 4 to find the best-fit model by reproducing the ratios  $r_{010}$  given in Eq. 4.5.

We start with the target Perky. Dushera will follow in Sect. 6.5. In Fig. 6.3 three evolutionary tracks constructed at solar metallicity are shown, where the model fitting the large frequency

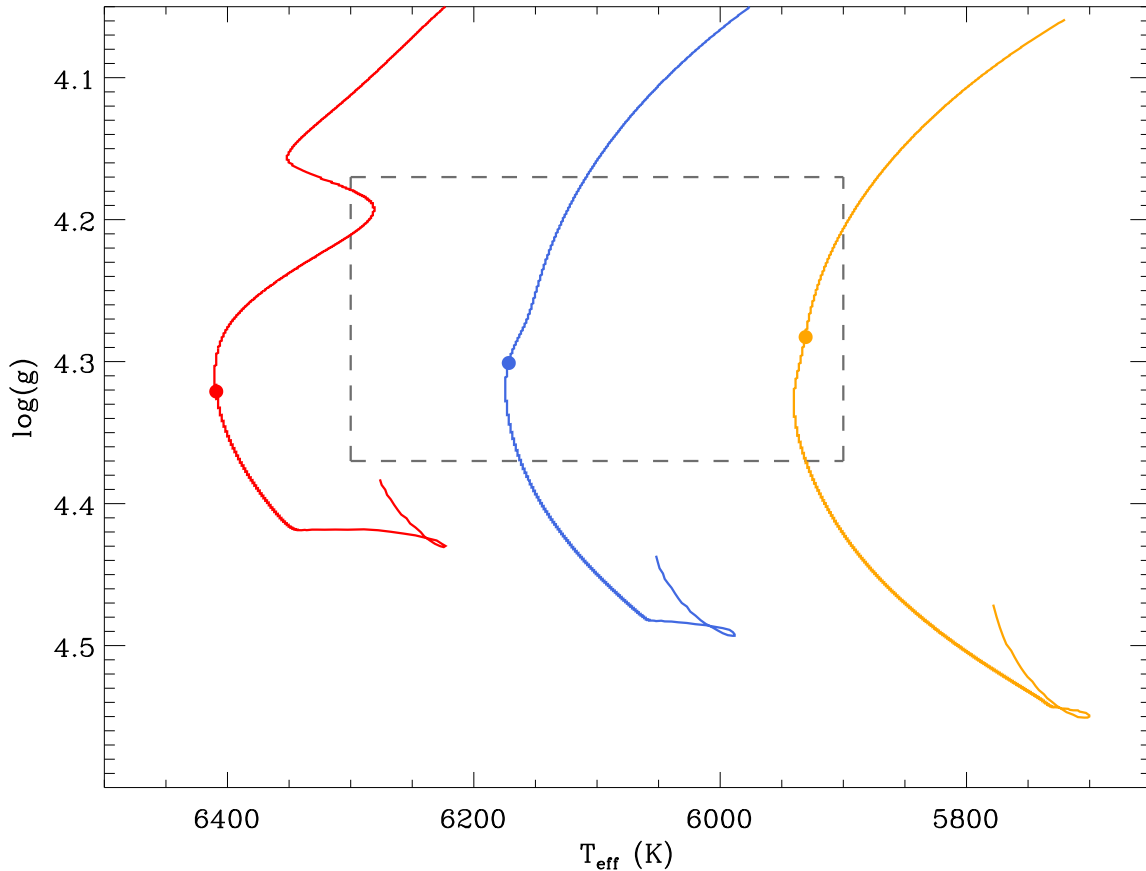


Figure 6.3: Evolutionary tracks computed at solar metallicity to match the observations of Perky. The filled circles represent the position of the model fitting the large frequency separation. The tracks are constructed for  $1.2 M_{\odot}$  (red),  $1.1 M_{\odot}$  (blue), and  $1.0 M_{\odot}$  (orange). Dashed line shows the observational error box. See text for details.

separation given in Table. 6.1 is marked with a filled circle on each track. The models were constructed at solar metallicity (Grevesse & Sauval 1998) with the same input physics as described in Sect. 5.3, using the Schwarzschild criterion for convective zones determination and no additional mixing beyond this boundary. In the figure the observational error box given as an input for the grid-based analysis is also depicted, and it can be seen that two of the possible best-fit models fall into the  $1\text{-}\sigma$  values of  $T_{\text{eff}}$  and  $\log g$ .

There are different ways of defining what exactly the best-fit model is for a particular target. It is common practice in asteroseismology to minimize the difference between the modeled frequencies and those observed, staying within the observational error box in the HRD. The problem with this approach is the well known issue of the surface effects, or the current inability of stellar models to correctly describe the outer layers of stars. This leads to a systematic offset of the modeled frequencies with respect to the real ones, which occurs even for the system that we

know to be best constrained: the standard solar model. In Fig. 6.4 we show an Echelle diagram comparing the solar frequencies observed by BiSON with those computed for the standard solar model by Serenelli et al. (2009). Although the agreement is quite good for frequencies below  $\sim 2500 \mu\text{Hz}$ , a large discrepancy between observed and calculated values appears as frequencies increase.

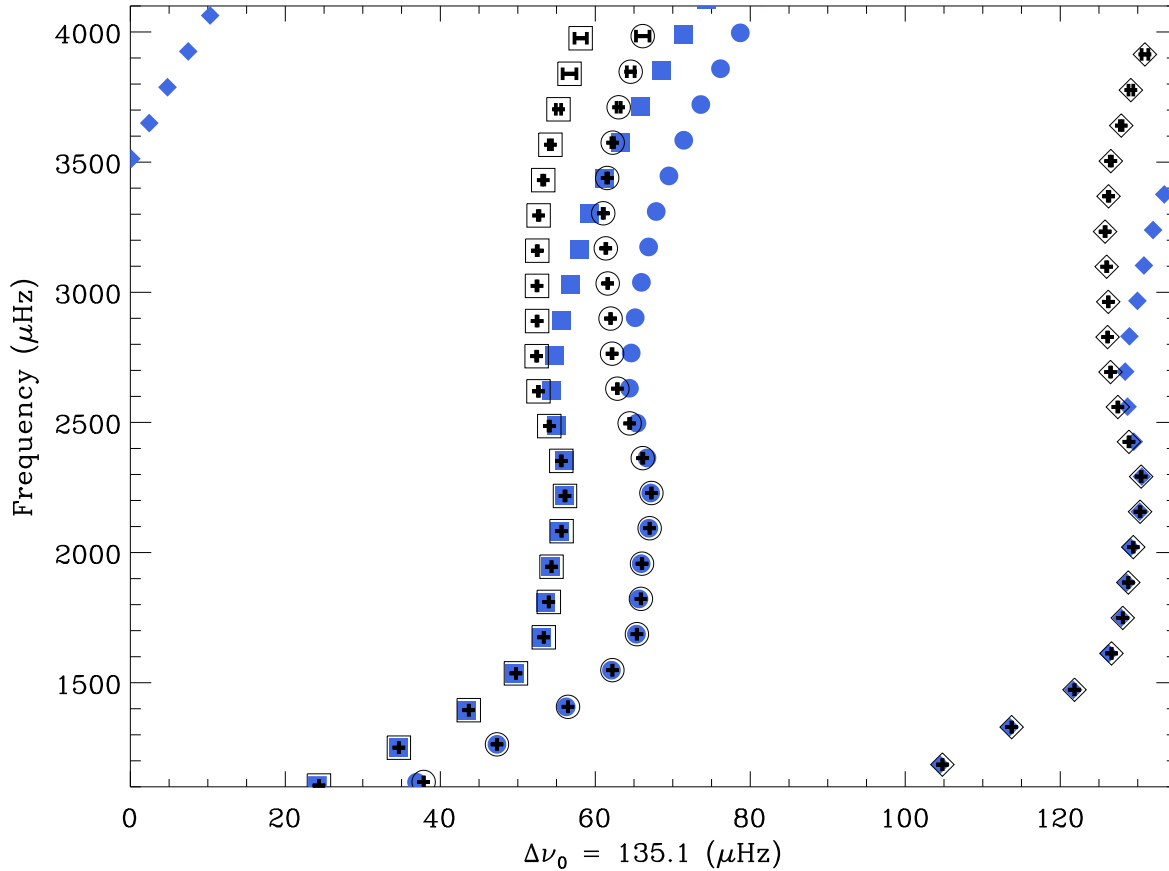


Figure 6.4: Echelle diagram for observed Sun. Solar frequencies obtained with the Birmingham Solar-Oscillations Network (BiSON Chaplin et al. 2002) are plotted in black, while the frequencies calculated from the standard solar model of Serenelli et al. (2009) are shown in blue. Circles, diamonds, squares and triangles are used for modes of degree  $\ell = 0, 1, 2$  and  $3$ , respectively. BiSON data kindly provided by W. J. Chaplin, and the theoretical frequencies of the solar model were provided by A. Serenelli.

A technique that is widely adopted to deal with this issue is to apply an empirical surface correction to the frequencies. In a nutshell, the shape of the necessary correction to fit the frequencies of the standard solar model to the solar data is used to match the observed frequencies of other stars (a power-law, see Kjeldsen et al. 2008). This procedure assumes that the overall behavior of the frequency differences are independent of the type of star, its effective tempera-

ture, gravity, metallicity, or evolutionary phase. We prefer not to use such an approach here, and instead we work with the original frequencies computed by the oscillations code.

Keeping this in mind, in Fig. 6.5 we show the Echelle diagram of the individual frequencies observed in Perky, and the three best-fit models marked in Fig. 6.3. They have been chosen to match the frequency value of the lowest  $\ell = 0$  mode within its  $1\text{-}\sigma$  uncertainty, as it is assumed that the surface effect shift is less important at low frequencies. Not surprisingly, from the figure

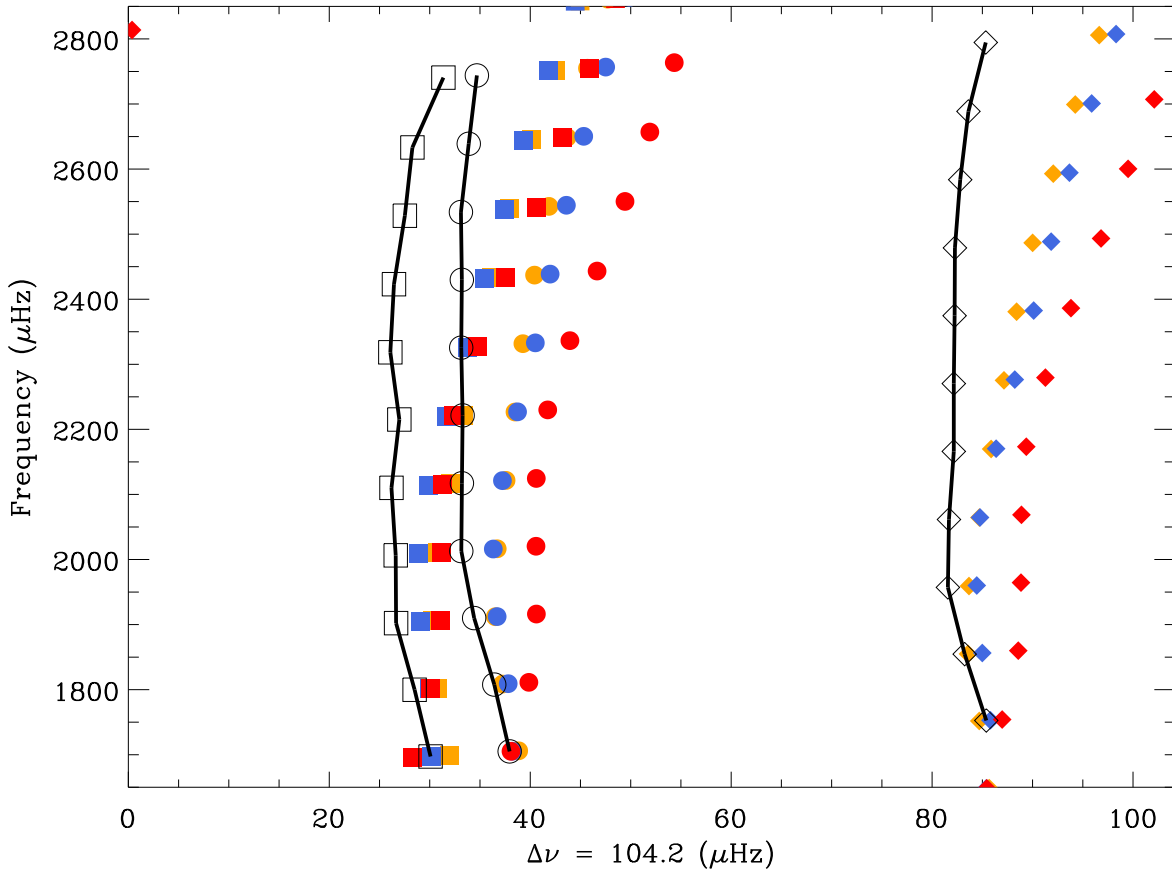


Figure 6.5: Echelle diagram of the models for Perky shown in Fig. 6.3. The symbols show the frequencies of  $\ell = 0$  (circles),  $\ell = 1$  (diamonds) and  $\ell = 2$  (squares). The data are shown in black connected with a solid line to guide the eye. Data plotted without error bars since they are smaller than the symbols. Colors represent the corresponding models of Fig. 6.3. See text for details.

it is clear that the computed frequencies deviate from those observed in the star as a function of frequency, and that the curvature and position of the ridges seem to favor the  $1.1 M_{\odot}$  or  $1.0 M_{\odot}$  models. However, for the reasons aforementioned, we refrain from making any inference about the quality of the fits using the Echelle diagram. We focus our attention in the frequency ratios  $r_{010}$ , which have been shown to cancel out almost completely the effects of the poorly model

outer layers (Roxburgh & Vorontsov 2003; Roxburgh 2005).

The three models considered are in different evolutionary stages, and only the more massive one has a convective core. By investigating the behavior of the frequency ratios given in Eq. 4.5, we intent first to discriminate between the masses of the models. Figure 6.6 shows the large frequency separation,  $\Delta\nu$ , and the frequency ratios,  $r_{010}$ , for the three models under consideration and the seismic data of Perky. As expected, there is a clear offset between the value of the large

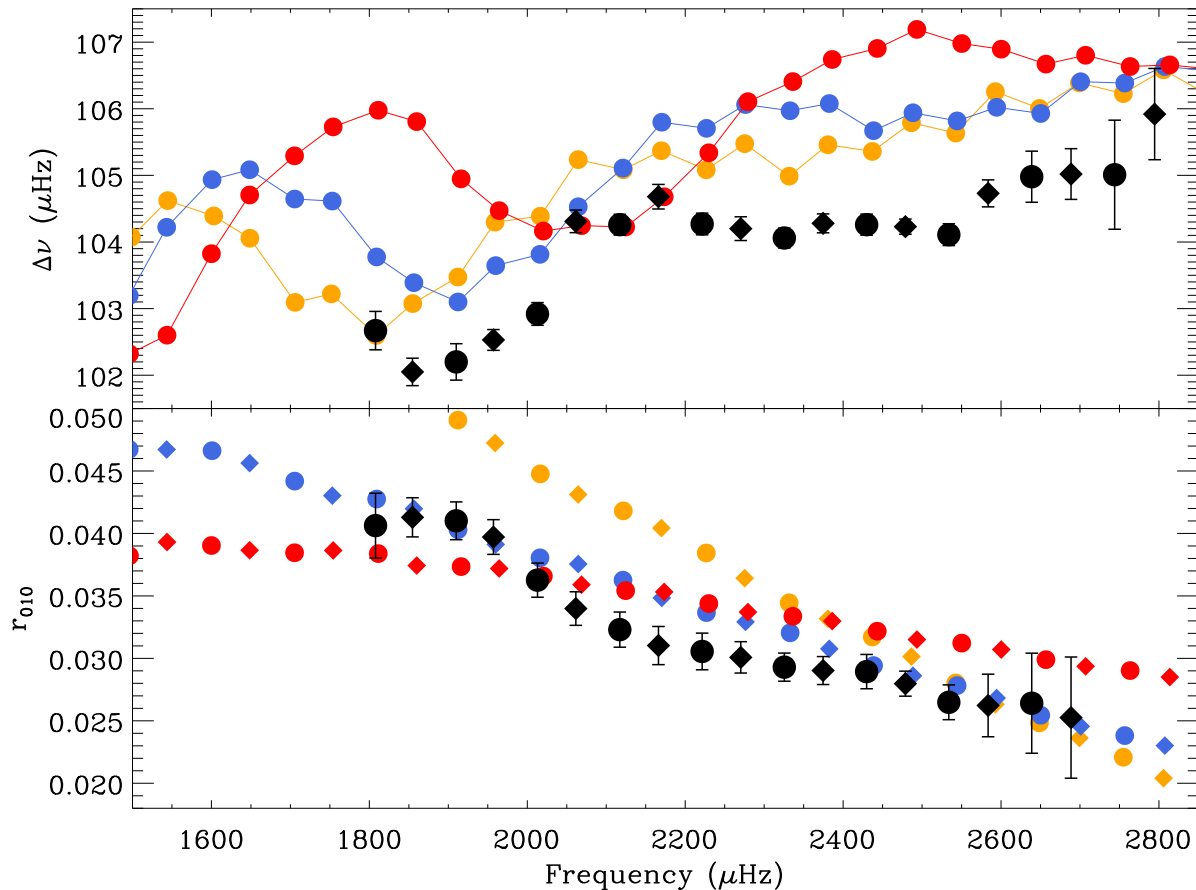


Figure 6.6: Frequency combinations for the three models of Perky at solar metallicity. Black symbols show the data obtained by the *Kepler* mission, plotted using circles (when centered in  $\ell = 0$ ) and diamonds (when centered in  $\ell = 1$ ). Colors as in Fig. 6.3. *Top panel*: large frequency separation for modes of degree  $\ell = 0, 1$ . *Bottom panel*: frequency ratios, plotted as a unique set called  $r_{010}$ . See text for details.

frequency separation calculated from the model and the observed one from the data. This is again due to the lack of realistic modeling of the outer layers of the star. However, the overall shape and the position in frequency of the minimum value of  $\Delta\nu$  suggest a better agreement with the  $1.1 M_{\odot}$  model. It is still left to be investigated what feature in the internal structure of the star defines the position in frequency were this minimum in  $\Delta\nu$  occurs.

More revealing than the large frequency separation are the ratios shown in the lower panel of Fig. 6.6. Both the position of the curves and the slopes shown by each of them strongly favor the model of  $1.1 M_{\odot}$  with respect to the other two cases. The frequency ratios show a clear sensitivity to the mass of the models which we only briefly mentioned in Sect. 5.4 (see Fig. 5.5), and is allowing us to discriminate between the models with the required precision of 10%.

There are other parameters that can affect the properties of stellar models and might lead us to confuse the effect of mass with other causes. In particular, the metallicity as determined from high-resolution spectroscopy suggest that the target is metal poor with respect to the Sun. We investigate this effect by constructing another evolutionary track for a  $1.1 M_{\odot}$  model at a metallicity of  $[\text{Fe}/\text{H}] = -0.1$ , scaled as always from the Grevesse & Sauval (1998) solar abundance ratios compilation. In Fig. 6.7 we show the evolutionary tracks for these cases, where we see that both solutions fall into the observational error box.

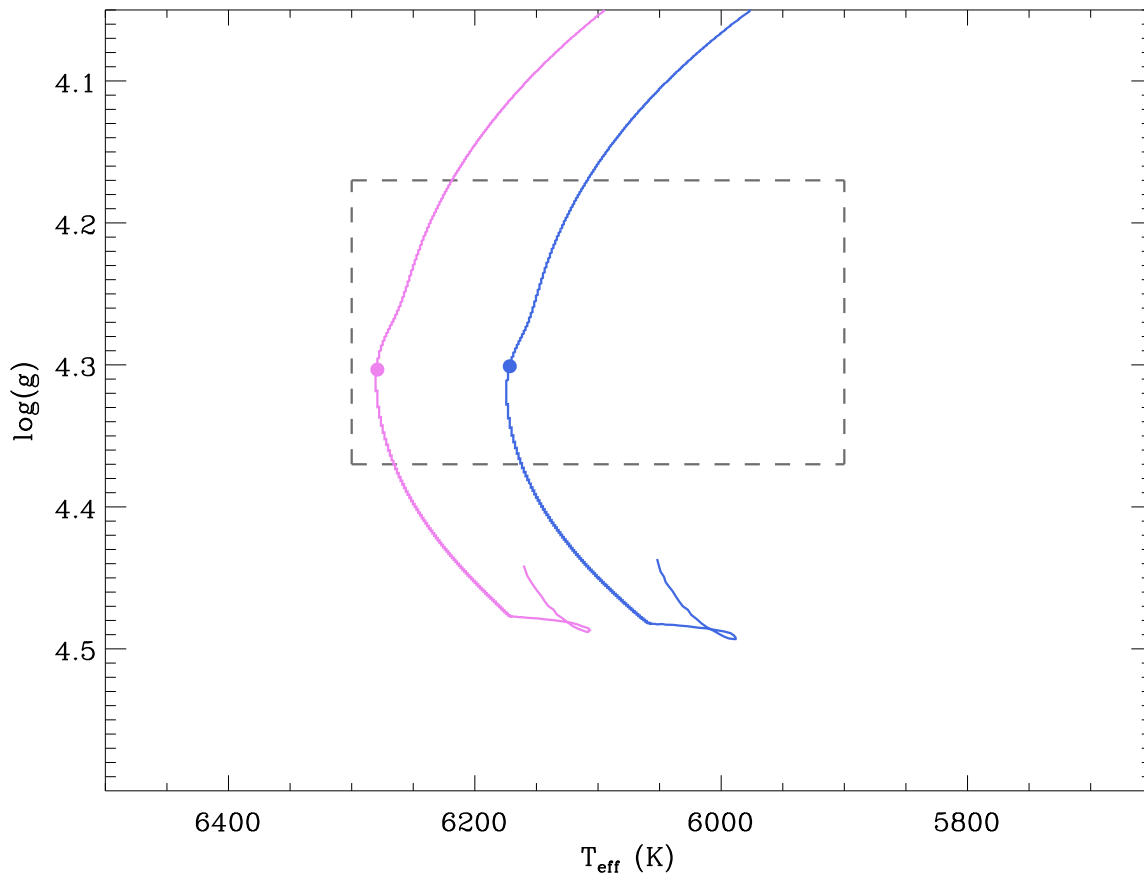


Figure 6.7: Evolutionary tracks of  $1.1 M_{\odot}$  stars constructed at solar (blue) and sub-solar (violet,  $[\text{Fe}/\text{H}] = -0.1$ ) metallicity. Best-fit model is marked with a circle, while the dashed line shows the observational error box. See text for details.

In Fig. 6.8 we show the frequency combinations for these models. The large frequency

separation and the frequency ratios show a very similar behavior for both models in the range of frequencies where data is available, which is almost insensitive to the metallicity. This is due to the fact that both stars have no convective core, and the central hydrogen contents are roughly similar ( $X_c \sim 0.130$  and  $X_c \sim 0.168$  for solar and sub-solar metallicity, respectively). In order to detect these differences, other frequency combinations such as the small frequency separations (cf., Eq. 4.1) could be used, although the current level of uncertainty in the determination of the  $\ell = 2$  modes is too high as to make a definitive statement (see Sect. 6.5 below for more details).

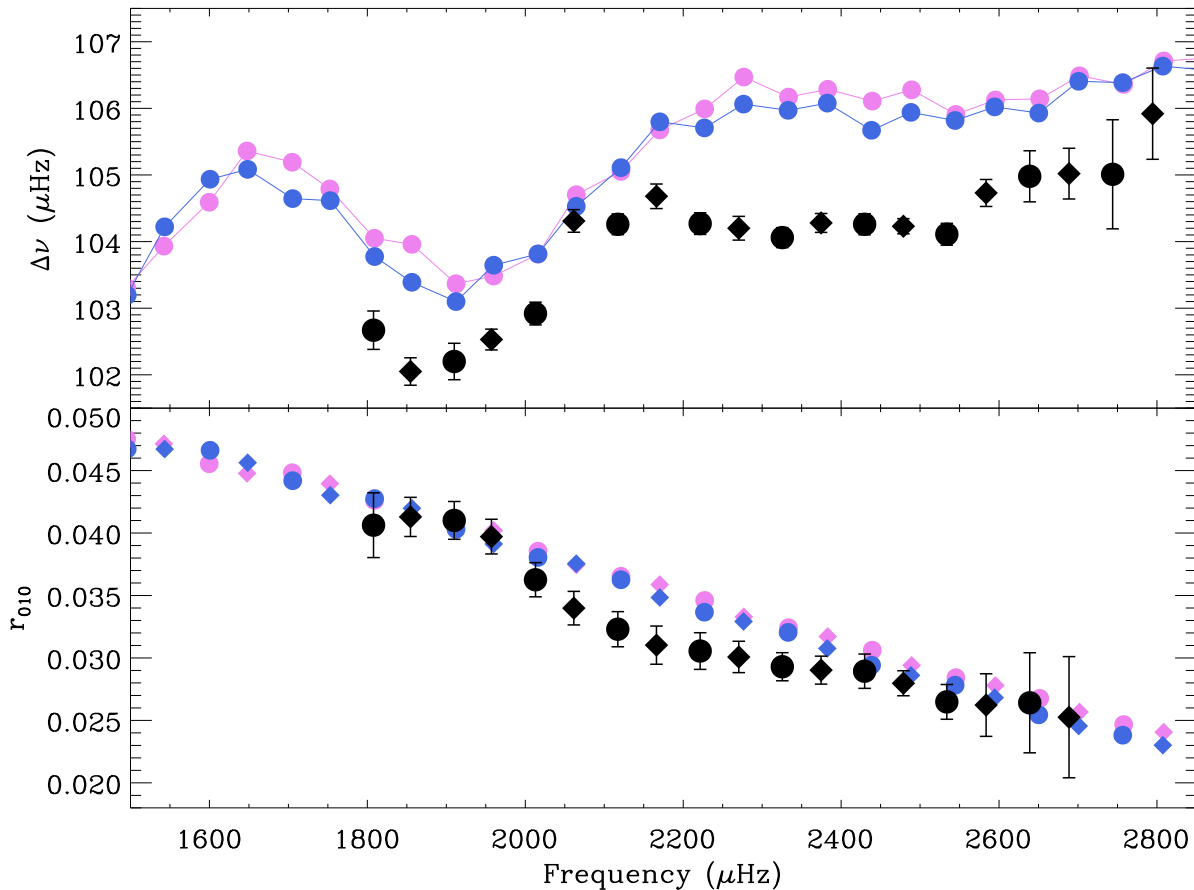


Figure 6.8: Frequency combinations for the two models of Perky constructed at different metallicities. Colors as in Fig. 6.7, and symbol convention as in Fig. 6.6.

Besides the fact that the frequency ratios are seemingly insensitive to the chemical composition, we have tested another important feature of these frequency combinations. It is clear that they are strongly dependent on the mass of the model, and this feature can help us constraining the models to a much better precision than that obtained from the grid-based analysis. It is interesting to notice that the mass we have derived is compatible with that estimated from the direct method (see Table 6.4). Some uncertainties still remain regarding the influence of other parameters such as metallicity or helium abundance, but we have established that a model with a

convective core cannot reproduce the frequency ratios as good as models with no core.

One can try to find a better match to the data by changing other input parameters in the stellar modeling to see the effect on the frequencies. However, an ‘oscillatory’ component is present in the frequency ratios which is not expected (and clearly not predicted) by the models (see curvature between frequencies  $\sim 2000$  and  $2400 \mu\text{Hz}$  in Figs. 6.6 and 6.8). It is not clear at this moment if such a feature is real or just an artifact introduced in the fitting procedure of individual frequencies due to very broad peaks of the oscillation power spectrum. It remains to be seen if this oscillatory component disappears once longer data sets of Perky are analyzed and the oscillation peaks in the power spectrum are better defined.

## 6.5 The frequency ratios: unveiling convective cores

In the previous section we showed the potential of the frequency ratios for establishing a very precise mass value and disentangling stars with and without convective cores. We move forward in our analysis and try to estimate the size of the homogeneously mixed central region when the data suggest one exists. The second target we analyzed (Dushera) has the added complexity of discrepant spectroscopic determinations from two sources in effective temperature, surface gravity, and metallicity (see Table 6.1). For these reasons, we start the modeling efforts using solar metallicity evolutionary tracks to determine, as done with Perky, an appropriate stellar mass using the frequency ratios. Initially we consider the Schwarzschild criterion for convection with no additional mixing beyond the convective boundaries.

In Fig. 6.9 we show the evolutionary tracks at solar metallicities for masses  $1.1 M_{\odot}$ ,  $1.2 M_{\odot}$ , and  $1.3 M_{\odot}$ , where the model best-fitting the Echelle diagram of Dushera is marked. The two observational error boxes from spectroscopic determinations are also depicted (see Table 6.1). As mentioned before, it is not surprising that the  $\log g$  value of the three models agree with the  $1\text{-}\sigma$  uncertainty of the VWA determinations, as they were tailored to reproduce this seismic feature. The  $1.1 M_{\odot}$  model does not have a convective core, while the two more massive cases do have one.

To discriminate between the masses, in Fig. 6.10 we show the large frequency separation for the data and the three models, as well as the frequency ratios. We will not consider frequencies above  $\sim 1900 \mu\text{Hz}$  for fitting the ratios, as the oscillatory component seen from that frequency value and above is likely due to difficulties in fitting the high-frequency data as peaks become broader. A similar behavior was observed at lower frequencies when 1-month data of Dushera was analyzed, and it disappeared once the 9-month long time-series were available. In a similar way, the first two points of the frequency ratios will not be considered to define a best fit, and are only shown for completeness.

The lowest mass model ( $1.1 M_{\odot}$ ) can be discarded as its mean value of  $r_{010}$  is not compatible with that shown by the data. Regarding the two more massive models, the ratios suggest by their mean level and slope that the  $1.2 M_{\odot}$  model reproduces the data better. Moreover, it can be seen in the top panel of Fig. 6.10 that the overall shape and the position of the minimum value of the large frequency separation are also compatible with the  $1.2 M_{\odot}$  case and not the more massive option.

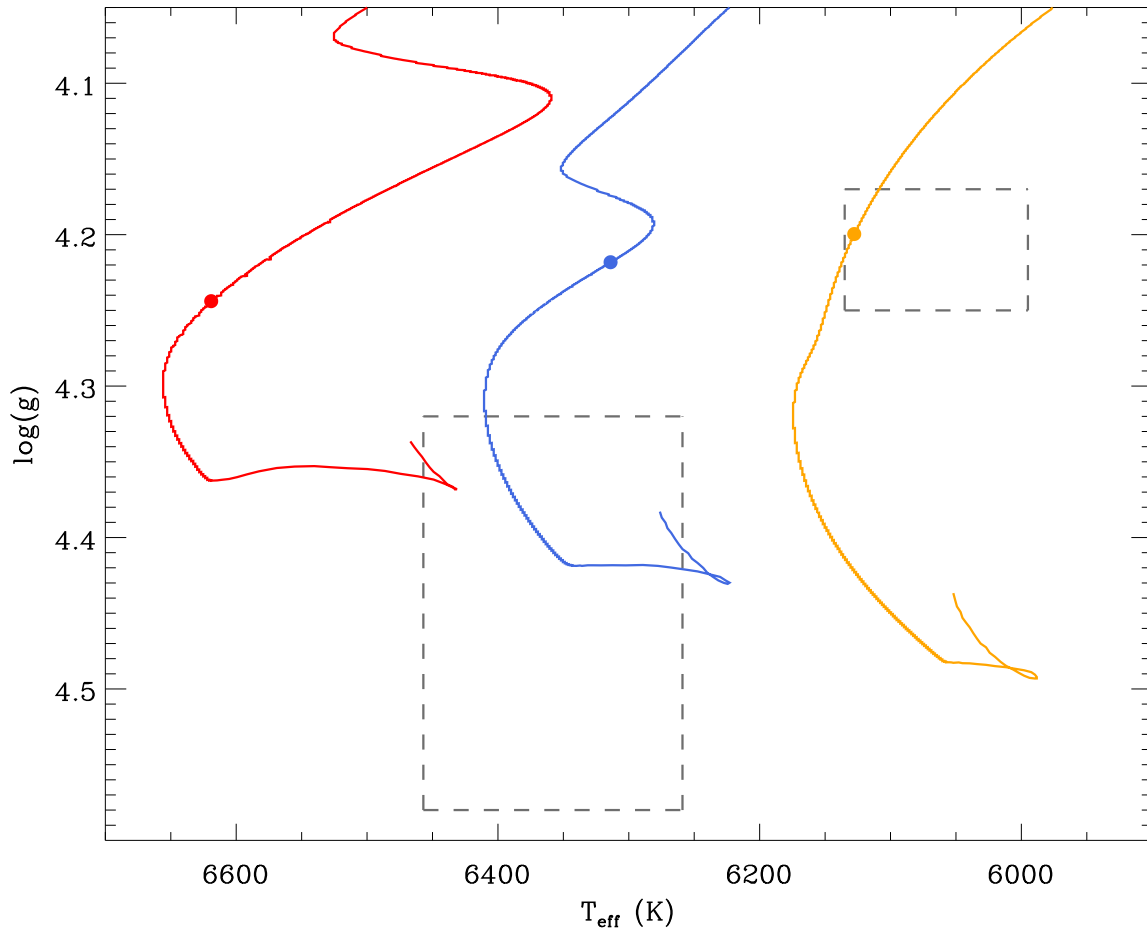


Figure 6.9: Evolutionary tracks computed at solar metallicity to match the observations of Dushera. The filled circles represent the position of the model fitting the large frequency separation. The tracks are constructed for  $1.3 M_{\odot}$  (red),  $1.2 M_{\odot}$  (blue), and  $1.1 M_{\odot}$  (orange). Dashed line shows the observational error box. See text for details.

An important point to keep in mind is that, although the  $1.2 M_{\odot}$  fits the data better, the frequency ratios do not completely overlap with the observed slope in the data for frequencies between  $\sim 1600$ - $1900 \mu\text{Hz}$ . In Chapter 4 we extensively discussed the physical reasons that could change the overall slope of the frequency ratios, most notably the existence and size of the convective core. Since the ratios favor a model with an already existent convective core, the possibilities to create a steeper slope are a more evolved star with a lower central hydrogen content, or a star harboring a larger convective core in its interior.

We proceed by carefully studying a mass range close to  $1.2 M_{\odot}$  in order to assess the uncertainties in our results due to stellar mass. Sets of evolutionary calculations were made at solar metallicities for  $1.18$  and  $1.22 M_{\odot}$ , including now overshooting until the ratios  $r_{010}$  for each case

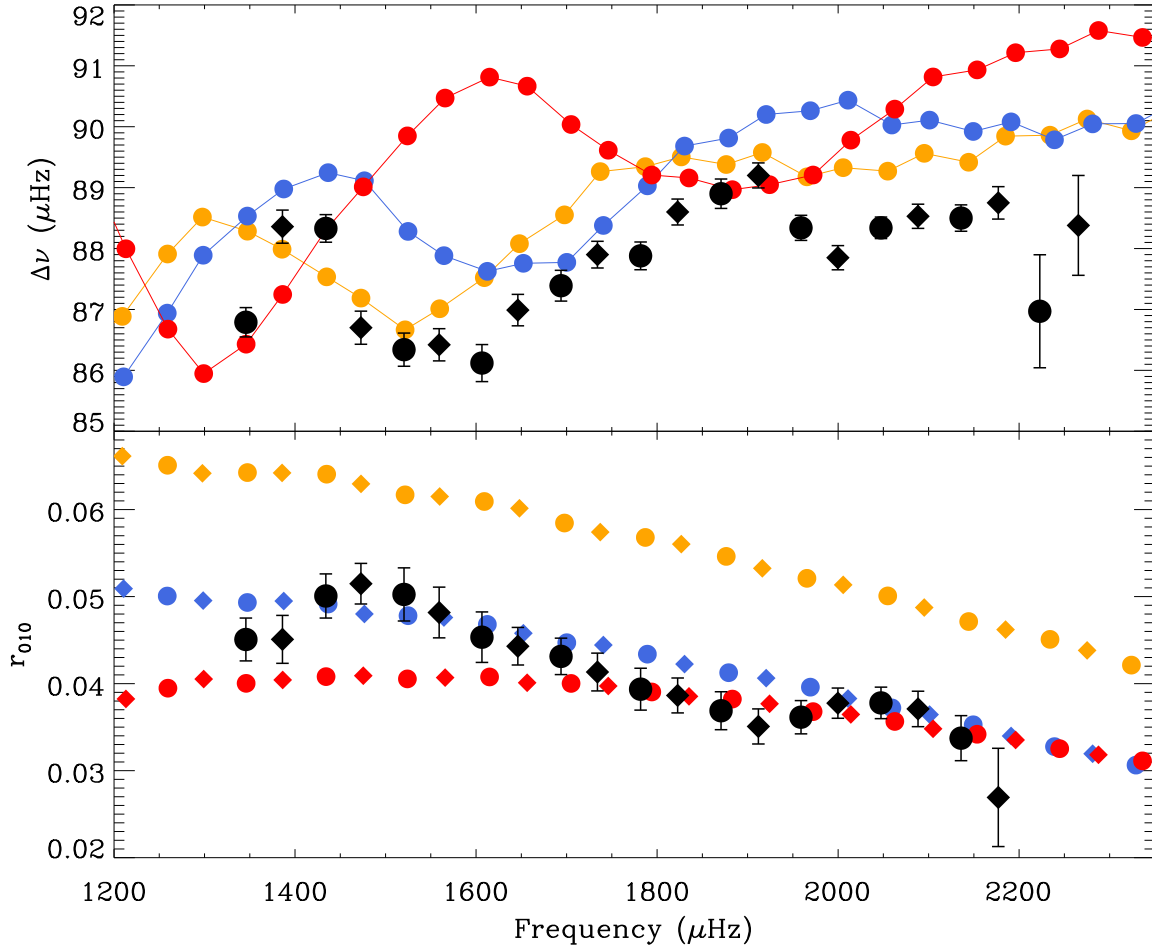


Figure 6.10: Frequency combinations for the three models of Dushera at solar metallicity. Symbols as in Fig. 6.6, while colors are the same as those used in Fig. 6.9. *Top panel*: large frequency separation for modes of degree  $\ell = 0, 1$ . *Bottom panel*: frequency ratios  $r_{010}$ .

closely reproduced the data. All the models fit the large frequency separation in the Echelle diagram as explained in Sect. 6.4 (see Fig. 6.5), and are plotted in Fig. 6.11. Their characteristics are given in Table 6.5.

In order to assess the deviations from the data and find the best fit models, we estimate the goodness of fit for the frequency ratios by calculating  $\chi^2$ :

$$\chi^2 = \frac{1}{N} \sum_n \left( \frac{r_{010}^{obs}(n) - r_{010}^{model}(n)}{\sigma(r_{010}^{obs}(n))} \right)^2, \quad (6.1)$$

where  $N$  is the total number of ratios fitted. We show in Fig. 6.11 only the data for the frequency ratios we are considering in the fit (the linear range, see Sect. 4.3).

Inspection of the figure reveals that, regardless of the mass considered, only models with

Table 6.5: Characteristics for the different models shown in Figs. 6.11 and 6.12. Columns give the mass in solar units, overshooting efficiency as implemented in GARSTEC (cf., Sect. 1.3.3), size of the convective core in mass coordinates, central hydrogen content, age, effective temperature, surface gravity, chemical composition, color in which the model is plotted in the figures, and the goodness of fit value. See text for details.

Mass	$\xi_{\text{ov}}$	$M_{\text{cc}}$	$X_{\text{c}}$	Age (Gyr)	$T_{\text{eff}}$ (K)	$\log g$	[Fe/H]	Color	$\chi^2$
1.18	0.0	0.0228	0.0818	4.034	6267	4.2147	0.0	Blue	8.675
	0.026	0.0560	0.2319	4.128	6234	4.2138	0.0	Red	0.255
	0.028	0.0608	0.2494	4.145	6227	4.2136	0.0	Green	1.063
	0.025	0.0563	0.1995	4.372	6112	4.2110	+0.1	Orange	0.150
	0.026	0.0582	0.2065	4.407	6109	4.2105	+0.1	Violet	0.808
	0.028	0.0587	0.2723	3.782	6354	4.2180	-0.1	Gray	0.388
	0.029	0.0672	0.2983	3.883	6340	4.2173	-0.1	Cyan	1.331
1.20	0.0	0.0314	0.1579	3.605	6315	4.2190	0.0	Blue	1.997
	0.024	0.0554	0.2638	3.674	6297	4.2185	0.0	Red	0.425
	0.026	0.0615	0.2803	3.692	6287	4.2181	0.0	Green	1.883
1.22	0.0	0.0342	0.2154	3.190	6376	4.2236	0.0	Blue	1.846
	0.022	0.0544	0.2946	3.252	6359	4.2230	0.0	Red	0.761
	0.024	0.0606	0.3110	3.284	6351	4.2225	0.0	Green	2.175

overshooting are able to consistently reproduce the frequency ratios within the  $1-\sigma$  error bars. In fact, the slope of the ratios can be best reproduced by models of  $1.18 M_{\odot}$  in the entire frequency range considered, giving a very strong constrain on the stellar mass that could have not been accomplished using fits of evolutionary tracks. The  $\chi^2$  of the models also point towards this conclusion, as it predicts the best fit models to be for cases with overshooting of  $1.18 M_{\odot}$  (see Table 6.5).

However, the issue of metallicity still remains unsolved. As the spectroscopic determinations give discrepant results, we explore the effects of chemical composition in models of  $1.18 M_{\odot}$ . We have performed the same type of analysis as before for evolutionary tracks computed at [Fe/H]= 0.1 and [Fe/H]= -0.1, finding the models best fitting the ratios and calculating their  $\chi^2$ . These frequency ratios are shown in Fig. 6.12, while their characteristics are also given in Table 6.5.

The models at [Fe/H]=0.1 and solar metallicity are able to reproduce within the  $1-\sigma$  uncertainties all the frequency ratios, while the low metallicity values show a slightly higher offset with respect to the data. Since they do not reproduce the highest value of the ratios within the errors, the models at [Fe/H]=-0.1 are not able to fit the slope properly, and this is reflected in a slightly higher value of the  $\chi^2$ . Nevertheless, one of the low-metallicity models has a comparatively low  $\chi^2$  as it fits very well the rest of the ratios (gray color model).

One way we could disentangle the mass values without directly using the  $\chi^2$  value is by using the seismic tool we developed in Sect. 4.5. Using the mean value and slope of the ratios  $r_{010}$  as defined in Eqs. 4.8 and 4.9, respectively, we can place the models in a diagram as that presented in Fig. 4.5 to assess the goodness of fit from each one to the data.

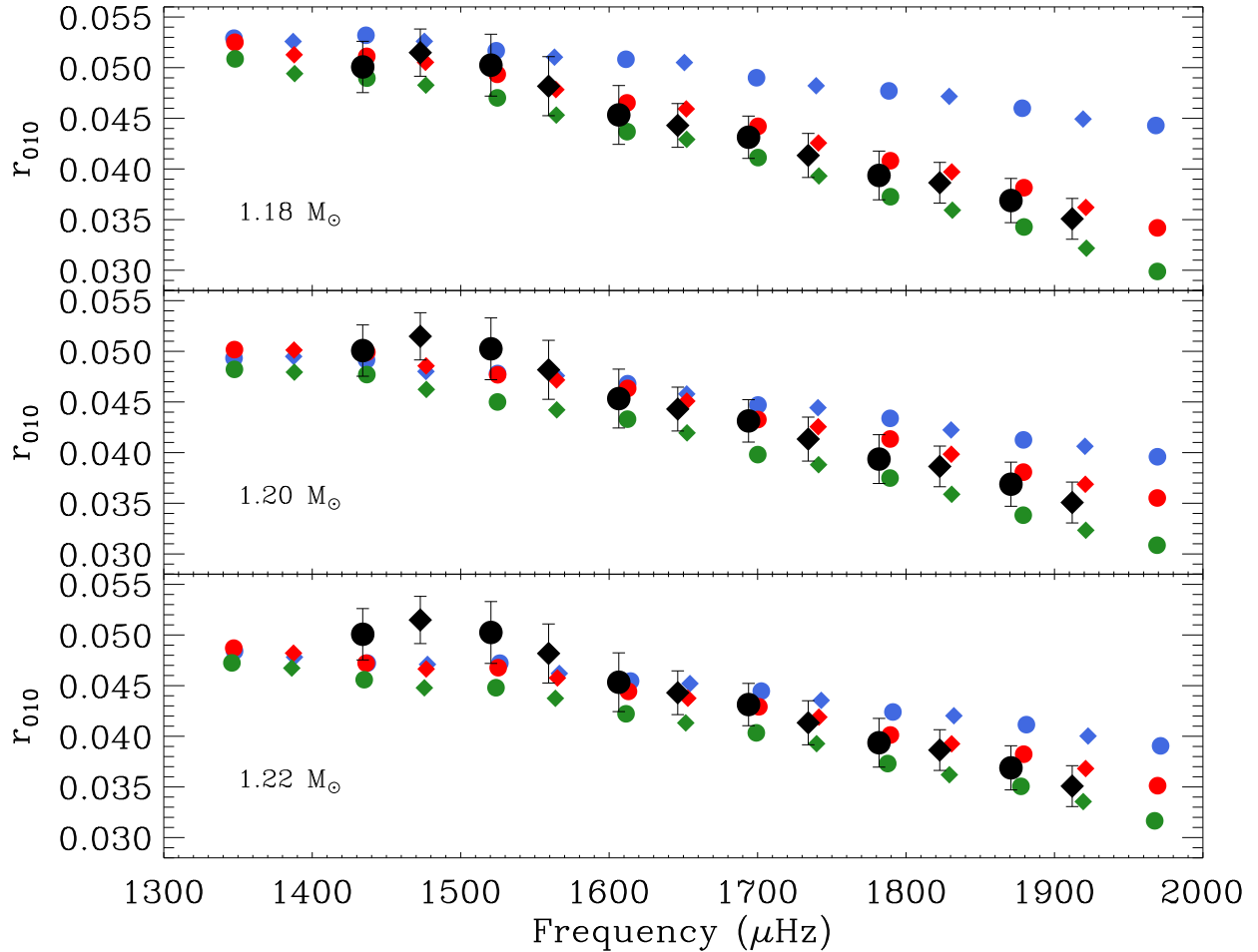


Figure 6.11: Frequency ratios for models of Dushera at solar metallicity, calculated with no overshooting (blue), and at two different overshooting values (red and green). Masses of the models are indicated in each panel. Symbols as in Fig. 6.6. Characteristics of the models (including the overshooting efficiencies) are given in Table 6.5.

In Fig. 6.13 we show such a slope versus mean diagram for the frequency ratios  $r_{010}$  of Dushera, where we have estimated the  $1\text{-}\sigma$  errors by means of a linear fit including the uncertainties in the data. Using the solar data from BiSON for comparison (see Fig. 6.4), we can also construct the frequency ratios for the Sun in a range of radial orders around the frequency of maximum oscillation power ( $\nu_{\max}$ , see Sect 5.2) similar to that of Dushera. This is also marked in Fig. 6.13, where the  $1\text{-}\sigma$  area for the Sun is naturally narrower than the one for Dushera as the error bars are much smaller.

Using the formulation proposed by Kjeldsen et al. (2008), we have computed the necessary surface correction to be applied to the frequencies of the standard solar model from Serenelli et al. (2009) in order to reproduce the solar data (as explained in Sect. 6.4 above). For both

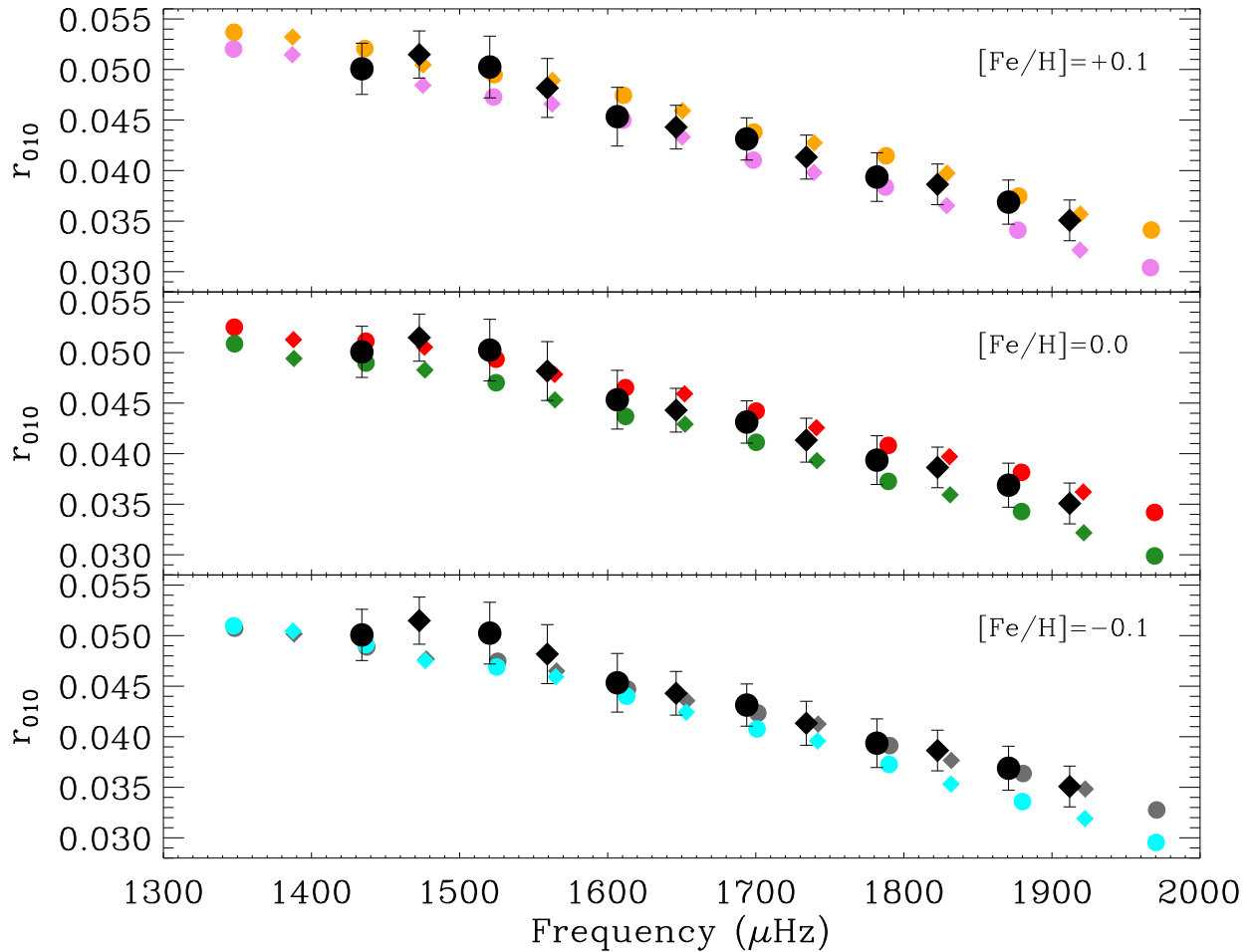


Figure 6.12: Frequency ratios for  $1.18 M_{\odot}$  models of Dushera at different metallicities, including overshooting with the efficiencies shown in Table 6.5. Panels show models for different values of  $[\text{Fe}/\text{H}]$ : +0.1 (top panel), 0.0 (middle panel), and -0.1 (bottom panel). Colors are those given in Table 6.5. Symbols as in Fig. 6.6. See text for details.

corrected and uncorrected sets of theoretical solar frequencies, we can calculate the mean and slope of the ratios  $r_{010}$  and compare them to the obtained values from the solar data. As it can be seen in Fig. 6.13, both sets of frequencies fit within the  $1\text{-}\sigma$  uncertainties the values observed in the Sun. This fact has important implications: it is a clear suggestion that we can use the tool  $r_{010}$  to find our best-fit models, regardless of the poor modeling we do of the outer layers of the star.

All the models we have computed to reproduce the ratios of Dushera have been depicted in Fig. 6.13, using their slopes and mean values in the frequency range where the fit has been performed (data shown in Figs. 6.11 and 6.12). We remind the reader that all these models have the same large frequency separation, as they have been chosen to fit the Echelle diagram of

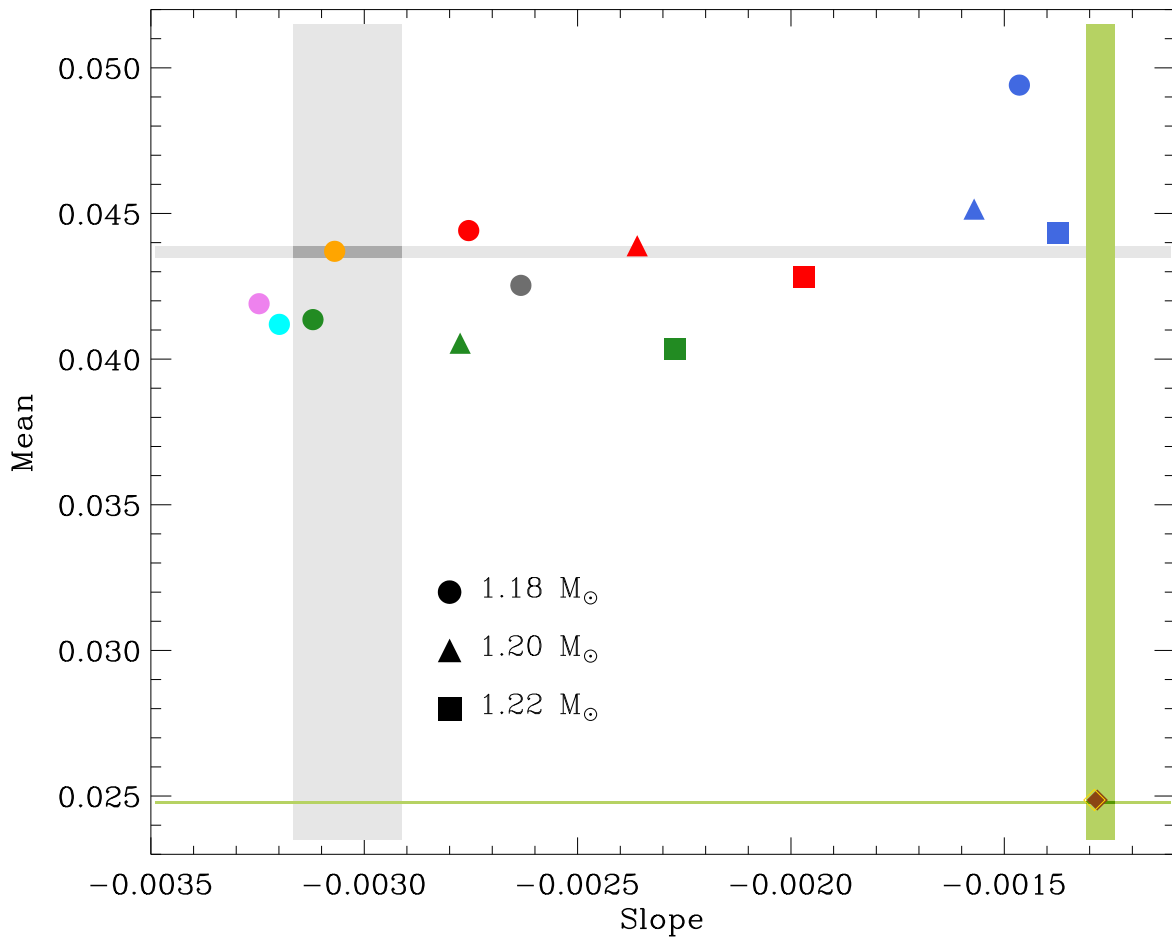


Figure 6.13: Slope versus mean diagram for the models and data of Dushera. The  $1\text{-}\sigma$  fit to the data of Dushera is depicted by the shaded gray zone, while a similar zone for the Solar data from BiSON is plotted for comparison in a green shaded area. Symbols show the result of the fit in each model to the frequency ratios, using the same colors as those given in Table 6.5. Fits to the solar model are shown for the fit to the uncorrected frequencies (filled brown diamond), and those corrected for surface effects (golden open diamond). See text for details.

Dushera. The first interesting feature to notice is that, for a given mass, the effect of overshooting (and thus of larger convective core and higher  $X_c$ ) is to increase the absolute slope and decrease the mean value. On the other hand, a change in mass of  $\pm 0.02 M_\odot$  has a larger effect than a change in metallicity of  $\pm 0.1 \text{dex}$ , probably due to the larger effect on the size of the convective core.

Figure 6.13 also shows that the  $1.18 M_\odot$  model of super-solar metallicity fits the mean value and slope of  $r_{010}$  within the  $1\text{-}\sigma$  uncertainties. Following the displacements in Fig. 6.13 caused by changes in mass and metallicity one can easily realize that, for instance, a model of  $1.17 M_\odot$  at

sub-solar metallicity should also fit the ratios. Preliminary calculations show that this is indeed the case: a model of  $1.17 M_{\odot}$  can also reproduce this feature with a convective core size of  $M_{cc} = 0.0589$ , a central hydrogen content of  $X_c = 0.2564$ , and an age of 4.010 Gyr. The amount of overshooting required for this case is  $\xi_{ov} = 0.030$ .

The remarkable feature of this analysis is that, regardless of the unknown metallicity, we are able to set very tight constrain on the mass of the star and the size of its convective core using the mean value and slope of  $r_{010}$ . However, one must keep in mind that these frequency ratios are calculated by a combination of five different frequencies. If one frequency in the data is ill-determined, it will affect the five frequency ratios where it is involved (to a larger or smaller degree depending on the numerical coefficient next to it, see Eqs.4.3 and 4.3). Thus, since the lowest frequencies used in the fit play a role in the determination of the highest ratio (and thus strongly impact the mean and slope obtained from the data), it could be that longer datasets change the results obtained. For the moment, we rather take a conservative approach and consider the three models with the lowest  $\chi^2$  values as the best ones, while also taking into account that the chemical composition allows a shift in mass of approximately  $\pm 0.01 M_{\odot}$ .

Considering all these uncertainties, the models that encompass best the observed frequency ratios suggest a star with a convective core comprising  $5.6\% \pm 0.3$  of its mass, an age of the order of  $4.1 \pm 0.4$  Gyr, and a central hydrogen content of  $X_c = 0.24 \pm 0.05$ . This is the first time a convective core can be identified and its size constrained to such a level of precision.

One interesting aspect of the results above is the large difference between the central hydrogen content of the models, which seems to have little impact in the frequency range where the ratios are available for Dushera. A different frequency combination that has long been known to be sensitive to the central hydrogen content is the small frequency separation ( $d_{l,l+2}(n)$ , see Eq. 4.1). In fact, they have been used to construct the so called C-D asteroseismic diagram of evolution (Christensen-Dalsgaard 1988). Although this frequency combination is affected by the poor modeling of the outer layers, it could be used to discriminate between the different central hydrogen contents, and therefore give insight into the chemical composition.

In Fig. 6.14 we show the small frequency separations for the  $1.18 M_{\odot}$  models shown in Fig 6.12. It can be seen in it that this quantity indeed separates the models into groups, ascending in metallicity from top to bottom. At each metallicity value, the two models shown have very similar central hydrogen content, reflecting the sensitivity of the separations to this parameter. Unfortunately, the current data does not allow to favor any of the models due to the large uncertainties still present in the  $\ell = 2$  modes. If longer time-series are able to determine these modes with better precision, a combination of the frequency ratios and the small frequency separations would be highly appropriate to further constrain the models and the physics involved in stellar interiors.

Another interesting point of our analysis is that, regardless of the metallicity, the amount of overshooting needed to reproduce the frequency ratios is larger than our calibrated value (see Sect 1.3.3). In every case, the size of the convective core needs to be over 60% larger than the size predicted by plain application of the Schwarzschild criterion. One must keep in mind, though, that we have used in our calculations the geometrical restriction to the overshooting efficiency described in Sect. 1.3.3. It is possible that the calibrated value is correct, but the geometrical cutoff factor is too restrictive. We have not investigated the possibility of producing models

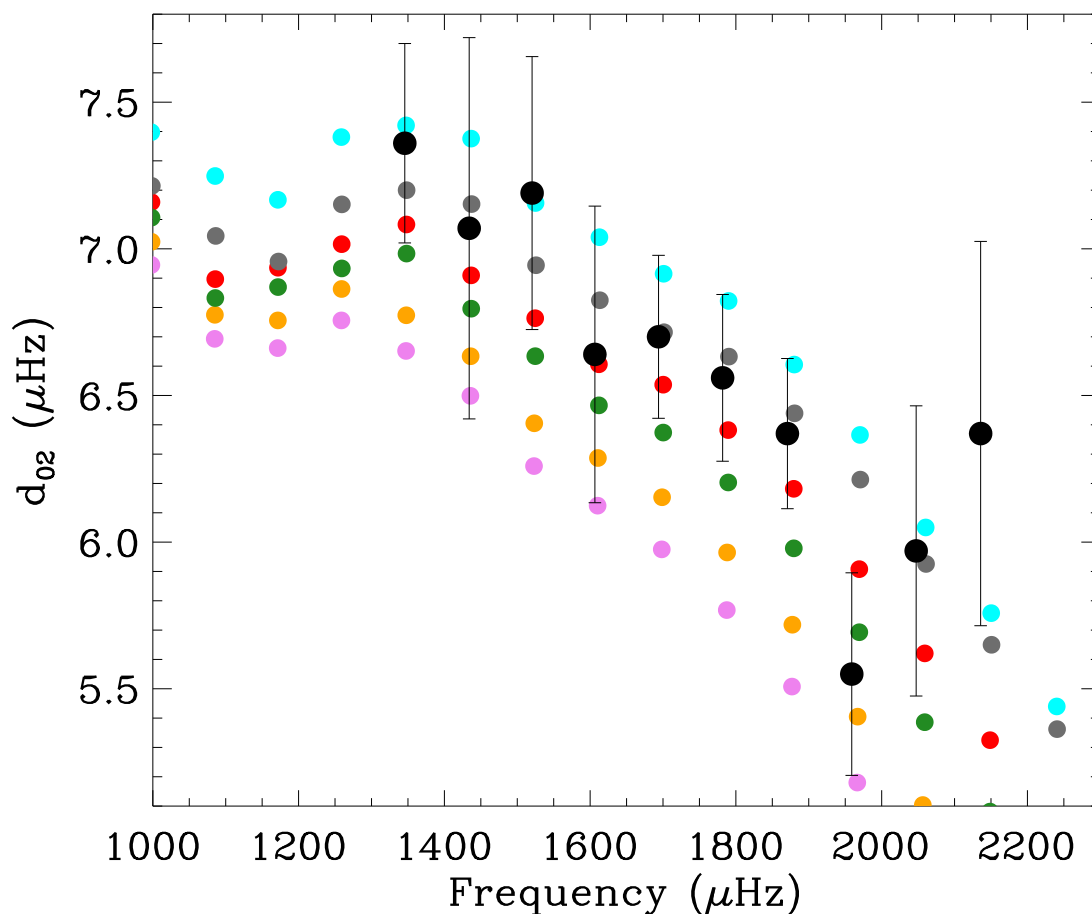


Figure 6.14: Small frequency separations for the models of Dushera shown in Fig. 6.12.

using the Ledoux criterion, as from Chapter 4 we know that such a steep slope is not possible to reproduce with this approach. Of course, overshooting can be included to enlarge the core and fit the ratios, but in that case there is no difference between the application of the Ledoux and Schwarzschild criterion (see Sect. 3.3.3).

Finally, it is worth mentioning that the mass we have determined from detailed modeling also agrees with that found using the direct method (Table 6.4).

## 6.6 Discussion and perspectives

The existence and extension of convective cores in low- and intermediate-mass main-sequence stars have been subject many studies throughout the years in the field of stellar astrophysics. Although theoretical predictions of their appearance in stellar models are clearly understood, the classical observations allowing to probe them are indirect and heavily dependent in many

different (and not well constrained) physical processes (e.g., Pietrinferni et al. 2004; Vandenberg et al. 2006). Asteroseismology has the unique capability of bridging the gap between theory and observations by giving direct probes of stellar interiors. Observations from the *Kepler* satellite spanning several months are now available, and we have access to sets of individual frequencies spanning several radial orders at an exquisite level of precision. We have analyzed such sets for two main-sequence targets, putting firm constraints in their fundamental parameters.

The star Perky has been found to have frequencies compatible with a low-mass main-sequence star with no convective core in its interior. Although a thorough analysis of this targets has not yet been possible due to some unexpected behavior in the frequencies, its data has served to find a very good determination of stellar mass. We have shown that, even within the uncertainties in the frequencies and the input physics of the models, the frequency ratios are able to constrain the total mass to  $\sim 1.1 M_{\odot}$  with an uncertainty smaller than  $\sim 10\%$ . This result is extremely encouraging, in particular considering the somewhat scattered mass determinations coming from the grid-based analysis.

A similar analysis was made for the second target Dushera, where the frequency ratios revealed a stellar mass close to  $1.2 M_{\odot}$  and the presence of a convective core. Exploring masses around that value, we found the best fits for models of  $1.18 \pm 0.01 M_{\odot}$ , the only mass values able to effectively reproduce the ratios in the whole frequency range. As the available spectroscopic determinations of chemical composition gave discrepant results, we modeled the star considering two more values of  $[\text{Fe}/\text{H}]$  for comparison. Regardless of the metallicity, the goodness of fit from the best models found allowed us to constrain the size of the convective core to be within  $\sim 5.3 \pm 0.3\%$  of the total stellar mass, reaching an unprecedented level of precision. The age and central hydrogen contents show larger discrepancies due to the unknown chemical composition, but they remain well constrained within  $\sim 20\%$ .

Of particular interest is to compare our results with the "classical" methods to calibrate overshooting and determine the existence of convective cores. One method that has been widely used to restrict the amount of overshooting in stars is to use binary stars with accurately determined mass and radius, such as the case of the eclipsing binary AI Phe (e.g. Pietrinferni et al. 2004). Masses and radii for the two components were very precisely determined by Milone et al. (1992), and were found to be  $1.190 \pm 0.006 M_{\odot}$  and  $1.231 \pm 0.005 M_{\odot}$ , and  $1.762 \pm 0.007 R_{\odot}$  and  $2.931 \pm 0.007 R_{\odot}$ . The mass of both components is very close to that we determined for Dushera, although the stars are in a slightly more evolved evolutionary phase than our target. Nevertheless, Pietrinferni et al. (2004) found that the mass and radius of both components could only be simultaneously fitted at a given age using BaSTI isochrones with no overshooting during the main sequence. This is in contrast with our findings that a considerable amount of overshooting is needed to reproduce the seismic data, and surely deserve further investigation.

Given that for these binaries the investigation done by Pietrinferni et al. (2004) used a different evolutionary code, it is much more instructive to compare our results with calibrations of clusters made with GARSTEC. For the particular case of M67, Magic et al. (2010) constructed several sets of isochrones aimed at reproducing the hook-like feature at the main-sequence turn-off for different combinations of solar abundances and input physics. Using as we do the Grevesse & Sauval (1998) compilation for the solar composition, they showed that two prescriptions for overshooting were capable of fitting the data of M67: one with overshooting as we have applied

it (described in Sect. 1.3.3), and another one where a mass-dependent ramp function for the overshooting efficiency was used. The latter case does not take into account the geometric restriction for overshooting in small convective cores.

Since an isochrone is constructed by means of interpolations over several stellar tracks at a given age, the closest evolutionary sequence we have to our mass results for Dushera is of  $1.2 M_{\odot}$  in both prescriptions (Z. Magic, private communication). We compare in Table 6.6 these tracks to our model of  $1.2 M_{\odot}$  that best fits the data from Dushera (red model for that mass value in Table 6.5).

Table 6.6: Comparison of a model fitting the frequency ratios of Dushera to models computed to match the CMD of M67. Columns show the model identification, overshoot efficiency, application of the geometrical cut factor, maximum convective core size during the evolution, and the age at the turn-off. See text for details.

Model	$\xi_{\text{ov}}$	Geo. cut	Max $M_{\text{cc}}$	T-O Age (Gyr)
Dushera	0.024	Yes	0.0590	4.990
M67 normal	0.018	Yes	0.0448	4.650
M67 ramp	0.00645	No	0.0503	4.806

M67 is the prototype cluster of solar metallicity; as we do not have reliable metallicities for Dushera, we do not consider in this case possible differences in the chemical composition. The overshooting efficiency in the case of the ramp function is much smaller than the calibrated one, showing the effect the geometrical cut off factor has in convective core sizes for this mass range. It is interesting to notice that, for both prescriptions of the calibrated values of overshooting, the maximum size of the convective core reached during the main sequence is smaller than the one we have obtained for Dushera. Although the  $1.2 M_{\odot}$  case is not exactly the mass of the best-fit model we found in the previous section, we showed that the size of the core is the most important parameter to reproduce effectively the ratios  $r_{010}$ , regardless of the mass. In fact, slightly smaller masses will have smaller convective cores when the calibrated efficiency values for M67 are used, in contrast to the equally large convective core size we found for models of  $1.18 M_{\odot}$ . Most importantly, as also shown in the previous section, for the metallicities studied the ratios  $r_{010}$  can always be fitted as long as a model with the appropriate size of the convective core can be produced. Asteroseismic data is clearly challenging the classical approaches to the topic of convective core sizes and overshooting.

We proposed the use of other frequency combination sensitive to the central hydrogen content, the small frequency separation, as possible diagnosis to help disentangling the chemical composition of the stars. Although this quantity is clearly different for the best-fit models found, the current uncertainties in the  $\ell = 2$  modes do not allow a firm preference for one set of models or another. We expect this to change as longer datasets are acquired. However, we caution that since the small separations are more affected by the outer layers, they are subject to the influence of the surface effects. It is not clear at this point how much impact this has on the small separations, but this issue surely deserves further attention.

The analysis presented in this Chapter constitutes the preliminary results of the investigation

carried out for these targets. We have based our conclusions on the outcome of one particular evolutionary code, thus we expect the scatter in the results to be larger when other codes are also included. Although the mass determinations and convective core sizes appear to be consistent among the different models received from other modelers (A. M. Serenelli, T. Metcalfe, S. Basu, J. Montalbán, and Y. Lebreton, private communication), there are differences in ages larger than those encountered here for one particular code. Still, further improvement of the models by minimizing the difference to the frequency ratios promises to reveal ages constrained to a level better than  $\sim 20\%$ .



# Chapter 7

## Conclusions and future outlook

The field of stellar structure and evolution has entered an era of accelerated development thanks to the advances of helio- and asteroseismology. Observations of stellar pulsations in the Sun and other stars have opened new doors for understanding physical processes and the condition of stellar matter in stars' interiors. There has been a huge leap in the amount of available data since the launch of the space missions *CoRoT* and *Kepler*, filling the gap between theoretical predictions and observations of stars.

In order to take full advantage of the observational results gathered by asteroseismic investigations, data mining must be accompanied by suitable theoretical developments capable of testing state-of-the-art models and compare their outcome with the observations. The work presented in this dissertation has aimed to provide a bridge between models of stellar evolution and observations of stellar pulsations, allowing us to constrain and learn about the physical process taking place in the deep interiors of stars.

### 7.1 Mixing, convective cores, and main-sequence evolution

Convective mixing in stellar interiors is a matter of great importance in theory of stellar evolution, where significant uncertainties still remain. We have explained in Sect. 1.3.1 the main ingredients of the theory of convective energy transport, highlighting the assumptions and parameterizations used in its description. Among the key issues is that of defining the exact boundary of convective regions, and determining if mixing of chemical elements beyond that boundary exists (convective overshooting).

Two criteria are commonly adopted in calculations of stellar evolution to define the boundary of convective regions. While the Schwarzschild criterion only compares the temperature gradients when energy is being transported adiabatically or entirely by radiation, the Ledoux criterion takes into account the existence of molecular weight gradients in stellar interiors. This difference becomes important in stars where a homogeneously mixed central core exists, which produces a discontinuity in the chemical composition at its boundary and may allow the appearance of a zone which, depending on the criterion used, should transport energy by means of radiation or convection. This situation, well known in massive stars, is referred to as semiconvection.

Keeping this in mind, in Chapter 3 we investigated the conditions in interiors of intermediate-mass stars for a semiconvective region to develop. By including the Ledoux criterion in our evolutionary code, we studied the impact during the main-sequence evolution of using different criteria for defining convective boundary, and considering overshooting beyond them. Our findings suggest that, when the Ledoux criterion is applied, a semiconvective region can develop at the top of the convective core in stars of masses  $\sim 1.2\text{--}1.7 M_{\odot}$ . Mixing inside of this zone can occur, at a speed that is parametrized by an efficiency coefficient. If the mixing within the semiconvective region is large, the zone disappears and becomes part of the convective core, recovering the condition given by the Schwarzschild criterion. Overshooting beyond the convective boundaries is also capable of washing out the semiconvective regions, and we have seen that it is the case for our calibrated value of overshooting efficiency.

Application of the Ledoux criterion, with no mixing in semiconvective regions when these exists, produces models with convective cores limited in size due to the molecular weight barrier created outside the fully-mixed convective core. In the opposite case, the largest convective cores are produced when overshooting is included. The differences in the HRD between these two cases for a given mass and metallicity are negligible, and certainly not distinguishable by common observation techniques such as stellar parameters determination from spectroscopy. However, the differences in age can be up to  $\sim 40\%$  for models of  $1.2 M_{\odot}$  at solar metallicity at the end of the main-sequence phase (cf., Fig. 3.7); this age difference is equivalent to a difference in central hydrogen content, which is measurable using asteroseismic diagnostics.

The appearance of a ‘hook-like’ feature in the HRD at the end of the main sequence can be suppressed when the Ledoux criterion is applied (see Fig. 3.6). This hook feature is used to estimate ages in simple stellar populations by means of isochrone fitting, thus large uncertainties remain due to the unknown size of convective cores. If we aim at decreasing the age uncertainties in stellar populations, and learn something about the physics processes dominating in stellar interiors, tighter constraints in convective core existence and size must be set.

## 7.2 Probing convective cores with stellar pulsations

We have extensively discussed the theoretical background of stellar oscillations in Chapter 1, emphasizing the dependence of the pulsation modes in the internal structure of stars. By recognizing that the frequencies of oscillations probe different parts of the star according to their propagation cavities, it seems natural to consider the possibility of combining some frequencies to test the conditions in certain regions of the star.

Since the application of the different mixing prescriptions in Chapter 3 effectively leads to different sizes of convective cores, we investigated in Chapter 4 the sensitivity of the frequency ratios proposed by Roxburgh & Vorontsov (2003) to the conditions in the stellar center. We have determined that in the high frequency regime (the linear range), the frequency ratios are sensitive to gradients in the adiabatic sound speed. As the presence of a convective core produces a discontinuity at its edge in the chemical composition, the ratios are strongly affected by this sharp feature and allow us to discriminate between a star harboring a convective core from one with a radiative central region.

In order to characterize the influence of convective cores in the frequency ratios, we have studied the impact of different mixing prescriptions in the absolute slope of the ratios in the linear range. Our findings indicate that the slope is mostly affected by the position of the sound speed discontinuity (the size of the core), but also by the size of the jump created by the edge of the core (related to the central hydrogen content). For a given stellar mass, the slope and mean value of the linear range would allow us to estimate the size of the homogeneously mixed central region and constrain the evolutionary stage of the star.

However, we assumed in this study that the stellar mass could be estimated with a precision better than  $\sim 10\%$  from stellar parameters and asteroseismic observations. The validity of that assumption could only be tested once enough targets with oscillations were detected.

### 7.3 From dreams to data: stellar cores as seen by *Kepler*

During the survey phase, the *Kepler* mission has detected over 500 stars oscillating in the main-sequence phase. These observations have allowed the determination of the two global asteroseismic parameters, namely the large frequency separation (see Fig. 2.4) and the frequency of maximum oscillation power (see Fig. 5.1). In Chapter 5 we showed how these two quantities, combined with an estimation of the effective temperature, can be used in scaling relations from the solar values to determine the mass and radius of a star.

Using the ensemble of stars from *Kepler* observations, together with effective temperatures determined via the IRFM, we were able for the first time to construct an evolutionary sequence of field stars of similar masses using asteroseismic scaling relations. This opens the exciting possibility of performing differential analysis on stars with similar masses but in different evolutionary stages, and follow for instance the evolution of a convective core along the main sequence. Since the stars in the sequence we identified in Chapter 5 do not yet have individual frequency determinations, in Sects. 4.3 and 5.4 we theoretically studied the behavior during the main sequence of the frequency ratios for compatible masses. We have shown that using the slope and mean value of the ratios  $r_{010}$  in the linear range, we are able to discriminate between the presence or absence of a convective core in stars of masses close to solar.

We have tested our determinations of stellar masses and  $\log g$  values with spectroscopic observations available for four targets. Our results are in excellent agreement with evolutionary tracks constructed at the metallicities from spectroscopy, as well as our  $\log g$  values. These encouraging results suggest that the technique is indeed capable of determining stellar masses with the appropriate precision needed for convective core studies.

Longer time-series from *Kepler* observations have also provided enough individual frequencies to construct the frequency ratios and study convective cores. We have done in Chapter 6 detailed modeling using GARSTEC of two of these targets, coupled with an adiabatic oscillations code to determine the theoretical modes of oscillations. For the first star we modeled (Perky), we found that the frequency ratios favored a model without a convective core. Moreover, we showed that the ratios are extremely sensitive to the stellar mass and allowed us to extract it with a high level of precision. The exact evolutionary stage of the star could not be determined due to a strange unexpected feature in the ratios that could be due to some ill-determined frequency

value. Longer time-series that will be analyzed in the near future should provide the answer to this issue, although if the feature remains its nature remains to be explained as it is not predicted by any of the theoretical models.

The method used for Perky was applied to the second target, Dushera. For this case, the sensitivity of frequency ratios to the stellar mass allowed us to pin-point its value to  $1.18 \pm 0.01 M_{\odot}$ , regardless of the fact that two spectroscopic determinations give discrepant metallicity values. Further exploring models for this mass showed that, even without exact information of the stellar metallicity, the frequency ratios constrain the size of the convective core to be  $\sim 5.6\%$  of the stellar mass. This value is larger than the one obtained from calibrations of clusters such as the case of M67, and poses important challenges the application of convective boundary definitions and overshooting efficiencies.

Although the central hydrogen content and the age of the star can not be constrained so tightly due to the lack of a reliable chemical composition, we propose a complementary analysis using the small frequency separations to determine more precisely the evolutionary stage of the star. The current seismic data does not allow to use this quantity yet due to the large uncertainties in the  $\ell = 2$  modes. We expect this situation to be circumvented as longer time-series are acquired.

## 7.4 From individual stars to stellar populations and galaxies: the future of asteroseismology

Considering the importance of constraining convective cores existence and size described in Chapter 3; applying the asteroseismic techniques developed in Chapter 4 to probe the deep stellar interior; and using the huge amount of available seismic data from space missions to precisely determine stellar masses; we have disentangled a star without a convective core and constrained the convective core size of another one to be  $\sim 5.6\%$  of its mass, while the uncertainty in its age and central hydrogen content has been constrained to  $\sim 20\%$ . Although the results are still code dependent, the level of precision reached is remarkable compared to classical techniques for determining stellar ages, where uncertainties of several gigayears are common. Most importantly, it is the first time that the size of a convective core is directly measured from observational data, and it has showed that for this particular target the amount of overshooting needed to reproduce the data is larger than the usually calibrated value.

Asteroseismology has the possibility of improving our understanding of stellar physics and galactic dynamics from at least two points of view, which we have developed extensively in this dissertation. First, measurement of internal characteristics from several targets will test our assumptions in stellar modeling, leading to better predictions of properties based on isochrone fitting. In particular, if we are able to measure convective core sizes for stars with different masses and metallicities, an accurate calibration of the overshooting efficiency can be made across the HRD and applied to our stellar evolution calculations. This results in less degrees of freedom for stellar modeling and more precise derived parameters, such as stellar ages.

The second interesting application comes from the capability of asteroseismology of characterizing stellar populations in a certain region of the sky. As we discussed in Chapter 5, seismic

observations coupled with effective temperatures estimates are capable of determining masses and radii to a very high level of precision for stars in different evolutionary phases. This opens the exciting possibility of deriving stellar ages to a precision that exceeds that possible by other techniques adopted in stellar population studies, e.g., isochrones or chromospheric activity dating. Combining these results with parameters obtained via the IRFM such as metallicities and angular diameters (and thus distances, by comparison with radii) could offer a complete picture of the stellar population in, for instance, the *Kepler* field.

It will be possible to study abundance gradients, the metallicity distribution function and the age-metallicity relation with an accuracy and a completeness that until now has been possible only for the Solar Neighborhood. The age-metallicity relation is possibly the most crucial constraint on Galactic models, yet it remains very uncertain. A very precise age-metallicity relation will also allow tighter constraints to be placed on the extent of stellar radial migration in the Galactic disc.

The possibilities are many, and the potential of asteroseismology to constrain theoretical models, unveil the underlying physical processes, and discover the dynamical history of our galaxy is finally being exploited.



# Appendix A

## Variable separation and spherical harmonics

Lets assume a scalar field  $\alpha$  and a vector field  $\boldsymbol{\beta}$ . In spherical coordinates, where the unit vectors are denoted by  $\mathbf{a}_r, \mathbf{a}_\theta, \mathbf{a}_\phi$ , the gradient of the scalar field is given by

$$\nabla\alpha = \frac{\partial\alpha}{\partial r}\mathbf{a}_r + \frac{1}{r}\frac{\partial\alpha}{\partial\theta}\mathbf{a}_\theta + \frac{1}{r\sin\theta}\frac{\partial\alpha}{\partial\phi}\mathbf{a}_\phi. \quad (\text{A.1})$$

The divergence of the vector field  $\boldsymbol{\beta} = \beta_r\mathbf{a}_r + \beta_\theta\mathbf{a}_\theta + \beta_\phi\mathbf{a}_\phi$  takes the following form:

$$\text{div}\boldsymbol{\beta} = \frac{1}{r^2}\frac{\partial}{\partial r}(r^2\beta_r) + \frac{1}{r\sin\theta}\frac{\partial}{\partial\theta}(\sin\theta\beta_\theta) + \frac{1}{r\sin\theta}\frac{\partial\beta_\phi}{\partial\phi}, \quad (\text{A.2})$$

while the Laplacian operator is written as:

$$\nabla^2\alpha = \text{div}(\nabla\alpha) \quad (\text{A.3})$$

$$= \frac{1}{r^2}\frac{\partial}{\partial r}\left(r^2\frac{\partial\alpha}{\partial r}\right) + \frac{1}{r^2\sin\theta}\frac{\partial}{\partial\theta}\left(\sin\theta\frac{\partial\alpha}{\partial\theta}\right) + \frac{1}{r^2\sin^2\theta}\frac{\partial^2\alpha}{\partial\phi^2}. \quad (\text{A.4})$$

For our particular case of interest, it is useful to define the horizontal (or tangential) components of the gradient, divergence and Laplacian as

$$\nabla_h\alpha = \frac{1}{r}\frac{\partial\alpha}{\partial\theta}\mathbf{a}_\theta + \frac{1}{r\sin\theta}\frac{\partial\alpha}{\partial\phi}\mathbf{a}_\phi, \quad (\text{A.5})$$

$$\nabla_h\cdot\boldsymbol{\beta} = \frac{1}{r\sin\theta}\frac{\partial}{\partial\theta}(\sin\theta\beta_\theta) + \frac{1}{r\sin\theta}\frac{\partial\beta_\phi}{\partial\phi}, \quad (\text{A.6})$$

$$\nabla_h^2\alpha = \frac{1}{r^2\sin\theta}\frac{\partial}{\partial\theta}\left(\sin\theta\frac{\partial\alpha}{\partial\theta}\right) + \frac{1}{r^2\sin^2\theta}\frac{\partial^2\alpha}{\partial\phi^2}. \quad (\text{A.7})$$

Now, lets start by slightly modifying Eq. 2.33 and expressing a random displacement in spherical coordinates as follows:

$$\delta\mathbf{r} = (\xi_r, r\xi_\theta, r\sin\theta\xi_\phi). \quad (\text{A.8})$$

Considering this formulation, and without loss of generality, we can write the perturbed continuity equation (Eq. 2.24) as

$$\rho' + \text{div}(\rho_0 \delta \mathbf{r}) = 0, \quad (\text{A.9})$$

$$\frac{\rho'}{\rho_0} + \frac{\xi_r}{\rho_0} \frac{\partial \rho_0}{\partial r} + \frac{1}{r^2} \frac{\partial}{\partial r}(r^2 \xi_r) + \frac{1}{r \sin \theta} \frac{\partial}{\partial \theta}(r \sin \theta \xi_\theta) + \frac{1}{r \sin \theta} \frac{\partial}{\partial \phi}(r \sin \theta \xi_\phi) = 0. \quad (\text{A.10})$$

In a similar manner, and assuming hydrostatic equilibrium, the perturbed equations for motion (Eq. 2.36 and 2.35) can be written for each of its components as

$$\frac{\partial^2 \xi_r}{\partial t^2} = \frac{1}{\rho_0} \frac{\partial P'}{\partial r} + \frac{\partial \Phi'}{\partial r} - \frac{\rho'}{\rho_0^2} \frac{\partial P_0}{\partial r}, \quad (\text{A.11})$$

$$\frac{\partial^2 (r \xi_\theta)}{\partial t^2} = \frac{1}{r} \frac{\partial}{\partial \theta} \left( \frac{P'}{\rho_0} + \Phi' \right), \quad (\text{A.12})$$

$$\frac{\partial^2 (r \sin \theta \xi_\phi)}{\partial t^2} = \frac{1}{r \sin \theta} \frac{\partial}{\partial \phi} \left( \frac{P'}{\rho_0} + \Phi' \right), \quad (\text{A.13})$$

where we remind the reader that the equilibrium structure depends only on the radial coordinate.

From the equations above, it is clear that the terms involved in the horizontal components ( $\xi_\theta$  and  $\xi_\phi$ ) include only derivatives in  $\theta$  and  $\phi$  as given by  $\nabla_h$  (Eq. A.5). Moreover, as the horizontal gradient in equilibrium quantities is zero, the horizontal divergence Eq. A.6 can be applied to the equations of motion and have all the tangential derivatives in terms of  $\nabla_h^2$ . A similar analysis can be carried out for the energy equation Eq. 2.28, where it can be shown (e.g., Ledoux & Walraven 1958) that it results in

$$P' + \xi_r \frac{\partial P_0}{\partial r} - \frac{\Gamma_{1,0} P_0}{\rho_0} \left( \rho' + \xi_r \frac{\partial \rho_0}{\partial r} \right) = \rho (\Gamma_{3,0} - 1) \delta q. \quad (\text{A.14})$$

On the left hand side of Eq. A.14, only radial derivatives appear. The term of the heat exchange  $\delta q$  (Eq. 2.29), if we consider the diffusion approximation for the flux given in Eq. 1.15, depends on the gradient of a scalar field (in this case the temperature  $T$ ). Once the perturbation is applied, the energy equation will only contain derivatives with respect to  $\theta$  and  $\phi$  in  $\nabla_h^2$ .

The advantages of this dependance are the following. We are trying to find the solutions as presented in Eq. 2.32, which we want to express in the form:

$$f(r, \theta, \phi, t) = \tilde{f}(r) f_2(\theta, \phi) \exp(-i\omega t). \quad (\text{A.15})$$

Due to the form of the equations, and that all tangential derivatives form part of  $\nabla_h^2$ , it is possible to factor out  $f_2(\theta, \phi)$  if it is an eigenfunction of the horizontal Laplace operator, and thus satisfies

$$\nabla_h^2 f_2(\theta, \phi) = -\frac{1}{r^2} k^2 f_2(\theta, \phi), \quad (\text{A.16})$$

where  $k^2$  is a constant. Using the horizontal Laplacian from Eq. A.7 we can write:

$$\frac{1}{\sin \theta} \frac{\partial}{\partial \theta} \left( \sin \theta \frac{\partial f_2}{\partial \theta} \right) + \frac{1}{\sin^2 \theta} \frac{\partial^2 f_2}{\partial \phi^2} = -k^2 f_2(\theta, \phi). \quad (\text{A.17})$$

Proposing a solution of the form  $f_2(\theta, \phi) = \Delta(\theta) \Omega(\phi)$ , Eq. A.17 reduces to

$$\frac{1}{\Delta \sin \theta} \frac{d}{d\theta} \left( \sin \theta \frac{d\Delta}{d\theta} \right) + \frac{1}{\Omega \sin^2 \theta} \frac{d^2 \Omega}{d\phi^2} = -k^2, \quad (\text{A.18})$$

$$\left[ -\frac{1}{\Delta \sin \theta} \frac{d}{d\theta} \left( \sin \theta \frac{d\Delta}{d\theta} \right) - k^2 \right] \sin^2 \theta = \frac{1}{\Omega} \frac{d^2 \Omega}{d\phi^2}. \quad (\text{A.19})$$

As the variables  $\theta$  and  $\phi$  are independent, each side of Eq. A.19 equates to a constant. Thus

$$\frac{1}{\Omega} \frac{d^2 \Omega}{d\phi^2} = -m^2, \quad (\text{A.20})$$

which has solutions of the form  $\Omega(\phi) = \exp(im\phi)$  when demanding the solution to be continuous and periodic. Normalization to make the function orthogonal in the azimuthal coordinate yields:

$$\Omega(\phi) = \frac{1}{\sqrt{2\pi}} \exp(im\phi). \quad (\text{A.21})$$

Replacing back into Eq. A.19, we obtain:

$$\frac{1}{\sin \theta} \frac{d}{d\theta} \left( \sin \theta \frac{d\Delta}{d\theta} \right) + \left( -\frac{m^2}{\sin^2 \theta} + k^2 \right) \Delta = 0, \quad (\text{A.22})$$

an equation known as an associated Legendre equation (e.g., Arfken & Weber 2005). It has only a regular solution when  $k^2 = \ell(\ell+1)$  and  $|m| \leq \ell$ . For those cases,  $\Delta$  is given by  $\Delta(\theta) = P_\ell^m(\cos \theta)$  where  $P_\ell^m$  are the associated Legendre functions.

The Legendre functions arise naturally as solutions of equations in many different physical situations. There are several ways of deriving these functions, and more than one general expression to define them. For instance, it can be shown that they follow:

$$P_\ell^m(x) = (1-x^2)^{m/2} \frac{d^m}{dx^m} P_\ell(x), \quad (\text{A.23})$$

$$P_\ell^m(x) = \frac{1}{2^\ell \ell!} (1-x^2)^{m/2} \frac{d^{m+\ell}}{dx^{m+\ell}} (x^2-1)^\ell, \quad -\ell \leq m \leq \ell; \quad (\text{A.24})$$

where  $P_\ell$  are the Legendre polynomials. The orthonormal function with respect to the polar angle  $\theta$  is obtained by a normalization, which gives an extra coefficient in Legendre functions

$$P_\ell^m(\cos \theta) = \sqrt{\frac{2\ell+1}{2} \frac{(\ell-m)!}{(\ell+m)!}} P_\ell^m(\cos \theta), \quad -\ell \leq m \leq \ell. \quad (\text{A.25})$$

In order to obtain a solution which is orthonormal to the spherical surface, we take the product of the two solutions and define:

$$\Delta(\theta) \Omega(\phi) = (-1)^m \sqrt{\frac{2\ell+1}{4\pi} \frac{(\ell-m)!}{(\ell+m)!}} P_\ell^m(\cos \theta) \exp(im\phi) \equiv Y_\ell^m(\theta, \phi), \quad (\text{A.26})$$

which is exactly the expression given in Eq. 2.38, and defines the spherical harmonics. This allowed to write the solutions of the equations, as shown in Eq. A.15, in the form given by Eq. 2.39. As a side remark, the factor  $(-1)^m$  is a phase factor introduced to alternate the sign of positive  $m$  spherical harmonics, which has important consequences in quantum theory of angular momentum.

From the above equations, it is clear that the geometry of the oscillations will be defined by the spherical harmonics comprising the eigenfunction of each oscillation mode. The simplest modes are the radial oscillation mode ( $\ell = 0$ ), and the simplest of those modes is the fundamental mode, where the star swells and contracts as a whole. The first overtone has a radial node in a concentric shell within the star; in terms of a radial displacement the node does not move, thus the motions above and below the node occur in antiphase.

Non-radial oscillations are modes with  $\ell \geq 1$ , with many examples of them shown in Fig. A.1. While the positive contours heat up and swell, the negative counterparts cool down and contract. The value of  $\ell$  and  $m$  define the number of nodal lines in latitude and longitude, respectively.

Only for the case of the Sun, observations of the oscillations are able to resolve the stellar disk and identify the nodal lines directly from the doppler maps. For other stars, as they cannot be resolved, we must deal with integrated observations along the stellar surface. It is clear from the cases presented in Fig. A.1 that, due to partial cancellation of positive and negative regions, the observed brightness variations are increasingly more difficult to detect for higher degree  $\ell$  (assuming an inclination angle). This means that even with the current precision attained with the space missions, in asteroseismic observations only low-degree modes  $\ell \lesssim 4$  can be observed.

Finally, a few words about the effects of rotation in the oscillation frequencies. From Eqs. 2.38 and 2.39 it can be seen that, for  $m \neq 0$ , the time dependence goes as  $\exp(-i(\omega t - m\phi))$ . This phase factor means that the solutions are traveling waves, which in our sign convention result in a wave traveling in the direction of the rotation for  $m > 0$  (prograde modes) and against the rotation for  $m < 0$  (retrograde modes). Remembering that  $-\ell \leq m \leq \ell$ , the  $2\ell + 1$  multiplets of a particular frequency are the same in the case of a spherically symmetric star. Rotation favors a particular axis, and thus this degeneracy can be lifted. The mode is then splitted into the components of the multiplet as:

$$\frac{\omega_{n,\ell,m}}{2\pi} = \nu_{n,\ell,m} = \nu_{n,\ell} + m(1 - C_{n,\ell})\frac{\Omega}{2\pi}, \quad (\text{A.27})$$

where  $C_{n,\ell}$  is a mode dependent quantity and  $\Omega$  is the angular frequency. This description holds as long as  $\nu_{n,\ell} \gg \Omega/2\pi$  and  $\Omega \ll \sqrt{GM/R^3}$  (e.g. Ballot et al. 2010). See Ledoux (1951) for detailed accounts on the derivation of this formula.

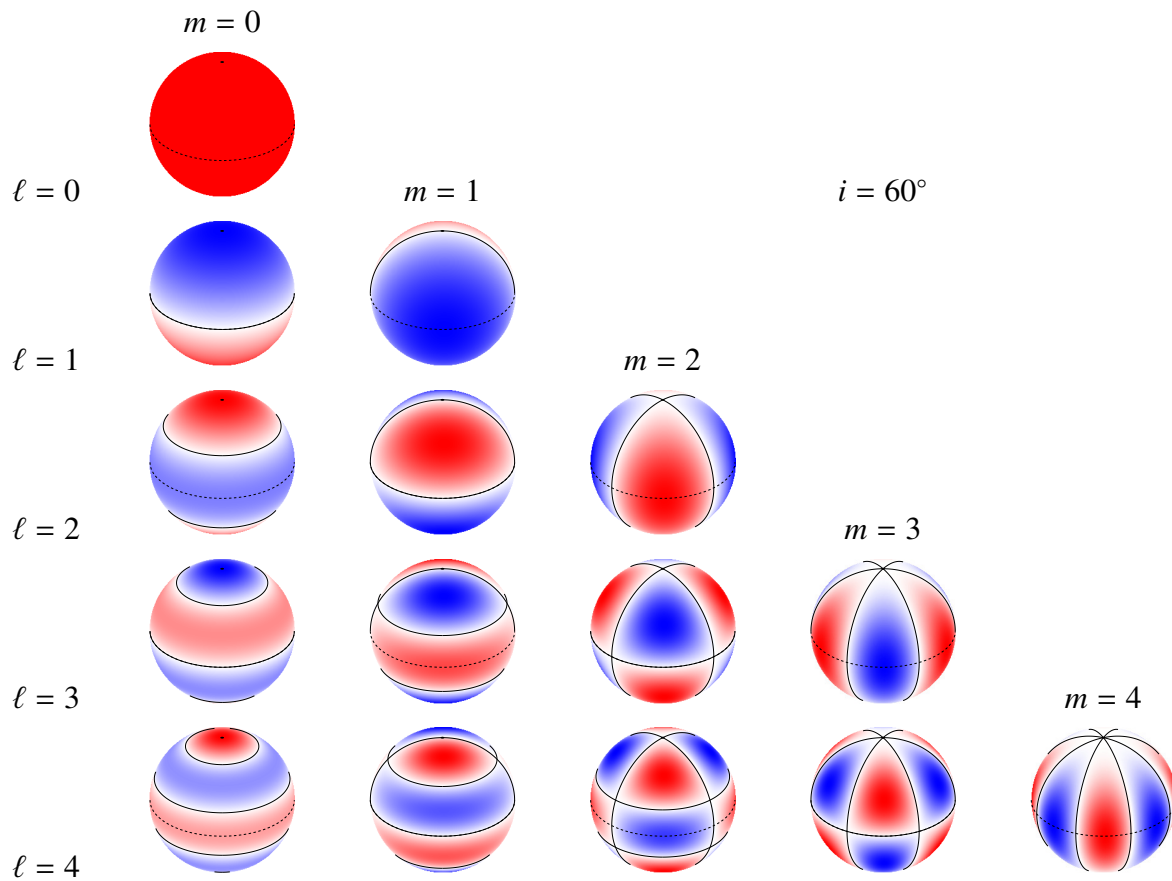


Figure A.1: Snapshot of the radial component of various modes as seen by an observer under an inclination angle of  $60^\circ$ . Solid lines show the positions of the nodes; red and blue represent sections of the star that are moving in (out) at any given time, then vice versa. Values of  $\ell$  and  $m$  are indicated. Figure kindly provided by J. Ballot.



# Bibliography

- Adelberger, E. G., Austin, S. M., Bahcall, J. N., et al. 1998, *Reviews of Modern Physics*, 70, 1265
- Aerts, C., Christensen-Dalsgaard, J., & Kurtz, D. W. 2010, *Asteroseismology*, ed. Aerts, C., Christensen-Dalsgaard, J., & Kurtz, D. W.
- Angulo, C., Arnould, M., Rayet, M., et al. 1999, *Nuclear Physics A*, 656, 3
- Antia, H. M. & Basu, S. 1994, *The Astrophysical Journal*, 426, 801
- Appourchaux, T., Michel, E., Auvergne, M., et al. 2008, *Astronomy and Astrophysics*, 488, 705
- Arfken, G. B. & Weber, H. J. 2005, *Mathematical methods for physicists* 6th ed. by George B. Arfken and Hans J. Weber. Published :Amsterdam
- Asplund, M., Grevesse, N., & Sauval, A. J. 2005, *Cosmic Abundances as Records of Stellar Evolution and Nucleosynthesis in honor of David L. Lambert*, 336, 25
- Asplund, M., Grevesse, N., Sauval, A. J., & Scott, P. 2009, *Annual Review of Astronomy & Astrophysics*, 47, 481
- Audard, N. & Provost, J. 1994, *Astronomy and Astrophysics*, 282, 73
- Audard, N., Provost, J., & Christensen-Dalsgaard, J. 1995, *Astronomy and Astrophysics*, 297, 427
- Baglin, A., Michel, E., Auvergne, M., & Team, T. C. 2006, *Proceedings of SOHO 18/GONG 2006/HELAS I*, 624, 34
- Bahcall, J. N., Basu, S., Pinsonneault, M., & Serenelli, A. M. 2005, *The Astrophysical Journal*, 618, 1049
- Bahcall, J. N., Pinsonneault, M. H., & Basu, S. 2001, *The Astrophysical Journal*, 555, 990
- Ballot, J., Lignières, F., Reese, D. R., & Rieutord, M. 2010, *Astronomy and Astrophysics*, 518, 30
- Ballot, J., Turck-Chièze, S., & García, R. A. 2004, *Astronomy and Astrophysics*, 423, 1051

- Bascoul, G. P. 2007, *Convection in Astrophysics*, 239, 317
- Basu, S. & Antia, H. M. 2004, *The Astrophysical Journal*, 606, L85
- Basu, S. & Antia, H. M. 2008, *Physics Reports*, 457, 217
- Basu, S., Chaplin, W. J., & Elsworth, Y. 2010, *The Astrophysical Journal*, 710, 1596
- Bazot, M., Ireland, M. J., Huber, D., et al. 2011, *Astronomy and Astrophysics*, 526, L4
- Beck, P. G., Bedding, T. R., Mosser, B., et al. 2011, *Science*, 332, 205
- Bedding, T. R., Butler, R. P., Kjeldsen, H., et al. 2001, *The Astrophysical Journal*, 549, L105
- Bedding, T. R., Huber, D., Stello, D., et al. 2010a, *The Astrophysical Journal Letters*, 713, L176
- Bedding, T. R. & Kjeldsen, H. 2003, *Publications of the Astronomical Society of Australia*, 20, 203
- Bedding, T. R. & Kjeldsen, H. 2007, *UNSOLVED PROBLEMS IN STELLAR PHYSICS: A Conference in Honor of Douglas Gough*. AIP Conference Proceedings, 948, 117
- Bedding, T. R., Kjeldsen, H., Campante, T. L., et al. 2010b, *The Astrophysical Journal*, 713, 935
- Bedding, T. R., Mosser, B., Huber, D., et al. 2011, *Nature*, 471, 608
- Belkacem, K., Goupil, M. J., Dupret, M. A., et al. 2011, *Astronomy and Astrophysics*, 530, 142
- Benomar, O., Baudin, F., Campante, T. L., et al. 2009, *Astronomy and Astrophysics*, 507, L13
- Böhm-Vitense, E. 1958, *Zeitschrift für Astrophysik*, 46, 108
- Borucki, W., Koch, D., Batalha, N., et al. 2009, *Transiting Planets*, 253, 289
- Bouchy, F. & Carrier, F. 2001, *Astronomy and Astrophysics*, 374, L5
- Brandão, I. M., Cunha, M. S., Creevey, O. L., & Christensen-Dalsgaard, J. 2010, *Astron. Nachr.*, 331, 940
- Broomhall, A.-M., Chaplin, W. J., Davies, G. R., et al. 2009, *Monthly Notices of the Royal Astronomical Society: Letters*, 396, L100
- Brown, T. M., Gilliland, R. L., Noyes, R. W., & Ramsey, L. W. 1991, *The Astrophysical Journal*, 368, 599
- Brown, T. M., Latham, D. W., Everett, M. E., & Esquerdo, G. A. 2011, *The Astronomical Journal*, 142, 112
- Bruntt, H., Bedding, T. R., Quirion, P.-O., et al. 2010, *Monthly Notices of the Royal Astronomical Society*, 405, 1907

- Bruntt, H., Cat, P. D., & Aerts, C. 2008, *Astronomy and Astrophysics*, 478, 487
- Buzasi, D., Catanzarite, J., Laher, R., et al. 2000, *The Astrophysical Journal*, 532, L133
- Campante, T. L., Karoff, C., Chaplin, W. J., et al. 2010, *Monthly Notices of the Royal Astronomical Society*, 408, 542
- Canuto, V. M. 1999, *The Astrophysical Journal*, 524, 311
- Canuto, V. M. & Mazzitelli, I. 1991, *The Astrophysical Journal*, 370, 295
- Canuto, V. M. & Mazzitelli, I. 1992, *The Astrophysical Journal*, 389, 724
- Casagrande, L., Flynn, C., Portinari, L., Girardi, L., & Jimenez, R. 2007, *Monthly Notices of the Royal Astronomical Society*, 382, 1516
- Casagrande, L., Ramírez, I., Meléndez, J., Bessell, M., & Asplund, M. 2010, *Astronomy and Astrophysics*, 512, 54
- Casagrande, L., Schönrich, R., Asplund, M., et al. 2011, *Astronomy and Astrophysics*, 530, 138
- Cassisi, S., Potekhin, A. Y., Pietrinferni, A., Catelan, M., & Salaris, M. 2007, *The Astrophysical Journal*, 661, 1094
- Catelan, M. 2007, *GRADUATE SCHOOL IN ASTRONOMY: XI Special Courses at the National Observatory of Rio de Janeiro (XI CCE)*. AIP Conference Proceedings, 930, 39
- Catelan, M. 2009, *Astrophys. Space Sci.*, 320, 261
- Catelan, M., Pritzl, B. J., & Smith, H. A. 2004, *The Astrophysical Journal Supplement Series*, 154, 633
- Chaplin, W. J., Appourchaux, T., Elsworth, Y., et al. 2010, *The Astrophysical Journal Letters*, 713, L169
- Chaplin, W. J., Bedding, T. R., Bonanno, A., et al. 2011a, *The Astrophysical Journal Letters*, 732, L5
- Chaplin, W. J., Elsworth, Y., Isaak, G. R., et al. 2002, *Monthly Notices of the Royal Astronomical Society*, 336, 979
- Chaplin, W. J., Kjeldsen, H., Bedding, T. R., et al. 2011b, *The Astrophysical Journal*, 732, 54
- Chaplin, W. J., Kjeldsen, H., Christensen-Dalsgaard, J., et al. 2011c, *Science*, 332, 213
- Chiosi, C. 1978, In: *The HR diagram - The 100th anniversary of Henry Norris Russell; Proceedings of the Symposium*, 80, 357
- Chiosi, C., Bertelli, G., & Bressan, A. 1992, *Annu. Rev. Astro. Astrophys.*, 30, 235

- Christensen-Dalsgaard, J. 1988, in IAU Symposium, Advances in Helio- and Asteroseismology, 123, 295
- Christensen-Dalsgaard, J. 2002, Reviews of Modern Physics, 74, 1073
- Christensen-Dalsgaard, J. 2004, Sol. Phys., 220, 137
- Christensen-Dalsgaard, J. 2008, Astrophys. Space Sci., 316, 113
- Christensen-Dalsgaard, J., Arentoft, T., Brown, T. M., et al. 2007, Communications in Asteroseismology, 150, 350
- Christensen-Dalsgaard, J., Dappen, W., Ajukov, S. V., et al. 1996, Science, 272, 1286
- Christensen-Dalsgaard, J., Gough, D. O., & Thompson, M. J. 1991, The Astrophysical Journal, 378, 413
- Christensen-Dalsgaard, J. & Hernández, F. P. 1991, Challenges to Theories of the Structure of Moderate-Mass Stars, 388, 43
- Christensen-Dalsgaard, J., Kjeldsen, H., Brown, T. M., et al. 2010, The Astrophysical Journal Letters, 713, L164
- Christensen-Dalsgaard, J. & Mauro, M. P. D. 2007, EAS Publications Series, 26, 3
- Christensen-Dalsgaard, J., Monteiro, M. J. P. F. G., & Thompson, M. J. 1995, Monthly Notices of the Royal Astronomical Society, 276, 283
- Clayton, D. D. 1983, Principles of stellar evolution and nucleosynthesis, University of Chicago Press
- Cowling, T. G. 1941, Monthly Notices of the Royal Astronomical Society, 101, 367
- Cox, J.-P. 1980, Theory of stellar pulsation, Princeton University Press, 1
- Crowe, R. A. & Mitalas, R. 1982, Astronomy and Astrophysics, 108, 55
- Cunha, M. S., Aerts, C., Christensen-Dalsgaard, J., et al. 2007, Astronomy and Astrophysics Review, 14, 217
- Cunha, M. S. & Brandão, I. M. 2011, Astronomy and Astrophysics, 529, 10
- Cunha, M. S. & Metcalfe, T. S. 2007, The Astrophysical Journal, 666, 413
- De-Meulenaer, P., Carrier, F., Miglio, A., et al. 2010, Astronomy and Astrophysics, 523, 54
- De-Ridder, J., Barban, C., Baudin, F., et al. 2009, Nature, 459, 398
- Deheuvels, S. & Michel, E. 2010, Astrophys. Space Sci., 328, 259

- Deheuvels, S., Michel, E., Goupil, M. J., et al. 2010, *Astronomy and Astrophysics*, 514, 31
- Deubner, F.-L. & Gough, D. 1984, *Annu. Rev. Astro. Astrophys.*, 22, 593
- Dintrans, B. 2009, *Communications in Asteroseismology*, 158, 45
- Duvall, T. L. 1982, *Nature*, 300, 242
- Dziembowski, W. A. & Pamyatnykh, A. A. 1991, *Astronomy and Astrophysics*, 248, L11
- Faulkner, D. J. & Cannon, R. D. 1973, *The Astrophysical Journal*, 180, 435
- Ferguson, J. W., Alexander, D. R., Allard, F., et al. 2005, *The Astrophysical Journal*, 623, 585
- Frandsen, S., Carrier, F., Aerts, C., et al. 2002, *Astronomy and Astrophysics*, 394, L5
- Freytag, B., Ludwig, H.-G., & Steffen, M. 1996, *Astronomy and Astrophysics*, 313, 497
- Gabriel, M. & Noels, A. 1977, *Astronomy and Astrophysics*, 54, 631
- Gai, N., Basu, S., Chaplin, W. J., & Elsworth, Y. 2011, *The Astrophysical Journal*, 730, 63
- García, R. A., Hekker, S., Stello, D., et al. 2011, *Monthly Notices of the Royal Astronomical Society: Letters*, 414, L6
- Gilliland, R. L. 1985, *The Astrophysical Journal*, 299, 286
- Gilliland, R. L., Brown, T. M., Christensen-Dalsgaard, J., et al. 2010a, *Publications of the Astronomical Society of the Pacific*, 122, 131
- Gilliland, R. L., Jenkins, J. M., Borucki, W. J., et al. 2010b, *The Astrophysical Journal Letters*, 713, L160
- Girardi, L. 1999, *Monthly Notices of the Royal Astronomical Society*, 308, 818
- Godart, M. 2007, *Communications in Asteroseismology*, 150, 185
- Gough, D. O. 1990, *Progress of Seismology of the Sun and Stars*, 367, 283
- Grevesse, N. & Noels, A. 1993, *Phys. Scr. T*, 47, 133
- Grevesse, N. & Sauval, A. J. 1998, *Space Sci. Rev.*, 85, 161
- Grigahcène, A., Antoci, V., Balona, L., et al. 2010, *The Astrophysical Journal Letters*, 713, L192
- Grossman, S. A. & Taam, R. E. 1996, *Monthly Notices of the Royal Astronomical Society*, 283, 1165
- Hansen, C. J., Kawaler, S. D., & Trimble, V. 2004, *Stellar interiors : physical principles, structure and evolution*, 2nd ed., New York: Springer-Verlag.

- Hekker, S., Broomhall, A.-M., Chaplin, W. J., et al. 2010, *Monthly Notices of the Royal Astronomical Society*, 402, 2049
- Hekker, S., Elsworth, Y., Ridder, J. D., et al. 2011a, *Astronomy and Astrophysics*, 525, 131
- Hekker, S., Gilliland, R. L., Elsworth, Y., et al. 2011b, *Monthly Notices of the Royal Astronomical Society*, 414, 2594
- Hekker, S., Kallinger, T., Baudin, F., et al. 2009, *Astronomy and Astrophysics*, 506, 465
- Herwig, F., Bloeker, T., Schoenberner, D., & Eid, M. E. 1997, *Astronomy and Astrophysics*, 324, L81
- Huber, D., Bedding, T. R., Stello, D., et al. 2010, *The Astrophysical Journal*, 723, 1607
- Huber, D., Stello, D., Bedding, T. R., et al. 2009, *Communications in Asteroseismology*, 160, 74
- Hummer, D. G. & Mihalas, D. 1988, *The Astrophysical Journal*, 331, 794
- Iglesias, C. A. & Rogers, F. J. 1996, *The Astrophysical Journal*, 464, 943
- Itoh, N., Mitake, S., Iyetomi, H., & Ichimaru, S. 1983, *The Astrophysical Journal*, 273, 774
- Jeans, J. H. 1928, *Astronomy and Cosmogony*, ed. Jeans, J. H., 4.
- Kallinger, T., Mosser, B., Hekker, S., et al. 2010, *Astronomy and Astrophysics*, 522, 1
- Karoff, C., Chaplin, W. J., Appourchaux, T., et al. 2010, *Astron. Nachr.*, 331, 972
- Kato, S. 1966, *Publications of the Astronomical Society of Japan*, 18, 374
- Kippenhahn, R. & Weigert, A. 1990, *Stellar structure and evolution*, Springer-Verlag.
- Kjeldsen, H. & Bedding, T. R. 1995, *Astronomy and Astrophysics*, 293, 87
- Kjeldsen, H. & Bedding, T. R. 2011, *Astronomy and Astrophysics*, 529, L8
- Kjeldsen, H., Bedding, T. R., & Christensen-Dalsgaard, J. 2008, *The Astrophysical Journal*, 683, L175
- Krishna-Swamy, K. 1966, *The Astrophysical Journal*, 145, 174
- Landau, L. D. & Lifshitz, E. M. 1959, *FLuid Mechanics, Course of theoretical physics*, Oxford: Pergamon Press
- Langer, N. 1991, *Astronomy and Astrophysics*, 252, 669
- Langer, N., Eid, M. F. E., & Fricke, K. J. 1985, *Astronomy and Astrophysics*, 145, 179
- Langer, N., Fricke, K. J., & Sugimoto, D. 1983, *Astronomy and Astrophysics*, 126, 207

- Leavitt, H. S. & Pickering, E. C. 1912, Harvard College Observatory Circular, 173, 1
- Lebreton, Y., Montalbán, J., Christensen-Dalsgaard, J., Roxburgh, I. W., & Weiss, A. 2008, *Astrophys. Space Sci.*, 316, 187
- Lebreton, Y., Montalbán, J., Godart, M., et al. 2009, *Communications in Asteroseismology*, 158, 277
- Ledoux, P. 1951, *The Astrophysical Journal*, 114, 373
- Ledoux, P. & Walraven, T. 1958, *Handbuch der Physik*, 51, 353
- Ledoux, W. P. 1947, *The Astrophysical Journal*, 105, 305
- Leeuwen, F. V. 2007, *Astronomy and Astrophysics*, 474, 653
- Leighton, R. B., Noyes, R. W., & Simon, G. W. 1962, *The Astrophysical Journal*, 135, 474
- Maeder, A. 1974a, *Stellar Instability and Evolution; Proceedings of the Symposium*, 59, 109
- Maeder, A. 1974b, *Astronomy and Astrophysics*, 32, 177
- Maeder, A. 2009, Springer
- Maeder, A. & Meynet, G. 1991, *Astronomy and Astrophysics Supplement Series*, 89, 451
- Maeder, A. & Meynet, G. 2000, *Annu. Rev. Astro. Astrophys.*, 38, 143
- Magic, Z., Serenelli, A., Weiss, A., & Chaboyer, B. 2010, *The Astrophysical Journal*, 718, 1378
- Marta, M., Formicola, A., Gyürky, G., et al. 2008, *Phys. Rev. C*, 78, 22802
- Martić, M., Schmitt, J., Lebrun, J.-C., et al. 1999, *Astronomy and Astrophysics*, 351, 993
- Mathur, S., García, R. A., Régulo, C., et al. 2010, *Astronomy and Astrophysics*, 511, 46
- Mazumdar, A. & Antia, H. M. 2001, *Astronomy and Astrophysics*, 377, 192
- Mazumdar, A., Basu, S., Collier, B. L., & Demarque, P. 2006, *Monthly Notices of the Royal Astronomical Society*, 372, 949
- Merryfield, W. J. 1995, *The Astrophysical Journal*, 444, 318
- Metcalf, T. S., Monteiro, M. J. P. F. G., Thompson, M. J., et al. 2010, *The Astrophysical Journal*, 723, 1583
- Michel, E., Baglin, A., Auvergne, M., et al. 2008, *Science*, 322, 558
- Miglio, A., Montalbán, J., Baudin, F., et al. 2009, *Astronomy and Astrophysics*, 503, L21

- Miglio, A., Montalbán, J., Noels, A., & Eggenberger, P. 2008, *Monthly Notices of the Royal Astronomical Society*, 386, 1487
- Mihalas, D. 1970, *Stellar Atmospheres*, Series of Books in Astronomy and Astrophysics
- Milone, E. F., Stagg, C. R., & Kurucz, R. L. 1992, *The Astrophysical Journal Supplement Series*, 79, 123
- Mitalas, R. 1972, *The Astrophysical Journal*, 177, 693
- Molenda-Żakowicz, J., Latham, D. W., Catanzaro, G., Frasca, A., & Quinn, S. N. 2011, *Monthly Notices of the Royal Astronomical Society*, 42
- Monteiro, M. J. P. F. G., Christensen-Dalsgaard, J., & Thompson, M. J. 1994, *Astronomy and Astrophysics*, 283, 247
- Monteiro, M. J. P. F. G., Christensen-Dalsgaard, J., & Thompson, M. J. 2000, *Monthly Notices of the Royal Astronomical Society*, 316, 165
- Monteiro, M. J. P. F. G. & Thompson, M. J. 1998, *New Eyes to See Inside the Sun and Stars: I.A.U. Symposium*, 185, 317
- Monteiro, M. J. P. F. G. & Thompson, M. J. 2005, *Monthly Notices of the Royal Astronomical Society*, 361, 1187
- Mosser, B. & Appourchaux, T. 2009, *Astronomy and Astrophysics*, 508, 877
- Mosser, B., Belkacem, K., Goupil, M.-J., et al. 2010, *Astronomy and Astrophysics*, 517, 22
- Noels, A., Montalbán, J., Miglio, A., Godart, M., & Ventura, P. 2010, *Astrophys. Space Sci.*, 328, 227
- Otí-Floranes, H., Christensen-Dalsgaard, J., & Thompson, M. J. 2005, *Monthly Notices of the Royal Astronomical Society*, 356, 671
- Pagel, B. E. J. & Portinari, L. 1998, *Monthly Notices of the Royal Astronomical Society*, 298, 747
- Peimbert, M. & Torres-Peimbert, S. 1976, *The Astrophysical Journal*, 203, 581
- Pietrinferni, A., Cassisi, S., Salaris, M., & Castelli, F. 2004, *The Astrophysical Journal*, 612, 168
- Pinsonneault, M. 1997, *Annu. Rev. Astro. Astrophys.*, 35, 557
- Popielski, B. L. & Dziembowski, W. A. 2005, *Acta Astronomica*, 55, 177
- Provost, J., Mosser, B., & Berthomieu, G. 1993, *Astronomy and Astrophysics*, 274, 595

- Quirion, P.-O., Christensen-Dalsgaard, J., & Arentoft, T. 2010, *The Astrophysical Journal*, 725, 2176
- Reese, D. R., Macgregor, K. B., Jackson, S., Skumanich, A., & Metcalfe, T. S. 2009, *Astronomy and Astrophysics*, 506, 189
- Reimers, D. 1975, *Mem. Soc. R. Liège 6 Sér.*, 8, 369
- Reimers, D. 1977, *Astronomy and Astrophysics*, 57, 395
- Rogers, F. J. & Nayfonov, A. 2002, *The Astrophysical Journal*, 576, 1064
- Rogers, F. J., Swenson, F. J., & Iglesias, C. A. 1996, *The Astrophysical Journal*, 456, 902
- Roxburgh, I. W. 2004, In: *Second Eddington Workshop: Stellar structure and habitable planet finding*, 538, 23
- Roxburgh, I. W. 2005, *Astronomy and Astrophysics*, 434, 665
- Roxburgh, I. W. 2009, *Astronomy and Astrophysics*, 493, 185
- Roxburgh, I. W. & Vorontsov, S. V. 1994, *Monthly Notices of the Royal Astronomical Society*, 268, 880
- Roxburgh, I. W. & Vorontsov, S. V. 2001, *Monthly Notices of the Royal Astronomical Society*, 322, 85
- Roxburgh, I. W. & Vorontsov, S. V. 2003, *Astronomy and Astrophysics*, 411, 215
- Roxburgh, I. W. & Vorontsov, S. V. 2007, *Monthly Notices of the Royal Astronomical Society*, 379, 801
- Salaris, M. & Cassisi, S. 2005, *Evolution of Stars and Stellar Populations*, Wiley-VCH.
- Salaris, M., Cassisi, S., & Weiss, A. 2002, *The Publications of the Astronomical Society of the Pacific*, 114, 375
- Samadi, R., Georgobiani, D., Trampedach, R., et al. 2007, *Astronomy and Astrophysics*, 463, 297
- Schlattl, H., Cassisi, S., Salaris, M., & Weiss, A. 2001, *The Astrophysical Journal*, 559, 1082
- Schlattl, H., Weiss, A., & Ludwig, H.-G. 1997, *Astronomy and Astrophysics*, 322, 646
- Schönberg, M. & Chandrasekhar, S. 1942, *The Astrophysical Journal*, 96, 161
- Schönrich, R. & Binney, J. 2009a, *Monthly Notices of the Royal Astronomical Society*, 396, 203
- Schönrich, R. & Binney, J. 2009b, *Monthly Notices of the Royal Astronomical Society*, 399, 1145

- Schunker, H. & Cally, P. S. 2006, *Monthly Notices of the Royal Astronomical Society*, 372, 551
- Schwarzschild, M. & Härm, R. 1958, *The Astrophysical Journal*, 128, 348
- Serenelli, A. & Weiss, A. 2005, *Astronomy and Astrophysics*, 442, 1041
- Serenelli, A. M. & Basu, S. 2010, *The Astrophysical Journal*, 719, 865
- Serenelli, A. M., Basu, S., Ferguson, J. W., & Asplund, M. 2009, *The Astrophysical Journal Letters*, 705, L123
- Silva-Aguirre, V., Ballot, J., Serenelli, A. M., & Weiss, A. 2011a, *Astronomy and Astrophysics*, 529, 63
- Silva-Aguirre, V., Basu, S., Chaplin, W. J., et al. 2011b, in preparation, *Astronomy and Astrophysics*
- Silva-Aguirre, V., Catelan, M., Weiss, A., & Valcarce, A. A. R. 2008, *Astronomy and Astrophysics*, 489, 1201
- Silva-Aguirre, V., Chaplin, W. J., Ballot, J., et al. 2011c, *The Astrophysical Journal Letters*, 740, L2
- Sousa, S. G., Santos, N. C., Mayor, M., et al. 2008, *Astronomy and Astrophysics*, 487, 373
- Spruit, H. C. 1992, *Astronomy and Astrophysics*, 253, 131
- Stello, D., Basu, S., Bruntt, H., et al. 2010, *The Astrophysical Journal Letters*, 713, L182
- Stello, D., Chaplin, W. J., Basu, S., Elsworth, Y., & Bedding, T. R. 2009a, *Monthly Notices of the Royal Astronomical Society: Letters*, 400, L80
- Stello, D., Chaplin, W. J., Bruntt, H., et al. 2009b, *The Astrophysical Journal*, 700, 1589
- Stevenson, D. J. 1979, *Monthly Notices of the Royal Astronomical Society*, 187, 129
- Stothers, R. 1970, *Monthly Notices of the Royal Astronomical Society*, 151, 65
- Stothers, R. & Chin, C.-W. 1975, *The Astrophysical Journal*, 198, 407
- Straka, C. W., Demarque, P., & Guenther, D. B. 2005, *The Astrophysical Journal*, 629, 1075
- Takata, M. 2005, *Publications of the Astronomical Society of Japan*, 57, 375
- Takata, M. 2006, *Publications of the Astronomical Society of Japan*, 58, 893
- Tassoul, M. 1980, *The Astrophysical Journal Supplement Series*, 43, 469
- Tassoul, M. 1990, *The Astrophysical Journal*, 358, 313

- Thompson, M. J. 2006, An introduction to astrophysical fluid dynamics, Imperial College Press.
- Thoul, A. A., Bahcall, J. N., & Loeb, A. 1994, *The Astrophysical Journal*, 421, 828
- Turcotte, S., Richer, J., Michaud, G., Iglesias, C. A., & Rogers, F. J. 1998, *The Astrophysical Journal*, 504, 539
- Ulrich, R. K. 1986, *The Astrophysical Journal*, 306, L37
- Unno, W., Osaki, Y., Ando, H., Saio, H., & Shibahashi, H. 1989, *Nonradial oscillations of stars*, Tokyo: University of Tokyo Press
- Unno, W. & Spiegel, E. A. 1966, *Publications of the Astronomical Society of Japan*, 18, 85
- Vandenberg, D. A., Bergbusch, P. A., & Dowler, P. D. 2006, *The Astrophysical Journal Supplement Series*, 162, 375
- Vandenberg, D. A., Gustafsson, B., Edvardsson, B., Eriksson, K., & Ferguson, J. 2007, *The Astrophysical Journal*, 666, L105
- Ventura, P. 2007, *EAS Publications Series*, 26, 79
- Verner, G. A., Elsworth, Y., Chaplin, W. J., et al. 2011, *Monthly Notices of the Royal Astronomical Society*, 892
- Vorontsov, S. V. 1988, *Advances in Helio-and Asteroseismology: I.A.U. Symposium*, 123, 151
- Weiss, A. & Ferguson, J. W. 2009, *Astronomy and Astrophysics*, 508, 1343
- Weiss, A., Hillebrandt, W., Thomas, H.-C., & Ritter, H. 2005, *Cox & Giuli's principles of stellar structure, extended second edition*, ed. *Advances in astronomy and astrophysics*
- Weiss, A. & Schlattl, H. 2008, *Astrophys. Space Sci.*, 316, 99
- White, T. R., Bedding, T. R., Stello, D., et al. 2011, *The Astrophysical Journal*, accepted (arXiv:1109.3455)
- Zahn, J.-P. 1991, *Astronomy and Astrophysics*, 252, 179
- Zahn, J.-P. 1992, *Astronomy and Astrophysics*, 265, 115



# Acknowledgments

Looking back at the last three years, the immense amount of experiences had and knowledge gained, and the wonderful people I got to know and share things with, it is hard to properly acknowledge everyone who has made this achievement possible. I will try my best in the following lines.

I would first like to thank International Max Planck Research School and the Max Planck Institute for Astrophysics for giving me the opportunity to start this new adventure. Under the shelter of this institution I was able to meet and learn from several outstanding scientists, who provided me with a broader view of science and research. A particular mention in this respect to Martin Asplund, who had the vision of forming a group of excellence in stellar physics that I was lucky enough to be a part of. In this environment I am thankful to Patrick Baumann, Maria Bergemann, Luca Casagrande, Remo Collet, Karin Lind, Fernanda Nieva, Ivan Ramirez, Luca Sbordone, and Ralph Schönrich, for patiently showing me different aspects of astrophysics.

Parts of my PhD work could not have been done if it weren't for the support, patience and knowledge of several members of the Kepler Asteroseismic community. I am truly indebted to Sarbani Basu, Tim Bedding, Bill Chaplin, Jørgen Christensen-Dalsgaard, Margarida Cunha, Rafael García, Daniel Huber, Mario Monteiro, Andrea Miglio, Graham Verner, and Tim White, for all their work, collaboration, and advice. This list undoubtedly falls short.

Naturally, I would not be writing these lines of acknowledgment if it wasn't for my supervisor, Achim Weiß, and my official (and unofficial) co-supervisors Jérôme Ballot and Aldo Serenelli. To you I'm forever grateful for critically analyzing every single statement I made, steering me into the right direction when I seemed lost, and having the patience to deal with my never-ending stream of (mostly silly) questions about astrophysics. Most importantly, thank you for believing in me.

An important part of this journey naturally involved my fellow students. Thanks to Davide Burlon, Francesca Iannuzzi, Silvia Fabello, Laura Mascetti, Lucia Morganti, Carolina Nuñez, Marcella Ugliano, and Irina Zhuravleva, for sharing experiences, concerns, happiness, and mostly being around at all times. It was also a pleasure for me to be your student representative, a task I truly enjoyed during these three years. I am also thankful to my officemate Robert Yates, who patiently explained to me the subtleties of the English language while I wrote this thesis.

I have been lucky enough to live in different places of the world. Friends I have made along this road have been the supporting pillars in different moments of my life, supporting me and encouraging me to be here today. I am forever thankful to Pamela Arriagada, Raul Cañas, Luca Casagrande, Felipe Cors, Andrés Guerrero, Francesca Iannuzzi, Claudia Lagos, Ignacio Perez

Quintana, Ignacio Perez Silva, Jorge Peña, Cristobal Petrovich, Oliver Pfuhl, Ian Somlai, and many others that, to one extent or another, are part of this story.

What started as a dream more than 15 years ago is now a reality: I am an astronomer. I owe this to my family, who blindly supported me regardless of the circumstances. My parents, Víctor and Lucia, and my sisters, Mariana and Maria-Paz, are the ones I will always be grateful to for making me who I am today. I hope, in return, I was able to marvel you with the wonders of the universe, and pass on my curiosity for understanding the world to my nieces and nephew Camila, Cristobal, Bárbara and Jazmín.

Last and definitely not least, to her, Daniela. For your sincere love and unconditional support, gently bringing me down from the clouds where I know sometimes my mind lives. More than anything, for agreeing to take the next trip with me.

Víctor Silva Aguirre  
München, 2011

# Curriculum Vitae

VICTOR SILVA AGUIRRE

14.07.1982      Born in Santiago, Chile.

## EDUCATION

- 01.12.2000      High School Diploma obtained at Instituto O'Higgins in Rancagua, Chile.
- 01.03.2001 - Degree in Master of Science in Astronomy, Pontificia Universidad Católica de Chile, Santiago, Chile. Master thesis project conducted at the department of Astronomy and Astrophysics.  
01.08.2007  
Master thesis supervisors:  
Dr. Márcio Catelan  
Dr. Manuela Zoccali
- 01.03.2001 - Degree in Master of Science in Mechanical Engineering, Pontificia Universidad Católica de Chile, Santiago, Chile.  
01.03.2008
- 01.08.2008 - International Max Planck Research School (IMPRS) PhD student at the  
31.07.2011 Max Planck Institute for Astrophysics, Garching bei München, Germany.  
PhD thesis supervisor:  
Dr. Achim Weiß

## REFEREED PUBLICATIONS

- 2008      **V. Silva Aguirre**, M. Catelan, A. Weiss, & A. A. R. Valcarce  
*Stellar evolution and variability in the pre-ZAHB phase*  
Astronomy and Astrophysics, 2008, 489, 1201

- 2010 **V. Silva Aguirre**, M. Catelan, A. Weiss, & A. A. R. Valcarce  
*Pulsation period changes as a tool to identify pre-zero age horizontal branch stars*  
Astrophys. Space Sci., 2010, 328, 123
- 2010 **V. Silva Aguirre**, J. Ballot, A. Serenelli, & A. Weiss  
*Semiconvective mixing in low-mass stars*  
Astrophys. Space Sci., 2010, 328, 129
- 2010 W. J. Chaplin, T. Appourchaux, Y. Elsworth, R. A. Garca, G. Houdek, et al.  
*The Asteroseismic Potential of Kepler: First Results for Solar-Type Stars*  
The Astrophysical Journal, 2010, 713, L169
- 2010 D. Stello, S. Basu, H. Bruntt, B. Mosser, I. R. Stevens, et al.  
*Detection of Solar-like Oscillations from Kepler Photometry of the Open Cluster NGC 6819*  
The Astrophysical Journal, 2010, 713, L182
- 2010 T. S. Metcalfe, M. J. P. F. G. Monteiro, M. J. Thompson, J. Molenda-Żakowicz, T. Appourchaux, et al.  
*A Precise Asteroseismic Age and Radius for the Evolved Sun-like Star KIC 11026764*  
The Astrophysical Journal, 2010, 723, 1583
- 2011 **V. Silva Aguirre**, J. Ballot, A. Serenelli, & A. Weiss  
*Constraining mixing processes in stellar cores using asteroseismology. Impact of semiconvection in low-mass stars*  
Astronomy and Astrophysics, 2011, 529, A63
- 2011 T. R. Bedding, B. Mosser, D. Huber, J. Montalbán, P. Beck, et al.  
*Gravity modes as a way to distinguish between hydrogen- and helium-burning red giant stars*  
Nature, 2011, 471, 608
- 2011 W. J. Chaplin, H. Kjeldsen, J. Christensen-Dalsgaard, S. Basu, A. Miglio, et al.  
*Ensemble Asteroseismology of Solar-Type Stars with the NASA Kepler Mission*  
Science, 2011, 332, 213
- 2011 **V. Silva Aguirre**, W. J. Chaplin, J. Ballot, S. Basu, T. R. Bedding, et al.  
*Constructing a One-solar-mass Evolutionary Sequence Using Asteroseismic Data from Kepler*  
The Astrophysical Journal, 2011, 740, L2

- 
- 2011 D. Huber, T. R. Bedding, D. Stello, S. Hekker, S. Mathur, et al.  
*Testing Scaling Relations for Solar-Like Oscillations from the Main Sequence to Red Giants using Kepler Data*  
The Astrophysical Journal, 2011, in press (arXiv:1109.3460)
- 2011 A. Miglio, K. Brogaard, D. Stello, W. J. Chaplin, F. D'Antona, et al.  
*Asteroseismology of old open clusters with Kepler: direct estimate of the integrated RGB mass loss in NGC6791 and NGC6819*  
Monthly Notices of the Royal Astronomical Society, 2011, in press (arXiv:1109.4376)
- 2011 T. R. White, T. R. Bedding, D. Stello, T. Appourchaux, J. Ballot, et al.  
*Asteroseismic diagrams from a survey of solar-like oscillations with Kepler*  
The Astrophysical Journal, in press (arXiv:1110.1375)

#### CONFERENCE TALKS AND SEMINARS

- 07.2011 Contributed talk, Fourth Kepler asteroseismology workshop, Boulder, USA. *Stellar interiors as seen by Kepler: the quest for convective cores.*
- 05.2011 Stellar seminar, European Southern Observatory, Garching, Germany . *Asteroseismology in the Space Era.*
- 03.2011 Institute seminar, Centro de Astrofísica da Universidade do Porto, Porto, Portugal . *Asteroseismology in the Space Era.*
- 09.2009 Contributed talk, Stellar Astrophysics and Galactic Archeology workshop II, Eibsee, Germany. *Asteroseismology in main-sequence stars: the case of HD49933.*
- 08.2008 Contributed talk, Stellar Astrophysics and Galactic Archeology workshop I, Wildbald-Kreuth, Germany. *Asteroseismology in open clusters.*



